High-Temperature Water Effects on the Fracture Behaviour of Low-Alloy Reactor Pressure Vessel Steels

Thèse N° 9391

Présentée le 12 avril 2019

à la Faculté des sciences de base
Laboratoire de physique des réacteurs et de comportement des systèmes
Programme doctoral en science et génie des

pour l'obtention du grade de Docteur ès Sciences

par

Zaiqing QUE

Acceptée sur proposition du jury

Prof. D. Damjanovic, président du jury
Prof. Ph. Spätig, directeur de thèse
Prof. H. Hänninen, rapporteur
Prof. T. Shoji, rapporteur
Dr D. Mari, rapporteur

2019

ÉCOLE POLYTECHNIQUE
FÉDÉRALE DE LAUSANNE

Acknowledgements

For me, PhD means many many lessons to my life.

At the very beginning, I would like to thank Hans-Peter for the “utmost importance regarding operation”. He is a considerate person with very smart mind and disciplined life style, setting a lifelong example to me. When we were discussing, he was actually like a handbook on corrosion and structural integrity, always coming up with great solutions and advices. I would like to thank Philippe for being my thesis advisor. He offered great assistance in all aspects of my PhD period and showed me how to live the life with positive attitude and keep an elegant balance. In 2017 and 2018, I was very lucky to have A. Zhang and J. Holzer as internship (master thesis) students. Not only great contribution for the projects, they gave me a good lesson on “how to be a teacher”. The funding for the “SAFE-II” and “LEAD” projects from the Swiss Federal Nuclear Safety Inspectorate (ENSI) is gratefully acknowledged.

I will never forget the work from Hans, Beat, Roger and Dominik. I tortured them too much over the four years with all the experimental preparation and loop tests. I hope Beat could quick recover from the illness and come back soon. G. S. Rao is always helpful and I wish him a bright career. Stefan, Juxing, Wen, Nicolo and Elisabeth offered me great discussion over many topics. Without the help of all the colleagues in BTS group and LNM lab, this work simply could not be possible. Prof. Hannu Hänninen, Prof. Tesuo Shoji, Dr. Daniele Mari were so kind to accept to be my examiners, which means extra workload as well as massive paper work. I would like to thank J. Wheeler, M. Heczko, V. Mazanova and Y. Yagodzinskyy for their support on nano-indentation, STEM and TDS, respectively.

Friends and family members provide me the original power to get through the dark moments. My parents and Jing repair me with their love everytime when I get damages from the external world. Looking forward to the tiny green pea.

Villigen, March 2019

Abstract

The structural integrity of the reactor pressure vessel (RPV) of light water reactors (LWR) is of utmost importance regarding operation safety and lifetime. High-temperature water (HTW) and hydrogen absorbed from environment, in synergy with irradiation embrittlement, dynamic strain aging (DSA), environmentally-assisted cracking (EAC) or temper embrittlement (TE) may reduce the fracture resistance of RPV steels. The fracture behaviour in the upper shelf region of low-alloy RPV steels with different microstructures and DSA, EAC and TE susceptibilities in various simulated LWR environments was evaluated by elastic-plastic fracture mechanics tests.

In the reference RPV steel with low sulphur and phosphorus contents and low DSA, EAC and TE susceptibilities, environmental effects on fracture resistance are absent or marginal in both oxygenated and hydrogenated HTW. However, moderate but clear reduction of fracture initiation resistance occurred in:

a) Simulated coarse-grain heat-affected zone material with high yield stress, since a higher yield stress facilitates the hydrogen enrichment in the fracture process zone;

b) Low-sulphur RPV steels with high DSA susceptibility, where the reduction of fracture initiation resistance increased with decreasing loading rate at 288 °C and was most pronounced in hydrogenated HTW due to the localization of plastic deformation by the interaction between DSA and hydrogen;

c) High-sulphur RPV steels with high EAC susceptibility in aggressive occluded crevice environment (oxygenated HTW with addition of impurities) with preceding EAC crack growth, resulting from the enhancement of hydrogen availability and uptake;

and d) High-phosphorus RPV steel with high TE susceptibility, where the reduction of fracture initiation resistance was most pronounced in hydrogenated HTW, indicating that TE effect dominates over effects of occluded crevice chemistry.

In hydrogenated HTW, the reduction of fracture resistance correlated fairly well with the DSA susceptibility of different steels and sulphur content played no or a minor role. In oxygenated HTW, the reduction of fracture resistance increased with steel sulphur content for steels with low DSA susceptibility. Stable ductile transgranular tearing by micro-void coalescence dominates in both air and HTW environments. The fracture surface of specimens tested in air was mainly ductile. In contrast, specimens tested in HTW environments, varying amounts (a few %) of secondary cracking, macro-voids, quasi-cleavage and intergranular cracking were observed on fracture surface. The observed fracture modes and morphology suggest a combination of hydrogen-enhanced local plasticity and hydrogen-enhanced strain-induced vacancies mechanisms with minor contributions of hydrogen-enhanced decohesion embrittlement mechanism.

The main reason for the moderate degradation effects is the low hydrogen availability in HTW together with a high density of (fine-dispersed and strong) hydrogen traps in RPV steels. In addition, the environmental reduction and softening by hydrogen and HTW environments was partially compensated by the toughness increase due to DSA. Although the environmental effects are moderate, effects can be more critical for RPV materials with low initial upper shelf toughness under unfavourable combinations (high sulphur content, increased strength, high EAC, TE and DSA susceptibilities) or old plants with small margins regarding irradiation embrittlement.

Keywords

Low-Alloy Steel, Reactor Pressure Vessel, Hydrogen Embrittlement, Dynamic Strain Aging, Environmentally-Assisted Cracking, Temper Embrittlement, Fracture Resistance Reduction

Résumé

L’intégrité structurale de la cuve pressurisée des réacteurs nucléaires à eau légère est d’importance capitale en ce qui concerne la sûreté des conditions d’opération et le temps de vie. L’environnement, caractérisé par l’eau à haute température (EHT), et l’absorption d’hydrogène par les matériaux sont susceptibles de détériorer la ténacité en fracture, en synergie avec la fragilisation d’irradiation (FI), le vieillissement dynamique (VD), la fissuration assistée par environnement (FAE) ou encore la fragilisation de revenu (FR). Le comportement en fracture sur le plateau ductile de différents aciers de cuve, présentant des microstructures différentes et des sensibilités distinctes en VP, FAE et FR, a été évalué avec des essais de fracture élastique-plastique.

Pour l’acier de référence à faible teneur en soufre et phosphore et sensibilité minimale en VD, FAE et FR, les effets d’environnement sur la ténacité en fracture sont soit absents, soit confidentiels dans les milieux en eau oxygénée et hydrogénée à haute température. Cependant, une réduction modérée mais claire de la ténacité s’est révélée dans les cas suivants :

a) Matériau ayant une zone simulée affectée par la chaleur (autour d’une soudure) avec de gros grains et une limite d’élasticité élevée favorisant l’absorption d’hydrogène dans la zone d’initiation de la fracture.

b) Les aciers à faible teneur en soufre avec un fort VD, où la réduction de la ténacité augmente avec la décroissance de la vitesse de charge à 288 °C et étant plus marquée dans l’eau hydrogénée en raison de phénomènes de localisation de déformation plastique résultant de l’interaction entre VD et hydrogène.

c) Les aciers à haute teneur en soufre et forte sensibilité de FAE dans des crevasses obstruées (eau oxygénée avec impuretés) résultant de la croissance de fissures, produisant un enrichissement et une absorption facilités d’hydrogène.

d) Les aciers à haute teneur en phosphore et forte sensibilité de FR où la réduction de ténacité est la plus marquée en eau hydrogénée, ce qui indique que l’effet de FR prévaut sur les effets chimiques des crevasses obstruées.

En eau hydrogénée, la diminution de ténacité est bien corrélée avec le VD des différents aciers et la teneur en soufre ne joue pas de rôle. En eau oxygénée, la diminution de la ténacité augmente avec la teneur en soufre pour les aciers à basse sensibilité de VD. Le mode de fracture ductile/transgranulaire dans l'air et dans l'eau est dominant avec coalescence de micro-vides. Les surfaces de fracture des échantillons testés dans l'air sont essentiellement ductiles, alors que celles des échantillons testés dans l'eau présentent quelques pourcents avec des fissures secondaires, des macro-vides, du quasi-clivage et de la fissuration intergranulaire. Les modes de fracture et la morphologie observés suggèrent une combinaison de déformation plastique locale favorisée par l'hydrogène et de déformation induite par des mécanismes impliquant des lacunes résultant de la présence d'hydrogène avec une contribution minimale de mécanismes de décohésion locale favorisée par l'hydrogène.

La raison principale de la diminution modérée de la ténacité en fracture réside dans la faible teneur en hydrogène dans les milieux ainsi que de la haute densité de puits forts pour l'hydrogène dans les aciers de cuve de réacteurs. De plus, les effets négatifs de l'hydrogène et des milieux EHT sont partiellement compensés par l'augmentation de ténacité due au VD. Bien que les effets d'environnement soient modérés, ils peuvent être plus critiques pour certains aciers ayant un plateau ductile avec une valeur de ténacité relativement basse dans des conditions défavorables, comme par exemple une haute teneur en soufre, forte contrainte, et haute sensibilité de FAE, FR et VD, ou alors pour des réacteurs opérant avec des marges étroites de sûreté en matière de fragilisation.

Mots-clés

Aciers faiblement alliés, aciers de cuve de réacteurs, fragilisation par hydrogène, vieillissement dynamique, fissuration assistée par environnement, fragilisation par revenu, réduction de ténacité en fracture

Contents

Acknowledgements iii

Abstract v

Résumé vii

Nomenclature xi

List of Figures xiii

List of Tables xix

Introduction 1

Chapter 1 Literature review 5

- 1.1 Light water reactors 6
  - 1.1.1 Boiling and pressurized water reactors 6
  - 1.1.2 Water chemistry 8
  - 1.1.3 Reactor pressure vessel structure and materials 10
  - 1.1.4 Reactor pressure vessel structural integrity 15
- 1.2 Fracture mechanisms and toughness of RPV steels 18
  - 1.2.1 Ductile and brittle fracture and ductile to brittle transition 18
  - 1.2.2 Factors of influence on fracture toughness 24
  - 1.2.3 Fracture toughness measurement 26
- 1.3 Hydrogen embrittlement and hydrogen effects 27
  - 1.3.1 Characteristics and effects of hydrogen in RPV steel 27
  - 1.3.2 Hydrogen sources, trapping, transport and uptake 30
  - 1.3.3 Mechanisms of hydrogen embrittlement 40
  - 1.3.4 Interactions of HE with other degradation and embrittlement mechanisms 45
- 1.4 High-temperature water and hydrogen effect on fracture behaviour of RPV steels under LWR conditions 59
- 1.5 Conclusions, statement of the problem and goals for the PhD project 70

Chapter 2 Materials and experiments 71

- 2.1 Materials 71
  - 2.1.1 Chemical composition and mechanical properties 71
  - 2.1.2 Microstructure and heat treatments 75
  - 2.1.3 Non-metallic inclusions analysis 79
- 2.2 Experiments 81
  - 2.2.1 High-temperature water loops 81
  - 2.2.2 Elastic-plastic fracture mechanics tests 83
- 2.3 Post-test characterizations 94

Chapter 3 Results and discussion 97

3.1 Fracture behaviour of RPV steels in air 97

3.2 Fracture behaviour of Biblis C steels as reference material 99

3.3 Effect of high yield stress 100

3.4 Effect of high dynamic strain aging susceptibility 102

3.4.1 Fracture behaviour of 277 material 104

3.4.2 Fracture behaviour of 508 material 112

3.4.3 Discussion on the effect of dynamic strain aging 117

3.5 Effect of high environmentally-assisted cracking and high temper embrittlement susceptibilities 124

3.5.1 Fracture behaviour of HSST material with high sulphur and EAC susceptibility 126

3.5.2 Fracture behaviour of JRQ material with high phosphorus content and TE susceptibility 129

3.5.3 Fracture behaviour of KS12 material with high sulphur and high phosphorus contents 135

3.5.4 Discussion of the effect of EAC and TE susceptibility 139

3.6 Fracture mode and mechanisms 143

3.7 Final thoughts 149

Chapter 4 Conclusions and outlook 151

4.1 Conclusions 151

4.2 Outlook 154

References 157

Appendix 167

Curriculum Vitae 175

Nomenclature

ASTM	American society for testing and materials standards
BCC	Body-centred cubic
BM	Base metal
BWR	Boiling water reactor
CERT	Constant extension rate test
CF	Corrosion fatigue
CGHAZ	Coarse-grain heat-affected zone
C(T)	Compact tension
CTOD	Crack-tip opening displacement
DBTT	Ductile-brittle transition temperature
DCPD	Direct current potential drop
DH	Dissolved hydrogen
DO	Dissolved oxygen
DSA	Dynamic strain aging
EAC	Environmentally-assisted cracking
EBSD	Electron backscatter diffraction
ECCI	Electron channelling contrast imaging
ECP	(Open-circuit, free) electrochemical corrosion potential
EDM	Electrical discharge machining
EDX	Energy-dispersive X-ray spectroscopy
EPFM	Elastic-plastic fracture mechanics
FAC	Flow-accerelerated corrosion
FCC	Face-centred cubic
FRAD	Film rupture/anodic dissolution
GB	Grain boundary
GROD	Grain reference orientation deviation
HAC	Hydrogen-assisted cracking
HAEAC	Hydrogen-assisted environmentally-assisted cracking
HAZ	Heat-affected zone
HE	Hydrogen embrittlement
HEDE	Hydrogen-enhanced decohesion embrittlement mechanism
HELP	Hydrogen-enhanced localized plasticity mechanism
HESIV	Hydrogen-enhanced strain induced vacancy mechanism
HPW	High-purity water (without dissolved hydrogen nor oxygen)
HTW	High-temperature water
HV	Vickers hardness
HWC	Hydrogen water chemistry
KAM	Kernel average misorientation
LAS	Low-alloy steel
LLD	Load-line displacement
LOCA	Loss of coolant accident
LWR	Light water reactors
MVC	Micro-void coalescence
NWC	Normal water chemistry
OLNC	On-line noblechem
PAGB	Prior-austenite grain boundary
PWR	Pressurized water reactor

QC	Quasi-cleavage
RPV	Reactor pressure vessel
SC	Step cooled
SCC	Stress corrosion cracking
SEM	Scanning electron microscope
SICC	Strain-induced corrosion cracking
SSRT	Slow strain rate test
TDS	Thermal desorption spectroscopy
TE	Temper embrittlement
TEM	Transmission electron microscope
ULC	Unloading compliance
UTS	Ultimate tensile strength (MPa)
YS	Yield stress (MPa)

a	Crack length (mm)
a/W	Ratio of crack length (a) and C(T) specimen width (W)
Δa	Increase in crack length (m)
B	C(T) specimen thickness (mm)
B_N	C(T) specimen net-section thickness (mm)
1T-C(T)	Compact tension specimen of 25 mm thickness (B)
0.5T-C(T)	Compact tension specimen of 12.5 mm thickness (B)
$\mathrm{d}K/\mathrm{d}t$	Rate of change in stress intensity factor during fracture toughness test (MPa·m$^{0.5}$·h^{-1})
$\mathrm{d}J/\mathrm{d}t$	Rate of change in J integral during fracture toughness test (kN·m^{-1}·h^{-1})
E	Young’s modulus (GPa)
J	Fracture toughness defined in ASTM E1820 (kN·m^{-1})
J_{DCPD}	J at initiation measured from DCPD signal (kN·m^{-1})
J_{el}	Elastic component of J integral (kN·m^{-1})
J_{limit}	Maximum allowable J integral of C(T) specimen (kN·m^{-1})
J_{pl}	Plastic component of J integral (kN·m^{-1})
J_Q, J_{1c}	Fracture toughness at initiation of stable crack growth (kN·m^{-1})
K	Stress intensity factor (MPa·m$^{0.5}$)
K_{max}	Stress intensity factor (K) at maximum load during cyclic loading (MPa·m$^{0.5}$)
K_{min}	Stress intensity factor (K) at minimum load during cyclic loading (MPa·m$^{0.5}$)
ΔK	K_{max} - K_{min} (MPa·m$^{0.5}$)
ppb	Parts per billion
ppm	Parts per million
appm	Atomic parts per million
wppm	Parts per million by weight
pH	-log(H$^+$), where H$^+$ is hydrogen ion concentration in water
Q	Activation energy
R	Ratio F_{min}/ F_{max}
T	Temperature
To	Reference temperature (transition temperature) according to ASTM E1921
t	Time (s)
ΔU	Potential drop
W	C(T) specimen width (mm)
ν	Poisson’s ratio
ε	Strain
$\dot{\varepsilon}$	Strain rate (s^{-1})
$\sigma_{ys}^{288°C}$	Yield stress at 288 °C (MPa)

List of Figures

Figure 1: Schematic of a PWR with materials used in different components [20]. 7

Figure 2: Schematic of a BWR with materials used in different components [20]. 8

Figure 3: Typical PWR and BWR pressure vessels [25]. 11

Figure 4: Deterministic fracture mechanics RPV integrity analysis. (NDT: non-destructive testing; ISI: in-service inspection; CFD: computational fluid dynamics) 16

Figure 5: Flaw tolerance evaluation on RPV. 17

Figure 6: The ductile to brittle transition behaviour of bcc LAS. 20

Figure 7: (a) Hardening embrittlement by increase of yield stress; (b) non-hardening embrittlement by reduction of cleavage fracture stress. 21

Figure 8: Fracture modes and paths in case of RPV steels. 23

Figure 9: Effects of (a) grain size, (b) sulphur content, (c) impurity grain boundary segregation and (d) segregation zones on fracture toughness [44][45][46][47]. 25

Figure 10: Schematic illustrations of sites and traps for hydrogen in materials (A) on the atomic scale and (B) on a microscopic scale [14]. 33

Figure 11: Illustration of binding and de-trapping energies [79]. 34

Figure 12: Dependence of trap occupancy on temperature, dissolved hydrogen and trap energies. 35

Figure 13: Effect of yield stress on hydrogen enrichment at crack tip. 36

Figure 14: Hydrogen redistribution probability between traps (with a binding energy E_B) far away from the crack tip to the crack tip. 36

Figure 15: Temperature dependence of proportionality constant $S(T) \cdot k(T)^{1/2}$ of Equation (7) (left axis) and ratio of absorbed hydrogen contents in the metal at temperature T with respect to 288 °C for a given dissolved hydrogen content in HTW (right axis) [83][84]. 38

Figure 16: Hydrogen gradient through the RPV structure. 39

Figure 17: Major factors of influence for HE in RPV steels. 42

Figure 18: Effect of yield stress on threshold K_{th} for sub-critical HAC and K_{IC} in high-strength LAS [60]. 43

Figure 19: Effect of n-irradiation (288 °C, 8×10^{19} n/cm^2 ($E > 0.5$ MeV)) and hydrogen content from hydrogen pre-charging on the toughness in the upper shelf and transition region of a VVER RPV steel [90]. 44

Figure 20: Localized hydrogen uptake, hydrogen-deformation interactions and hydrogen embrittlement in the crack-tip system during an EPFM test [63]. 46

Figure 21: FRAD mechanism with controlling factors and conjoint requirement for EAC [100]. 48

Figure 22: Variation of tearing resistance (J values at a crack growth of 2.54 mm), with temperature and loading rate [11]. 52

Figure 23: Effect of neutron irradiation on temperature dependence of upper shelf crack initiation fracture toughness [122] and energy to fracture [123]. 53

Figure 24: Effect of hydrogen on DSA in SA 508 Cl. 3 pressure vessel steel [88]. 53

Figure 25: Illustration of the correlation between phosphorus concentration at grain boundaries and Charpy DBTT [132]. 55

Figure 26: Tensile stress-strain curves of a high DSA steel in air (with and without hydrogen pre-charging) and in hydrogenated water at 288 °C. 60

Figure 27: Nominal notched tensile stress-strain curves for different RPV steels in air and hydrogenated water at 288 °C. 61

Figure 28: (a) Effect of hydrogen concentration at crack tip on HAC growth at different temperatures; (b) temperature dependence of critical hydrogen concentration at crack tip [153]. 61

Figure 29: *J-R* curves for the material 20MnMoNi 5 5 with 0.003 wt.% sulphur (a) and 0.011wt.% sulphur (b) in HTW and in air, respectively [15]. 62

Figure 30: (a) *J-R* curve for SA533B Cl. 1 steel in BWR environment and air; (b) dependence of toughness reduction factor in HTW on yield strength with different fracture modes [154]. 63

Figure 31: Effect of hydrogen content on stress-strain curves in tensile tests in Biblis C base metal (BM) and simulated CGHAZ at 288 °C. 64

Figure 32: Maximum in hydrogen embrittlement (loss of ductility as the reduction of area) at a strain rate of 10^{-2} s^{-1} in Biblis C base metal and simulated coarse-grain heat-affected zone (CGHAZ) at 288 °C. 65

Figure 33: Effect of hydrogen content on ductility and hydrogen embrittlement in Biblis C base metal and simulated coarse-grain heat-affected zone (CGHAZ) at 288 °C with 10^{-2} s^{-1}. 65

Figure 34: Hydrogen-induced softening in ultimate tensile strength (UTS) and yield stress (YS) in Biblis C base metal (BM) (a) and coarse-grain heat-affected zone (CGHAZ) (b). 66

Figure 35: Hydrogen-induced reduction of strain hardening capacity in UTS (ultimate tensile strength) and YS (yield stress) for steels with different DSA susceptibilities. 66

Figure 36: Amplification of magnitude and extension of strain rate range of hydrogen embrittlement in case of a high DSA susceptibility. 67

Figure 37: Comparison of hydrogen embrittlement susceptibility of different RPV steels by hydrogen embrittlement index (ratio of reduction of area under hydrogen pre-charged and uncharged conditions). 67

Figure 38: Fractography of 20 MnMoNi 5 5 steel in air at 288 °C and strain rate 10^{-2} s^{-1} without hydrogen and after hydrogen pre-charging. 68

Figure 39: Overview on typical fracture features in tensile tests after hydrogen pre-charging or in tests in hydrogenated HTW (predominantly MVC with various amounts of QC, macro-void, secondary and intergranular cracks). 69

Figure 40: Maximum in UTS at intermediate temperatures in various RPV steels at strain rate of 10^{-5} s^{-1}. 74

Figure 41: Minimum in reduction of area at intermediate temperatures due to DSA. 74

Figure 42: Shift of peak in yield stress (YS) and ultimate tensile strength (UTS) to higher temperatures with increasing strain rate. 74

Figure 43: Ranking of RPV steels by DSA index. 75

Figure 44: Inversed pole figures of as-received Biblis C (a), HT 1 (b), 277 (c), 508 (d), HSST (e), and KS12 (f), as-received (g) and step-cooled (h) JRQ material materials. 76

Figure 45: Tensile tests with as-received and step-cooled JRQ materials with various loading rates at 288 °C. 78

Figure 46: Fatigue crack growth rates for each pre-cracking sequence of the investigated RPV materials...........78

Figure 47: Fractography of pre-cracked fracture surface of HSST (a to c), KS12 (d to f), as-received (g to i) and step-cooled (j to l) JRQ materials...79

Figure 48: Illustration of HTW loop and autoclave systems for EPFM tests. 82

Figure 49: Configuration of 1T-C(T) specimens. 84

Figure 50: Configuration of 0.5T-C(T) specimens. 84

Figure 51: Schematic diagram of (a) crack plane orientation identification and (b) inclusion orientation in relation to specimen orientation: L = longitudinal; T = transverse; S = short transverse [160]. 85

Figure 52: Definition of plastic area for resistance curve *J* calculation 87

Figure 53: DCPD configuration. 88

Figure 54: Applied procedure for development of *J*-Δa curve by the DCPD technique. 89

Figure 55: Example of load-line displacement, DCPD recording and the evaluated *J-R* curve.............................90

Figure 56: (a) and (b) Fractographs showing ductile crack growth in CGHAZ material (HT1) during EPFM test in PWR HTW at 288 °C with a loading rate of 25 µm/min with sudden and large load drop. 91

Figure 57: (a), (b) and (c) Load - pull rod stroke displacement curve, load - specimen load line displacement curve and the Q-K_M curve of HT1 material tested with a loading rate of 2.5 µm/min at 288 °C in PWR HTW (air fatigue pre-crack a_o = 13.5 mm) without tearing instabilities; (d), (e) and (f) the corresponding curves of HT1 material tested with loading rate of 2.5 µm/min at 288 °C in air (air fatigue pre-crack length a_o = 13.2 mm) with two instability sequences. 93

Figure 58: Effect of loading rate on fracture initiation resistance J_Q in air. 98

Figure 59: Effect of temperature on fracture initiation resistance J_Q in air. 98

Figure 60: Fracture initiation resistance J_Q of Biblis C base metal in air and various HTW environments at 288 °C with a loading rate of 0.25 to 0.35 mm/min. 99

Figure 61: Example of fracture resistance curves of Biblis CGHAZ material in air and PWR environment at 288 °C. Reduction of fracture initiation resistance in PWR environment. 100

Figure 62: Moderate reduction in fracture initiation resistance in Biblis C CGHAZ in BWR/HWC environment at various loading rates. 101

Figure 63: Effect of loading rate on fracture initiation resistance J_Q of Biblis C base metal and CGHAZ in air. 101

Figure 64: Correlation between hydrogen embrittlement and DSA susceptibility in tensile tests for the RPV steels investigated in this work. 103

Figure 65: (a) Correlation between environmental reduction of fracture initiation resistance and DSA susceptibility of different RPV steels in hydrogenated HTW; (b) correlation between environmental reduction of fracture initiation resistance in hydrogenated HTW and hydrogen-induced softening in tensile tests with hydrogen pre-charged specimens under identical (crack-tip) strain rate conditions. 103

Figure 66: (a) *J-R* curves of 277 material tested in hydrogenated high-temperature water and air at 250 °C with various loading rates (the arrows indicate the fracture resistance reduction from air to hydrogenated HTW); (b) *J-R* curves of 277 material tested in air and various HTW environments at 288 °C with 35 µm/min; (c) fracture initiation resistance of 277 in air and various HTW environments at 250 and 288 °C with various loading rates. 105

Figure 67: (a) Fracture surface of 277 steel tested with 0.35 µm/min in air at 250 °C; (b) magnification of inset *b* in (a); (c) fracture surface of 277 steel tested with 0.35 µm/min in HTW with 2 ppm H_2 at 250 °C; (d) and (e) magnifications of insets *d* and *e* in (c). 106

Figure 68: (a) Comparison of ductile and SICC growth rates in EPFM and slow rising load tests under various conditions; (b) significantly higher K_J values at the onset of ductile fracture and subsequent SICC initiation in hydrogenated HTW than for SICC initiation in oxygenated HTW. 107

Figure 69: Relative reduction of tearing resistance $J_{\Delta a}$ for different crack advances Δa in the high DSA steel 277 in hydrogenated HTW at 250 °C with various loading rates. Onset of SICC at slowest loading rate of 0.35 µm/min after some preceding ductile crack growth. 108

Figure 70: Fracture surface of 277 steel tested with 35 µm/min at 288 °C in (a) air; (b) high-temperature water with 2 ppm O_2; (d) high-temperature water with 2 ppm H_2; (d) and (e) are magnifications of inset *d* and *e* in (a) and (c); (f) and (g) of inset *f* and *g* in (e). 110

Figure 71: (a) *J-R* curves, (b) fracture initiation resistance and (c) relative reduction of fracture initiation resistance of 277 material tested in hydrogenated HTW and air at various temperatures with 35 µm/min. 111

Figure 72: (a) Summary of fracture initiation resistance J_Q of 508 material in air and various HTW environments at 288 °C; (b) *J-R* curves of 508 material in air and various high-temperature water environments at 288 °C at 3.5 µm/min; (c) comparison of ductile and SICC growth rates in EPFM tests in different environments. 113

Figure 73: Fracture surface of 508 steel tested with 3.5 µm/min at 288 °C in (a) air; (b) to (c) hydrogenated HTW with 2 ppm H_2; (d) nitrogenated high-purity water; (e) to (f) oxygenated HTW with 2 ppm O_2. 114

Figure 74: The relation of crack growth rate with (a) K_I and (b) crack opening displacement rate under different conditions. 115

Figure 75: SEM and EDX investigations on secondary cracks of 277 specimen tested at 288 °C with 35 µm/min in hydrogenated HTW. (a) SEM images showing a deep crack on the cross section beneath the secondary crack on the fracture surface; (b) EDX area mapping of marked area in (a); (c) SEM images showing the dissolved cavity at the crack tip on cross section; (d) EDX point scanning of spot *A*, *B* and *C* in (c). 120

Figure 76: EBSD maps at crack tips of 277 material tested in air ($J_{Q,AIR}$ = 370 kN/m) (a–c) and hydrogenated HTW ($J_{Q,HWC}$ = 297 kN/m) (d–f) at 288 °C with 35 µm/min, respectively. ((b) and (e) show grain reference orientation deviation mapping with an angle range of 0° to 40°, while (c) and (d) show grain reference orientation deviation mapping with an angle range of 0° to 38°). 121

Figure 77: EBSD maps at crack tips of 508 material tested in air ($J_{Q,AIR}$ = 380 kN/m) (a–c) and hydrogenated HTW ($J_{Q,HWC}$ = 316 kN/m) (d–f) at 288 °C with 35 µm/min, respectively. ((b) and (e) show grain reference orientation deviation mapping with an angle range of 0° to 40°, while (c) and (f) show kernel average misorientation mapping with a misorientation range of 0° to 5°). 121

Figure 78: Correlation between environmental reduction of fracture initiation resistance and DSA susceptibility and steel sulphur content in hydrogenated and oxygenated HTW. A good correlation is observed with DSA susceptibility in hydrogenated HTW. 125

Figure 79: Effect of steel sulphur content on the environmental reduction of fracture initiation resistance in oxygenated HTW. In oxygenated HTW, the steel sulphur content seems to play a more important role. 125

Figure 80: Effect of loading rate and water chemistry on fracture initiation resistance of high-sulphur steel HSST. 126

Figure 81: Effect of water chemistries and preceding EAC crack growth on reduction in fracture initiation resistance of high-sulphur steel HSST. 128

Figure 82: Fracture surface of high-sulphur steel HSST after EPFM tests in oxygenated HTW at 288 °C with a loading rate of 250 μm/min in a standard test (left), with preceding SICC growth (middle) and preceding SICC and chloride addition (right). 128

Figure 83: Fracture initiation resistance of as-received and step-cooled JRQ material in air, hydrogenated and oxygenated HTW at 288 °C with various loading rates. 130

Figure 84: J-*R* curves of as-received and step-cooled JRQ material tested in air, hydrogenated and oxygenated HTW environments at 288 °C with 25 μm/min. 130

Figure 85: Correlation between environmental reduction of fracture initiation resistance and DSA susceptibility of different RPV steels in hydrogenated HTW. The JRQ steel shows a stronger reduction than it may be expected on its DSA susceptibility. 131

Figure 86: Fracture surface of as-received JRQ material tested with 25 μm/min at 288 °C in (a) air, (b) HWC and (c) NWC; fracture surface of step-cooled JRQ material tested with 25 μm/min at 288 °C in (d) air, (e) HWC and (f) NWC. The fracture surface of both step-cooled and as-received JRQ material in NWC had a smaller amount of secondary cracks and quasi-cleavage facets than in HWC, while the fracture surface after the EPFM test in air was mainly MVC. 132

Figure 87: Fracture surface of as-received JRQ material tested with 25 μm/min at 288 °C in (a)–(b): HTW with 2 ppm H_2 and (c)–(d) HTW with 2 ppm O_2; fracture surface of step-cooled JRQ material tested with 25 μm/min at 288 °C in (e)–(f) HTW with 2 ppm H_2 and (g)–(h) HTW with 2 ppm O_2. Regions with limited and localized SICC features were observed in both step-cooled and as-received materials in oxygenated and hydrogenated HTW. 133

Figure 88: Effect of water chemistries and preceding EAC crack growth on the reduction in fracture initiation resistance of KS12 steel with loading rate of 2.5 μm/min. Similar effects as for the high-sulphur steel HSST (Figure 81). 136

Figure 89: Fracture surface of KS12 steel tested with 25 μm/min at 288 °C in air (a to b) and in oxygenated HTW with 2 ppm O_2 (c to d). 137

Figure 90: SEM and EDX investigations on secondary cracks of KS12 specimens tested at 288 °C with 25 μm/min in (a) air, (b) hydrogenated HTW and (c) oxygenated HTW. 138

Figure 91: (a) to (c), (d) to (f) and (g) to (i) EBSD maps at crack tips of HSST material tested in air ($J_{Q, AIR}$ = 302 kN/m), hydrogenated HTW ($J_{Q, HWC}$ = 273 kN/m) and oxygenated HTW ($J_{Q, NWC}$ = 235 kN/m) at 288 °C with 250 μm/min, respectively. ((c), (f) and (i) show grain reference orientation deviation mapping with an angle range of 0^o to 36^o). 141

Figure 92: Examples of macro-voids after EPFM tests in HTW. (*A*: pre-crack by fatigue in air; *B*: cross section of crack propagation path; *C*: end of EPFM test). 144

Figure 93: Example of secondary crack with “brittle” quasi-cleavage features (*A* and *B*) and ductile micro-voids at the border of the cavity (*C*). 145

Figure 94: Examples of various local “brittle” and relatively flat quasi-cleavage features on the fracture surface after EPFM tests in HTW or tensile tests after hydrogen pre-charging. 146

Figure 95: Examples of intergranular fracture features after tensile testing with hydrogen pre-charged specimens in air with grain boundary precipitates and/or nano-void features. 146

Figure 96: Dislocation structure in 277 steel after fracture mechanics test at 288 °C and strain rate of 10^{-3} s^{-1} in hydrogenated HTW (a) and in air (b). 148

List of Tables

Table 1: PWR and BWR reactor water chemistries for stationary power operation [24]. 10

Table 2: Typical carbon steel (CS) & LAS piping and pressure vessel materials in Western LWRs (US designation, according to Section II of ASME BPV Code) [27]. 12

Table 3: Influencing parameters on fracture toughness. 25

Table 4: The binding energy and the trap sites in steels [55][56][75]...34

Table 5: Basic types of EAC in LAS and relevant nuclear codes [28] 45

Table 6: Overview on investigated RPV steels...71

Table 7: Chemical compositions of investigated RPV steels *(*in *wt.%* and wppm for N_{tot}, N_{free} and O_{tot}*)*. 72

Table 8: Overview of properties on investigated reactor pressure vessel steels. 73

Table 9: Heat treatment of investigated steels. 75

Table 10: Grain morphology and lath dimension of the seven investigated materials..77

Table 11: Spatial distribution and morphology of the MnS inclusions in the investigated materials. 80

Table 12: Overview on investigated high-temperature water environments...82

Table 13: Resulting approximate crack crevice conditions and potential gradient between crack-mouth and crack-tip ECP. 83

Table 14: Crack opening displacement rates and corresponding crack-tip strain rates for CT specimens. 85

Introduction

Structural integrity of reactor pressure vessel (RPV) is of utmost importance regarding operation safety and service lifetime of light water reactors (LWR) and assuring sufficient margins against brittle and ductile failure are crucial in this context [1]. Commercial RPVs are made of fine-grained low-alloy steel (LAS) with granular upper bainite microstructure, such as MnMoNi or NiMoCr steel grades [2]. The fracture resistance of RPV can be reduced during service by irradiation embrittlement due to neutron irradiation [1] and thermal ageing [3][4], and potentially by the high-temperature water (HTW) environment and the absorption of hydrogen from the reactor coolant and corrosion reactions [5]. The fracture behaviour of RPV steels in HTW is affected by material (strength, chemical composition, microstructure, etc.), environmental (temperature, chemistry of the HTW, hydrogen content, etc.) and mechanical loading parameters (strain rate, constraints, etc.). There is a growing concern that HTW environment together with hydrogen absorbed from environment and corrosion reactions, may reduce the fracture resistance of the RPV steel in synergy (or competition) with other embrittlement and degradation mechanisms like irradiation embrittlement, environmentally-assisted cracking (EAC) [6][7][8], temper embrittlement (TE) [9][10] or dynamic strain aging (DSA) [11][12]. Even small HTW effects can be critical for long-term operation for plants with small margins with regard to irradiation embrittlement and/or low upper shelf toughness. It is thus crucial to know if and under which conditions HTW effects on fracture resistance may occur.

There are only very few investigations on HTW and hydrogen effects on the fracture behaviour of low-alloy RPV steels in the LWR operating temperature range, since hydrogen effects are usually claimed to be negligible under such conditions (due to the low hydrogen trapping efficiency and fast effusion rates or low hydrogen availability) [13]. The hydrogen concentration in the RPV from corrosion and dissolved hydrogen in the coolant in case of an intact cladding and under typical steady-state LWR power operation conditions is usually low (< 0.1 wppm). Therefore, the bulk hydrogen embrittlement (HE) appears as extremely unlikely, as confirmed by slow strain rate tests with smooth un-notched tensile specimen in hydrogenated HTW [8]. This also applies for unclad regions. However, cracks can be present in the cladding from fabrication (e.g., hot and relaxation cracks), or be formed during service by fatigue, or EAC as shown, e.g., by the corrosion fatigue (CF) cracking in RPV feedwater nozzles in boiling water reactors (BWR) or the stress corrosion cracking in Alloy 182 RPV internal attachment or penetration welds in LWR [14]. Furthermore, incipient cracks in the

RPV always have to be assumed in safety assessments. Increased hydrogen levels higher than the critical concentration for HE may be reached in the plastically deformed fracture process zone of cracks. Hydrogen can be enriched at stressed and plastically strained bare crack tips with an aggressive occluded crack crevice chemistry, and a high hydrostatic triaxial stress state, e.g., in fracture mechanics tests in HTW or in a loss of coolant accident (LOCA). Since the hydrogen diffusion rate in RPV steel is much higher than the ductile crack growth rates and sufficiently fast for intermittent brittle crack extension, e.g., in a LOCA situation, crack-tip HE cannot be completely excluded.

Schellenberger et al. observed that the *J-R* curves of RPV steels were significantly lower in oxygenated HTW than in air and the reduction increased with decreasing strain rate and increasing steel sulphur content [15]. Furthermore, a change of tensile properties and embrittlement of base metal and coarse-grain heat-affected zone of RPV steels and synergistic effects with DSA at LWR operating temperature in hydrogen pre-charged specimens (~ 2 to 5 wppm) were also reported, in which embrittlement increased with increasing hydrogen concentration, yield stress and DSA susceptibility [16]. These studies clearly indicated a need for systematic investigations of HE and HTW effects on environmental degradation of the fracture resistance at LWR operating temperatures.

The main goal of this PhD thesis project is to systematically study the unexplored effects of various simulated HTW environments and hydrogen on the fracture behaviour of RPV steels with different DSA, TE and EAC susceptibilities and microstructures (base metal, simulated weld coarse-grain heat-affected zone) in the upper shelf region. The fracture behaviour of low-alloy RPV steels in simulated LWR environments is evaluated by elastic-plastic fracture mechanics (EPFM) tests with different strain rates and temperatures. The metallo- and fractographic post-test observations on the fracture mechanisms and corrosion-hydrogen-deformation interactions supplement the mechanical tests. The major influential parameters and critical combinations of material (strength level, DSA, TE and EAC susceptibility), environmental (temperature, hydrogen concentration) and loading (strain rate) conditions, which may result in most pronounced environmental and hydrogen effects need to be identified. Potential synergies with other mechanisms like DSA, TE or EAC that affect the fracture behaviour in these steels will be investigated and tentative mechanistic explanations will be given.

The present thesis is divided into four chapters: Literature review, Materials and experiments, Results and discussion and Conclusions and outlook. The Literature review chapter covers mainly three parts. First, a brief general introduction of LWRs, RPV materials and RPV ageing and degradation mechanisms is given. An overview of HE and hydrogen effects on the mechanical and fracture behaviour of RPV materials and their potential interactions with other degradation and embrittlement mechanisms like EAC, DSA or TE, is introduced in the second part. The very limited current knowledge of HTW effects on the fracture resistance is reviewed in the third part. The Materials and experiments chapter describes the material compositions and properties of the investigated RPV steels, the EPFM tests in HTW and the characterization approaches. The Results and discussion chapter concisely discusses the effects of yield stress, DSA, EAC and TE susceptibilities on fracture resistance of various RPV steels and underlying potential mechanisms. In the last chapter, Conclusions and outlook, the main conclusions and potential future follow-up work are outlined. The Appendix contains the database with the fracture resistance values of the RPV steels investigated in this work.

Chapter 1 Literature review

Nuclear power plants use nuclear fission reactions to generate heat, which most frequently is used in steam turbines to produce electricity [17]. The fission reaction can occur with thermal and fast neutrons. Thermal reactors need a moderator to slow down the fast fission neutrons to increase the probability of the fission reactions. Depending on the neutron energy (fast or thermal), the coolant (light and heavy water, carbon dioxide, helium or liquid sodium) and moderator (water or graphite), different types of reactors can be differentiated. Most of the commercial power plants are thermal reactors. By the end of 2016, there are currently 448 nuclear power plants in operation in 31 countries, with a total net capacity of over 390 GW [17]. About 80% of the civil nuclear power plants are light water reactor (LWR) that use light water as reactor coolant and moderator. About 10% are pressurized heavy water reactors that are operated mainly in Canada and India, where unenriched natural uranium can be used as fuel. In LWRs, 25% are boiling water reactors (BWR) and 75% pressurized water reactors (PWR).

Operating safety in LWRs is assured through the integrity of three distinct safety barriers between the fission products and the environment. Firstly, the fuel element cladding contains and confines the nuclear reaction products [18]. Secondly, the reactor pressure vessel (RPV) and the reactor coolant system contain the core and primary coolant water under high temperature and pressure. Thirdly, the containment as the external barrier is typically a steel or combined steel-concrete structure.

The RPV contains the reactor core, core internals and reactor coolant (together with the primary pressure boundary components). The RPV is the most critical component regarding lifetime and safety (enclosure of radioactive inventory, tightness of safety barriers, core coolability, reactivity and criticality control as well as safe shut-down ability). The RPV may exhibit a catastrophic brittle fracture in case of loss of coolant accidents (LOCA) or strong irradiation embrittlement with massive release of radioactivity to the environment. Besides, RPV cannot be exchanged and it determines the maximum technical lifetime. Under the simultaneous effects of irradiation, thermo-mechanical operational loads, reactor coolant and increased temperatures over prolonged periods, the RPV is subjected to different potential ageing and degradation mechanisms during service. These can result in an embrittlement of the RPV material or the formation and sub-critical growth of cracks by fatigue or environmentally-assisted cracking (EAC). The structural integrity and material ageing of the RPV over the whole lifetime are central elements in ageing and lifetime management programme of LWRs.

1.1 Light water reactors

There are two main variants of LWRs: PWR and BWR [18]. They share many similarities. Uranium is the basic fuel for LWRs, which is usually in the form of pellets of uranium oxide (UO_2) packed in Zircalloy tubes to form fuel rods [18]. The rods are arranged into fuel assemblies in the reactor core. The moderator is light water, which slows down the neutrons to cause more fission. Control rods are made with neutron-absorbing material such as cadmium, hafnium or boron. They are inserted or withdrawn from the core to control the rate of reaction, or to stop it. These operations are crucial in enabling a chain reacting system to be controllable and to be held precisely critical.

1.1.1 Boiling and pressurized water reactors

PWR reactors (Figure 1) are closed systems that operate at high pressure (~ 16 MPa) and high temperatures (~ 326 °C) in the primary coolant circuit with liquid phase only. The system pressure is kept above the vapour pressure by the pressurizer. The heat from the reactor core is removed by water flowing through the primary cooling loop. In the steam generator, the heat from the primary loop is transferred to a secondary (non-radioactive) loop, which operates at lower pressure (~ 7 MPa) allowing production of superheated steam that drives a steam turbine to produce electricity.

BWR reactors (Figure 2) are open, direct-cycle systems that operate at about 7 MPa and 288 °C, where the steam is directly generated in the reactor core. The primary loop of the BWR reactors contains water in the liquid (feedwater and reactor water) and gaseous phase (steam). Unlike a PWR, there is no primary and secondary loop. Due to the absence of a secondary loop, BWR has a greater overall thermal efficiency than a PWR, but a certain amount of radioactive contamination may get into the turbine system.

The reactivity, i.e. the neutron thermalization and absorption, is controlled by different mechanisms in BWRs and PWRs. In BWR reactors, generally, the control rods and the feedwater flow rate control the reactivity and the outlet power. In PWR reactors, the boric acid (H_3BO_3) dissolved in the feed water compensates the decrease of reactivity due to the fuel burn-up. In addition, the neutron poison material in the fuel pellet made of gadolinium oxide (Gd_2O_3) absorbs the excess of reactivity at the beginning of the cycle. The neutron thermalization is less effective in BWRs since the water density is lower (gaseous phase). For this reason, the BWR core is bigger, resulting in a neutron flux of about an order of magnitude lower than in PWRs [19]. The operation of these two reactors and their water chemistries are quite different.

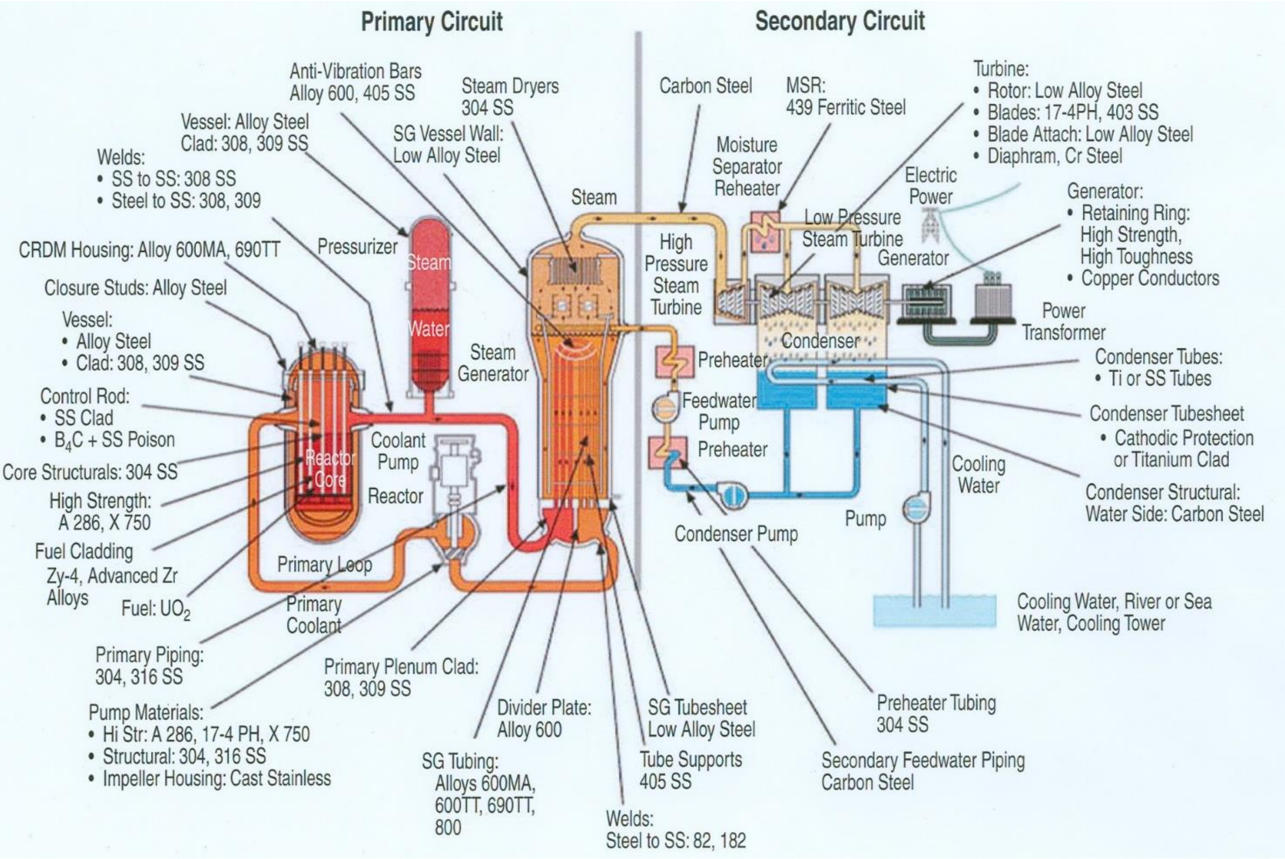
Primary Circuit
Secondary Circuit
Anti-Vibration Bars Alloy 600, 405 SS
Steam Dryers 304 SS
Vessel: Alloy Steel Clad: 308, 309 SS
SG Vessel Wall: Low Alloy Steel
Welds:
• SS to SS: 308 SS
• Steel to SS: 308, 309
CRDM Housing: Alloy 600MA, 690TT
Pressurizer
Steam
Water
Closure Studs: Alloy Steel
Vessel:
• Alloy Steel
• Clad: 308, 309 SS
Control Rod:
• SS Clad
• B_4C + SS Poison
Core Structurals: 304 SS
High Strength: A 286, X 750
Fuel Cladding Zy-4, Advanced Zr Alloys
Fuel: UO_2
Reactor Core
Coolant Pump
Reactor
Steam Generator
Primary Loop
Primary Coolant
Primary Piping: 304, 316 SS
Primary Plenum Clad: 308, 309 SS
Pump Materials:
• Hi Str: A 286, 17-4 PH, X 750
• Structural: 304, 316 SS
• Impeller Housing: Cast Stainless
Divider Plate: Alloy 600
SG Tubing: Alloys 600MA, 600TT, 690TT, 800
SG Tubesheet Low Alloy Steel
Tube Supports 405 SS
Welds: Steel to SS: 82, 182
Steam
Carbon Steel
MSR: 439 Ferritic Steel
Moisture Separator Reheater
High Pressure Steam Turbine
Low Pressure Steam Turbine
Electric Power
Generator
Turbine:
• Rotor: Low Alloy Steel
• Blades: 17-4PH, 403 SS
• Blade Attach: Low Alloy Steel
• Diaphram, Cr Steel
Generator:
• Retaining Ring: High Strength, High Toughness
• Copper Conductors
Power Transformer
Condenser
Preheater
Feedwater Pump
Preheater
Condenser Pump
Pump
Cooling Water
Condenser Tubes:
• Ti or SS Tubes
Condenser Tubesheet
• Cathodic Protection or Titanium Clad
Condenser Structural: Water Side: Carbon Steel
Cooling Water, River or Sea Water, Cooling Tower
Preheater Tubing 304 SS
Secondary Feedwater Piping Carbon Steel

Figure 1: Schematic of a PWR with materials used in different components [20].

PWR RPVs are smaller than BWR RPVs due to their smaller cores and smaller water gap between the core and RPV wall as well as the lack of steam separator and dryer equipment in the upper shell (Figure 3). A PWR RPV has a typical wall thickness of 20 to 25 cm. But the wall thickness is only 10 to 15 cm thick for a BWR RPV due to its lower operating pressure [1]. PWRs are more susceptible to irradiation embrittlement than BWRs due to a magnitude higher fast neutron flux and end of life fluence at the RPV wall, because of the larger water gap and different core design [21]. In addition, PWRs may experience more severe overcooling transients during loss of coolant transients (e.g., pressurized thermal shock with re-pressurization in some cases) than BWRs. In case of LOCAs (e.g., due to a break or large leak in the reactor coolant system), cold water is injected by the safety systems to cool the core and to avoid a core melt accident. The radioactive decay of fission products produces a huge amount of heat even after the stop of fission reactions for quite long time. This cold water hits the hot RPV surfaces and produces high thermal tensile stresses that may result in a brittle failure, especially in case of cracks in the highly embrittled core beltline region of the RPV [22].

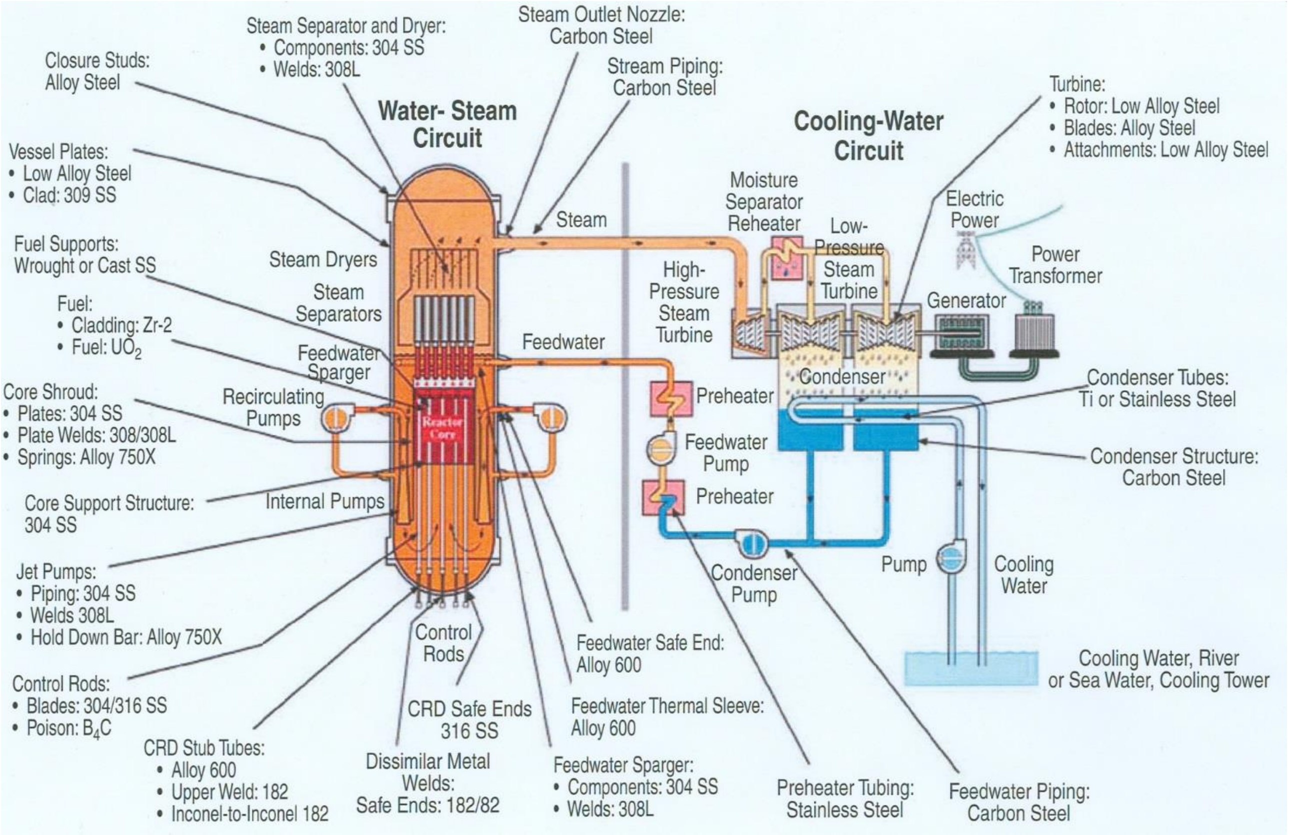
Steam Separator and Dryer:
• Components: 304 SS
• Welds: 308L
Steam Outlet Nozzle: Carbon Steel
Stream Piping: Carbon Steel
Closure Studs: Alloy Steel
Water- Steam Circuit
Cooling-Water Circuit
Turbine:
• Rotor: Low Alloy Steel
• Blades: Alloy Steel
• Attachments: Low Alloy Steel
Vessel Plates:
• Low Alloy Steel
• Clad: 309 SS
Steam
Moisture Separator Reheater
Low-Pressure Steam Turbine
Electric Power
Power Transformer
Fuel Supports: Wrought or Cast SS
Steam Dryers
Steam Separators
High-Pressure Steam Turbine
Generator
Fuel:
• Cladding: Zr-2
• Fuel: UO2
Feedwater Sparger
Feedwater
Condenser
Condenser Tubes: Ti or Stainless Steel
Core Shroud:
• Plates: 304 SS
• Plate Welds: 308/308L
• Springs: Alloy 750X
Recirculating Pumps
Reactor Core
Preheater
Feedwater Pump
Condenser Structure: Carbon Steel
Core Support Structure: 304 SS
Internal Pumps
Preheater
Jet Pumps:
• Piping: 304 SS
• Welds 308L
• Hold Down Bar: Alloy 750X
Condenser Pump
Pump
Cooling Water
Control Rods
Feedwater Safe End: Alloy 600
Control Rods:
• Blades: 304/316 SS
• Poison: B4C
CRD Safe Ends 316 SS
Feedwater Thermal Sleeve: Alloy 600
Cooling Water, River or Sea Water, Cooling Tower
CRD Stub Tubes:
• Alloy 600
• Upper Weld: 182
• Inconel-to-Inconel 182
Dissimilar Metal Welds: Safe Ends: 182/82
Feedwater Sparger:
• Components: 304 SS
• Welds: 308L
Preheater Tubing: Stainless Steel
Feedwater Piping: Carbon Steel

Figure 2: Schematic of a BWR with materials used in different components [20].

1.1.2 Water chemistry

Both PWRs and BWRs use light water as coolant and moderator. In a PWR, water acts as moderator, coolant and reactivity controller (absorber) in the primary circuit and as coolant and medium for the turbine in secondary circuit. In a BWR, water is moderator, coolant, medium for the turbine and reactivity controller (by void adjustment). However, PWRs and BWRs have different water chemistries that result in different electrochemical corrosion potentials (ECP) of the structural materials, as shown in Table 1.

Western PWRs operate with slightly alkaline, borated, lithiated and hydrogenated water in the primary coolant circuit. The inlet and outlet core temperatures are about 290 and 325 °C, respectively. H_3BO_3 is added to control the reactivity and its concentration reduces with increasing fuel burn-up. In order to minimize the release of corrosion product, activation and CRUD formation on the fuel elements (CRUD is a term for “Chalk River unidentified deposits”, which is the corrosive particle build-up on primary components of nuclear reactors), LiOH is added accordingly to keep the $pH_{290°C}$ at ~ 7, where solubility of the protecting oxide film is minimal. Some amount of hydrogen is added to supress the radiolysis (to shift the equilibrium towards the H_2O side) in the reactor core and to achieve low ECP of the structural materials from −800 to −700 mV_{SHE}. The resulting dissolved hydrogen (DH) content in the reactor water is typically 2 to 3 ppm.

BWRs are operated with neutral ($pH_{290°C}$ of ~ 5.7), high-purity water. The inlet and outlet core temperatures are about 274 and 290 °C, respectively. In BWRs, due to boiling, high-purity water is needed to avoid excessive crud formation on the fuel elements and to reduce the enrichment of aggressive anions in cracks/crevices at high ECP to mitigate stress corrosion cracking (SCC). In normal water chemistry (NWC), no hydrogen is added to the system. The radiolysis of the cooling water in the reactor core produces stoichiometric amounts of reducing (H_2) and oxidizing (O_2, H_2O_2) species. Due to the non-volatility of H_2O_2 and strong partitioning of H_2 into the steam phase, there is an excess of oxidizing species in the reactor water. This results in high ECPs of the reactor internals or the RPV in the range of 100 to 250 mV_{SHE}. The reactor water typically contains 200 to 400 ppb dissolved oxygen (DO) and hydrogen peroxide as well as 15 to 35 ppb H_2. In hydrogen water chemistry (HWC), H_2 is injected into the feed water that recombines with O_2 and H_2O_2 to H_2O and reduces the ECP. Due to the strong H_2 partitioning to the steam phase, this technique is less efficient than in the PWRs and the ECP are (together with the lower pH) higher than in PWRs and in the range from −500 to −200 mV_{SHE}. Above the upper core level and in the upper plenum or in the region of the feedwater nozzle corners, the environment remains highly oxidizing. To increase the efficiency and to reduce some negative side effects of HWC (increased ^{16}N dose rates), the On-line Noblechem (OLNC) technique was developed, where platinum complex solutions are injected to the feed water during reactor operation and they finally deposit as nano-sized platinum particles on the water-wetted surfaces [23]. Platinum particles electrocatalyze the recombination of H_2 with O_2 and H_2O_2 to produce H_2O. The reactor water typically contains 20 to 40 ppb (OLNC) or 100 to 300 ppb (moderate HWC) DH here. The majority of BWRs are now operating with HWC or HWC/OLNC. The main differences between BWR/NWC, BWR/HWC/OLNC and PWR with regard to corrosion are the different ECP, pH, H_2 contents and temperatures.

Due to the high ECP, NWC environment is more aggressive than HWC and PWR environments. SCC and irradiation-assisted SCC of reactor internals and pipings are a bigger issue. An aggressive occluded crevice chemistry can be formed in NWC environment with strong enrichment of harmful anions like sulphate and chloride or sulphides from the dissolution of MnS inclusions in case of low-alloy RPV steels, and this is the other reason to keep the impurity level in water as low as possible for BWRs with NWC. The main difference with regard to SCC and IASCC between BWR/HWC and PWR is the higher temperature and H_2 contents of the later, whereas pH (in the plant relevant range) has little effect on SCC in deoxygenated water. On the other hand, the crack tips are always deoxygenated and at low ECP in all three environments, and the environmental conditions under which cracks grow are quite similar. H_2 and pH in the crack crevice environment are also crucial for hydrogen uptake and hydrogen embrittlement (HE) of RPV steels.

Table 1: PWR and BWR reactor water chemistries for stationary power operation [24].

Reactor type	Operation temperature [°C]	Operation pressure [MPa]	Water condition	ECP [mV_{SHE}]	$pH_{290\,°C}$	Important chemical species
PWR	290–325	15	Primary water	–800 to –700	6.9–7.4	10–4000 ppm B 0.5–3.5 ppm Li 2–3 ppm H_2 < 10 ppb O_2 and H_2O_2 < 10 ppb Cl^-, SO_4^{2-}
BWR	274–290	7	HWC or OLNC	–500 to –200	5.65	0.1–0.3 ppm H_2 (HWC) 0.02–0.04 ppm H_2 (OLNC) < 10 ppb O_2 < 1 ppb Cl^-, SO_4^{2-}
			NWC	100 to 250	5.65	200–800 ppb O_2 and H_2O_2 5–40 ppb H_2 < 1 ppb Cl^-, SO_4^{2-}

1.1.3 Reactor pressure vessel structure and materials

The RPV is the major safety barrier against the release of radioactive fission products to the environment. The RPV may exhibit a catastrophic brittle fracture in case of LOCAs and strong irradiation embrittlement. The RPV determines the maximum technical lifetime, since it cannot be exchanged and the annealing heat treatment to restore mechanical properties after irradiation is very challenging. During service, cracks can be formed and grow sub-critically by EAC and fatigue. The core beltline of vessel is the primary concern with regard to irradiation embrittlement, which is the region of shell material directly surrounding the effective height of the fuel element assemblies [25]. The RPV material in the high neutron flux core region embrittles increasingly with time. Periodic in-service inspection is performed to detect defects before they reach a size that is critical for the safety. Monitoring the toughness properties and assuring sufficient margins against brittle failure by surveillance programmes are essential.

The selection of materials and the construction practices used in the manufacturing process may affect the ageing sensitivity and integrity of the RPV throughout its service life. Quality control including non-destructive testing during the fabrication process is crucial to achieve the best component quality.

RPV structures of PWRs and BWRs are shown in Figure 3. RPV steels should have the combination of good strength and toughness properties in thick sections (hardenability), good weldability, good formability, high fatigue and SCC resistance (in primary coolant environments), low thermal aging and neutron irradiation embrittlement susceptibility together with relatively high thermal conductivity and low thermal expansion (properties that make them more resistant to thermal shock [26]).

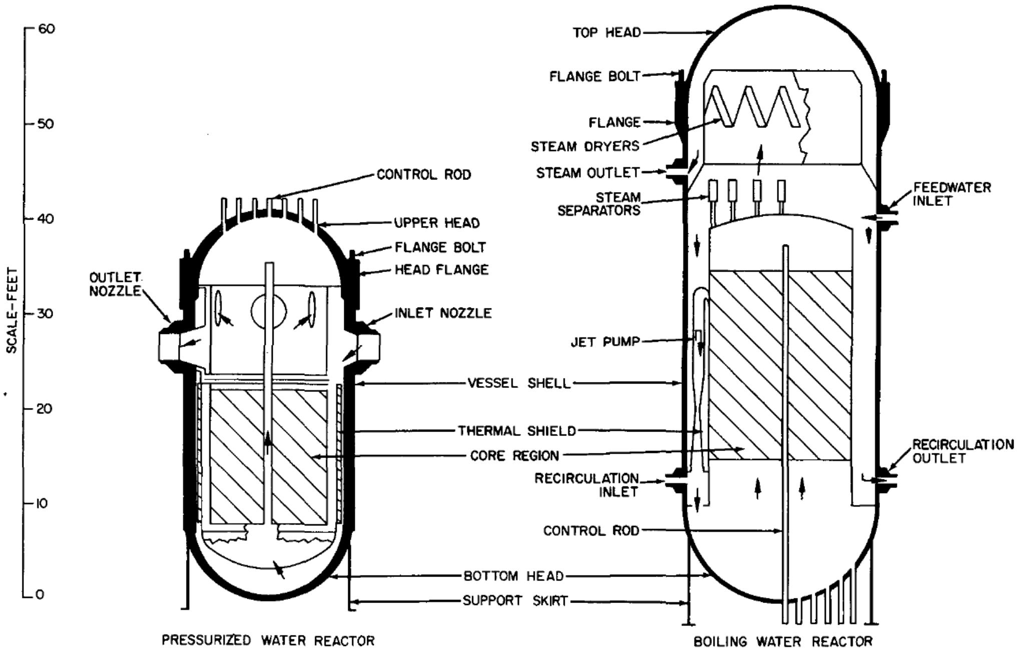
SCALE-FEET
60
50
40
30
20
10
0
CONTROL ROD
UPPER HEAD
FLANGE BOLT
HEAD FLANGE
OUTLET NOZZLE
INLET NOZZLE
VESSEL SHELL
THERMAL SHIELD
CORE REGION
BOTTOM HEAD
SUPPORT SKIRT
PRESSURIZED WATER REACTOR
TOP HEAD
FLANGE BOLT
FLANGE
STEAM DRYERS
STEAM OUTLET
STEAM SEPARATORS
FEEDWATER INLET
JET PUMP
RECIRCULATION OUTLET
RECIRCULATION INLET
CONTROL ROD
BOILING WATER REACTOR

Figure 3: Typical PWR and BWR pressure vessels [25].

The cylindrical shell, bottom and upper head and nozzles of RPVs are usually made of fine-grained low-alloy steel (LAS) with granular/upper bainite microstructure (body-centred cubic structure: bcc). MnMoNi (SA 508 Cl. 3 forgings, SA 533 Gr. B Cl. 1 plates), or NiMoCr (SA 508 Cl. 2 forgings) are commonly used steels. The MnMoNi has higher manganese and the NiMoCr has higher chromium contents, otherwise the chemical compositions are similar. Alloying (manganese, molybdenum, nickel, chromium and vanadium), iron accompanying (silicon, manganese and phosphorus) and impurity (copper, tin) elements have a great influence on the properties of RPV steels. Table 2 gives an overview on the chemical compositions of typical Western RPV vessel and piping materials.

Table 2: Typical carbon steel (CS) & LAS piping and pressure vessel materials in Western LWRs (US designation, according to Section II of ASME BPV Code) [27].

Designation	**Type**	**Product form**	**C^{max} [%]**	**Mn [%]**	**P^{max} [%]**	**S^{max} [%]**	**Si^{min} [%]**	**Cu^{max} [%]**	**Ni^{max} [%]**	**Cr^{max} [%]**	**Mo^{max} [%]**	**V^{max} [%]**	**YS$^{25\,°C}$ [MPa]**	**Heat treatment**	**Microstructure**
SA 106 Gr. B	CS C-Mn	Pipe drawn	0.30	0.29 1.06	0.035[B]	0.035[B]	0.10	0.40[A]	0.40[A]	0.40[A]	0.15[A]	0.08[A]	≥ 240 *300–400*[E]	N	Ferritic-pearlitic
SA 333 Gr. 6	CS C-Mn	Pipe drawn	0.30	0.29 1.06	0.025[B]	0.025[B]	0.10	-	-	-	-	-	≥ 240 *300–400*[E]	N	Ferritic-pearlitic
SA 516 Gr. 70	CS C-Mn	Vessel plate	0.27[C]	0.79 1.30	0.03[B]	0.035[B]	0.13 0.45	-	-	-	-	-	≥ 260 *300–400*[E]	N	Ferritic-pearlitic
SA 533 B Cl. 1	LAS Mn-Mo-Ni	(R)PV plates	0.25	1.07 1.62	0.12[D] (0.35)	0.15[D] (0.35)	0.13 0.45	0.10[D]	0.37 0.73	-	0.41 0.64	0.05	≥ 345 *450–550*[E]	Q & T	Bainitic
SA 508 Gr. 3 Cl. 1	LAS Mn-Mo-Ni	(R)PV forging	0.25	1.20 1.50	0.12[D] (0.25)	0.15[D] (0.25)	0.15 0.40	0.10[D]	0.40 1.00	0.25	0.45 0.60	0.05	≥ 345 *450–550*[E]	Q & T	Bainitic
SA 508 Gr. 2 Cl. 1	LAS Ni-Mo-Cr	(R)PV forging	0.27	0.50 1.00	0.12[D] (0.25)	0.15[D] (0.25)	0.15 0.40	0.10[D]	0.50 1.00	0.25 0.45	0.55 0.70	0.05	≥ 345 *450–550*[E]	Q & T	Bainitic

A = combination should not exceed 1.0%; B = in modern steels these values are smaller than 0.015%; C = carbon varies with thickness up to 0.31%; D = requirement for core belt region; E = typical range; YS = yield stress; N = normalized; Q & T = quenched and tempered.

Modern steels usually have a low (0.001–0.006 wt.%) or medium (0.007–0.015 wt.%) sulphur content. Some old plants have steels with high sulphur content (0.016–0.035 wt.% sulphur) and distinct segregation zones. The sulphur content is mainly from the coal/fuel in the blast furnace for heating and direct/indirect reduction of iron ores. With high sulphur content (formation of MnS), EAC susceptibility increases, while upper shelf fracture toughness reduces [28]. For the core belt region, the copper content is limited to ≤ 0.05% (in old plants, weldments contain up to 0.35% copper and nozzle forgings can also have increased copper levels). Higher copper content leads to an increase in irradiation embrittlement and reduction in fracture toughness. Carbon forms carbides, which increase strength and decrease toughness. The remaining carbon in solid solution affects the dynamic strain aging (DSA) behaviour and toughness. Molybdenum, vanadium and chromium are special carbide formers, which increase strength at higher temperatures as well. Chromium improves corrosion resistance. Nickel, manganese, molybdenum and chromium influence the hardenability, weldability and toughness at low temperatures (nickel) [29]. Manganese forms ductile MnS inclusions (instead of brittle and low melting FeS) and avoids red shortness.

Silica and aluminium are alloyed mainly in deoxydation processes during steelmaking. A part of the formed oxides stays in the steel. Nitrogen, oxygen and hydrogen come from air and humidity ingress during steel making. Aluminium killed steels usually have a lower free interstitial nitrogen content than silicon killed steels, since it is a strong AlN former, which results in a lower DSA susceptibility. Welds, on the other hand, usually have a low aluminium, but high oxygen content, which favours an increased DSA susceptibility (Al_2O_3 instead of AlN formation).

Irradiation embrittlement sensitivity is mainly affected by copper, nickel, manganese and phosphorus contents. The microstructure mainly affects the initial transition temperature, but has little effect on the transition temperature shift by irradiation. Temper embrittlement (TE) susceptibility is mainly influenced by phosphorus, tin, antimony and arsenic segregation, while boron has a beneficial effect here. EAC, HE and fracture in the upper shelf are strongly influenced by MnS inclusions (sulphur content) and DSA (free carbon and nitrogen contents).

The RPVs are normally in the quenched, tempered, post-weld heat-treated and stress-relieved conditions. The inner surface of the RPV is cladded with a 3 to 10 mm thick single or double layer of corrosion-resistant austenitic stainless steel [21]. The aim is to reduce the corrosion product ingress, activation of corrosion products in the reactor core and subsequent activity built-up in the coolant circuit. The cladding is usually produced by automatic submerged arc welding (SAW) and manual local SAW welding for nozzle regions. In some BWR RPV designs, RPV parts have been left unclad (RPV heads). In some cases, the cladded layer has been removed (feedwater nozzle) after some corrosion fatigue (CF) incidents. Some locations contain weld pads of Alloy 182 for reactor internal attachment or penetrations welds. Alloy 182 is highly susceptible to SCC in BWRs and PWRs. Several SCC incidents occurred at such locations and represent a serious safety concern [14].

Old RPVs were fabricated by hot-rolled and bent plates that were welded together to form separate shell steel courses. They contain circumferential and axial weld seams in the high neutron flux core region. In some of the older (pre-1972) PWR RPVs, these longitudinal seams are of particular concern for RPV integrity, due to high levels of copper and phosphorus in the welds and high stress intensity factors in case of axial cracks. In contrast, modern RPVs are fabricated by welded forged rings containing only circumferential welds. The most recent RPVs do not contain any welds in the core region. The welds were usually fabricated by SAW welding with narrow-gap weld techniques here.

Large, thick-wall vessels that consist of forged or hot-rolled and bent welded plate segments inherently show a certain through-thickness variation in mechanical properties and microstructure. Orientation and location dependence of mechanical properties, microstructure and EAC or HE susceptibility exist. This inhomogeneity and anisotropy arises from the fabrication (casting and forming) and heat ratreatment processes. The large ingots contain regions with segregation (elements like sulphur, phosphorus, carbon), high density of non-metallic inclusions (oxides, sulphides) from the complex solidification process or hydrogen flakes. The most severe segregation zones from the solidification process at the bottom, top and centre of large ingots are discarded by cropping and piercing before the final forging steps. Nevertheless, some parts of segregation zones with inclusion lines (“ghost lines”) may survive these steps. Hydrogen flaking can be avoided, e.g., by vacuum degassing during casting and special hydrogen release heat treatments. Due to the short diffusion distances, hydrogen flaking is not an issue for continuous (strand) cast and hot-rolled plates. Sulphide content is usually highest in the centre of the plate. In segregation zones, local sulphur content can be several times higher than the mean bulk sulphur content. MnS inclusions show high plasticity at hot working temperatures. The MnS inclusions affect the EAC susceptibility (aggressive occluded crevice chemistry by dissolution of MnS and MnS as EAC initiation site), upper shelf fracture (MnS as preferred nucleation site for micro-void formation) and HE susceptibility (MnS as strong hydrogen traps and absorbed sulphides as hydrogen recombination poison). The anisotropic forming process and different cooling rates between the surface and centre of the plates during heat treatment lead to slightly different and anisotropic microstructures.

The microstructure and chemical compositions of the RPV steels have an important influence on its service performance and ageing sensitivity. RPV materials mainly consist of bainite and ferrite and, to a lesser extent, (high-carbon twinned) martensite and retained austenite. There are many regions with high local plastic strains (with high dislocation densities) and internal stresses. Both high- and low-angle grain boundaries (GB) are present in the microstructure. These boundaries include prior-austenite (high-angle) GB with grain size of 10 to 30 µm and (low-angle) ferrite laths (width: a few µm) gathered in packets (length: 10 to 15 µm). Fine-dispersed carbide precipitates are distributed in the RPV material including cementite Fe_3C (3 µm, on lath and GB as well as intra lath) and other carbides or nitrides like Mo_2C, AlN, V (N, C), $M_{23}C_6$ and M_7C_3, with size of 100 nm (inside laths) or 1 µm (on lath and GB). Non-metallic inclusions in RPV mainly consist of sulphides (MnS, CaS, spherical or elongated) and oxides (Al_2O_3, spherical), which are inhomogeneously distributed. Furthermore, irradiation produces a wide range of very fine-dispersed and nano-sized defects like copper-rich precipitates, solute atoms and point defect complexes, dislocation loops and nano-voids that result in a hardening and embrittlement of the material. Phosphorus and metalloid segregation to prior-austenite grain boundary (PAGB) may occur during heat treatment and during service (under irradiation and by thermal ageing). This results in a non-hardening embrittlement and weakening of the GB strength and can cause intergranular cracking.

1.1.4 Reactor pressure vessel structural integrity

Due to drastic consequences, brittle RPV failure has to be excluded and should be an extremely low probability event. Sufficient margins against a brittle failure and a sufficient toughness of the material have to be assured during the whole lifetime. Deterministic fracture mechanics RPV integrity analysis is usually conducted by the consideration of the irradiation embrittlement (surveillance programmes) with conservative fracture toughness curves, a few bounding and limiting LOCAs (e.g., pressurized thermal shock) and other thermal-hydraulic transients. An initial crack at most critical locations (core belt region, feedwater nozzle corners) with a crack depth, which is two times the resolution limit of the non-destructive examination of the periodic in-service inspection (Figure 4), is considered in such analysis. Brittle crack initiation has to be safely excluded ($K_I < K_{IC}$). The exact procedure may vary from country to country. Some countries allow the use of (simplified) probabilistic fracture mechanics analysis or the consideration of warm pre-stress effects. Crack arrest is regarded as an additional margin, since many of the initiating cracks are not very severe (large break). LOCAs are expected to arrest after some crack growth. This is due to the high temperature and toughness of the remaining part of the RPV. Constraints and stress state effects (e.g., biaxiality, shallow cracks) are usually not considered. The operation window (limits for temperature and pressure) for service is determined in a similar way, but with a much deeper crack (with a depth of 25% of wall thickness).

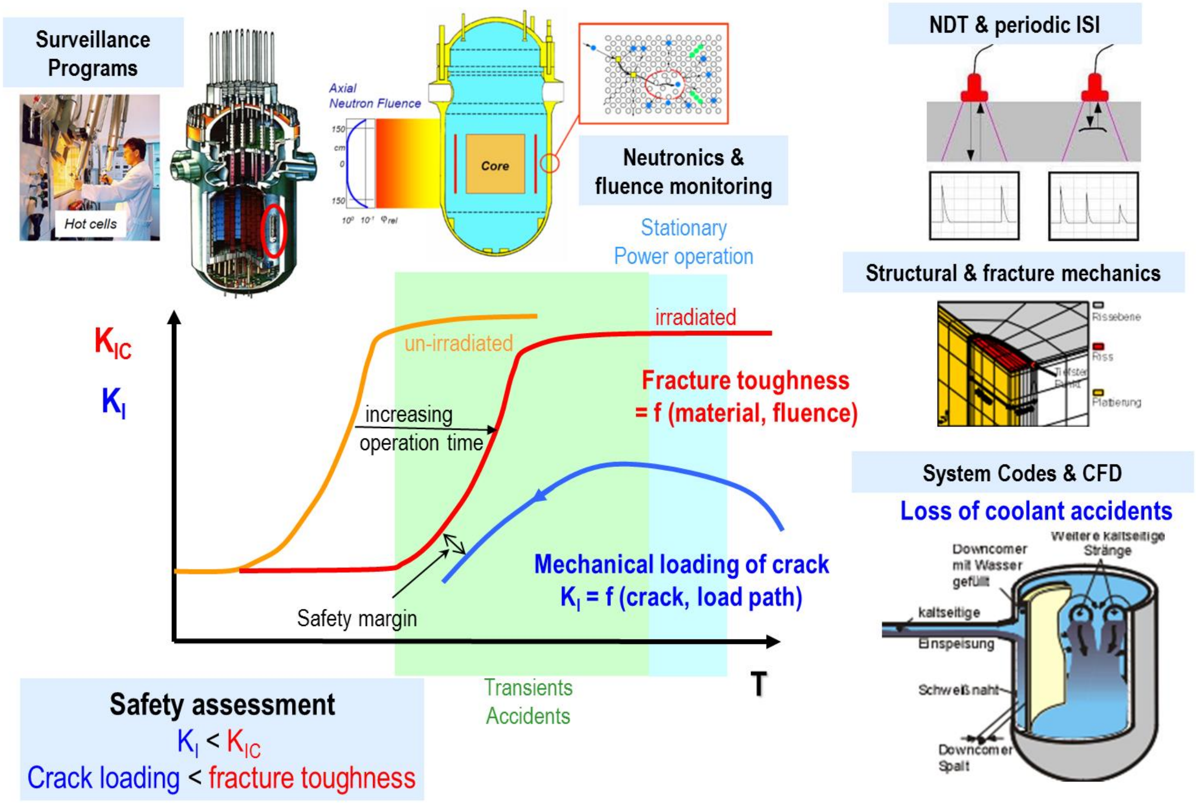
Surveillance Programs
Hot cells
Axial Neutron Fluence
150
cm
0
150
10⁰ 10⁻¹ φrel
Core
Neutronics & fluence monitoring
Stationary Power operation
NDT & periodic ISI
Structural & fracture mechanics
Rissebene
Riss
Tiefster Punkt
Plattierung
KIC
KI
un-irradiated
irradiated
increasing operation time
Fracture toughness = f (material, fluence)
Mechanical loading of crack KI = f (crack, load path)
Safety margin
T
Transients Accidents
Safety assessment
KI < KIC
Crack loading < fracture toughness
System Codes & CFD
Loss of coolant accidents
Weitere kaltseitige Stränge
Downcomer mit Wasser gefüllt
kaltseitige Einspeisung
Schweißnaht
Downcomer Spalt

Figure 4: Deterministic fracture mechanics RPV integrity analysis. (NDT: non-destructive testing; ISI: in-service inspection; CFD: computational fluid dynamics)

During service, cracks can be formed and sub-critically grow ($K_I < K_{IC}$) by thermo-mechanical fatigue or EAC. These very rare cracking events occurred under very specific conditions and sometimes-unusual circumstances. However, sufficient margins against failure due to such potential ageing and degradation mechanisms have to be demonstrated as well. This is usually done by a flaw tolerance evaluation in combination with non-destructive pre- and in-service inspection (Figure 5), since the presence of small cracks cannot be fully excluded. Starting from an initial crack that can be either a postulated one (e.g., 2 times the resolution limit of NDT method) or the findings of the in-service inspection, a potential fatigue or EAC crack growth during service under the operational loads has to be detected by in-service inspection, before it reaches the maximum allowable crack depth and a size that is critical for safety. If this requirement is not satisfied, the inspection interval has to be reduced until the criteria is fulfilled. Otherwise, further operation cannot be justified and immediate component replacement or repair is necessary. The maximal allowable crack depth is usually derived from the critical crack length, calculated by a (linear elastic) fracture mechanics analysis, most severe operating transients (safety factor of 10) and accident conditions (safety factor of 2). The potential degradation of the material fracture toughness due to irradiation embrittlement, thermal ageing, DSA or environmental effects with fluence and time, should also be considered in such an analysis. Apart from irradiation embrittlement, such effects are usually claimed to be absent or to have minor effects only, which are covered by the high overall degree of conservatism in such integrity analysis.

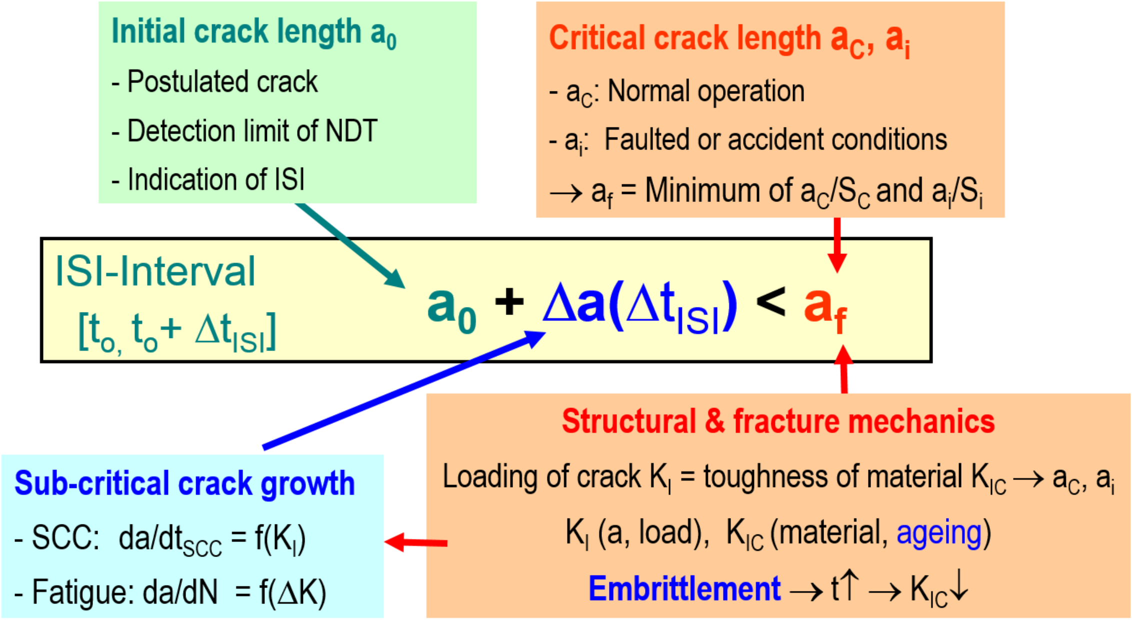
Initial crack length a_0
- Postulated crack
- Detection limit of NDT
- Indication of ISI
Critical crack length a_C, a_i
- a_C: Normal operation
- a_i: Faulted or accident conditions
$\rightarrow a_f$ = Minimum of a_C/S_C and a_i/S_i
ISI-Interval
$[t_o, t_o + \Delta t_{ISI}]$
$a_0 + \Delta a(\Delta t_{ISI}) < a_f$
Structural & fracture mechanics
Loading of crack K_I = toughness of material $K_{IC} \rightarrow a_C, a_i$
K_I (a, load), K_{IC} (material, ageing)
Embrittlement $\rightarrow t\uparrow \rightarrow K_{IC}\downarrow$
Sub-critical crack growth
- SCC: $da/dt_{SCC} = f(K_I)$
- Fatigue: $da/dN = f(\Delta K)$

Figure 5: Flaw tolerance evaluation on RPV.

Such integrity analysis requires a precise knowledge of the material fracture toughness over a wide range of conditions (temperature, strain rate, …) and its degradation in the service environments over prolonged operation periods (ageing, hydrogen, …). The loading/strain rates of operational and LOCA transients can vary over a wide range. The LOCAs usually give higher loading rates than those considered in quasi-static elastic-plastic fracture mechanics (EPFM) tests. The peak K_I in such transients is usually reached at intermediate temperatures between 80 and 200 °C, which is lower than the steady state RPV operation temperature of 320 and 288 °C for PWRs and BWRs, respectively. The peak K_I can reach high values of 120 to 150 $\text{MPa}\cdot\text{m}^{1/2}$ at critical conditions and locations for shallow cracks as well. Most operational transients usually result in slow strain rates and high K_I values are only reached for deep cracks. Slow (thermal) transients with potentially stronger environmental effects usually produce small peak K_I values only. A semi-elliptical axial crack (with a depth of 25% of wall thickness) in the cylindrical shell of a BWR and PWR RPV under steady state operation at 16.5 and 7.2 MPa pressure, results in a K_I value of approximately 50 to 60 $\text{MPa}\cdot\text{m}^{1/2}$.

1.2 Fracture mechanisms and toughness of RPV steels

The following section briefly discusses the mechanisms for rapid fracture by mechanical overloading and the major factor of influences on fracture toughness in RPV steels. This section does not cover sub-critical crack growth by fatigue or EAC. It is focussed to a few aspects that are important for this work. The bcc RPV steels show a ductile to brittle transition in the fracture behaviour. At low temperatures, bcc material fails in an unstable and brittle manner by fast (~ speed of sound waves) quasi-cleavage (QC) at low stress or stress intensity levels. At high temperatures, it fails by slow and stable ductile tearing by micro-void formation and coalescence at high stress or stress intensity levels. This fracture process involves significant plastic deformation and consumes a lot of energy. The crack path is usually transgranular, but can be intergranular in some special cases.

1.2.1 Ductile and brittle fracture and ductile to brittle transition

According to whether a material can accommodate significant plastic deformation before fracture in tensile test, two main fracture modes can be differentiated: brittle fracture (strain $\varepsilon < 5\%$) and ductile fracture ($\varepsilon > 5\%$) [30][31]. Components made out of ductile alloys can also fail by plastic collapse, which need to be considered in integrity assessment.

Ductile fracture: In ductile fracture, extensive plastic deformation (necking) takes place before fracture, which is typical for the fracture behaviour of LAS in the upper shelf region. Ductile fracture is a slow stable crack growth and fracture process, and requires an increasing crack-driving force with crack advance, since the fracture resistance of the material is also increasing with crack advance. This damage mode involves the nucleation of micro-voids followed by void growth and coalescence driven by plastic deformation [32]. Micro-voids form when a high stress concentration causes formation of free surfaces by separation of the metal at GBs and, in particular, at interfaces between the metal and inclusions (or second-phase particles) [33][34] or by particle cracking. The physical reasons are the high interfacial energy and incompatibility strains [35]. In materials, where the second-phase particles and inclusions are well bonded to the matrix, void nucleation is often the critical step. When void nucleation occurs with little difficulty, the fracture properties are controlled by the growth and coalescence of voids. When the growing voids reach a critical size relative to their spacing, a local plastic instability develops between voids with necking, resulting in failure. Large particles tend to favour void nucleation and crack initiation in the presence of plastic strain, because they are more likely to contain small defects, which can act like Griffith cracks. Furthermore, large non-metallic inclusions, such as oxides and sulphides, may be cracked or debonded prior to plastic deformation, making void nucleation relatively easy. The exact nature of failure is dependent on the nature (interface strength and bonding), content and size distribution of second-phase particles and plastic deformation mechanism. In very high-purity materials, the tensile specimen may completely neck down, resulting in extremely large local plastic strains and nearly 100% reduction in area.

In tensile tests with smooth specimens, void formation and growth usually start in the centre of the specimen, when macroscopic necking starts. Necking appears when the strain hardening cannot compensate the geometrical softening by the reduction of cross section. The neck produces a triaxial stress state in the centre of the specimen, which promotes void nucleation and growth. Upon further strain, the voids coalesce, resulting in a penny-shaped flaw perpendicular to the specimen gauge length. The outer ring of the specimen contains relatively few voids, because the hydrostatic stress is lower than in the centre (plane stress at the surface). With decreasing ligament size, the penny-shaped flaw finally produces deformation bands at 45° angle from the tensile axis, where plastic strain is maximal. This concentration of strain provides sufficient plasticity to nucleate voids. Since the small voids are closely spaced, an instability occurs soon after these smaller voids are formed, resulting in total fracture of the specimen and the cup and cone shape of the matching surfaces [36][37]. The ligament can also fail by plastic collapse in alloys with low particle content.

In case of a pre-existing sharp crack, micro-void initiation, growth, and coalescence may occur at the crack tip. The high triaxial and hydrostatic stress favours the nucleation of micro-voids in this region. Growth and coalescence of micro-voids are usually the critical steps in ductile crack advance. Void formation typically starts in the peak stress region that is about two times the crack-tip opening displacement (CTOD) ahead of the crack tip. With increasing loading, the crack tip blunts and then the voids grow and link with the main crack. As this process continues, the crack grows. For a crack subject to plane strain Mode-I loading, the maximum plastic strain occurs at 45° angle from the crack plane. On a local level, this angle is the preferred path for void coalescence by plastic necking, but global constraints require that the crack propagation remains in its original plane. Therefore, ductile growth often has a microscopic zig-zag shape at an angle of 45°. The fracture behaviour in the upper shelf region can be described by local damage models like the Gurson model and the further evaluation of the models [38].

Ductile fracture mainly occurs in a transgranular manner. The ductile fracture surface contains parabolic-shaped dimples and they often contain second-phase particles. The shape of the dimples is affected by the dominant stress state. The shape of the dimples can be elongated in case of shear-dominated failure. In some cases, micro-void coalescence (MVC) in a region close to the GB can result in an intergranular appearance of fracture surface at small magnifications.

Brittle fracture: Brittle fracture is fast (speed of acoustic waves) unstable crack growth and fracture by cleavage or QC without any apparent macroscopic plastic deformation. Brittle fracture occurs when K_I at the crack tip reaches the fracture toughness K_{IC}. This phenomenon is typical for LAS in the lower shelf and ductile to brittle transition region (Figure 6). In the lower shelf and transition region, there is an inherent large scatter due to the nature of the fracture process, whereas the scatter is much smaller in the upper shelf. Although cleavage is a brittle fracture process, it can be preceded with large-scale plasticity and ductile crack growth in the upper transition region. In ductile metals and in the upper transition region, it always involves some microscopic (or localized) plastic deformation.

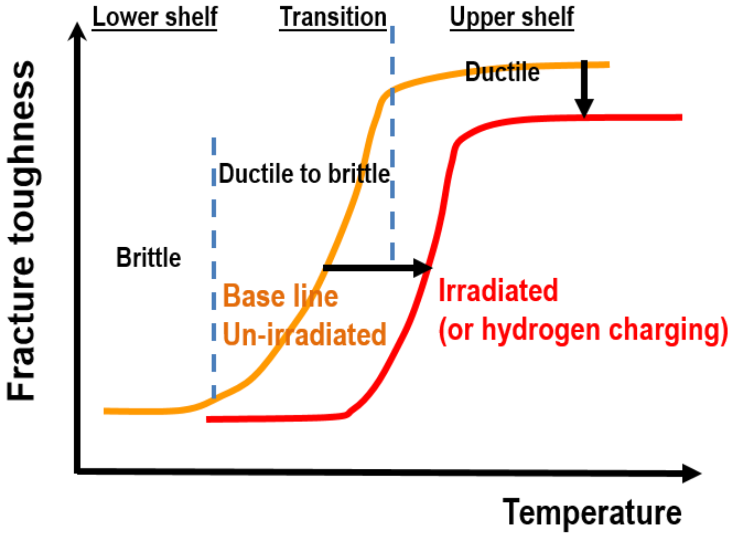

Figure 6: The ductile to brittle transition behaviour of bcc LAS.

The main reason for cleavage fracture at low temperatures and the ductile to brittle transition in bcc alloys is the high yield stress (higher than cleavage fracture stress) and its strong temperature dependence at low temperatures (Figure 7). In contrast to yield stress, the cleavage fracture stress shows little temperature dependence. At low temperatures, the yield stress is higher than the cleavage fracture stress, favouring cleavage fracture. At high temperatures, the cleavage fracture stress is higher than the yield stress, promoting the ductile failure. The high yield stress at low temperatures is due to the low mobility of screw dislocations in bcc steels. Their special dislocation core configuration, result in a very high Peierls potential and friction stress. The strong temperature dependence is caused by the thermally activated double kink formation mechanism. Factors that increase the yield stress (irradiation, precipitation hardening, increase in strain rate or strain ageing) usually shift the transition temperature to higher temperatures (Figure 7 (a)). Factors that decrease the cleavage fracture stress (HE or TE) have the same effect (Figure 7 (b)). Factors that impede and constrain plastic deformation facilitate cleavage fracture. Therefore, high triaxial stress state or alloys with bcc or hcp lattice (with few independent slip systems) promote cleavage fracture. Factors that result in plastic strain localization and planar slip also favour brittle crack extension processes.

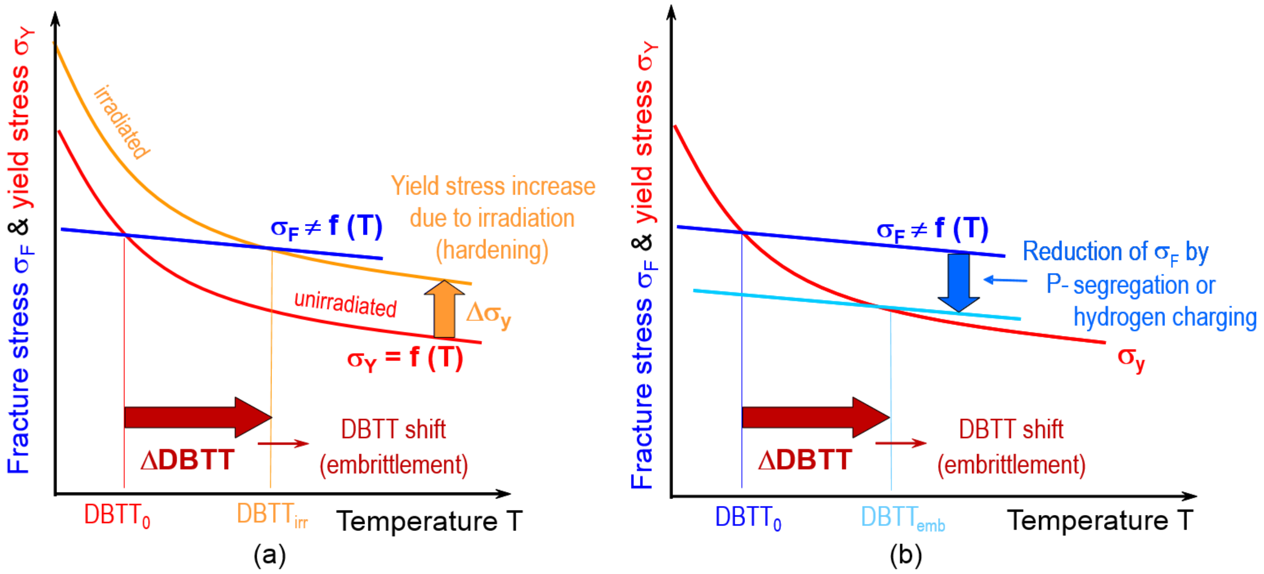

Figure 7: (a) Hardening embrittlement by increase of yield stress; (b) non-hardening embrittlement by reduction of cleavage fracture stress.

Cleavage fracture is the rapid propagation of a crack along a particular crystallographic plane [39]. The preferred cleavage planes are those with the lowest packing density, since fewer bonds must be broken and the spacing between planes is greater. In bcc materials, cleavage occurs on {100} planes. The crack surfaces are relatively smooth on the microscopic scale and fracture path is transgranular in polycrystalline materials. The propagating crack changes direction each time it crosses a GB. The crack seeks the most favourably oriented cleavage plane in each grain and this causes some steps on the fracture surface. Twisted boundaries produce the typical river pattern. Initially, the crack accommodates the twist mismatch by forming cleavage on several parallel planes. As the multiple cracks propagate, they are joined by tearing between planes and converge into a single crack. The direction of crack propagation can be directly inferred from the river patterns. In some specific cases, cleavage can also be intergranular (e.g., hydrogen trapping or phosphorus segregation to PAGBs (HE or TE), brittle GB carbides). Ductile metals usually show QC that exhibits characteristics of both cleavage and dimple fracture [40], often with ductile tear ridges between brittle micro-cracks or at microstructural barriers for micro-cracks [41].

Since cleavage involves the simultaneous breaking of many atomic bonds, the local stress must be sufficient to overcome the local cohesive strength of the material. The theoretical cleavage fracture strength of the metallic matrix is roughly 10% of the Young's modulus E and is about 20000 MPa for a RPV steel. The maximum peak tensile stress ahead of a crack tip is about 3 to 4 times the yield stress and is around 1200 to 1600 MPa. The peak tensile stress is thus more than a magnitude lower than theoretical strength. Therefore, a macroscopic crack does not provide sufficient stress concentration to exceed the bond strength. Therefore, cleavage initiation in ductile alloys requires a local discontinuity or defect (e.g., sharp micro-crack) ahead of the macroscopic crack. It should be sufficient to exceed the bond strength of a microstructural weak point by the stress concentration. In RPV steels, initiation of brittle cracks usually occurs locally at small brittle carbide or second-phase particles [37]. If the local stress or strain is high enough, such a particle can break and act as a micro-crack. With enough local stress, this micro-crack can grow into the ferritic matrix as a cleavage crack. The necessary stress can be estimated by the Griffith criterion [42]:

$$\sigma_f = (\frac{2E(\gamma_s + \gamma_p)}{\pi a})^{1/2} \tag{1}$$

where E is the Young's modulus, γ_P and γ_S are the plastic work energy and surface energy (per unit area) to produce a crack in the matrix, and a is the initial micro-crack or particle diameter.

In ductile alloys, γ_P is usually much larger than γ_S. With typical values of γ_P for ferrite (8 to 14 J/m^2) and the assumption of a maximum crack-tip stress of 3 to 4 times of the yield stress, the fracture stress can already be exceeded by small particles with a diameter of a few µm in RPV steels. The cleavage process consists of the micro-crack formation at a hard particle, its propagation into the ferrite matrix and, later on, in the neighbouring grains, and finally in a coalescence with other cleavage cracks to form a macroscopic crack. This process can be nucleation or propagation controlled. The micro-crack can arrest at the particle-matrix interface, in the ferrite matrix by blunting or at grain and phase boundaries. Even if the crack propagates through several grains it may arrest, if there is a steep gradient ahead of the main macroscopic crack. This tends to occur at low K_I values [43].

In the transition region between ductile and brittle behaviour, both micro-mechanisms of fracture can occur in the same specimen. In the lower transition region, the fracture mechanism is pure cleavage, but the toughness increases rapidly with temperature as cleavage becomes more difficult. In the upper transition region, a crack initiates by MVC, but ultimate failure occurs by cleavage. On initial loading in the upper transition region, cleavage does not occur because there are no critical particles near the crack tip. As the crack grows by ductile tearing, however, more material under high stress is sampled. Eventually, the growing crack samples a critical particle and cleavage occurs. Cleavage propagation in the upper transition region often shows isolated islands of ductile fracture and arrested macroscopic cleavage cracks as well as unbroken ligaments at microstructural barriers behind the arrested crack tip. The share of such ductile features is increasing with temperature.

Crack path (Figure 8): Ductile steels and alloys usually fail due to nucleation, growth and coalescence of micro-voids that initiate at inclusions and second-phase particles in the grains. Cleavage fracture involves the separation along specific crystallographic planes. The fracture path is usually transgranular in both cases. Intergranular cracking may occasionally occur under specific circumstances by brittle or ductile processes, in particular in sub-critical SCC and creep crack growth. The reduction of the GB strength due to precipitation or formation of brittle phases on the GB (GB oxidation, helium bubbles, liquid metal embrittlement) or phosphorus and metalloid segregation (TE) and hydrogen trapping (HE) at PAGB that cause decohesion may both promote intergranular cracking. Whether intergranular cracking occurs or not depends on the GB and intra-grain strength and the plastic deformation mechanism in the grain and at the GBs, but also on the GB stress/strains, grain size, type of GBs and the grain misorientations. Chromium depletion or silicon enrichment on GBs by thermal or radiation-induced segregation can increase the electrochemical/corrosion activity of GBs with respect to the matrix and cause intergranular SCC. GB cavitation and sliding at high temperatures during creep are other reasons for intergranular cracking.

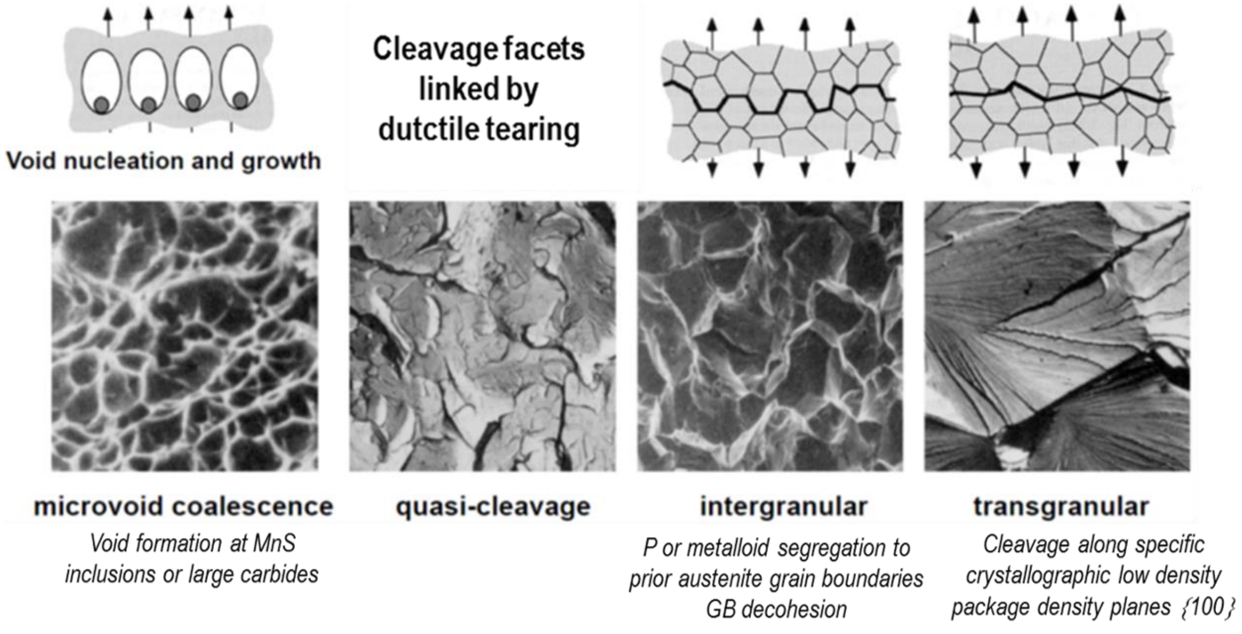
Void nucleation and growth
Cleavage facets linked by dutctile tearing
microvoid coalescence
quasi-cleavage
intergranular
transgranular
Void formation at MnS inclusions or large carbides
P or metalloid segregation to prior austenite grain boundaries GB decohesion
Cleavage along specific crystallographic low density package density planes {100}

Figure 8: Fracture modes and paths in case of RPV steels.

1.2.2 Factors of influence on fracture toughness

The fracture process and toughness are affected by material (yield stress, microstructure, carbides morphology and distribution, inclusions and second-phase particles, GB segregation or DSA), mechanical loading (strain rate, constraints and stress state) and environmental (temperature, irradiation and hydrogen) parameters and can be specimen size dependent. The individual parameter effects in the lower shelf, transition region and upper shelf can be different and the overall behaviour can be quite complex. Some examples of important parameter effects on toughness in RPV steels are summarised in Figure 9 and Table 3, which are discussed in the following paragraph.

An increase in yield stress usually results in an increase of the ductile-brittle transition temperature (DBTT) and decrease of the upper shelf toughness. One exception is the grain size, where a decrease in grain size increases both yield stress and upper shelf toughness. The upper shelf toughness is strongly affected by MnS inclusions and it decreases with increasing sulphur content. On the other hand, carbide precipitates and their morphology (which depends on annealing temperature) have a strong impact on cleavage in the lower shelf and transition region. The toughness usually decreases with increasing carbon content. A high nickel content results in a low initial DBTT, but can result in large DBTT shifts under irradiation at high neutron fluencies. Certain impurities (phosphorus, , antimony, arsenic and tin) can segregate to the prior-austenite GBs and result in intergranular cleavage. In contrast, boron GB segregation is beneficial in this context. Furthermore, the toughness properties are orientation and thickness dependent. In old RPVs, distinct macro-segregation zones with lower fracture toughness exist.

A higher loading rate shifts the DBTT to higher temperatures and increases the upper shelf toughness. In the DSA temperature-strain rate range in a DSA susceptible steel, a lower strain rate can increase the fracture toughness. Constraints and stress state as well as specimen or component size affect the fracture behaviour in the lower shelf, transition and upper shelf regions.

Due to the ductile to brittle transition, temperature inherently has a strong effect on the fracture process. Irradiation increases the DBTT and reduces the upper shelf toughness. Irradiation hardening is strongly dependent on copper, phosphorus, nickel and manganese contents. In contrast to the initial (unirradiated) DBTT, the microstructure has little effect on the radiation-induced shifts. The irradiation embrittlement can be in synergy or competition with other embrittlement mechanisms like TE, HE or static and dynamic strain ageing.

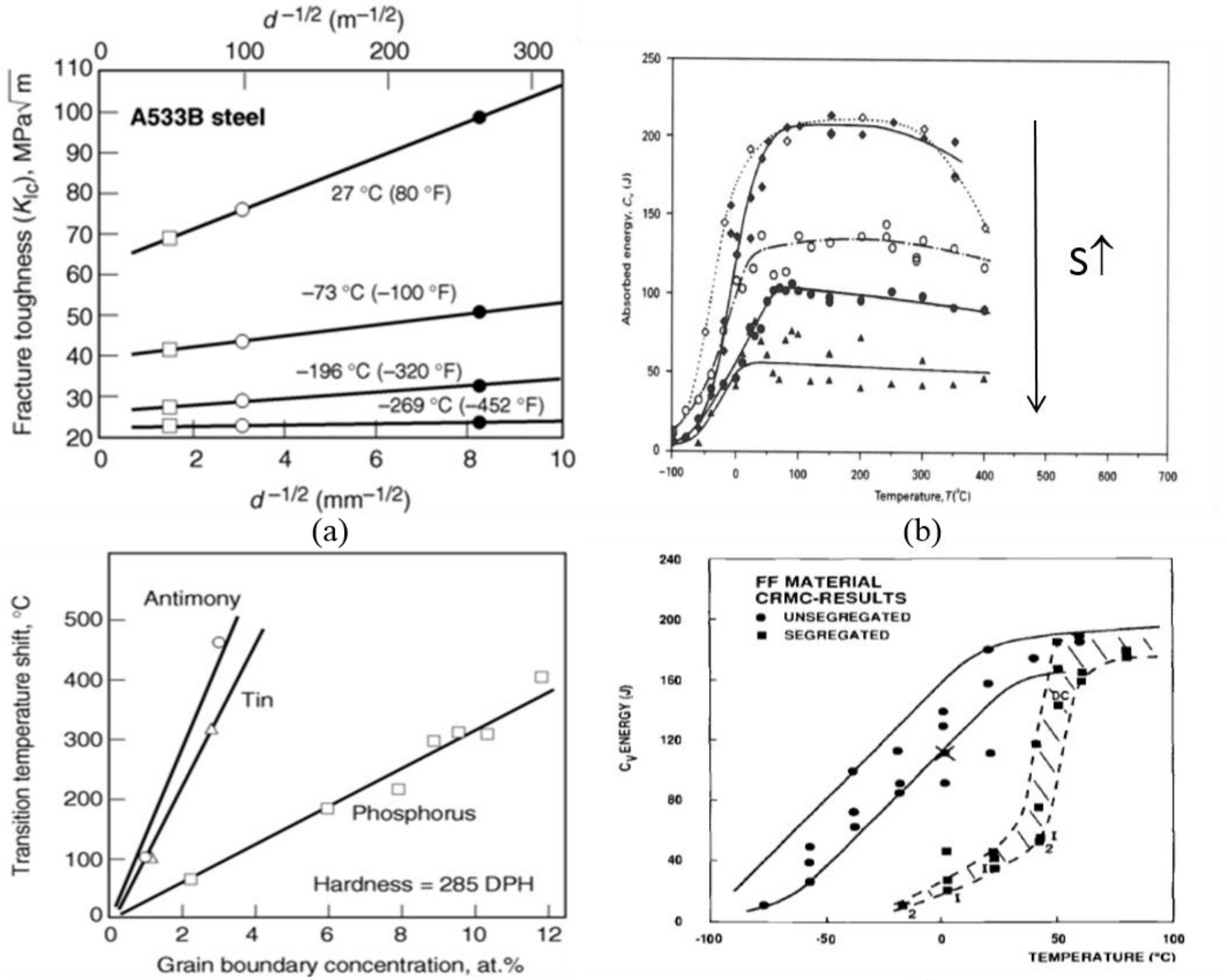

(a) (b)

(c) (d)

Figure 9: Effects of (a) grain size, (b) sulphur content, (c) impurity grain boundary segregation and (d) segregation zones on fracture toughness [44][45][46][47].

Table 3: Influencing parameters on fracture toughness.

Parameter	Effect on toughness
Yield stress	Yield stress ↑ → DBTT ↑, K_{Ic} in upper shelf ↓
Grain size	Increase in grain size decreases K_{Ic}
Inter-lath and intra-lath carbides	Decrease K_{Ic} by increasing the tendency to cleave
Impurities (phosphorus, antimony, arsenic, tin)	Decrease K_{Ic} by temper embrittlement
Free interstitial (carbon and nitrogen)	K_{Ic} in upper shelf ↓ by dynamic & static strain ageing
Sulphide inclusions	Decrease K_{Ic} by promoting void nucleation
Loading rate	Loading rate ↑ → DBTT ↑ and upper shelf K_{Ic} ↑

1.2.3 Fracture toughness measurement

In the last decades, various quasi-static and dynamic fracture mechanics testing methods and standards were developed involving brittle initiation, growth and crack arrest as well as ductile initiation and growth. A recent review is given by Zhu [48]. The development of EPFM was a key milestone and major progress. It allows the determination of the fracture toughness of irradiated steels with rather small samples.

The fracture toughness K_{IC} in the lower shelf region can be determined according to the American Society for Testing and Materials standards (ASTM) E399 [49] or E1820 [50] in case of small samples. The transition temperature, fracture toughness curve K_{IC} (T) and distribution in the transition region can be determined by the Master Curve method of ASTM E1921 [51] with small number of specimens. The upper shelf toughness J_{IC} and tearing resistance (*J-R* curves) are measured according to ASTM E1820.

The tearing resistance can be measured by the multiple or single specimen method. The most common procedure for the upper shelf toughness and tearing resistance is the single specimen incremental procedure with unloading compliance (ULC) method [50] for crack length measurement. Crack length can also be measured by the direct current potential drop method (DCPD) method without partial unloading [52]. The initiation toughness J_{IC} can also be measured by the stretch zone method provided that a clear stretch zone is formed, which is rarely the case for tests in corrosive environments [53]. Various simplified procedures like the normalization method [54] were also developed, in particular for challenging boundary conditions.

1.3 Hydrogen embrittlement and hydrogen effects

Hydrogen pick-up, as a result of prolonged exposure to high-temperature aqueous environment, either due to corrosion, intentional hydrogen additions (HWC, PWR) or water radiolysis, potentially leads to an embrittlement of the RPV.

The following sub-sections briefly summarize the characteristics and effects of hydrogen in RPV steels (1.3.1), the sources, uptake, trapping and transport of hydrogen with a special emphasis to LWR conditions (1.3.2), the HE, underlying mechanisms and major factors of influence (1.3.3). The potential interactions with other degradation and embrittlement mechanisms such as EAC, DSA, TE or irradiation embrittlement are discussed in 1.3.4. These degradation mechanisms are only briefly introduced to an extent that is necessary for understanding the potential interactions with HE. The experimental observations of HTW and hydrogen effects at LWR operating temperatures are summarized in a separate Section 1.4.

1.3.1 Characteristics and effects of hydrogen in RPV steel

Hydrogen is the element with the smallest atomic size and mass. As with other small elements like carbon, nitrogen, oxygen or sulphur, hydrogen is therefore located on interstitial lattice places. It can be also in molecular form at voids and small micro-cracks. In bcc steels, hydrogen is on tetrahedral (T) interstitial lattice places due to their bigger size ($r_T \sim 3.7\times10^{-2}$ nm, $r_O \sim 1.9\times10^{-2}$ nm, 6 T and 3 O sites per iron atom) [55]. Octahedral (O) sites are increasingly occupied at high temperatures. In fcc (face-centred cubic) steels, hydrogen is located on the bigger octahedral sites ($r_O \sim 5.2\times10^{-2}$ nm, $r_T \sim 2.9\times10^{-2}$ nm, 2 T and 1 O sites per iron atom) [55]. The bigger size of the octahedral sites in fcc than the tetrahedral sites in bcc is also the main reason for the higher hydrogen solubility in fcc iron.

Hydrogen has a negative solution enthalpy in bcc (−28.6 kJ/mol) [56] and fcc iron, i.e., the energy of electronic interaction of the metal with hydrogen is smaller than the energy of dissociation of molecular hydrogen (endothermic reaction). The energy of hydrogen in solid solution in iron is higher than in a hydrogen molecule. Therefore, the solubility of hydrogen increases with increasing temperature and the absolute solubility is very low. The solubility of hydrogen in iron (as atom ratio) at standard atmosphere (atm) H_2 gas partial pressure is about 1 appm (1×10^{-6}) at room temperature and it increases with temperature to about 60 appm at 1300 °C.

The volume of hydrogen in the metal is bigger than that of the interstitial site, which causes lattice expansion ($r_H \sim 5.3\times10^{-2}$ nm, $r_T \sim 3.7\times10^{-2}$ nm in bcc, M-H ~ 1.5×10^{-1} nm) [55] and volume increase of the metal, when hydrogen is dissolved. The large molar volume of hydrogen (1 to 2 cm^3/mol) in iron makes it sensitive to hydrostatic stress and dilatation strain fields [56].

Hydrogen has an extremely high mobility in steels [57][58]. The reasons for the high mobility are twofold: Hydrogen (as an interstitial) migrates by the direct interstitial mechanism, which does not require the presence of a vacancy, as it is the case for the self-diffusion of iron or solute atoms (on ordinary lattice sites). The migration from one interstitial to the other position may occur by quantum tunnelling effect at low temperatures. Therefore, the activation energy for hydrogen diffusion is very low (4 to 10 kJ/mol for hydrogen in bcc iron in comparison to 80 and 148 kJ/mol for interstitial carbon in bcc and fcc iron or 251 and 284 kJ/mol for iron in bcc and fcc iron). The combination of small size (small activation volume), low mass (increased jumping frequency) and the large number of free interstitial lattice places (6 T sites per iron atom in bcc and between 10^{-6} to 10^{-3} vacancies per iron atom between room temperature and the melting point), results in a very high mobility of hydrogen. The lower packing density in bcc results in a lower activation energy for hydrogen diffusion (e.g., 8 kJ/mol in a bcc quenched and tempered 4130 LAS vs. 54 kJ/mol in a fcc austenitic stainless steel 304) and faster diffusion.

Hydrogen shows a strong electronic interaction with the neighbouring metal atoms by providing its 1s electron to the 3d valence band [57]. This changes the density of states at the Fermi surface and causes shifts of the energy bands. The Fermi electrons then concentrate around the positively charged hydrogen nucleus to produce a closely screened entity, which may be regarded as a “neutral” atom, although the screening electrons are not in bound states. Since hydrogen changes the local and the global electronic structure of the metal, as well as increases the mean distance between the metal atoms, it is not surprising to find that the cohesive force (the force needed to increase the interatomic distance) and strength between the metal atoms is strongly affected by hydrogen.

The main characteristics of atomic hydrogen in ferritic steels are its very low solubility (2−3 times lower than in fcc) and its fast diffusion with high mobility (4−5 times faster than in fcc at room temperature) and permeation rate (2−3 times faster than in fcc), which favour its segregation. The large molar partial volume of hydrogen in the material results in hydrogen accumulation in positive hydrostatic stress and dilatation strain fields and at microstructural trap centres [59]. Due to its strong segregation and trapping tendency, small bulk concentrations in the wppm range can have significant macroscopic effects. Furthermore, the strong electronic interaction of hydrogen with the metal matrix can modify the electronic environment and cohesive energy of the metal atoms, which may affect the dislocation motion and their interactions as well as the critical stress for cleavage fracture. Moreover, hydrogen reduces the formation energy of vacancies and facilitates their agglomeration and collapse to micro-voids. Depending on temperature, strain, strain rate and microstructure, hydrogen may strongly influence the local plastic deformation as well as the fracture behaviour. HE and sub-critical hydrogen-assisted cracking (HAC) can occur due to its effects on cohesive strength, dislocation mobility and vacancies. If a critical hydrogen concentration over a critical volume is achieved in the process zone at the crack tip, cracking may occur by various brittle or ductile cracking mechanisms [60][61]. The magnitude of the embrittling effect of hydrogen is finally governed by three factors: (1) the availability, source and nature of hydrogen; (2) its ease in entering the material and the transport velocity to the susceptible locations; and (3) the nature and concentration of traps in the susceptible location. Enhancing at least one of these factors will raise the embrittlement effect of hydrogen. The details of hydrogen source, transport, trapping and uptake are discussed in 1.3.2.

Tensile and various fracture tests with RPV steels at different temperatures with electrochemical hydrogen pre-charging, indicated a critical hydrogen concentration of 1 to 2 wppm for irradiated RPV steels, which was slightly lower than in un-irradiated steels (2 to 4 wppm) [62]. At high hydrogen contents of 7 to 10 wppm, the materials sometimes failed in a completely brittle manner, in particular at temperatures below 100 to 200 °C. The hydrogen pre-charging resulted in a loss of tensile ductility and decrease in fracture toughness or increase in DBTT. In-situ charging under loading produced the strongest effects. Furthermore, hydrogen effects on the mechanical tensile behaviour were observed at LWR operating temperatures of 300 °C [63][64].

It is currently unclear, if and under which conditions, the necessary hydrogen levels can be reached in the bulk material or at crack tips in HTW (with or without the effect of irradiation and mechanical stress). The literature data is very sparse and does not contain sufficient information on experimental details for a proper assessment. Broomfield estimated that up to about 2 wppm of hydrogen can be easily absorbed in RPV steels from corrosion reactions [65], while Westinghouse predicted three times higher hydrogen levels after prolonged shut-down periods [66], but both evaluations were based on very conservative and rather unrealistic assumptions. Unstressed, pre-irradiated (8×10^{19} n/cm^2, 288 °C) RPV samples exposed to primary water at 255 °C in a PWR for ten years, revealed total hydrogen contents of 1 to 3.5 wppm [67]. Pre-irradiated RPV steel samples (8.4×10^{18} n/cm^2) exposed to HTW in a loop in the NRI test reactor at 288 °C for 332 h, showed total hydrogen concentrations of 1 to 2.9 wppm (compared to 0.4 to 1 wppm in the initial condition) [68]. Un-irradiated Eastern RVP steel samples exposed to simulated PWR at 325 °C, showed a hydrogen uptake from 0.5 to 1.5 wppm (with local peaks up to 6 wppm) [69]. Irradiated RPV steels usually revealed a higher hydrogen pick-up under identical electrochemical charging conditions, due to higher trap density of dispersed defects. In addition, heat-affected zone (HAZ) materials usually revealed a higher hydrogen uptake than the corresponding base metals, due to higher internal stress and strains or a higher trap density.

The bulk hydrogen levels in above-mentioned tests are close to the critical hydrogen contents for embrittling effects. Therefore, HE cannot be excluded for notches and crack tips in HTW. This clearly shows the need for corresponding fracture tests in HTW.

1.3.2 Hydrogen sources, trapping, transport and uptake

1.3.2.1 Source of hydrogen

Hydrogen pick-up in RPV steels may occur during LWR service and during fabrication, welding or surface treatment [70]. However, the three latter cases are usually minimized by adequate precaution measures. Hydrogen pick-up from humidity during the casting is minimized by vacuum degassing and special hydrogen heat treatments at high temperature during the subsequent fabrication steps. Furthermore, hydrogen mobility at room temperature is high and the free hydrogen can easily effuse out of the steel. Therefore, RPV usually has a low initial “metallurgical” (trapped) hydrogen content well below 1 ppm (typically a few hundreds of ppb).

The main hydrogen source in LWRs [5] is the DH in the water coolant, which comes from radiolysis of the reactor coolant (which mainly occurs in the reactor core), intentional hydrogen addition and, to a lesser extent, as a corrosion reactions by-product. Intentional hydrogen addition is to surpress radiolysis in PWRs and to mitigate SCC in BWRs with HWC or ONLC. The contribution from transmutation (n, p) reactions or proton recoil injection is neglectable with regard to the other sources. Corrosion includes uniform or local corrosion reactions, e.g., due to oxide film formation and growth, hydrolysis of metal cations from local anodic dissolution after film rupture and dissolution of MnS inclusions. The bulk hydrogen content in the steel close to the surface is usually controlled by the Sievert’s law and DH content in the water, which results in a rather low hydrogen availability. In case of cracks or crevices, the situation is totally dominated by the complex local occluded crevice chemistry and the local corrosion processes at plastically strained crack tip (which is much more aggressive than the bulk environment).

In each case (internal or external source), the local hydrogen concentration at the microstructural inhomogeneities is more important than the uniform bulk hydrogen in the matrix. The hydrogen availability in LWRs is usually believed to be too small for bulk embrittlement, but crack-tip embrittlement cannot be excluded.

Hydrogen atoms are usually located interstitially (on solute or trap sites) and molecular H_2 can form in micro-cracks or/and voids. Hydrogen is present inside metals as an interstitial in the crystal lattice, always in the monoatomic form (atomic hydrogen) [71]. Entry of hydrogen into the solid steel from the gaseous phase involves adsorption of hydrogen onto the surface of the metal followed by dissociation of hydrogen molecule into hydrogen atoms. The hydrogen atoms then subsequently enter into the metal lattice. The molecule to atom dissociation step is the rate-controlling step governing hydrogen pick-up kinetics. On the contrary, hydrogen formation due to corrosion reaction on the metal surface occurs as atomic form and two atoms of hydrogen subsequently combine to form a molecule. Once a hydrogen molecule is formed, it is liberated and does not enter into the metal. Presence of atomic hydrogen will result in easier hydrogen pick-up compared to gaseous hydrogen, since these two processes are kinetically different. Presence of recombination poisons (sulphide, arsenic etc.) which prevent formation of molecule from hydrogen atoms, results in prolonged presence of atomic hydrogen and greater chance of entering into the metal lattice.

1.3.2.2 Hydrogen transport

Hydrogen in bcc steels has a very high mobility and fast diffusion and permeation rate. The diffusion rate in bcc steels at 300 °C is in a similar range as that of protons in liquid water. At room temperature, the diffusion distance $x = \sqrt{(D \cdot t)}$ for a time of 1 s for bcc and fcc iron is about 100 µm and 20 nm, respectively. The much faster diffusion in bcc alloys is related to the different lattice structure and much lower activation energy for hydrogen diffusion. The hydrogen transport, in particular at lower temperatures, is strongly dependent on microstructure (by the concentration and type of hydrogen traps) and chemical composition. At lower temperatures, the trapping of diffusing hydrogen at trap centres may result in (several orders of magnitude) lower apparent hydrogen diffusion coefficients in permeation experiments, compared to the effective diffusion coefficient based on the activation energy in the bulk lattice at higher temperatures. Presence of retained austenite in steels has a beneficial effect in reducing susceptibility to HE, since austenite acts as a barrier to hydrogen diffusion (low diffusion rate and high solubility). Hydrogen diffusion decreases by about two orders of magnitude in the order of ferrite, pearlite/bainite and martensite [72].

Hydrogen transport in steels may be aided by microstructural short-cuts (along dislocation cores or GBs) as well as by moving dislocations during plastic deformation. This results in much faster hydrogen transport compared to lattice diffusion during plastic deformation. Therefore, hydrogen atoms can reach susceptible locations more easily and magnify the embrittling effect [73]. Such effects were observed in fcc alloys with slow hydrogen diffusivity [74]. However, plastic deformation plays a minor role to hydrogen diffusion in bcc steels only, in particular at higher temperatures (LWR regime) with very fast hydrogen diffusion rates. On the other hand, during plastic deformation, an increasing amount of defects like dislocations and vacancies are formed with plastic strain. These defects can act as traps and reduce the apparent hydrogen diffusion rate. Accumulation of hydrogen atoms near dislocations is also reported to enhance dislocation motion and increase mobile dislocation density, which eventually results in enhanced localized plasticity.

1.3.2.3 Hydrogen trapping

Hydrogen is always very heterogeneously distributed in steels. It accumulates in regions of high hydrostatic stress or dilatation strain fields and with strong traps or high trap density as well as at surfaces. Trapping can be due to elastic and chemical effects or forces. The trapping may affect the apparent hydrogen diffusion and solubility as well as the plastic deformation and fracture behaviour.

Hydrogen trapping is an issue highly related to the microstructure of the materials. Hydrogen is not only present in interstitial lattice positions (freely diffusing), but is mainly bound to various microstructural features (trapped, not diffusing), as shown in Figure 10. The strength of the microstructural features in binding hydrogen atoms is characterized by the binding energy E_B, which is the energy difference between the interstitial lattice and trap position (Figure 11). The de-trapping energy E_A is the sum of the binding energy $\mathrm{E_B}$ and height of the saddle point E_T (Figure 11). Therefore, de-trapping is more difficult than trapping. Trap sites for hydrogen can be classified as weak (reversible) and strong (irreversible) ones depending upon the binding energy [75] (Table 4), and temperature (Figure 12). Hydrogen is strongly bonded to the irreversible traps like second-phases (carbides, nitrides and oxides) and is loosely bonded to the reversible traps (GBs, dislocations, vacancies or substitutional elements). At room temperatures, traps with a binding energy of 60 kJ/mol or more are usually regarded as strong and irreversible traps. For strong traps, both binding and de-trapping energies are significantly higher than the activation energy of lattice diffusion.

Furthermore, traps can be saturable (limited number of hydrogen sites at the trap, e.g., GBs or dislocation core) or non-saturable (hydrogen enrichment continuously increases with bulk hydrogen content, e.g., at voids or micro-cracks). Hydrogen traps can also be classified by the nature of the binding/trapping, the spatial extension of the trapping forces or by their dimensions. Therefore, they are classified as point (solute atoms, vacancies), linear (dislocations, intersection of three GBs), planar (interface particle-matrix, GBs, twins, internal and external surfaces) and volume traps (vacancy clusters, voids, micro-cracks, hydrostatic stress or dilatation strain fields).

For a fixed hydrogen concentration, presence of a large number of homogeneously distributed trap sites may reduce HE tendency, since hydrogen is fixed at these sites at low concentrations [76] and cannot accumulate preferentially at the other susceptible locations (GBs). However, in the presence of a continuous source of hydrogen, it can accumulate to a higher level at these irreversible trap sites and may become potential sites for damage initiation. To sum up, the concentration of hydrogen trapped in LAS depends on the availability of hydrogen and the nature and concentration of traps, the local stresses and strains [76][77][78], which can be several orders of magnitude higher than the theoretical solubility in defect-free and stress-relieved bcc iron.

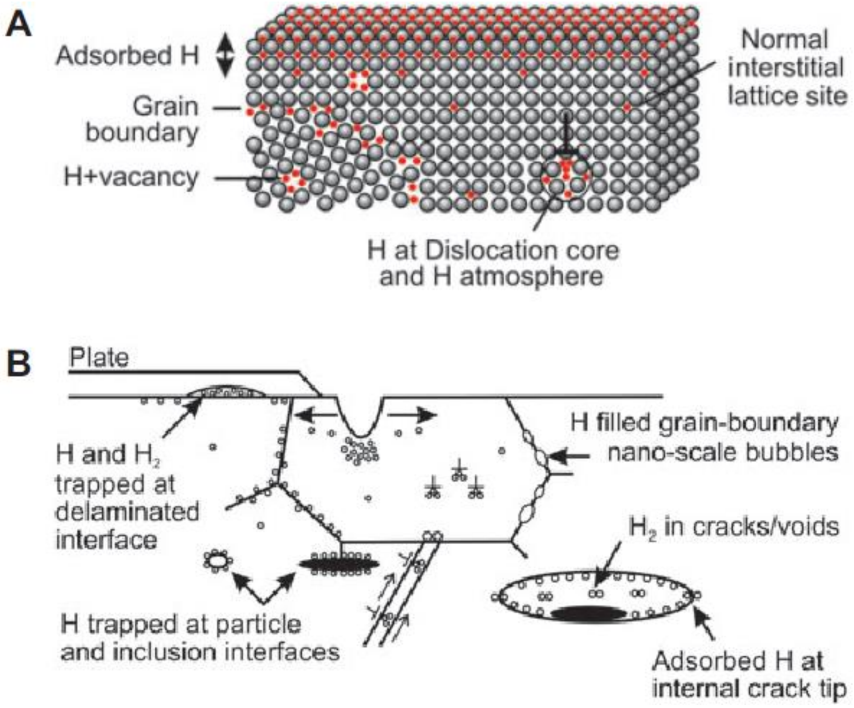
A
Adsorbed H
Grain boundary
H+vacancy
Normal interstitial lattice site
H at Dislocation core and H atmosphere
B
Plate
H and H₂ trapped at delaminated interface
H filled grain-boundary nano-scale bubbles
H₂ in cracks/voids
H trapped at particle and inclusion interfaces
Adsorbed H at internal crack tip

Figure 10: Schematic illustrations of sites and traps for hydrogen in materials (A) on the atomic scale and (B) on a microscopic scale [14].

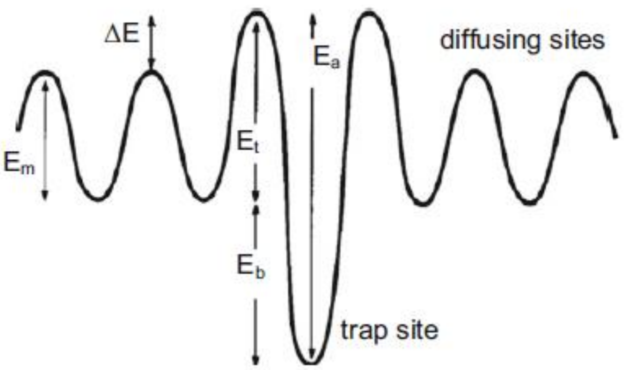

Figure 11: Illustration of binding and de-trapping energies [79].

Table 4: The binding energy and the trap sites in steels [55][56][75].

Trap type	**Binding energy E_B [KJ·mol^{-1}]**	**Trap density [cm^{-3}]**	**Degree of reversibility**
Perfect lattice	0	8.5×10^{22}	-
Elastic dislocation	20 (**b**/r)	$4\times10^{14} - 4\times10^{20}$	Reversible
H_2 vapour phase or in void	28	Dependent on steel properties	-
Dislocation core (screw)	20–30	$10^{13} - 10^{19}$	Reversible
Vacancy	30–58	10^{19}	-
Dislocation core (mixed)	58	$4\times10^{13} - 4\times10^{19}$	-
Grain boundary	~ 58	$10^{13} - 10^{17}$	Reversible/irreversible
AIN particle interface	65	5×10^{18}	-
Free surface	70	10^{15}	-
MnS interface	57–72	10^{18}	Irreversible
Al_2O_3 interface	79	5×10^{17}	Irreversible
Fe_3C interface	~ 84	5×10^{18}	Irreversible
TiC interface	94–95	5×10^{18}	Irreversible
Roughened free surface	95–96	10^{15}	Irreversible

Reference state is hydrogen in a perfect lattice; Binding energy is inversely proportional to the distance from the dislocation; ***b*** *is Burgers vector.*

Hydrogen increasingly accumulates at traps with increasing binding energy according to Equation (2) and Figure 12 shows the trap occupancy for different trap energies, temperatures and DH contents in water. With increasing temperature due to increasing thermal activation, trapping efficiency is decreasing. Therefore, hydrogen redistribution from weaker to stronger traps [79] or even complete hydrogen effusion out of the steel may occur. Above 300 °C, there is only limited hydrogen trapping at strong traps [56][80]. Figure 12 to Figure 14 are by courtesy of H. P. Seifert.

The concentration *c* of hydrogen in trap site *X*, where near saturation occurs at low temperatures was expressed with a corresponding equilibrium distribution [56]:

$$\frac{c_X}{(1-c_X)} \cong c_0 \exp\left(\frac{E_B}{RT}\right) \tag{2}$$

Due to its high partial molar volume V_H, hydrogen also accumulates in regions with high hydrostatic and triaxial stress, e.g., at crack tips or notches. The hydrogen enrichment exponentially increases with hydrostatic stress $\sigma_H = (\sigma_{11} + \sigma_{22} + \sigma_{33})/3$ according to Equation (3):

$$c = c_0 \exp\left(\frac{\sigma_H V_H}{k_B T}\right) \tag{3}$$

In case of cracks, the hydrostatic stress σ_H shows a maximum slightly ahead (~ 2 times of CTOD) of the crack tip. The ratio of peak σ_H over yield stress at the crack tip for plane strain conditions is ~ 3 (linear-elastic fracture mechanics), ~ 5–8 (HRR singular crack-tip fields) or ≥ 10 (strain-gradient plasticity) and increases with increasing yield stress [81][82]. This can result in a (10 to 20 times) hydrogen enrichment of the bulk hydrogen content at the crack tip (Figure 13).

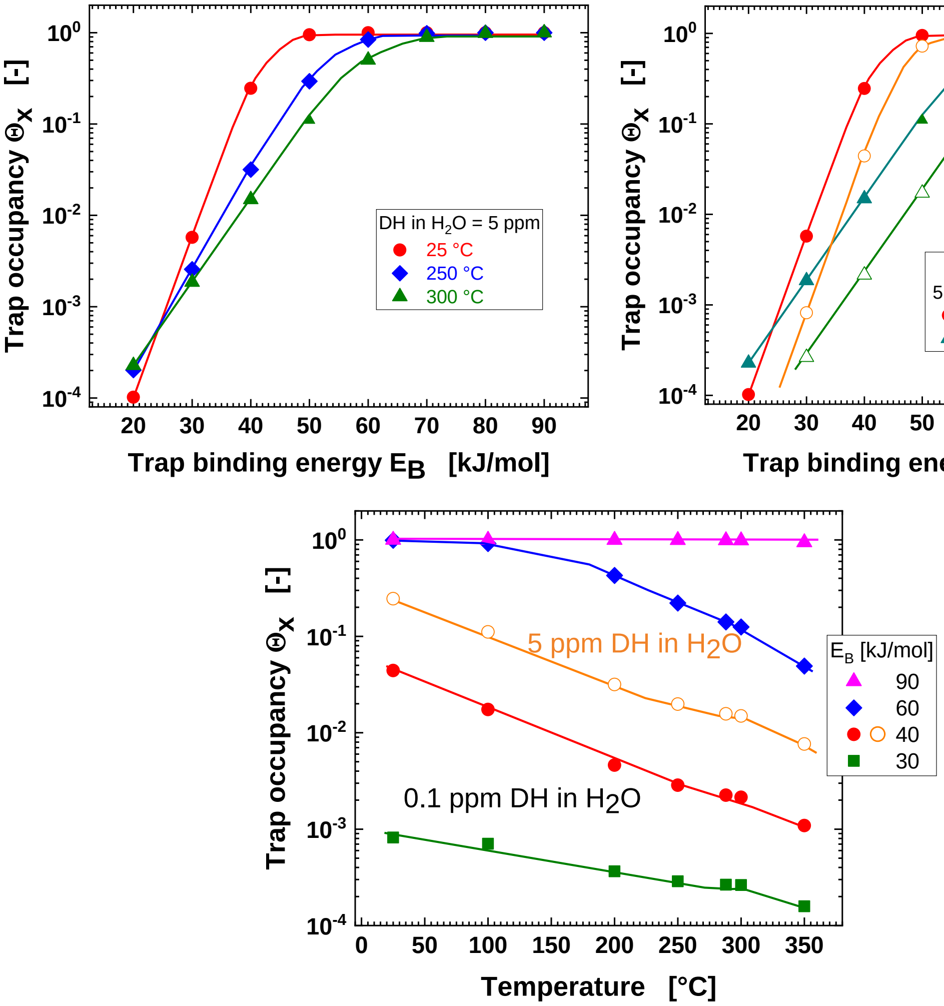

Figure 12: Dependence of trap occupancy on temperature, dissolved hydrogen and trap energies.

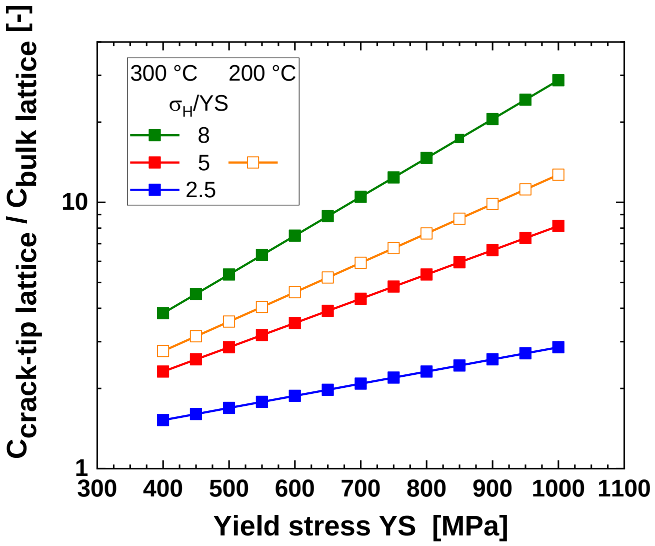

Figure 13: Effect of yield stress on hydrogen enrichment at crack tip.

The hydrogen redistribution probability between traps (with a binding energy E_B) far away from the crack tip to the crack tip is described by Equation (4) and Figure 14. There is little redistribution from strong traps to the crack tip.

$$P_\sigma = \frac{\exp(\frac{\sigma_H \overline{V_H}}{RT})}{\left[\exp\left(\frac{E_B}{RT}\right) + \exp(\frac{\sigma_H \overline{V_H}}{RT})\right]} \tag{4}$$

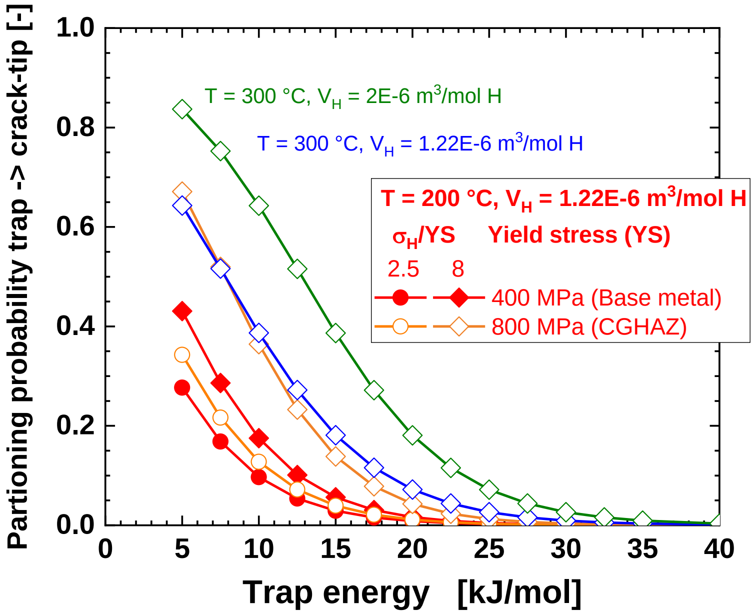

Figure 14: Hydrogen redistribution probability between traps (with a binding energy E_B) far away from the crack tip to the crack tip.

1.3.2.4 Hydrogen pick-up and concentrations in RPVs under LWR conditions

A key question is, whether the critical hydrogen concentration for HE in RPV steels can be achieved in HTW or not? This aspect is discussed in more detail in the following chapter.

The RPV is normally protected by an austenitic stainless steel cladding (RPV head and feedwater nozzle corner in some GE BWR are unclad). The corrosion rate of the cladding is significantly lower (< 0.1 µm/year) than that of the RPV steel (< 1 µm/year). Direct contact of RPV steel and coolant may occur in cracks in the cladding formed during fabrication or welding (e.g., hot cracks and relaxation cracks in the cladding or cladding/RPV interface), or during reactor operation. Important examples from the field are, e.g., the RPV feedwater nozzle corner cracking by thermo-mechanical fatigue and CF in BWRs or the SCC in RPV penetration and attachment welds in BWRs and PWRs. Furthermore, the presence of open, incipient surface cracks has always to be assumed in safety analysis.

Hydrogen absorption during LWR service arises from the contact with the H_2 containing reactor coolant and, to a lesser extent, as a by-product of corrosion reactions. The hydrogen uptake increases with increasing DH concentration and corrosion rate (both are usually closely linked in HTW and not independent). Hydrogen uptake is assumed proportional to the square root of DH content in the environment. In case of corrosion, the DH and H^+ content in the water are expected to be proportional to the corrosion current density and exponentially increase with cathodic overpotential η_c of the H_2/H_2O reaction. Both corrosion current density and cathodic overpotential increase with decreasing pH and increasing H^+ concentration. Increase in local (EAC, crevice corrosion) or uniform corrosion rate (e.g., by flow-accelerated corrosion, FAC) inevitably increases the hydrogen pick-up. Contributions from transmutation (*n*, *p*) reactions or proton recoil injection as well as the hydrogen generation by radiolysis of the water (at the RPV surfaces or in cracks) are usually believed to be insignificant compared to the other two sources. The effect of irradiation is mainly indirect, by the creation of radiation defects as potential hydrogen traps and the increase of yield stress, for HE. Hydrogen diffusion, permeation and release rates are high in RPV steels at operating temperatures. Furthermore, the oxide film do not represent a significant hydrogen diffusion barrier and do not remarkably impede H_2 dissociation. Therefore, the average free and diffusible bulk lattice hydrogen content in the steel and the hydrogen enrichment at various traps close to the surface are believed to be controlled by the DH content of the local environment in HTW.

For a given DH content in the water, the hydrogen content absorbed in the bulk metal lattice close to the surface (C_H) can be estimated by the combinations of the Sievert's [83] and Henry's [84] laws in Equations (5), (6) and (7), respectively:

$$\text{Sievert's: } C_H = S(T) \cdot \sqrt{f_{H_2}} \tag{5}$$

$$\text{Henry's: } f_{H_2} = k(T) \cdot DH \tag{6}$$

$$C_H = S(T) \cdot \sqrt{k(T)} \cdot \sqrt{DH} \tag{7}$$

with $S(T)$ = Sievert's constant, $k(T)$ = (inverse) Henry's constant and f_{H2} = hydrogen fugacity.

The absorbed hydrogen content in the bulk metal lattice is proportional to the square root of the DH. It shows a maximum at 320 to 330 °C for a given DH, since $S(T)$ and $k(T)$ increase and decrease with increasing temperature, respectively (Figure 15). Between 288 °C and 350 °C, there is only a small difference (less than 10%) of absorbed hydrogen contents. But at 250, 200 and 100 °C, the absorbed hydrogen contents are only about 80, 50 and 10% of the absorbed hydrogen at 288 °C for a given DH, respectively.

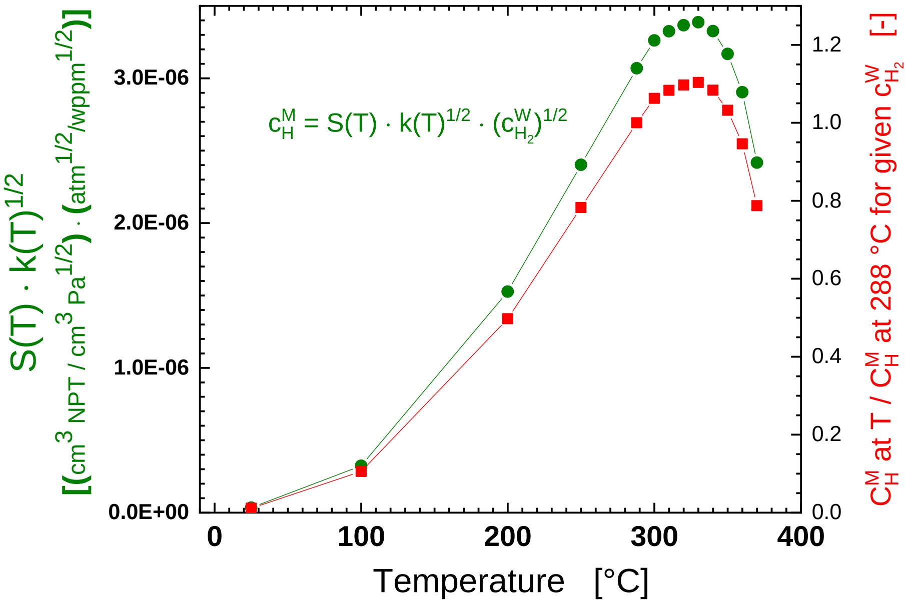

Figure 15: Temperature dependence of proportionality constant $S(T) \cdot k(T)^{1/2}$ of Equation (7) (left axis) and ratio of absorbed hydrogen contents in the metal at temperature T with respect to 288 °C for a given dissolved hydrogen content in HTW (right axis) [83][84].

In case of an intact cladding and under typical steady-state LWR power operation conditions, DH is usually low (< 0.1 wppm). Depending on the trap types, respective density, and hydrogen availability, the total hydrogen content can be much higher than the lattice hydrogen content, which is in equilibrium with the DH content in the reactor coolant. After long-term exposure in LWRs, total (free and trapped) bulk hydrogen contents of a very few wppm (with some local higher peaks) were measured in unstressed steels. In contrast, irradiated steels usually showed a higher hydrogen content. Bulk HE appears as rather unlikely, as confirmed by slow strain rate test (SSRT) tests with smooth un-notched tensile specimen in hydrogenated HTW (see Section 1.4). The continuous flux of hydrogen from the inner water-wetted surface through the wall thickness to the “hydrogen-free” environment results in a corresponding hydrogen gradient (Figure 16). In case of cracks/crevices, the situation is totally dominated by the complex local occluded crack/crevice chemistry and the local corrosion processes at plastically strained crack tip (which is much more aggressive than the bulk environment). Although the DH content in PWR primary water is significantly higher than in BWR coolants, similar or even higher concentrations of absorbed hydrogen occur in BWR components, especially in crevices/cracks with aggressive occluded crevice chemistry (differential aeration cell). Crevice environments are discussed in Section 1.3.4 in the paragraphs on EAC.

Even in oxygenated HTW, the crack-tip environment is always completely de-aerated and crack-tip potentials are controlled by the H_2/H_2O reaction. The H_2/H_2O and Fe/Fe_3O_4 lines in the Pourbaix diagram are parallel in the intermediate pH range. The potential difference and potential for hydrogen production by polarization does not change with pH shifts. A pH decrease only increases the H^+ concentration. The exchange current density of the hydrogen redox reaction in the hydrogenated HTW on RPV steels is (one to two orders of magnitude) higher than the stationary uniform corrosion rates. Hence, the corrosion potential of RPVs is usually close to the equilibrium electrode potential of the hydrogen redox reaction. Additionally, the low conductivity of LWR coolants further limits cathodic overpotential η_c and possibility for hydrogen enrichment from local corrosion reactions.

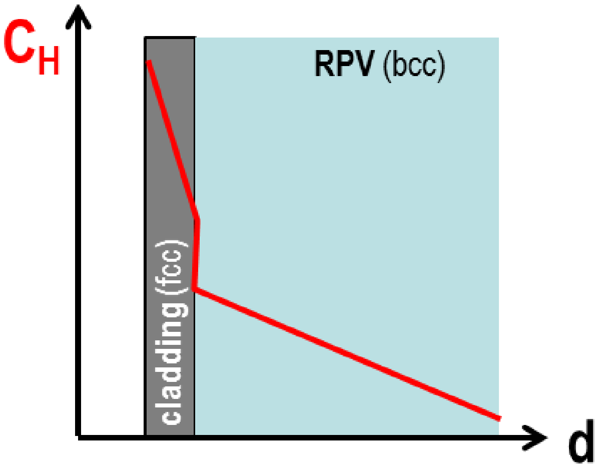

Figure 16: Hydrogen gradient through the RPV structure.

At the locally fractured oxide film at the crack tip, the potential can temporarily drop to the Fe/Fe_3O_4 line that may significantly increase the hydrogen uptake, but reformation of oxide film usually starts almost immediately after the film rupture and the bare metal area is relatively small with respect to the plastic zone size and volume. The latter two limit the hydrogen content in the crack-tip process zone in spite of initially high, but very local dissolution current densities. In an EPFM test, quasi-continuous bare metal dissolution may occur at the plastically strained crack tip and an aggressive crack crevice environment can evolve under suitable loading rate conditions with increased hydrogen uptake at the crack tip. The enrichment of this hydrogen at the crack tip increases exponentially with the hydrostatic stress σ_H (discussed in 1.3.2.3). At the crack-tip surface, there is the highest (equivalent) plastic strain with high dislocation and vacancy concentration, which also increases the hydrogen uptake in this region and results in a second hydrogen peak. Based on all these aspects and together with the very localized nature of hydrogen-deformation interactions and hydrogen transport (e.g., by dislocations), it is almost impossible to estimate, if a critical hydrogen concentration can be reached in the process zone during an EPFM test. There is a clear need to systematically study such potential effects on the fracture behaviour in HTW directly.

1.3.3 Mechanisms of hydrogen embrittlement

1.3.3.1 Hydrogen embrittlement mechanisms

HE mechanisms that may occur in RPV steels are [63]:

1. Hydrogen-enhanced decohesion embrittlement (HEDE): hydrogen atoms weaken the interatomic bonding and lead to brittle or QC micro-cracks at strong traps, like MnS/oxide inclusions or intergranular cracking at GBs.

2. Hydrogen-enhanced local plasticity (HELP): hydrogen reduces the elastic interaction forces between dislocations and dislocation obstacles (shielding effect), resulting in (local) softening. This requires small distances between dislocations, high dislocation density and high plastic strains. Under certain temperature and strain rate conditions, hydrogen can also have a drag effect on mobile dislocations. In fcc steels, hydrogen may also reduce the stacking fault energy, restrict cross slip and favour shear localization and planar coarse slip.

3. Hydrogen-enhanced strain-induced vacancies (HESIV): hydrogen atoms reduce the formation energy of vacancies and facilitate their agglomeration/clustering and collapse to micro-voids. Very

high vacancy and hydrogen concentrations in highly cold-worked regions can occur, affecting plastic deformation behaviour (climbing of edge dislocations, vacancy clusters and nano-voids as dislocation obstacles) and enhancing MVC [85].

4. Adsorption-induced dislocation emission (AIDE): hydrogen atoms facilitate nucleation of dislocations at surface (crack tip, voids) and their emission into the plastic zone.

Combinations of and synergies between these mechanisms are possible in RPV steels under LWR conditions, if sufficient amount of hydrogen is present in the steel. The relative contributions of these mechanisms depend on temperature, strain rate and microstructure, etc. [86]. Mechanisms 2 to 4 are not only enhancing ductile failure by MVC, but also facilitating brittle cleavage or QC cracking by various mechanisms (e.g., due to dislocation pile-ups) at interfaces, such as second-phase particles, GBs or along preferred highly active slip planes. Mechanism 1 (HEDE) may explain the quasi-brittle features around MnS inclusions observed in EPFM and EAC tests in HTW. HE cracking can be trans- or intergranular by ductile nano-/micro-void coalescence or (quasi-) brittle crack extension. Some of these mechanisms (e.g., HELP) also reveal positive feedback effects (e.g. plastic strain localization increases hydrogen accumulation in these zones, which in turn further amplifies the plastic strain localization).

HE may be synergistic (or competitive) with other embrittlement and degradation mechanisms, like irradiation embrittlement and DSA, EAC or TE. For example, the interaction of localized deformation bands (by HELP) with weakened GBs (by HEDE and TE) may result in intergranular cracking, or the strain localization (by DSA and HELP) and accumulation of hydrogen in these zones. This can lead to the formation of shear bands or the early formation and growth of micro-voids by HESIV [87] and subsequent increased inter-void strain localization by HELP.

1.3.3.2 Factors of influence for hydrogen embrittlement

The magnitude of HE is synergistically controlled by material, environmental and mechanical loading parameters (Figure 17). Hydrogen may affect brittle and ductile fracture as well as sub-critical crack growth (HAC, EAC) due to its effects on cohesive strength, dislocation mobility and vacancies. Mechanisms like HEDE, HELP or HESIV, can be simultaneously or successively active in the process zone.

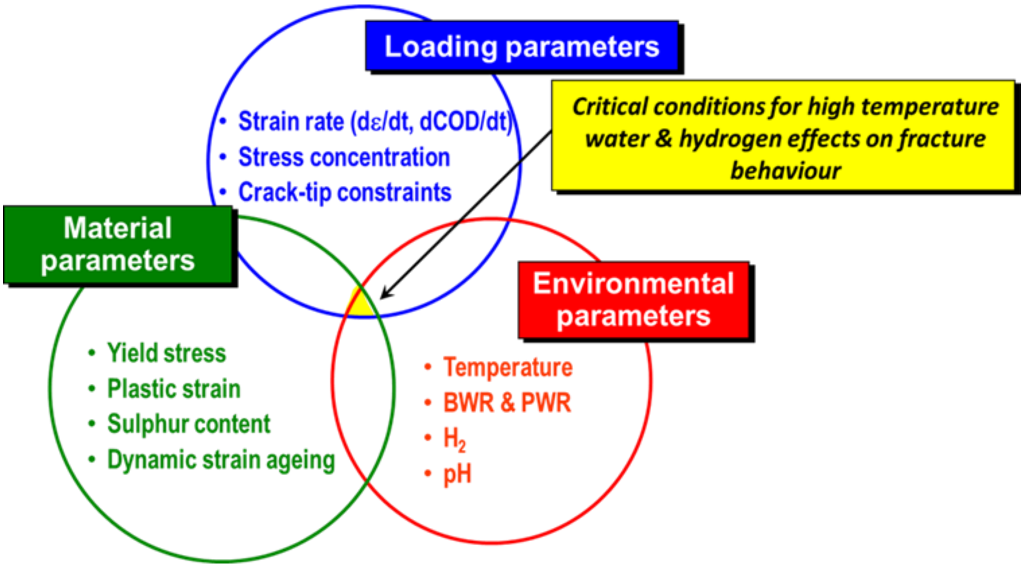
Loading parameters
• Strain rate (dε/dt, dCOD/dt)
• Stress concentration
• Crack-tip constraints
Critical conditions for high temperature water & hydrogen effects on fracture behaviour
Material parameters
• Yield stress
• Plastic strain
• Sulphur content
• Dynamic strain ageing
Environmental parameters
• Temperature
• BWR & PWR
• H2
• pH

Figure 17: Major factors of influence for HE in RPV steels.

Depending on microstructure (traps or fracture initiation sites), hydrogen content and availability, temperature, strain rate or hydrostatic stress, the mechanisms and controlling factors for fracture can change within the same material. The controlling factors of HE are strongly system (material-environment-loading) specific and dependent on the exact boundary conditions. Furthermore, the interactions are extremely localized at micro- to nano-level. The number of observations and effects are tremendous and manifold. The influential parameters are interrelated and can be synergistic or competitive. Yield stress, e.g., cannot be varied without change of microstructure. Temperature affects almost all thermodynamic and kinetic aspects (hydrogen trapping, diffusion and uptake/release, corrosion and plastic deformation).

Both hydrogen transport and hydrogen-dislocation or -vacancy interactions are dependent on factors like temperature, strain rate, plastic strain and microstructure. Accelerated local hydrogen transport is possible by mobile dislocation (or by pipe diffusion) in crack-tip plastic zone (due to strain and strain rate effect), although this is more relevant for fcc alloys with slower hydrogen diffusion. On the other hand, the apparent diffusion rate of hydrogen is decreasing with increasing trap density (microstructure effect), in particular at lower temperatures. The hydrogen trapping efficiency decreases with increasing temperatures and is low above 300 °C.

Hydrogen migrates towards stress concentrations and enriches in regions of high hydrostatic stress or dilatation strain fields, e.g., at crack tips and sharp notches. If a critical hydrogen concentration (and stress/strain) over a critical volume is achieved in the process zone at the crack tip, cracking may occur by brittle or ductile cracking mechanisms, starting from specific initiation sites at stress/strain levels below those without hydrogen. Hydrogen may reduce the critical stress or strain for cleavage or micro-void formation and affect the plastic deformation behaviour (softening, hardening, and localization) and the stress/strain state at the crack tip. Furthermore, a high hydrostatic stress also favours both micro-void formation and brittle QC cracking (see Section 1.2). The peak tensile stress at the crack tip is about three times the flow stress for plane strain conditions. For the same level of hydrogen, the effects are less severe for plane stress condition, in particular for brittle cracking processes. Factors that increase the hydrostatic stress or yield stress are expected to increase the HE susceptibility (Figure 18). Plane strain and Mode-I loading usually result in most severe HE and HAC.

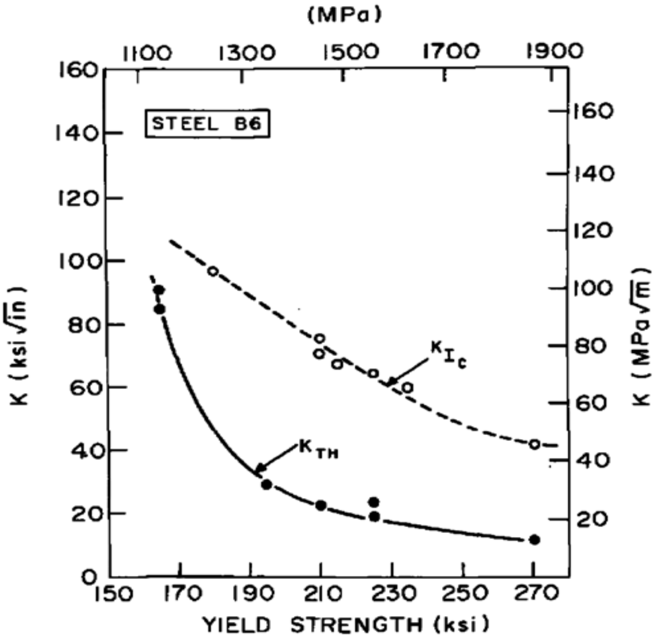

Figure 18: Effect of yield stress on threshold K_{th} for sub-critical HAC and K_{IC} in high-strength LAS [60].

Therefore, HE is usually related to high-strength steels (hydrogen enrichment by high hydrostatic stress at crack tip) and temperatures below 150 °C (more efficient hydrogen trapping), but it may occur also at 300 °C, if sufficient hydrogen is still present in the steel, as shown by this work.

Hydrogen diffusion decreases (by about two orders of magnitude) in the order of ferrite, pearlite/bainite and martensite. However, the martensitic structures usually show the highest tendency to HE compared to other microstructures, which is attributed to higher strength of martensite. It further confirms the effect of yield stress or hardness. GB hydrogen concentration is expected to be higher in coarse- than in fine-grained steels for a fixed hydrogen level, which is because of the presence of a larger GB area in fine-grained steels, which results in a lower GB hydrogen concentration. The larger grain size can also cause higher GB stresses by dislocation pile-ups at GBs and usually results in a lower initial toughness without hydrogen. Therefore, fine-grained steels are often expected to have a higher resistance to HE compared to coarse-grained steel [76]. The hydrogen solubility and diffusion rates are (two to three orders of magnitude) higher and slower in fcc steels, respectively. Combination with the absence of a ductile to brittle transition in air without hydrogen and the higher number of independent slip systems results in a smaller HE tendency in fcc alloys.

1.3.3.3 Evidence for hydrogen embrittlement in RPV steels

HE studies with very ductile and moderate strength LAS (300 to 800 MPa) with high upper shelf toughness were mainly performed by electrochemical hydrogen pre-charging and to a lesser extent in gaseous hydrogen (since this requires very high hydrogen partial pressures), mainly at room temperature. These tests showed hydrogen effects on the mechanical tensile behaviour and on brittle or ductile fracture in these steels. Hydrogen effects on the mechanical behaviour of RPV steels were observed up to 300 °C [88]. The critical hydrogen content for HE in RPV steels is in the range of 2 to 4 wppm for unirradiated RPV steels and 1 to 2 wppm for highly irradiated RPV steels. Hydrogen effects become drastic with completely brittle failure above 7 to 10 wppm. At 300 °C, the HE effects were usually moderate and often claimed to be negligible. Some investigations showed synergies (additive behaviour) between HE and irradiation (Figure 19) [89][90] and TE [91][92], whereas other rather indicated the opposite behaviour [93].

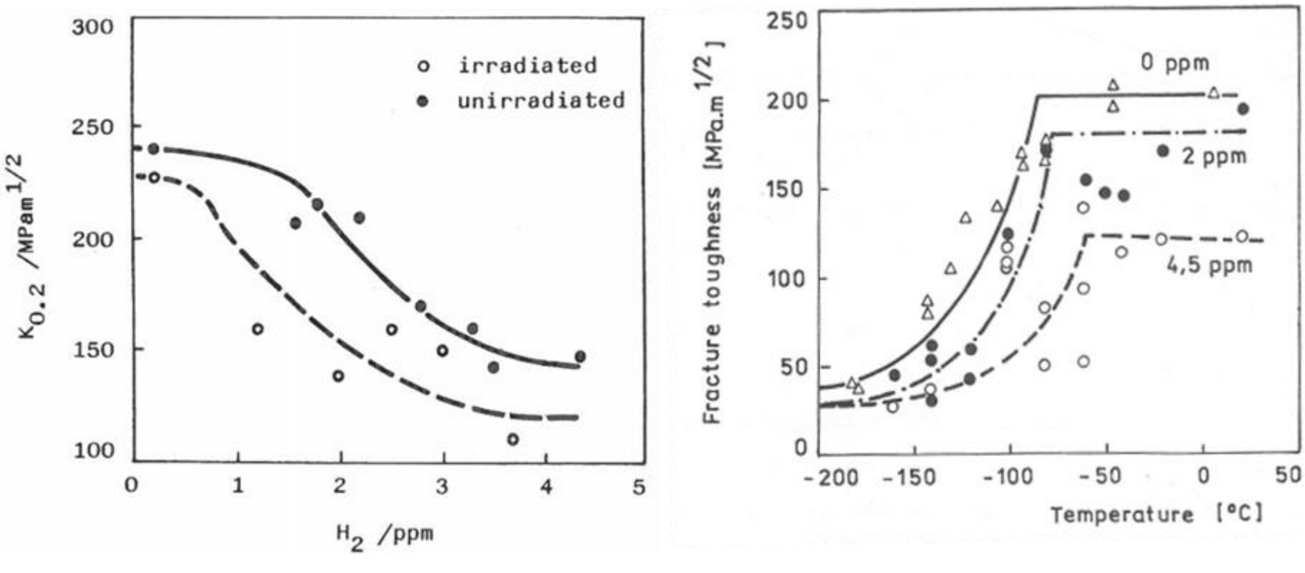

Figure 19: Effect of n-irradiation (288 °C, 8×10^{19} n/cm^2 (E > 0.5 MeV)) and hydrogen content from hydrogen pre-charging on the toughness in the upper shelf and transition region of a VVER RPV steel [90].

There is an ongoing debate, if such hydrogen contents can be reached in the RPV during LWR service. The limited and partially contradicting database is not fully conclusive. The limited hydrogen availability and high trap density as well as the fast hydrogen effusion and release rates rather suggest moderate effects only, but the experimental proof is pending. Even moderate effects may be critical for long-term operation for plants with small margins to irradiation embrittlement.

1.3.4 Interactions of HE with other degradation and embrittlement mechanisms

HE may be synergistic (or competitive) with other degradation and embrittlement mechanisms like EAC, DSA, TE or irradiation embrittlement. Those mechanisms are elaborated in the following section.

1.3.4.1 Environmentally-assisted cracking

EAC in LAS [94] is the formation and sub-critical (at $K_I < K_{Ic}$) growth of cracks under the simultaneous and synergistic interaction of mechanical (tensile) stress and the HTW environment. EAC is used as a general term to cover the full spectrum of corrosion cracking ranging from SCC [94][95] under static load to CF under cyclic loading conditions. SCC is the term given to the sub-critical crack formation of susceptible alloys subjected to a static external or residual tensile stress and exposed to a system specific environment [96][97][98]. Strain-induced corrosion cracking (SICC) [99][100] involves slow and dynamic straining with localized plastic deformation of materials, but where obvious cyclic loading is either absent, or is restricted to a limited number of infrequent events such as plant start-up and shut-down [6][101][102][103]. SICC is increasingly used as an appropriate term to describe the area of overlap between SCC and CF for LAS. The detailed differences of EAC types in LAS are listed in Table 5.

Table 5: Basic types of EAC in LAS and relevant nuclear codes [28]

Mechanism	**Environmentally-assisted cracking (EAC)**		
	Stress corrosion cracking (SCC)	Strain-induced corrosion cracking (SICC)	Corrosion fatigue (CF)
Type of loading	Static	Slow monotonically rising or very low-cycle	Cyclic: low-cycle, high-cycle
LWR operation condition	Transient-free, steadystate power operation	Start-up/shut-down, thermal stratification	Thermal fatigue, thermal stratification, …
Characterization of crack growth	BWRVIP-60 disposition lines	?	ASME XI, Code Case N-643 (PWR)
Characterization of crack initiation	? (σ > YS)	Susceptibility conditions: ECPcrit, $d\varepsilon/dt$crit, εcrit	ASME III, F_{env}-approach

SCC is characteristic for transient-free steady-state power operation, where pure static loading of large vessels usually prevails. SICC is characteristic for global plant transients like start-up/shut-down, hot stand-by with related pressurization and thermal cycles or with severe thermal stratification. CF is related to system conditions and locations with distinct cyclic loading (and clear fatigue contribution) with thermal stratification and striping or turbulent mixing, flow-induced vibrations or pressure pulsation and moments from pumps forces etc.

The main reason to make this differentiation between SCC and SICC for LAS is their very high SCC crack initiation and crack growth resistance in high-purity HTW up to high K_I values and absence of SCC incidents in the field, where cracking was always related to SICC, oxidizing conditions and specific plant transients and conditions with severe plastic straining. There is a continuous spectrum from SCC to CF (and possibly environmental rapid fracture and hydrogen embrittlement) in LAS, which suggests that there is a similar underlying mechanism for all three types of EAC. The very similar influencing parameter dependencies and general fracture appearance for SCC, SICC and even CF (at least for strong environmental acceleration of fatigue crack growth) is further confirming that EAC is governed by the same basic process for all three loading modes.

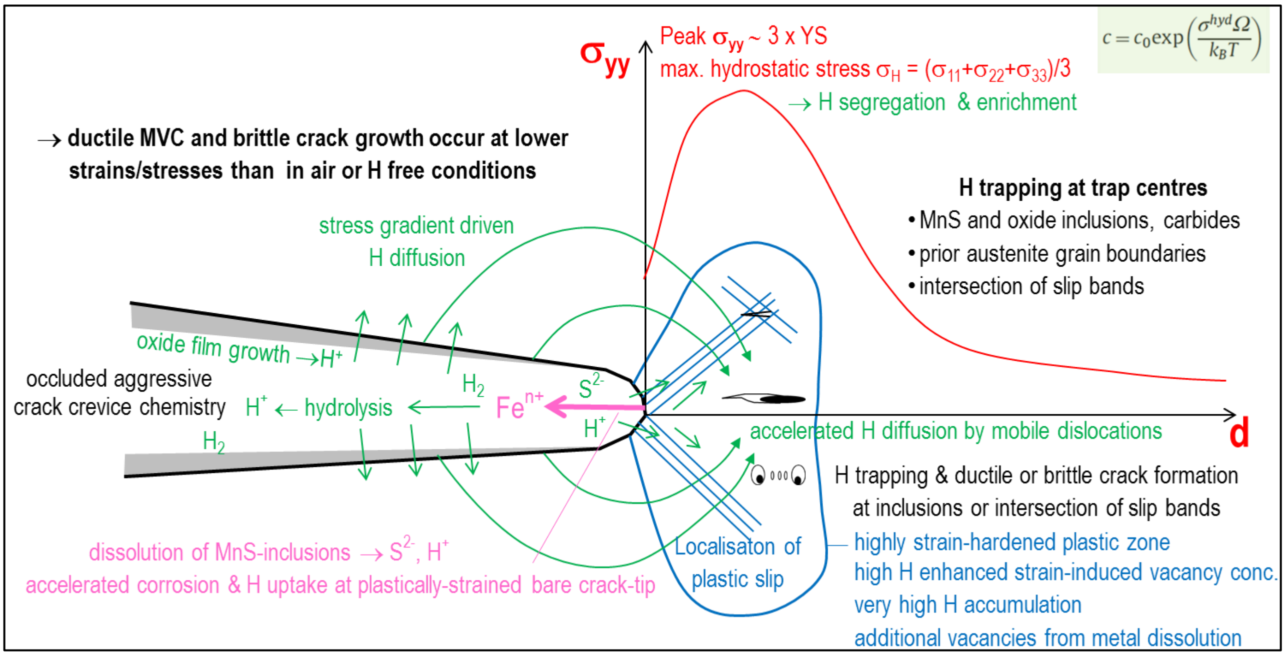
σ_{yy}
Peak σ_{yy} ~ 3 x YS
max. hydrostatic stress $\sigma_H = (\sigma_{11}+\sigma_{22}+\sigma_{33})/3$
→ H segregation & enrichment
$c = c_0 \exp\left(\frac{\sigma^{hyd}\Omega}{k_B T}\right)$
→ ductile MVC and brittle crack growth occur at lower strains/stresses than in air or H free conditions
H trapping at trap centres
• MnS and oxide inclusions, carbides
• prior austenite grain boundaries
• intersection of slip bands
stress gradient driven H diffusion
oxide film growth →H^+
occluded aggressive crack crevice chemistry
H^+ ← hydrolysis
H_2
Fe^{n+}
S^{2-}
H^+
H_2
accelerated H diffusion by mobile dislocations
d
H trapping & ductile or brittle crack formation at inclusions or intersection of slip bands
highly strain-hardened plastic zone
high H enhanced strain-induced vacancy conc.
very high H accumulation
additional vacancies from metal dissolution
Localisaton of plastic slip
dissolution of MnS-inclusions → S^{2-}, H^+
accelerated corrosion & H uptake at plastically-strained bare crack-tip

Figure 20: Localized hydrogen uptake, hydrogen-deformation interactions and hydrogen embrittlement in the crack-tip system during an EPFM test [63].

Figure 20 illustrates the potential mechanisms of HE in RPV steels. In HTW, there is a continuous spectrum from sub-critical EAC to environmental-assisted rapid fracture and HE [14]. These phenomena are controlled by similar parameters and are closely linked, showing many commonalities. It is plausible that parameters and other phenomena, which affect EAC, may also influence HE in RPV steels in a similar way. Potential HTW effects on rapid fracture are most probably related to hydrogen effects.

Mechanisms and models of EAC in LAS

EAC crack growth in LAS in HTW is best rationalized as a superposition/combination of the film-rupture anodic dissolution (FRAD) model [104][105][106] and hydrogen-assisted EAC (HAEAC) mechanisms [93][104], whereas dissolution seems to dominate the crack advance at higher temperatures (> 150 °C) and slow strain rates ($< 10^{-3}$ s^{-1}). HAEAC may become dominant at lower temperatures (< 100 °C) in high-strength steels and at higher strain rates [107]. In HTW (> 150 °C), no sub-critical EAC is observed above a strain rate of 10^{-2} s^{-1}. Therefore, under most conditions of this test program, dissolution is the dominant EAC growth mechanism [91][105]. The proposed mechanisms relate EAC susceptibility to electrochemical and mechanical processes occurring at the crack-tip region.

In the FRAD mechanism, the protective oxide film formed on LAS in HTW is ruptured by plastic straining at the crack tip. The crack tip then advances by anodic dissolution of the bare metal matrix. Anodic dissolution is slowed down and finally stopped by the nucleation and reformation of the oxide film (repassivation) [108]. Therefore, continued crack advance will depend on a further oxide rupture process, due to the action of a strain rate at the crack tip. The crack propagation rate is controlled by both anodic dissolution/repassivation kinetics and the frequency of oxide film rupture at the strained crack tip. The first part is governed by the chemical composition of the local crack-tip electrolyte and the material. The second part is determined by the fracture strain of the oxide film and the crack-tip strain rate. The crack-tip strain rate and sulphur anion concentration in the crack-tip environment are the main controlling factors for EAC in this model.

Oxide film rupture-repassivation events at the strained crack tip are also involved in the HAEAC model. However, in HAEAC, hydrogen-induced micro-crack formation ahead of the crack tip and linkage of these micro-cracks to the main crack, are the prime sources of EAC crack growth, and the reason for discontinuous crack propagation. The hydrolysis of metal cations from anodic dissolution is an important source of hydrogen, but in contrast to the FRAD mechanism, anodic dissolution does not contribute significantly to crack advance. The generation of bare metal surface by film rupture and film reformation may be the rate-controlling steps and explain the strain rate dependence of EAC [109], since hydrogen transport in the electrolyte and in the metal lattice is believed to be fast [91][110].

Controlling factors for EAC crack growth

In the following section, the main EAC growth controlling parameters [100][111][112], the role of MnS inclusions and effect of DSA on EAC of LAS are briefly discussed. EAC is controlled by the crack-tip strain rate [95][113] and sulphur-anion concentration in the occluded crack crevice environment (Figure 21), which in turn are governed by interrelated material (sulphur content, yield stress, DSA), environmental (ECP/DO, SO_4^{2-}, Cl^-, temperature) and loading parameters (K_I or J, dK/dt, dK/da) [96][104][114].

EAC thresholds are directly related to crack crevice chemistry and crack-tip strain rate rather than to bulk chemistry or loading conditions. A unique aspect of EAC in LAS is that the crevice chemistry is also dependent on the crack growth rate itself by the exposure of new and dissolvable MnS inclusions, which are intersected by the growing crack. Above a certain critical crack growth rate, this can result in a sulphide-rich crevice environment even in high-purity hydrogenated water, when the production rate of sulphides from the dissolution of MnS is faster than their slow transport out of the crack by diffusion.

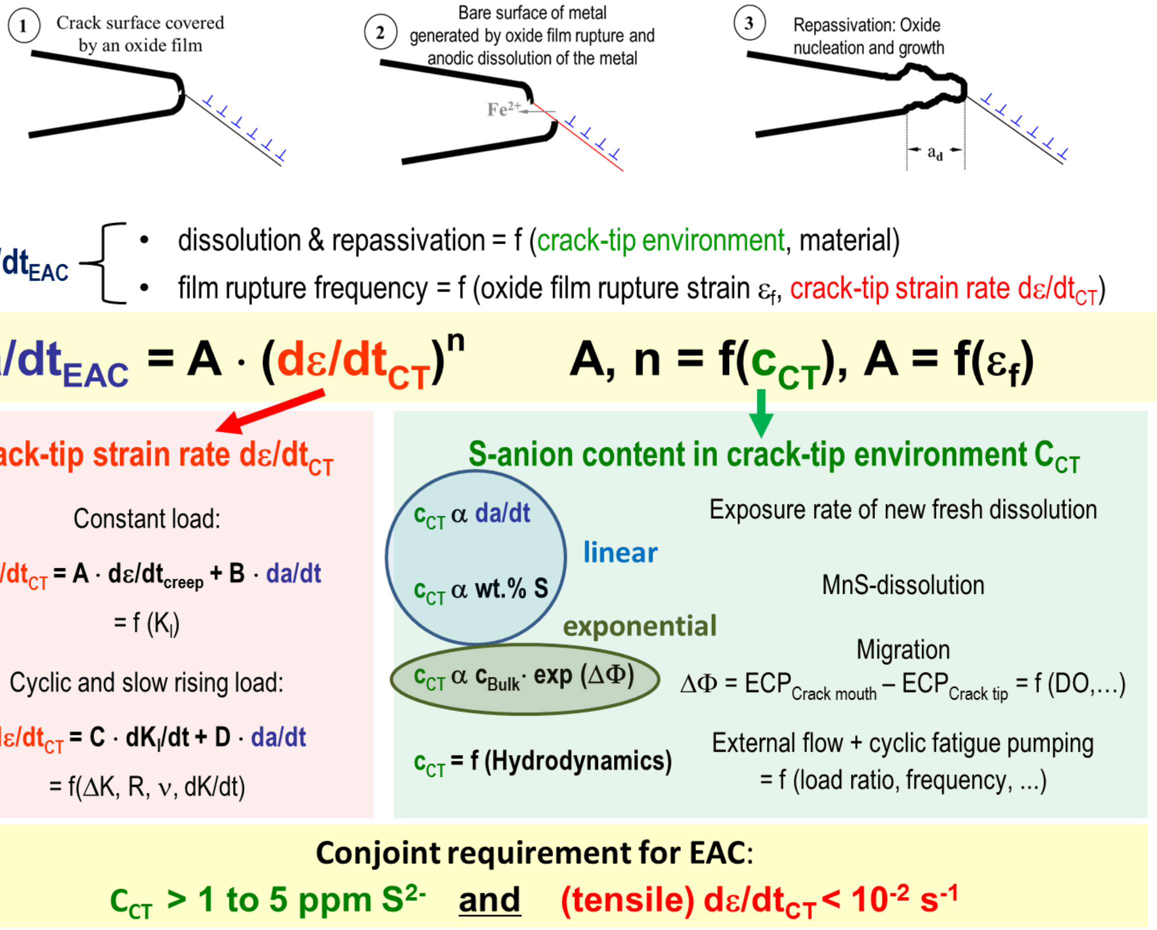
① Crack surface covered by an oxide film
② Bare surface of metal generated by oxide film rupture and anodic dissolution of the metal
Fe2+
③ Repassivation: Oxide nucleation and growth
a_d

da/dt_{EAC}

- dissolution & repassivation = f (crack-tip environment, material)
- film rupture frequency = f (oxide film rupture strain ε_f, crack-tip strain rate $d\varepsilon/dt_{CT}$)

$$da/dt_{EAC} = A \cdot (d\varepsilon/dt_{CT})^n \qquad A, n = f(c_{CT}), A = f(\varepsilon_f)$$

Crack-tip strain rate $d\varepsilon/dt_{CT}$

Constant load:

$$d\varepsilon/dt_{CT} = A \cdot d\varepsilon/dt_{creep} + B \cdot da/dt = f(K_I)$$

Cyclic and slow rising load:

$$d\varepsilon/dt_{CT} = C \cdot dK_I/dt + D \cdot da/dt = f(\Delta K, R, \nu, dK/dt)$$

S-anion content in crack-tip environment C_{CT}

$c_{CT} \alpha\ da/dt$ — linear — Exposure rate of new fresh dissolution

$c_{CT} \alpha$ wt.% S — exponential — MnS-dissolution

$c_{CT} \alpha\ c_{Bulk} \cdot \exp(\Delta\Phi)$ — Migration: $\Delta\Phi = ECP_{Crack\ mouth} - ECP_{Crack\ tip} = f(DO, \ldots)$

$c_{CT} = f$ (Hydrodynamics) — External flow + cyclic fatigue pumping = f (load ratio, frequency, ...)

Conjoint requirement for EAC:

$C_{CT} > 1$ to 5 ppm S^{2-} and (tensile) $d\varepsilon/dt_{CT} < 10^{-2}\ s^{-1}$

Figure 21: FRAD mechanism with controlling factors and conjoint requirement for EAC [100].

Crack crevice chemistry and environmental parameters [96][115]: As already mentioned, the local crack crevice environment controls HE and EAC in case of cracks. An aggressive occluded crack crevice environment can be formed in oxygenated HTW that is more aggressive than the bulk environment. Oxygen mass transport by diffusion into the cracks is slower than its reduction and consumption on oxide film. Crack crevices with restricted mass transport (high depth to width ratio) readily consume all the oxygen over a short distance from the crack mouth. This effect produces a potential drop between the de-aerated crack tip (~ -500 mV_{SHE}) and the aerated crack mouth ($\sim +100$ mV_{SHE}). This effect also leads to migration of anions and cations towards the crack tip and crack mouth, respectively. Therefore, the crack tip enriches with critical anionic impurities that affect the repassivation and can produce acidic pH shifts, e.g., in case of bulk environment impurities like Cl^- or SO_4^{2-}. Hydrolysis of metal cations produced during anodic dissolution at the strained crack tip and the dissolution of MnS inclusions may produce small acidic pH shift.

The differential aeration cell in the crack-mouth region and the evolution of an aggressive occluded crevice chemistry are the main reasons for the strong effect of ECP or DO on EAC. This effect is synergistic with anionic impurities in the bulk environment as well. The lower pH of the crack-tip environment and retardation of repassivation after film ruptures (due to sulphate/sulphides and chloride enrichment), increase the hydrogen uptake under NWC conditions. At the de-aerated crack tip, the potential is always low and close to the equilibrium potential of the H_2/H_2O reaction. In oxygen-free, hydrogenated BWR/HWC or PWR water, the H_2/H_2O reaction controls the ECP at both the crack tip and crack mouth. For this reason, there is no potential gradient between the crack tip and crack mouth and the mass transport is controlled by diffusion only. Therefore, there is no enrichment of anionic impurities in the crack crevice environment. The DH concentration in the environment at the crack tip is similar or higher as in the bulk environment, since there is almost no consumption of hydrogen.

The crack-tip environment conditions in high-purity water, which govern the hydrogen uptake at the crack tip in EPFM tests, are not fundamentally different for BWR/NWC, HWC and PWR conditions in this project. The crack-tip potential is low in all three environments. The DH content is similar as in the bulk environment and is about 10 to 35 ppb in BWR/NWC, 80 ppb in BWR/HWC and 2 to 3 ppm in PWR environment. The pH is slightly acidic ($pH_{288\,°C} = 4.5$ to 5.7) in BWR/NWC, neutral ($pH_{288\,°C} = 5.7$) in BWR/HWC and slightly alkaline ($pH_{288\,°C} = 7$) in primary PWR water, respectively. Therefore, there is a higher DH content, but lower corrosion rate in alkaline PWR water. In low-sulphur steels, in BWR/NWC environment, the pH is neutral. However, in case of anionic impurities in the bulk environment or high-sulphur steels, a moderate acidic pH shift of at maximum 1 to 1.5 units is possible (which corresponds to a 10 to 30 times increase in H^+ concentration in the water).

A sulphide-rich environment with increased hydrogen uptake can also be formed by a sufficiently fast growing crack under suitable loading conditions in high-purity hydrogenated HTW. Based on the DH content, the absorbed hydrogen content in steels can be a factor of 5 to 20 higher in PWR than in BWR environments. However, this is partially compensated by the higher corrosion rates and 20 to 300 times higher H^+ availability in neutral or slightly acidic BWR environments, in particular, if an aggressive occluded crack crevice environment is formed. This is also confirmed by the following simple comparison: The 2 wppm dissolved H_2 corresponds to 4×10^{-6} mol/L or 8×10^{-6} mol/L as H_2 or hydrogen, pH of 7, 5.7 (neutral) and 4.5 and H^+ concentrations of 10^{-7}, 2×10^{-6} and 3.2×10^{-5} mol/L.

The EAC growth rates increase with temperatures between 150 and 320 °C with a potential maximum around 250 °C for steels with high DSA susceptibility. Below 150 °C, crack growth rates are very low for RPV steels at normal strength levels [100]. In case of high Vickers hardness (≥ ~ 350 HV) and high yield stress, fast EAC and SCC may also occur below 150 °C. Temperature effects may be different for EAC and HE. In HE, the efficiency of hydrogen trapping decreases strongly with increasing temperature and most of the weakly trapped hydrogen may quickly effuse out of the steel at higher temperatures.

<ins>Material parameters</ins>: Yield stress, MnS inclusions and DSA [12][116] are the material parameters having the strongest effect on sub-critical EAC in RPV steels and also potentially affect HE .

In SCC, a higher yield stress [100] results in a steeper strain gradient at crack tip and a higher crack-tip strain rate for a growing crack under otherwise identical conditions, which is the main reason for its strong effect in the FRAD mechanism. For HAEAC and HE, the higher yield stress results in a higher peak and hydrostatic stress ahead of crack tip and this favours the hydrogen enrichment in this region. Furthermore, due to the smaller plastic zone size, the available hydrogen is concentrated at a smaller volume. The diffusion distances for hydrogen to the critical region in the process zone are also smaller.

Sulphur-anions such as HS^-, S^{2-} and SO_4^{2-} (from the dissolution of MnS inclusions), may significantly retard repassivation after oxide film rupture and therefore increase crack advance by anodic dissolution in the FRAD-model [117]. Above a sulphide concentration of ~ 0.02 ppm (low sulphur threshold in crevice environment), the formation of a new oxide layer is increasingly delayed by sulphide content, leading to a larger increment of crack advance by anodic dissolution per oxide-rupture event. Above a sulphide content of ~ 2 ppm (high sulphur threshold), the sulphide effect on repassivation saturates. Retarded repassivation of the film-free surface and adsorbed HS^-, S^{2-} or H_2S increase the hydrogen absorption into the metal lattice, and favour HAEAC [100]. Furthermore, the dissolution of MnS is a potential source of hydrogen. The interface between the MnS inclusions and metal matrix (in the region of maximum hydrostatic stress ahead of the crack tip), may act as strong hydrogen traps and HAEAC QC micro-crack initiation sites [91][93]. The MnS inclusions can act as initiation sites for micro-void formation in ductile fracture as well. Therefore, upper shelf toughness usually decreases with steel sulphur content.

In HTW, the effects of steel sulphur content are synergistic with environmental variables, such as (sulphur-) anionic impurities in the bulk environment, ECP (DO content) and flow rate. This is due to the creation of a sulphur-rich crack-tip environment for EAC, which arises from the dissolution of MnS and the transport of sulphur anions by migration/diffusion/convection within the crack enclave.

1.3.4.2 Dynamic strain aging

DSA is a phenomenon occurring at intermediate strain rates and temperatures, and arises due to an elastic interaction of (moving) dislocations and free interstitials like carbon and nitrogen during plastic deformation, in which carbon and nitrogen atoms diffuse to the dislocation core region, forming Cottrell atmosphere and pinning dislocations [12][118][119]. DSA typically occurs in the temperature and strain rate range of 100 to 350 °C and 10^{-8} to 10^{-2} s^{-1}, respectively. DSA increases with increasing free carbon and nitrogen contents that in turn depend on the chemical composition, heat treatment and steel making process [12]. The DSA effect is most pronounced, if the diffusion rate of interstitial carbon and nitrogen atoms (which is dependent on temperature) and the dislocation velocity (which is dependent on strain rate) are similar [120]. Due to its higher solubility and lower precipitation tendency, nitrogen often dominates the DSA response.

Macroscopically, DSA results in a maximum in strength and strain hardening and minimum of ductility (at intermediate temperatures), serrations in stress-strain curve and a negative strain rate sensitivity (see Figure 40 to Figure 42 in Section 2.1) [121]. Microscopically, it results in a localization of plastic deformation and lead to the increase in planar deformation and dislocation density [12]. A minimum in upper shelf fracture initiation and tearing resistance was observed in air at intermediate temperatures between 150 and 300 °C [119], which was shifted to higher temperatures with increasing loading rates and was more pronounced in steels with increased DSA susceptibility

(Figure 22) [11]. Under irradiation, this minimum was either shifted to slightly higher temperatures (Figure 23) or completely vanished in some cases [122][123].

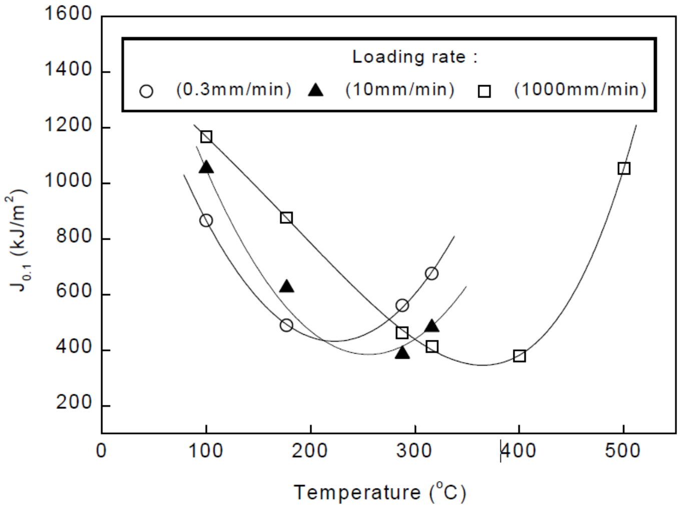

Figure 22: Variation of tearing resistance (*J* values at a crack growth of 2.54 mm), with temperature and loading rate [11].

In LAS, the DSA phenomenon is often observed during plastic straining at sufficiently slow strain rates in the temperature range from 100 to 350 °C, where EAC is also typically observed [100]. DSA may synergistically interact with EAC and HE in LAS, e.g. due to the localization of plastic deformation (film rupture and HELP) or increase in strength. In Wu's report it was suggested that the combined effects of hydrogen and DSA may aggravate the EAC of RPV steels [100]. DSA may increase EAC susceptibility and provide an additional contribution to the crack growth process. DSA may result in the occurrence of a higher crack-tip strain/strain rate than for loading outside the peak DSA range, or than in a material that is not susceptible to DSA. The localization of plastic deformation and increase in planar deformation from DSA probably enhance mechanical rupture of the oxide film and result in a reduction of the local fracture toughness, favouring quasi-brittle crack extension [12]. The concentrations of free, interstitial nitrogen and carbon (which mainly govern the DSA susceptibility in LAS) may therefore be just as relevant for EAC susceptibility as the steel sulphur content. Some data suggest that DSA may even overwhelm sulphur effects under certain conditions [124][125]. DSA generally results in an extension of the susceptibility region and can affect the temperature and strain-rate dependence of EAC. The most pronounced effects of DSA on EAC [100] are typically observed close to crack growth thresholds (e.g., for SCC under static load [94], or for CF close to critical frequencies under cyclic load [92]).

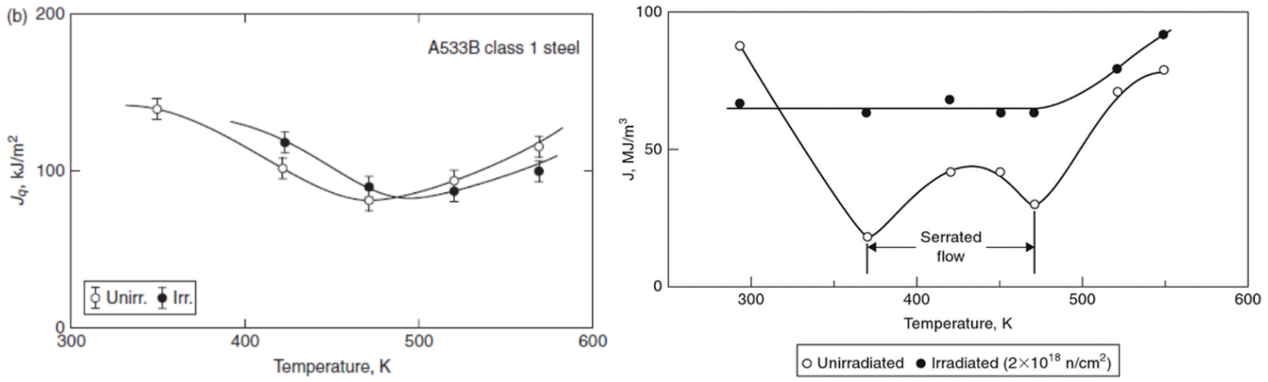

Figure 23: Effect of neutron irradiation on temperature dependence of upper shelf crack initiation fracture toughness [122] and energy to fracture [123].

Synergic effects between DSA and HE were observed in tensile tests in air with hydrogen pre-charged specimens in the DSA temperature-strain rate range (see Section 1.4). In contrast to room temperature, the hydrogen charging resulted in a marginal softening in yield stress, more pronounced softening in ultimate tensile strength (UTS) and a distinct reduction of ductility (reduction of area). Hydrogen seemed to partially compensate the increase in yield stress and UTS by DSA (Figure 24). This softening produced an (apparent) shift of the DSA peak to higher temperatures.

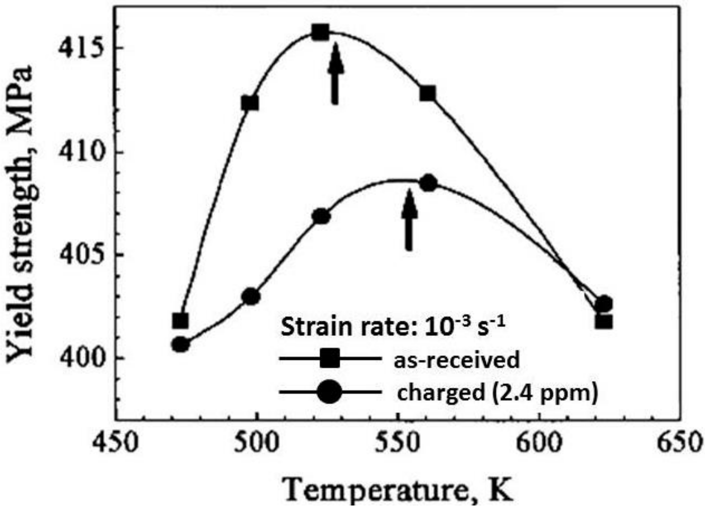

Figure 24: Effect of hydrogen on DSA in SA 508 Cl. 3 pressure vessel steel [88].

The localization of plastic deformation and increase in strength may be reasons for a potential increase in HE by DSA [88], but competitive effects (hardening by DSA and softening by hydrogen) may also be possible. The temperature-strain rate range of DSA and HE may partially overlap, although the peak effects may occur at different temperatures. The binding energy of carbon and nitrogen to dislocations cores of ~ 0.8 eV is higher than that of hydrogen of ~ 0.2 to 0.6 eV. The diffusion rates of hydrogen, in contrast are orders of magnitudes higher [16]. The typical free carbon and nitrogen contents in RPV steels are usually higher than the bulk hydrogen content, but hydrogen can strongly accumulate at traps and in strained/stressed regions. Therefore, the local hydrogen content can be much higher. Hydrogen can reduce the pinning of dislocations by solute atoms and elevate the mobility of dislocations through HELP mechanism [59][126]. The strain localizations by DSA or hydrogen are regions, where hydrogen is further enriched and where the initiation and growth of micro-cracks or micro-voids occur at relatively lower strain, which will further induce plastic instability and a loss in ductility [127].

1.3.4.3 Temper embrittlement

LAS tempered in the range of 350–600 °C or slowly cooled through this temperature range may reveal TE, which is another phenomenon in RPV steels that may affect EAC and HE. TE is related to the impurity atoms phosphorus and metalloid (tin, antimony, arsenic, and tellurium) segregation as well as the precipitation and coarsening of carbides at lath or GBs, which are also affected by phosphorus. Phosphorus segregation to the PAGBs during long-term exposures at increased temperatures lowers the GB cohesion [128][129]. It results in a non-hardening embrittlement by the weakening of the GBs (due to decohesion), reduction of fracture stress and an increase in the DBTT [3][130], accompanied by a change in the low temperature fracture mode from transgranular to intergranular [131][132]. The phosphorus segregation can occur during fabrication (especially during the slow cooling stage of a post-weld heat treatment) or during service over prolonged periods at 300 °C, and can be further enhanced by irradiation [9][133][134]. Due to the low solubility for impurities in the carbide particles, phosphorus is enriched in the direct vicinity of carbide precipitates and may also result in cleavage along the carbide interface or facilitate micro-void formation at such locations. Two kinds of experimental heat treatments are available to enhance TE in materials: isothermal heating [135][136] and step cooling [137][138].

Phosphorus plays the most critical role in TE [10][128][132]. A linear correlation was obtained in various studies between phosphorus concentration and embrittlement effects [132][139] (as shown in Figure 25). In addition to phosphorus, other elements may play a role in enhancing/controlling TE. Molybdenum and carbon usually retard TE [131][140]. Other elements like antimony, tin or tellurium are more effective in GB embrittlement than phosphorus (Figure 9 (c)), but are usually present in much lower concentrations in steels. Alloying elements like manganese, boron, chromium and nickel can intensify TE [128][133]. Since the RPV steels with a high phosphorus concentration often contain a rather high concentration of copper, a synergistic effect of hardening embrittlement (copper) and non-hardening embrittlement (phosphorus) will be a concern of the RPV steels [9]. The transition temperature shifts from non-hardening TE can be additive with the irradiation hardening embrittlement.

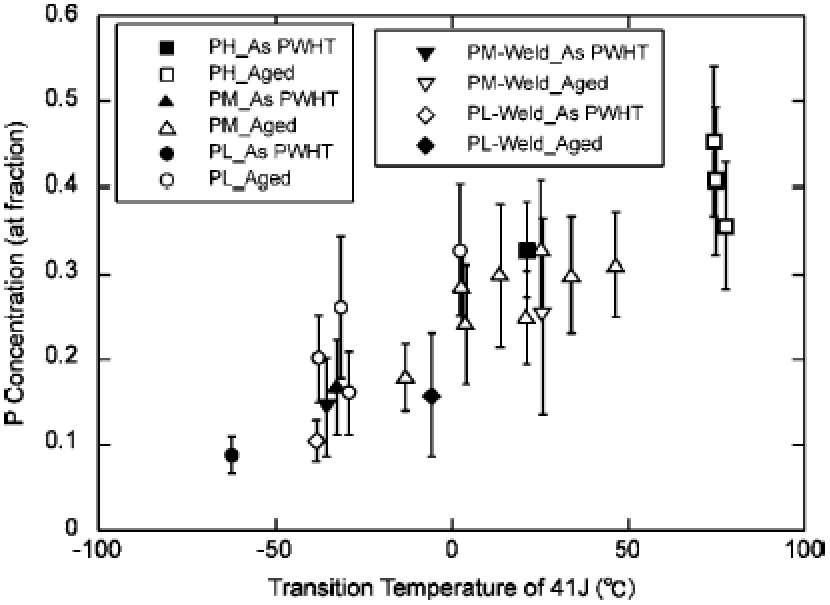

Figure 25: Illustration of the correlation between phosphorus concentration at grain boundaries and Charpy DBTT [132].

TE can be synergistic with EAC and HE resulting in intergranular fracture. The interaction of weakened GBs (by TE and HEDE) with localized deformation (by HELP and DSA) may result in intergranular cracking at lower stresses/strains than without hydrogen. A higher intra-grain strength and coarser grain size favour both TE and HE. A high strength shifts the brittle intergranular (or cleavage) to ductile fracture transition to higher temperatures [10][133]. Phosphorus content (in contrast to sulphur) and phosphorus segregation at GB have little effect on EAC and GB electrochemical activity in HTW. Although it may result in intergranular or mixed intergranular-transgranular EAC in RPV steels, it hardly accelerates the EAC rates in HTW. Interganular EAC in HTW is typically observed in high-strength LAS with Vickers hardness levels > 350 HV5 and sometimes in the coarse-grain heat-affected zone (CGHAZ) of welds [8][100][141]. The acceleration of EAC is mainly due to the effect of yield stress on crack-tip strain rate rather than due to phosphorus segregation at GB or TE. Due to the limited phosphorus content, it has only a minor effect in Western RPV for typical service temperatures and plant lifetimes. Clear synergic effects between TE and HE were observed in higher strength steels (e.g., bainitic turbine disc steels) with higher phosphorus contents (> 0.03 wt.%) [142].

1.3.4.4 Irradiation

The embrittlement and hardening in ferritic steels after exposure to fast neutron ($E > 1$ MeV) radiation is an issue of utmost importance concerning the structural integrity of RPV [143]. The core beltline region directly surrounding the effective height of the fuel element assemblies is of primary concern regarding embrittlement. Macroscopically, prolonged exposure of RPV to neutron flux by RPV during LWR operation results in the formation of large number of defects in the material and in a decrease in toughness and ductility, and an increase in the hardness, yield strength and DBTT [144].

Mechanisms of irradiation embrittlement in LAS

Fast and high-energy neutron irradiation produces displacement damage in RPV steels. During neutron irradiation, collisions between the incident neutron and constituent atoms result in momentum transfer to the lattice atoms [4]. Atoms may be knocked out of their lattice position by elastic collisions with fast high-energy neutrons. The knock-on atoms may produce further displacements and result in displacement cascade until the energy of all displaced atoms is below the threshold energy for displacement [145]. These results in the generation of a large number of interstitials and vacancies. Most of them almost immediately recombine, but some of them survive the cascade phase and result in a supersaturation of interstitials (i) and vacancies (v) with respect to the thermal equilibrium concentration.

The interstitials and vacancies can recombine ($v + i \rightarrow 0$), migrate to and annihilate at specific microstructural sinks ($v + s \rightarrow s$, $i + s \rightarrow s$) or form defect clusters that further grow ($i + i \rightarrow 2i$, $2i + i \rightarrow 3i, \ldots$) with time. This produces fine-dispersed nano-sized defects such as dislocation loops, cavities or solute atom clusters, which impede dislocation motion, increase the yield stress and produce hardening embrittlement [146]. Small features, such as self-interstitial atoms and vacancies, raise the friction stress (Peierls stress) and create a generalised drag. Larger localised features, such as precipitates or point defect clusters, cause pinning [147]. The higher defect density, flux of defects to sinks and coupling of solute atoms to these defect fluxes enhance diffusion and produce radiation-induced segregation (e.g. GB phosphorus segregation) or precipitation (e.g., copper clusters) at shorter times than it would be observed at these temperatures without irradiation. The phosphorus segregation at GB produces non-hardening embrittlement and causes intergranular cracking, but usually plays a minor role in Western RPV steels only. Depending on the defect production rate, neutron flux and temperature, the radiation-enhanced diffusion coefficient can be orders of magnitude higher than the ordinary coefficients. The microstructure and chemical composition have little effect on the primary damage, but strongly affect the further microstructure evolution with time.

The effects of variables on the irradiation embrittlement are briefly explained as follows. Irradiation embrittlement is mainly caused by the displacement damage by fast neutron irradiation (E > 1 MeV) and significant effects are observed at fast neutron fluencies above 10^{18} n/cm^2 and in the core beltline region of the RPV only. It results in an increase in yield stress (< 200 MPa, often < 100 MPa) and DBTT (up to 200 °C at high fluencies in very sensitive steels) as well as a moderate decrease in upper shelf toughness. The irradiation embrittlement is mainly governed by the neutron fluence, irradiation temperature and chemical composition (copper, phosphorus, nickel, manganese). Radiation temperature has been recognized to have an effect on the extent of radiation damage and can influence the diffusion process. Data show that lower embrittlement occurs with increasing radiation temperature. Microstructural characteristics, such as grain size and metallurgical phases (lower or upper bainite and ferrite), can influence the sensitivity of radiation damage [148]. The microstructure mainly affects the initial transition temperature in the un-irradiated conditions, but has little effect on the transition temperature shifts. γ-irradiation and dose rate effects play a little role under plant relevant conditions [8]. The end of life (40 to 60 years) fast neutron fluence (E > 1 MeV) in the beltline region (peak flux) of BWR RPVs (1 to 5×10^{18} n/cm^2) is typically (one order of magnitude) lower than that of PWR PWRs (1 to 5×10^{19} n/cm^2). Therefore, irradiation embrittlement is a smaller concern in BWRs. This is due to larger water gap and different core design in BWRs. Estimated displacement damage is around 0.01 to 0.05 dpa (displacement per atom) at end of life, which means 1 to 5% of atoms displaced over the design lifetime.

Interaction of irradiation embrittlement with other embrittlement mechanisms

Irradiation embrittlement may interact with other degradation and embrittlement mechanisms [149]. Exposure to high-energy neutrons results in increased dislocation density along with other defect complexes. The free interstitial carbon and nitrogen contents that cause DSA may be reduced under irradiation (by trapping at defect clusters). This partially eliminates DSA effects. As shown by Murty [150] in mild steel, the concentration of interstitial impurity atoms in solution decreases with radiation fluence, resulting in essentially non-aging steel by high levels of radiation exposure. On the other hand, interactions of interstitial impurities and radiation-induced defects can shifts the DSA region to higher temperatures (Figure 23). It is important to realize that radiation exposure does not completely eliminate DSA but reduces it, signifying the fact that the concentration of interstitial impurity atoms in solution decreases. This is also clear from the fact that the dip in the fracture energy is shifted to higher temperature following radiation exposure. TE may be accelerated and enhanced under irradiation and transition temperature shifts of irradiation embrittlement and TE may be additive.

HE susceptibility may be aggravated after irradiation (Figure 19). The higher strength due to irradiation embrittlement facilitates the enrichment of hydrogen in the high hydrostatic stress region at crack tip [90]. However, it was reported that hydrogen pick-up in irradiated material does not cause any additional significant reduction in ductility or toughness, which was attributed to the large number of fine-dispersed defects (homogeneously distributed) in the irradiated material (10^{17}–10^{18} /cm^3) which act as strong trap sites for hydrogen. Radiation-enhanced diffusion is of little importance for hydrogen, since its mobility is very high in bcc steels. The radiation hardening in combination with TE can increase HE in combination with HEDE and HELP, but hydrogen availability is probably too low under LWR conditions. The contribution of transmutation (n, p) reactions or proton recoil injection is neglectable with respect to the hydrogen content from HTW and corrosion reactions.

Irradiation can affect the EAC behaviour of RPV steels in two major ways, by an increase of the oxidizing capacity of the environment (due to radiolysis of the reactor coolant by n- and γ-irradiation), and by the change of the microstructure and mechanical properties by n-irradiation (n-embrittlement). Under plant relevant water chemistry conditions, only small positive ECP shifts of 50 to 100 mV occur under irradiation [100]. The small ECP-shift due to irradiation is unlikely to have an accelerating effect on crack propagation rates. In SCC, a higher yield stress due to irradiation hardening results in a steeper strain gradient at crack tip and a higher crack-tip strain rate for a growing crack under otherwise identical conditions. Under cyclic loading, apart from the threshold regions, yield stress has little effect on CF or SICC crack growth. In fact, fatigue and CF tests with irradiated RPV steels in HTW showed no accelerating effect of irradiation [100]. For HAEAC and HE, the higher yield stress results in a higher peak and hydrostatic stress ahead of crack tip and this favours the hydrogen enrichment in this region. However, the high radiation defect density can act as strong hydrogen traps. Irradiation embrittlement is more relevant for PWR, but for EAC this aspect is compensated by the very low ECPs, which are significantly below the critical cracking potentials for SICC. The biggest concern is that the transition of slow to fast SCC in BWR/NWC environment is shifted to lower K_I values by the irradiation hardening [100]. However, this aspect has not been investigated so far.

1.4 High-temperature water and hydrogen effect on fracture behaviour of RPV steels under LWR conditions

The following section is focused on potential hydrogen and HTW effects on the fracture and mechanical behaviour of RPV steels in the LWR operating temperature range (274 to 320 °C for stationary power operation and 100 to 320 °C for LOCA transients).

A large amount of literature on hydrogen effects (often controversial and contradictory, even for the same alloy) on the mechanical properties and fracture behaviour of LAS exists, in particular at temperatures below 100 °C [144] and for higher strength LAS [88][127]. There are few investigations on hydrogen effects [151] on fracture toughness above 100 °C and only a couple of references on potential HTW effects [13][15], since hydrogen effects usually are claimed to be negligible under such conditions. However, it was reported that a few wppm of hydrogen (2 to 5 wppm) from hydrogen pre-charging may be sufficient to reduce upper shelf toughness of RPV steels and increase the DBTT of unirradiated RPV steels [62][88][127][152]. The few investigations with irradiated RPV steels are summarized in [62][70] and Section 1.3.4, which indicate a slightly lower threshold of 1 to 2 ppm of hydrogen in highly irradiated steels. Some of these investigations indicate a synergy between HE and irradiation embrittlement, whereas others suggest that hydrogen pre-charging does not further amplify the irradiation embrittlement (no additional shift in DBTT by hydrogen pre-charging). These investigations clearly reveal that there can be hydrogen effects in the whole LWR operating temperature range, provided that there is sufficient hydrogen in the material [89].

As discussed in Section 1.3.2.4, in case of an intact cladding and under typical steady-state LWR power operation conditions, hydrogen concentration in the RPV from corrosion and DH in the coolant is usually low. The free and diffusible hydrogen concentration close to the surface is < 0.1 wppm and is usually controlled by the Sievert's law and DH content in the coolant [63]. The resulting total free and trapped hydrogen content are dependent on the hydrogen availability, the type and concentration of traps as well as the local stresses/strains. The total hydrogen content only can reach a few wppm in case of extreme conditions, e.g., with accelerated corrosion or under irradiation. A bulk embrittlement seems to be rather unlikely due to the limited hydrogen availability, as shown by the absence of environmental reduction in constant extension rate tests (CERT) with smooth tensile specimens in hydrogenated HTW [5] (Figure 26).

However, increased hydrogen levels higher than the critical concentration may be reached in the plastically deformed fracture process zone. Enhanced hydrogen uptake can occur with cracks with stressed and plastically strained bare crack tips, an aggressive occluded crack crevice chemistry (lower pH, hydrolysis of metal cations, etc.), and a high hydrostatic triaxial stress state, e.g., in fracture mechanics tests in HTW or in a LOCA. Since the hydrogen diffusion rate in RPV steel is much faster than the ductile crack growth rates and sufficiently fast for intermittent brittle crack extension, e.g., in a LOCA situation, crack-tip HE cannot be completely excluded. Ductile crack advance rate is about 10 µm/s under standard loading conditions in an EPFM test at 300 °C, which is more than one order of magnitude lower than the hydrogen diffusion rate of about 300 µm/s. In contrast to the test in Figure 26, CERT experiments with notched tensile specimens with triaxial stress state at the notch root, revealed clear evidence for HTW effects (Figure 27), although the effects were smaller than in smooth specimens with hydrogen pre-charging in air.

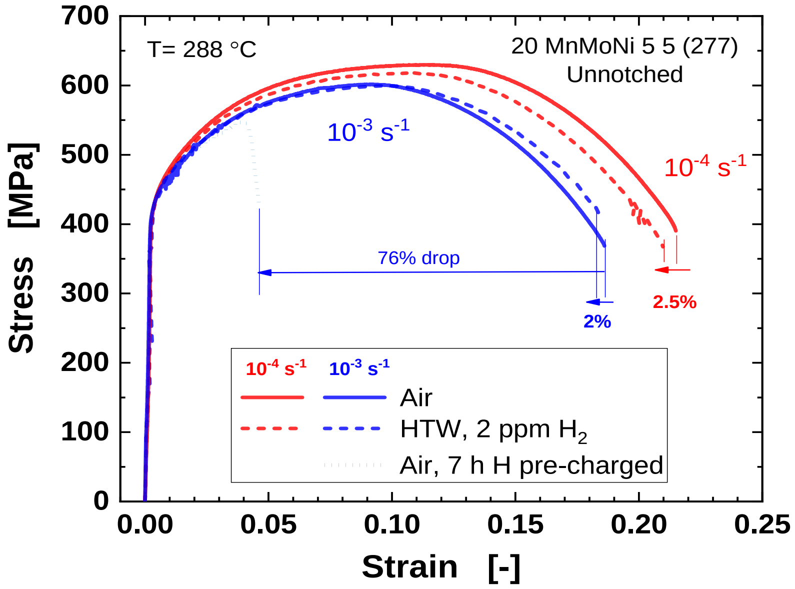

Figure 26: Tensile stress-strain curves of a high DSA steel in air (with and without hydrogen pre-charging) and in hydrogenated water at 288 °C.

Similarly, CERT tests in hydrogen gas in autoclaves with notched tensile RPV steel specimens, revealed fast sub-critical HAC under continuous plastic straining up to temperatures of about 160 °C [153], as shown in Figure 28. At 190 °C or under pure constant load, no HAC was observed. For a nominal strain rate of 10^{-3} s^{-1}, the HAC crack growth rates were in the range of 2 to 5×10^{-6} m/s and increased with hydrogen content in the RPV steel (as estimated by Sievert's law and consideration of hydrostatic stress at the notch root). These rates were a factor of 10 to 100 higher than the maximum SICC rates in HTW at 200 to 300 °C at the same strain rates. Below a temperature dependent threshold concentration, no HAC was observed, and this threshold increased with temperature. At 150 °C, it was in the range of 0.5 ppm. An extrapolation to 300 °C indicated a critical hydrogen content for HAC in the range of 10 ppm. These tests clearly confirmed the possibility of HAC and HE at temperatures well above 100 °C.

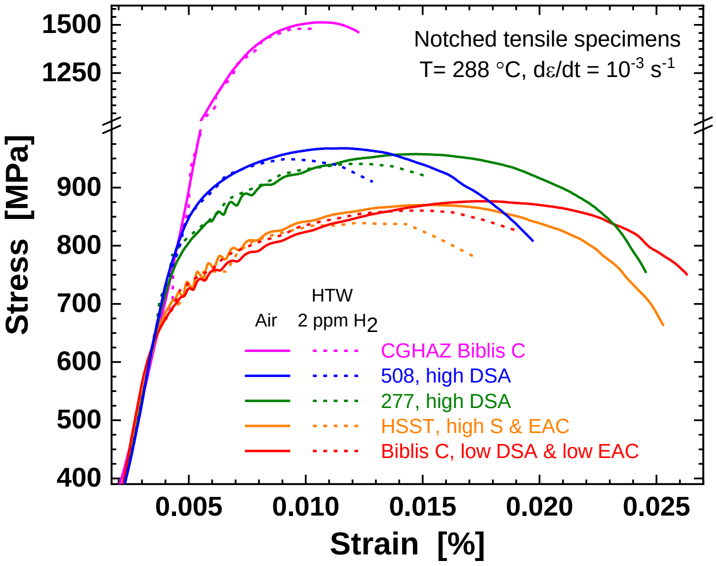

Figure 27: Nominal notched tensile stress-strain curves for different RPV steels in air and hydrogenated water at 288 °C.

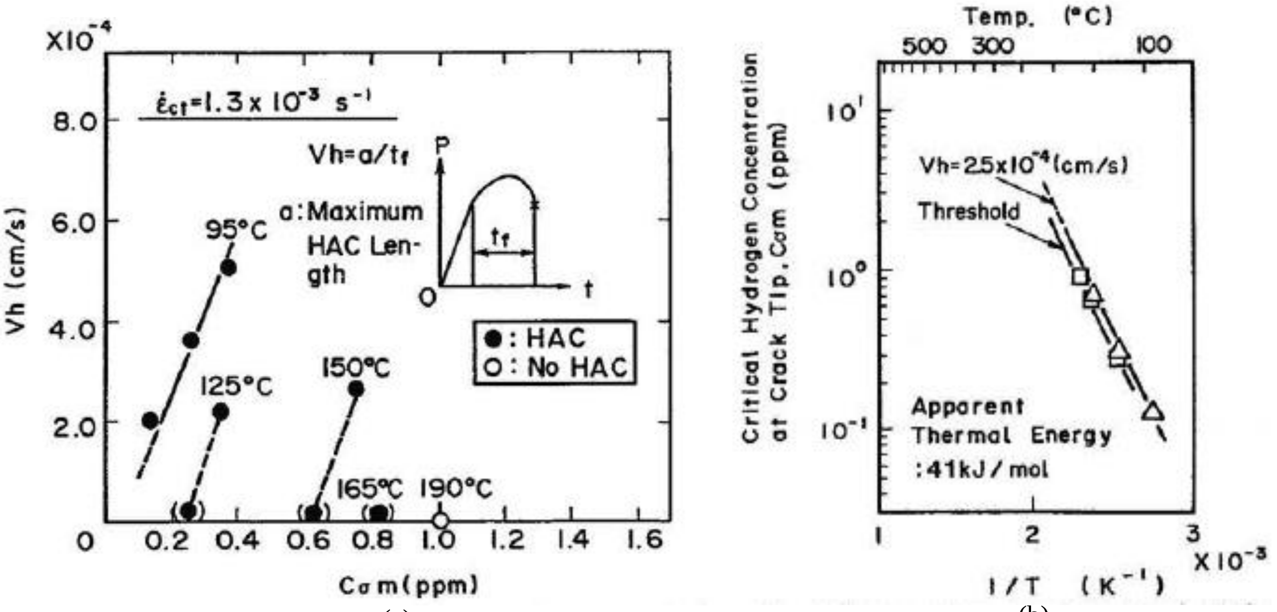

(a) (b)

Figure 28: (a) Effect of hydrogen concentration at crack tip on HAC growth at different temperatures; (b) temperature dependence of critical hydrogen concentration at crack tip [153].

A very limited number of EPFM tests (normalization method with multiple specimen technology without on-line crack growth monitoring) in air and hydrogenated HTW (2.5 to 3.5 ppm H_2) at 243 °C with a SA 508 Cl.2 RPV steel at a loading rate of 25 µm/min, were performed by James et al. [13]. The fracture initiation and tearing resistance were similar in air and HTW, but scatter was significant and used technique not appropriate for solid conclusions. Pop-ins (load drops) were observed in some specimens in air and HTW, usually after reaching the peak load, which were probably caused due to DSA that typically occurs in this temperature-strain rate range.

Schellenberger [15] observed by EPFM tests (ULC method) with 2T-C(T) specimens that the *J-R* curves of RPV steels were significantly lower in oxygenated HTW (8 ppm O_2) at 240 °C than in air. The environmental reduction increased with decreasing strain rate and increasing steel sulphur content, as shown in Figure 29. A stretch zone was only observed for the highest loading rate of 6 µm/min. The initiation toughness J_i (from stretch zone) for the low- and high-sulphur steel was about 39 and 7% of the corresponding values in air, respectively. Due to the slow strain rate in this study, the significant toughness reduction was primarily caused by sub-critical SICC that typically occurs under these conditions. Furthermore, the partial un-/reloading may affect the test results in HTW.

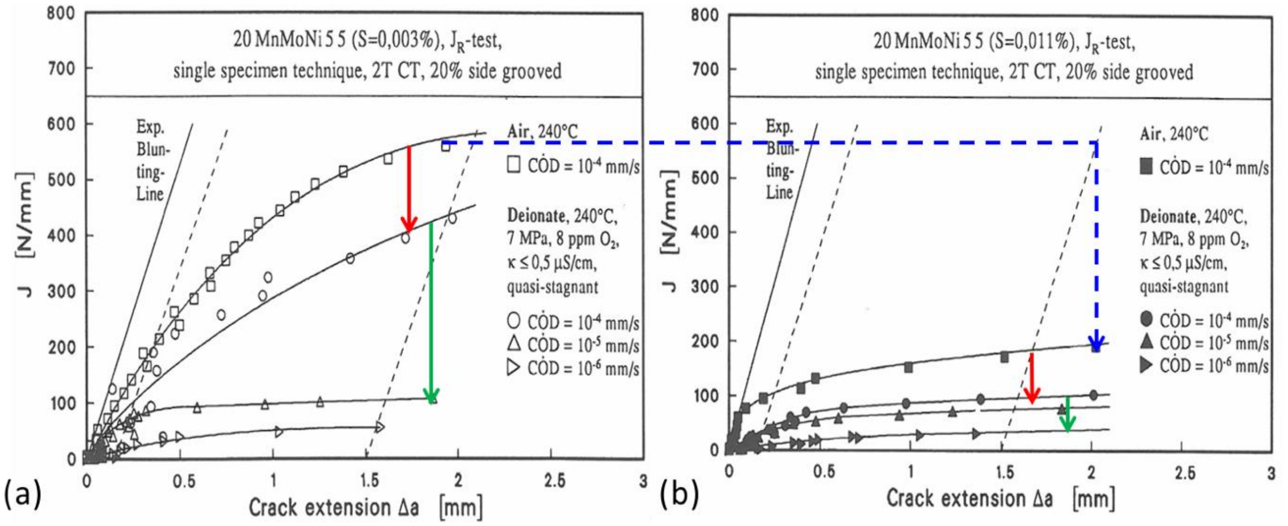

Figure 29: *J-R* curves for the material 20MnMoNi 5 5 with 0.003 wt.% sulphur (a) and 0.011wt.% sulphur (b) in HTW and in air, respectively [15].

Similarly, multiple specimen EPFM tests (without on-line crack growth monitoring) with pre-cracked fracture mechanics specimen in oxygenated HTW and air at 288 °C at a slow crack opening displacement rate of 2 µm/min by Shoji et al. [154][155] with a RPV steel SA 533 B Cl. 1 and high-strength LAS 4340, revealed a reduction of fracture initiation and tearing resistance in HTW (Figure 30 (a)). Stable ductile tearing was observed in the RPV steels with dimple fracture, whereas unstable cracking in the high-strength steel with dimple fracture in air and intergranular cracking in HTW for yield stress levels above 1000 MPa (Figure 30 (b)). Due to the very slow loading rate, these results may have been affected by sub-critical SICC also and, unfortunately, detailed fractography was not reported. Nevertheless, these tests clearly indicate potential moderate reduction effects of HTW on fracture resistance in LAS that can increase with yield stress. The transition from ductile to intergranular fracture in the high-strength steel, clearly demonstrates the possibility of HE at 288 °C. This is also in line with the observation of fast trans- or intergranular SCC of LAS in HTW under constant load at hardness and yield stress levels above 350 HV5 and 1000 MPa [8][100][141], whereas no SCC is observed in RPV steels with moderate strength levels (400 to 500 MPa) up to high K_I values of 60 MPa·m$^{1/2}$.

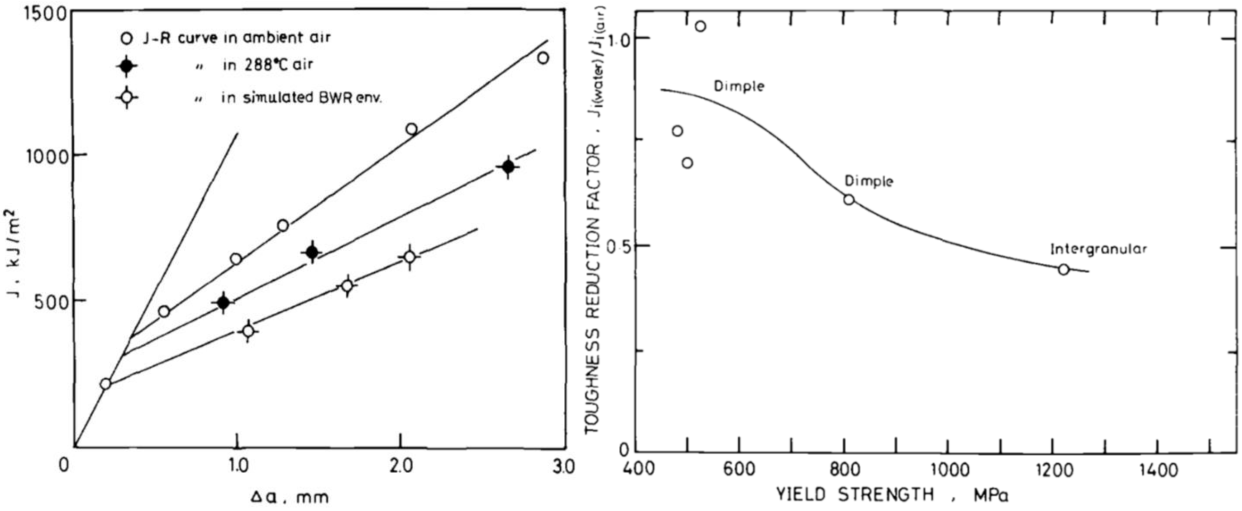

(a) (b)

Figure 30: (a) *J-R* curve for SA533B Cl. 1 steel in BWR environment and air; (b) dependence of toughness reduction factor in HTW on yield strength with different fracture modes [154].

The few EPFM tests in HTW indicated some environmental effects on fracture resistance, but were finally not conclusive due to absence of on-line crack growth monitoring, lack of detailed fractography, insufficient testing quality or inadequate test techniques (from a current perspective). Very probably, most test results were affected by sub-critical SICC. Slow raising load tests with pre-cracked fracture mechanics specimens in HTW under highly oxidizing conditions (8 ppm O_2) at slow loading rates at Paul Scherrer Institut (PSI) [28] revealed the initiation of sub-critical SICC at stress intensity factors K_I as low as 30 MPa·m$^{1/2}$, which is about 8 times smaller than the corresponding fracture toughness in air. This is a kind of $K_{I,SICC}$ threshold for sub-critical SICC from incipient cracks under slow rising load and should not be mixed up with an environmental reduction of fracture resistance. After initiation, these SICC cracks were growing with a constant rate that increased with loading rate (but was independent on K_I) until the stop of the test at K_I values of 60 to 80 MPa·m$^{1/2}$.

In a recent PSI test programme [64][82] that was linked to this PhD project, the effects of hydrogen on the mechanical and fracture behaviour of some of the RPV material of this PhD project, were evaluated by tensile tests in air with electrochemical pre-charging. The used materials cover the steel grades and chemical composition range of the RPVs in the Swiss LWRs. These materials include five different RPV steels (forgings and hot-rolled plates, 0.004 to 0.018% sulphur, $YS_{288\,°C}$ of 400 to 460 MPa, low and high DSA susceptibility) and a simulated CGHAZ material ($YS_{288\,°C}$ of 750 MPa). The effect of hydrogen on the mechanical tensile properties was studied with the RPV steels Biblis C (low DSA susceptibility), HSST (moderate DSA susceptibility), 277 and 508 (high DSA susceptibility) as well as a simulated CGHAZ at 250 and 288 °C in the strain rate range from 10^{-4} to 10^{-1} s^{-1} (Figure 31 to Figure 37) [5][16]. Figure 31 to Figure 37 are by courtesy of G.S. Rao.

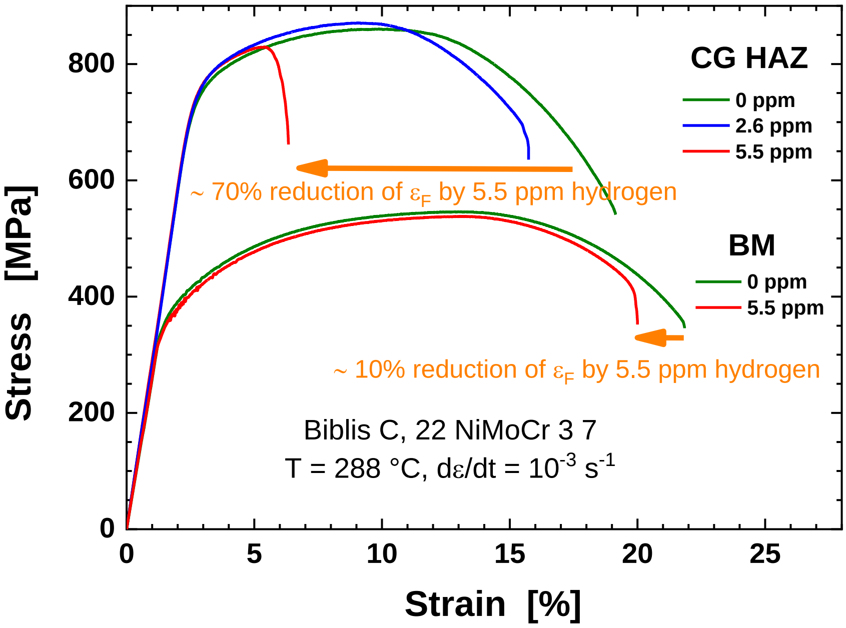

Figure 31: Effect of hydrogen content on stress-strain curves in tensile tests in Biblis C base metal (BM) and simulated CGHAZ at 288 °C.

2 to 5 ppm of hydrogen in the RPV steels caused a moderate softening in UTS (Figure 34 and Figure 35) and a more pronounced reduction in ductility (Figure 31 to Figure 33 and Figure 36 to Figure 37) at both temperatures, in combination with a clear change in fracture morphology and failure mode. The hydrogen effects increased with plastic strain and became particularly strong in the post-necking region (with local damage evolution). The effects hereby increased with increasing DSA susceptibility (Figure 35 to Figure 37) and yield stress (Figure 31, Figure 33 and Figure 34) and were slightly higher at 288 than at 250 °C. Apart from the 508 steel (with an atypical mixed bainitic/ferritic microstructure) that showed some moderate hardening, the effects on the yield stress were absent or marginal at both temperatures and at all strain rates. The yield stress of these tests was in the typical specimen-to-specimen scatter range (-1 to 2%).

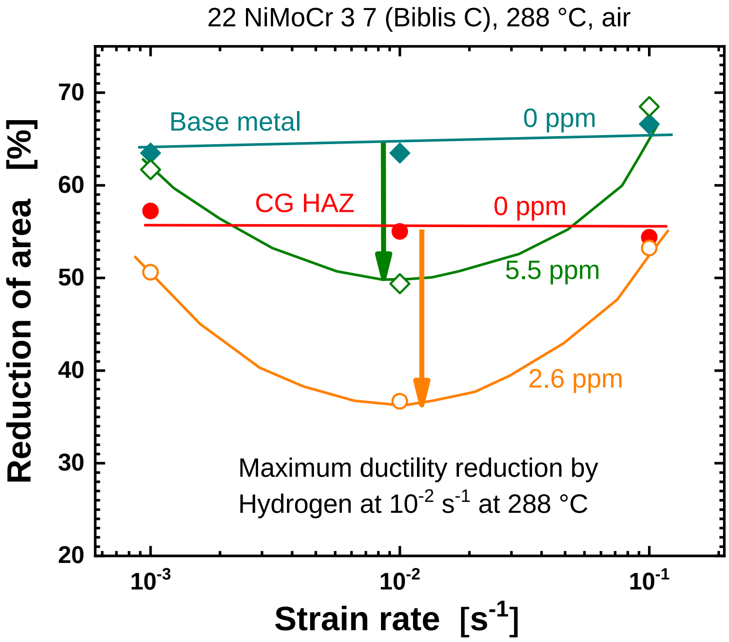

Figure 32: Maximum in hydrogen embrittlement (loss of ductility as the reduction of area) at a strain rate of 10^{-2} s^{-1} in Biblis C base metal and simulated coarse-grain heat-affected zone (CGHAZ) at 288 °C.

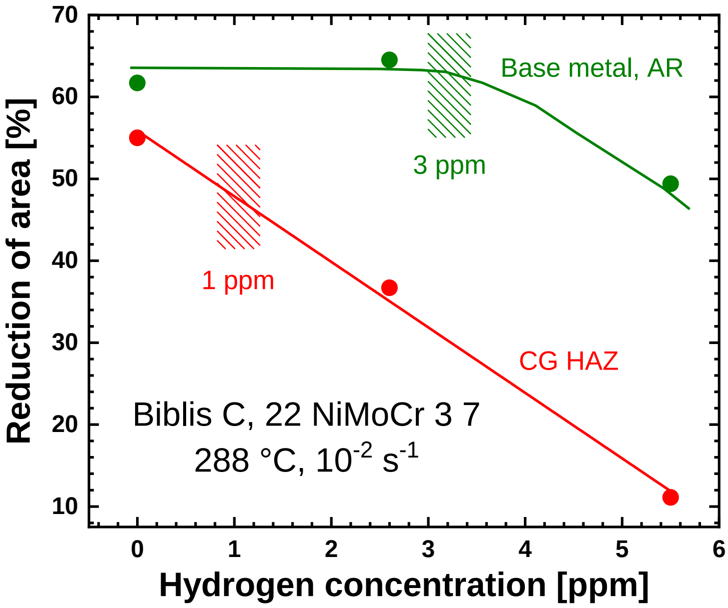

Figure 33: Effect of hydrogen content on ductility and hydrogen embrittlement in Biblis C base metal and simulated coarse-grain heat-affected zone (CGHAZ) at 288 °C with 10^{-2} s^{-1}.

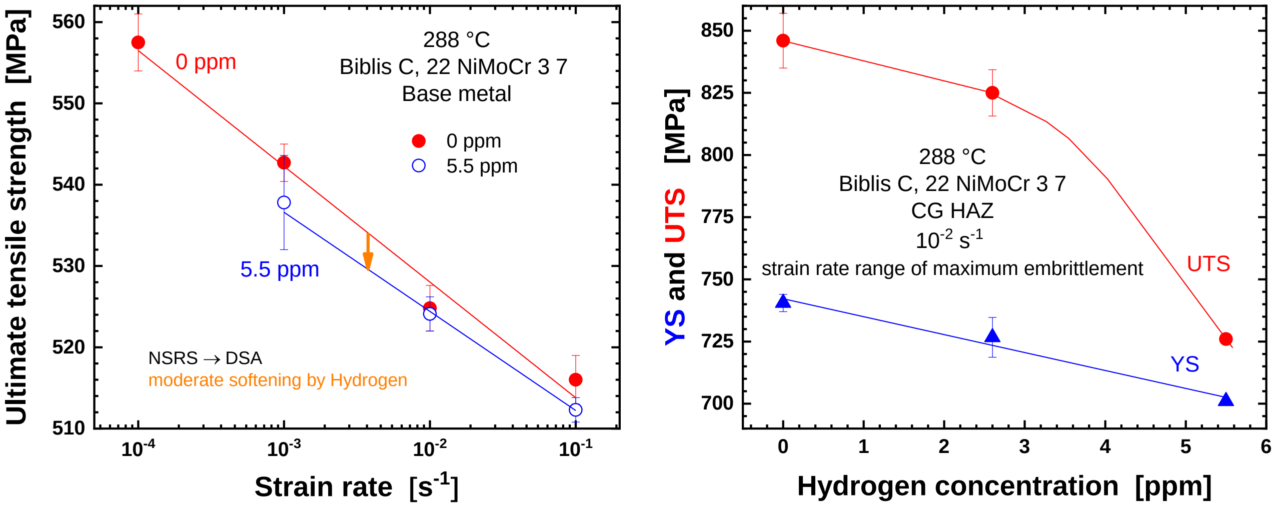

(a)

(b)

Figure 34: Hydrogen-induced softening in ultimate tensile strength (UTS) and yield stress (YS) in Biblis C base metal (BM) (a) and coarse-grain heat-affected zone (CGHAZ) (b).

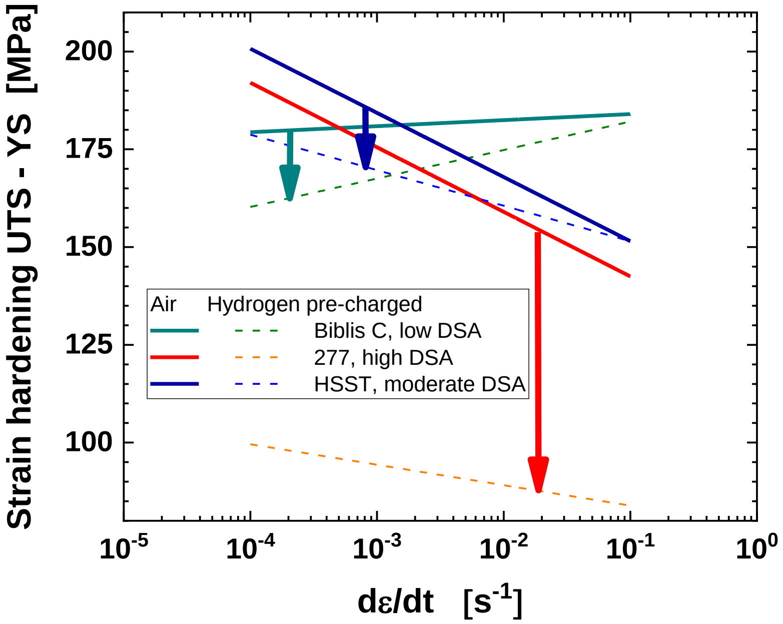

Figure 35: Hydrogen-induced reduction of strain hardening capacity in UTS (ultimate tensile strength) and YS (yield stress) for steels with different DSA susceptibilities.

HE (loss of ductility) increased with increasing hydrogen concentration (Figure 33), yield stress (Figure 33) and DSA susceptibility (Figure 36 and Figure 37) [5]. The critical hydrogen concentration for the onset of hydrogen effects seemed to decrease with increasing yield stress (Figure 33) and DSA susceptibility. For the steels (Biblis C, HSST) with low and medium DSA susceptibility, the HE was moderate with a peak at a strain rate of 10^{-3} to 10^{-2} s^{-1} (Figure 32, Figure 36 and Figure 37). The strain rate range and amplitude of HE effects were significantly amplified by a high DSA susceptibility in the DSA temperature-strain rate range (Figure 36 and Figure 37). It suggests synergic effects between DSA and hydrogen, resulting from the localization of plastic deformation due to DSA and the shielding effect of hydrogen. No effect of steel sulphur content (MnS inclusions as potential hydrogen traps) was observed in these tests. The HSST steel with high sulphur content of 0.018 wt.% and moderate DSA susceptibility only showed moderate HE, whereas two RPV steels 277 and 508 with low sulphur content of 0.004 wt.%, but high DSA susceptibility, revealed significant HE.

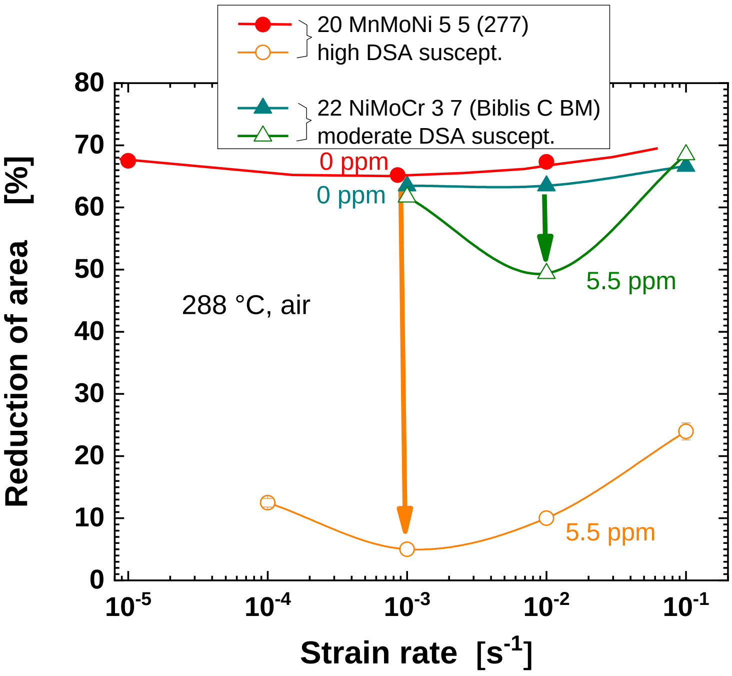

Figure 36: Amplification of magnitude and extension of strain rate range of hydrogen embrittlement in case of a high DSA susceptibility.

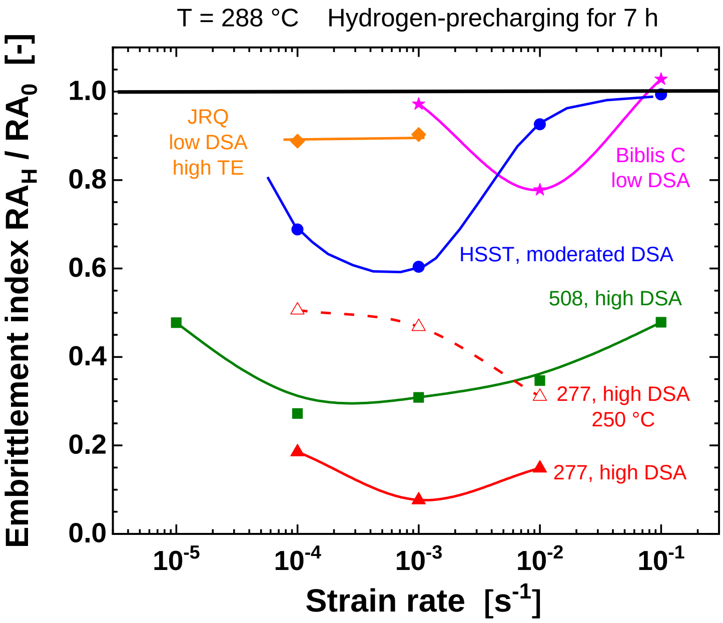

Figure 37: Comparison of hydrogen embrittlement susceptibility of different RPV steels by hydrogen embrittlement index (ratio of reduction of area under hydrogen pre-charged and uncharged conditions).

In presence of hydrogen, shear-dominated mixed-mode fracture (Figure 38) with varying amounts of ductile MVC, QC regions and secondary cracking at inclusions and along the PAGBs were observed (Figure 39). Ductile MVC was always the dominant failure mode, but the area of brittle crack extension clearly increased with HE in the tests. Interestingly, the RPV steels with high-sulphur content did not reveal QC features at MnS inclusions, as they were observed in EAC tests in HTW [28][92][94]. The observed behaviour suggests that HE is due to a combination of the HELP and HESIV mechanisms, with additional minor contributions by HEDE in some materials.

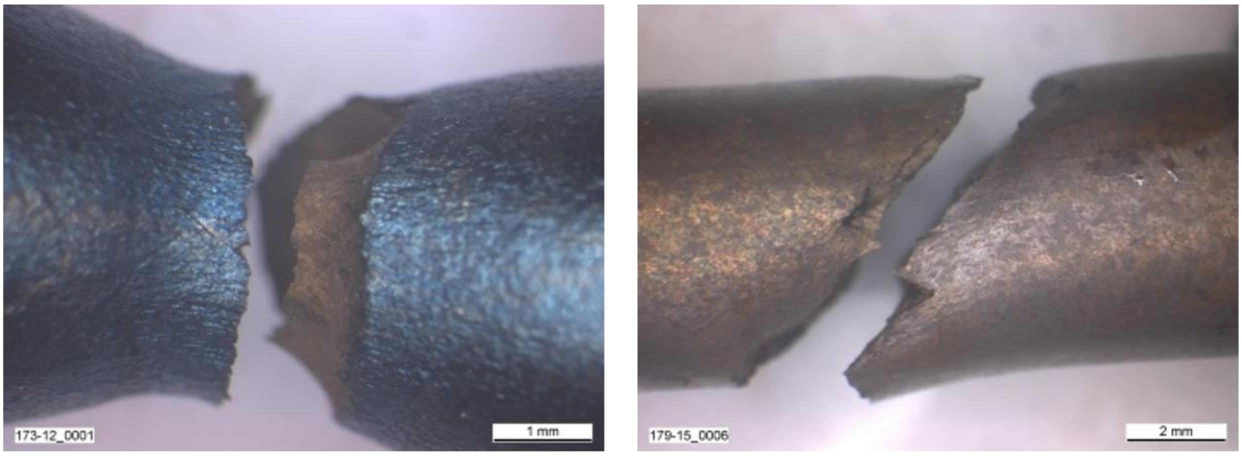

Without hydrogen:
Cup and cone fracture by pure MVC

With hydrogen
Shear dominated fracture by MVC and
various amounts of QC and IG facets

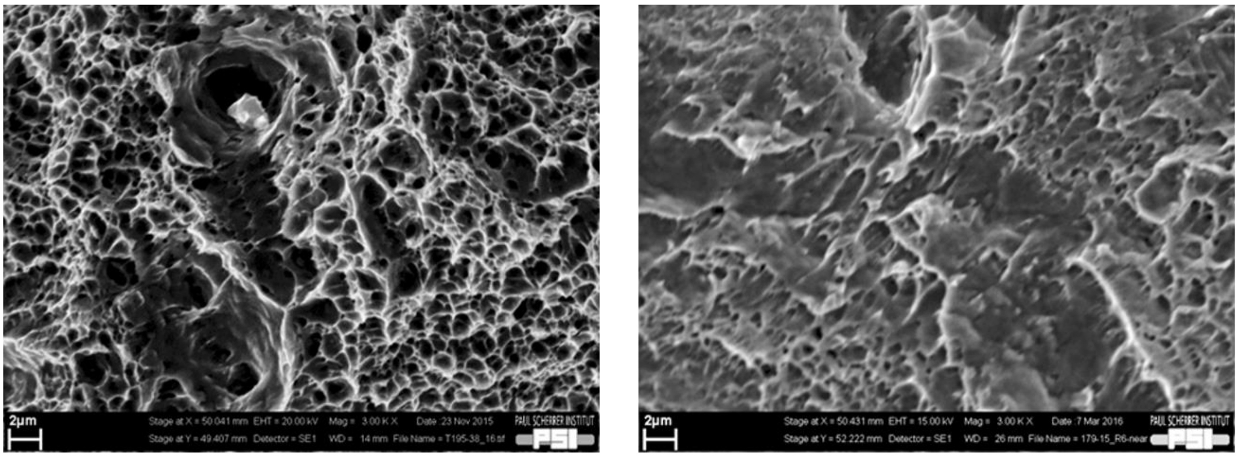

Figure 38: Fractography of 20 MnMoNi 5 5 steel in air at 288 °C and strain rate 10^{-2} s^{-1} without hydrogen and after hydrogen pre-charging.

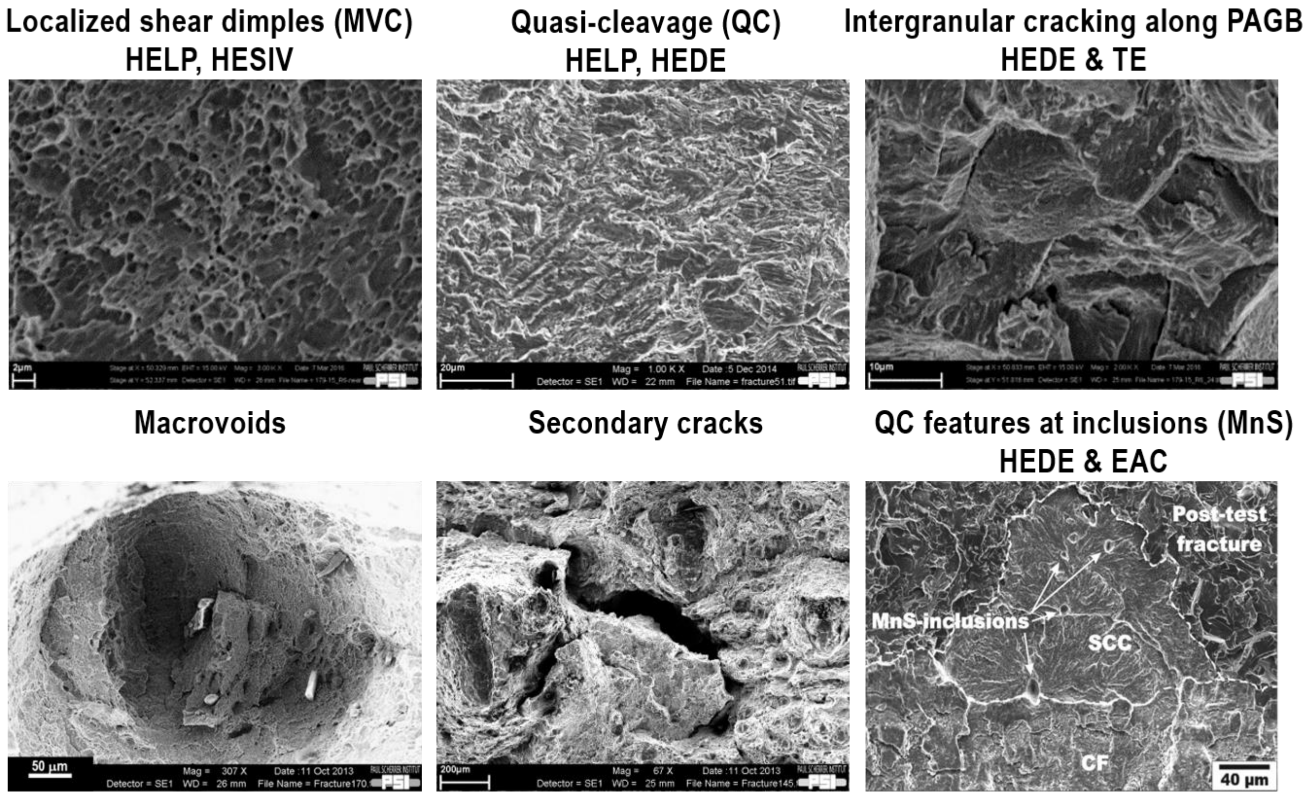
Localized shear dimples (MVC)
HELP, HESIV
Quasi-cleavage (QC)
HELP, HEDE
Intergranular cracking along PAGB
HEDE & TE
2µm
20µm
10µm
Macrovoids
Secondary cracks
QC features at inclusions (MnS)
HEDE & EAC
50 µm
200µm
Post-test fracture
MnS-inclusions
SCC
CF
40 µm

Figure 39: Overview on typical fracture features in tensile tests after hydrogen pre-charging or in tests in hydrogenated HTW (predominantly MVC with various amounts of QC, macro-void, secondary and intergranular cracks).

The PSI work clearly shows that hydrogen effects and HE may occur at temperatures of 288 °C and can be summarized as follows [16]. 2 to 5 ppm of hydrogen in the RPV steel by electrochemical hydrogen pre-charging caused a marginal and moderate softening in yield stress and UTS in tensile tests at 250 and 288 °C, respectively. A significantly more pronounced reduction in ductility (reduction of area and strain at failure) in combination with a clear change in fracture morphology and failure mode were observed. The effects increased with plastic strain and became particularly strong in the post-necking region (with local damage evolution). The resulting embrittlement increased with hydrogen concentration, yield stress and DSA susceptibility. The critical hydrogen concentration for the onset of hydrogen effects decreased with increasing yield stress and DSA susceptibility. The strain rate range and amplitude of HE was significantly amplified by a high DSA susceptibility in the DSA temperature-strain rate range. This suggests some synergies between DSA and hydrogen effects, which results from the localization of plastic deformation due to DSA and the shielding effect of hydrogen. In the presence of hydrogen, shear-dominated fracture mode with varying amounts of QC regions, macro-void and secondary cracking at inclusions and along the PAGB, were observed.

1.5 Conclusions, statement of the problem and goals for the PhD project

The literature survey clearly shows that HE can occur in RPV steels at LWR operating temperatures, if sufficient hydrogen is present in the steel. It is currently unclear, if the necessary critical hydrogen concentrations of a few wppm can be achieved in HTW or not. The corresponding conclusive fracture tests in HTW are missing as well. Bulk HE seems to be unlikely, but crack-tip HE appears possible. The HE of RPV steels in HTW can be in synergy (or competition) with other embrittlement and degradation mechanisms in RPV steels like irradiation embrittlement, TE, DSA or EAC.

Due to very complex hydrogen uptake, hydrogen transport and hydrogen-deformation/fracture interactions and their highly localized nature, it is almost impossible to estimate or measure the local hydrogen concentration in the process zone under dynamic crack-tip plasticity conditions in an occluded crevice environment. Definite evidence for (or against) the environmental reduction effects on the fracture resistance of RPV in HTW, can only be derived by corresponding fracture mechanics tests in HTW. Even small environmental reduction effects may be practically significant in this context for plants that are approaching life-limiting situations and with small margins with regard to irradiation embrittlement.

The goal of this PhD project is to evaluate the unexplored effect of HTW on the fracture initiation and tearing resistance of various RPV steels in the upper shelf region under different water chemistry conditions. Critical combinations of material (strength, chemical composition, EAC, TE and DSA susceptibilities, etc.), environmental (temperature, water chemistry, etc.) and loading conditions (strain rate, constraints, etc.) that may result in a fracture resistance reduction should be identified. The synergies with other embrittlement and degradation mechanisms like TE, DSA and EAC need to be evaluated. Correspondingly, challenging and expensive investigation with irradiated RPV steels will be covered in a follow-up project depending on the outcome of this project. The underlying mechanisms should be evaluated by various post-test characterization methods on the fracture and deformation modes and a tentative mechanistic explanation should be worked out as far as possible.

Chapter 2 Materials and experiments

2.1 Materials

2.1.1 Chemical composition and mechanical properties

EPFM tests on base metal and simulated weld CGHAZ specimens of RPV steels were conducted between 25 and 320 °C with various loading rates in air and different simulated LWR environments. EPFM tests were performed according to ASTM E1820 [50] with air fatigue pre-cracked and side-grooved C(T) specimens. The chemical composition, microstructure, mechanical tensile properties, heat treatments and non-metallic inclusions as well as DSA, EAC and TE susceptibilities of these materials have been characterized in this work and previous investigations by PSI [63][64][92], which are summarized in Table 6 to Table 11.

Table 6: Overview on investigated RPV steels.

Material		**Product form**	**Micro-structure**	**S [wt.%]**	**P [wt.%]**	**$YS_{288°C}$ [MPa]**	**Remarks**
Biblis C	22 NiMoCr 3 7	Forging	BM	0.007	0.008	400	Low DSA & low EAC susceptibility
HT 1	22 NiMoCr 3 7	Forging	CGHAZ	0.007	0.008	740	High strength
277	20 MnMoNi 5 5	Forging	BM	0.004	0.004	418	High DSA susceptibility
508	SA 508 Cl. 2	Forging	BM	0.004	0.005	396	High DSA susceptibility
HSST	SA 533 B Cl. 1	Hot-rolled plate	BM	0.018	0.006	412	High sulphur & high EAC & moderate DSA susceptibility
KS12	20 MnMoNi 5 5	Forging	BM	0.015	0.014	462	High sulphur & high EAC & moderate DSA susceptibility, low upper shelf toughness
JRQ	SA 533 B Cl. 1	Hot-rolled plate	BM	0.004	0.02	445 (AR) 415 (SC)	High phosphorus & high TE susceptibility

BM: base metal; CGHAZ: coarse-grain heat-affected zone; AR: as-received; SC: step-cooled.

During this work, seven types of low-alloy RPVs were investigated: Biblis C BM, HT1, 277, 508, HSST, KS12 and JRQ. The Biblis C base metal with low sulphur and phosphorus contents and with low DSA, TE and EAC susceptibilities is from the lower cylindrical shell of a PWR RPV, which was not commissioned. The fracture behaviour of this material in HTW was systematically characterized in [63]. Therefore, this material is the reference material for this study. With this material, a simulated CGHAZ material (HT1) was fabricated through a specific two-step heat treatment (Chapter 2.1.2). The prior-austenite grain size, micro-hardness, yield stress and annealed martensite microstructure are very similar to that of the CGHAZ of the actual circumferential core girth weld of the corresponding PWR RPV.

Table 7: Chemical compositions of investigated RPV steels *(*in *wt.%* and wppm for N_{tot}, N_{free} and O_{tot}*)*.

Materials	**C**	**Si**	**Mn**	**P**	**S**	**Ni**	**Cr**	**Mo**	**V**	**Cu**	**Al**	$\mathbf{N_{total}}$	$\mathbf{N_{free}}$	$\mathbf{O_{total}}$
	[wt.%]											[ppm]		
Biblis C & HT 1	0.22	0.20	0.91	0.008	0.007	0.88	0.42	0.53	0.007	0.04	0.018	80	3	-
277	0.21	0.25	1.26	0.004	0.004	0.77	0.15	0.50	0.008	0.06	0.013	70	30	140
508	0.21	0.27	0.69	0.005	0.004	0.78	0.38	0.63	0.006	0.16	0.015	110	2	-
HSST	0.25	0.24	1.42	0.006	0.018	0.62	0.12	0.54	0.007	0.15	0.03	60	<1	20
KS12	0.25	0.33	1.54	0.014	0.015	0.62	0.18	0.68	0.024	0.15	0.021	-	-	-
JRQ	0.07	0.21	1.34	0.020	0.004	0.70	0.11	0.49	0.002	0.15	0.012	-	-	-

The KS12 and HSST materials have a higher steel sulphur content and EAC susceptibility. The HSST material is from the US Heavy-Section Steel Technology (HSST) project [156]. It has high sulphur and low phosphorus content with a high EAC and low TE susceptibility. The inhomogeneous KS12 material is a lower bound RPV material from the German Component Safety programme [157]. It has high sulphur and phosphorus contents with high EAC and TE susceptibilities.

JRQ is used as a monitor material for irradiation embrittlement studies in several International Atomic Energy Agency coordinated research projects [158]. It has high phosphorus, but low sulphur content and is susceptible to GB segregation and TE (as well as to irradiation embrittlement). It was used for TE investigations due to its intrinsic high phosphorus content [128].

Apart from KS12 and HT1, all RPV steels had a similar yield stress and upper shelf toughness at 288 °C with standard loading rates (Table 8). KS12 has a lower upper shelf toughness K_{JC} (~ 150 vs. 250 ± 20 MPa·m$^{1/2}$) with a standard loading rate of 0.25 to 0.35 mm/min and slightly higher yield stress (460 vs. 415 ± 15 MPa) at 288 °C. KS12 is rather inhomogeneous with significantly stronger specimen-to-specimen scatter in fracture resistance (30 vs. 10%) compared to the other materials. The CGHAZ material HT1 had a slightly lower toughness K_{JC} of ~ 220 MPa·m$^{1/2}$, but significantly higher yield stress of 750 MPa.

All the investigated RPV steels revealed clear indications of DSA in tensile and fracture tests (e.g., an increase of the fracture initiation resistance with decreasing loading rate at 288 and 250 °C in air) [5]. Manifestations of DSA were serrations in the stress-strain curves, negative strain rate sensitivity of strength properties or maximum in UTS (Figure 40) and strain hardening rate as well as minimum in ductility (elongation at fracture and reduction of area) (Figure 41) at intermediate temperatures between 250 and 350 °C at a strain rate of 10^{-5} to 10^{-4} s^{-1}. This DSA peak was shifted to higher temperatures with increasing strain rate (Figure 42). The magnitude of the effects and temperature-strain rate range with DSA and negative strain rate sensitivity slightly varied from steel to steel. The peak temperature, e.g., seemed to be slightly higher for the NiMoCr steels compared to the MnMoNi grades. The DSA effects on yield stress were similar as, but smaller than for UTS. Yield stress is usually more affected by static strain aging than DSA.

Table 8: Overview of properties on investigated reactor pressure vessel steels.

Desig.	**$YS_{288°C}$ [MPa]**	**$UTS_{288°C}$ [MPa]**	**K_{IC} [MPa·m$^{1/2}$]**	**DSA index-1 [%]**	**DSA index-2 [%]**
Biblis C BM	400	578	245	–0.6	–2.5
HT 1	740	860	220	–0.58	–2.72
277	418	566	280	–12.3	–14.3
508	396	565	265	–16.4	–19.7
HSST	412	588	250	–8.9	–10.4
KS12	462	618	150	–9.12	–6.02
JRQ	445 (AR) 415 (SC)	577 (AR) 540 (SC)	245 (AR) 240 (SC)	-	6.47 (AR)* 1.52 (SC)*

*(DSA index-1: the relative decrease in the reduction of area by a change of temperature from room temperature to 250 °C at a strain rate of 10^{-5} s^{-1}; DSA index-2: the relative decrease in the reduction of area by a change of the strain rate from 10^{-3} to 10^{-5} s^{-1} at 250 °C); *Tensile test at 288 °C.*

The RPV steels revealed a low (Biblis C, JRQ), moderate (HSST, KS 12) and high (277, 508) DSA susceptibility [5], respectively (Figure 43), based on the relative decrease in the reduction of area (Z) by a change of strain rate from 10^{-3} to 10^{-5} s^{-1} at 250 °C. This ranking from high to low is relative among the investigated RPV steels. The absolute DSA susceptibility is moderate compared to that of silicon-killed carbon piping steels with high free interstitial nitrogen contents.

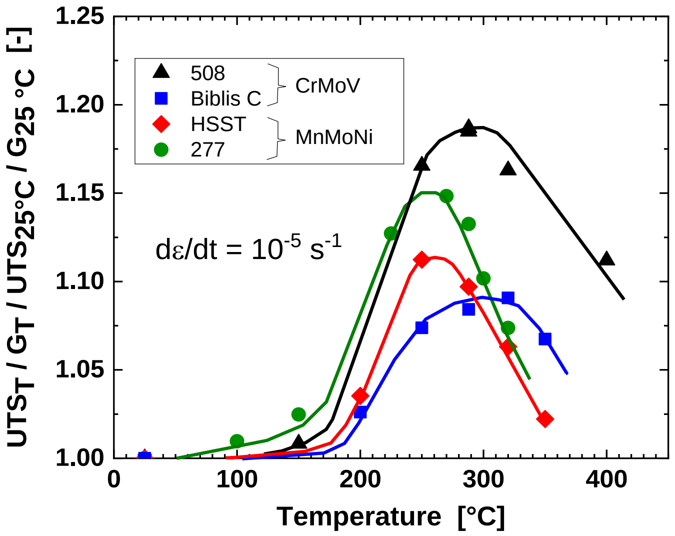

Figure 40: Maximum in UTS at intermediate temperatures in various RPV steels at strain rate of 10^{-5} s^{-1}.

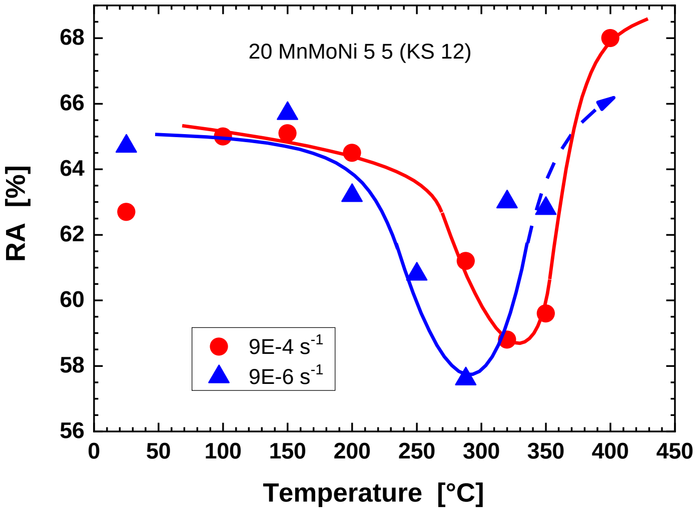

Figure 41: Minimum in reduction of area at intermediate temperatures due to DSA.

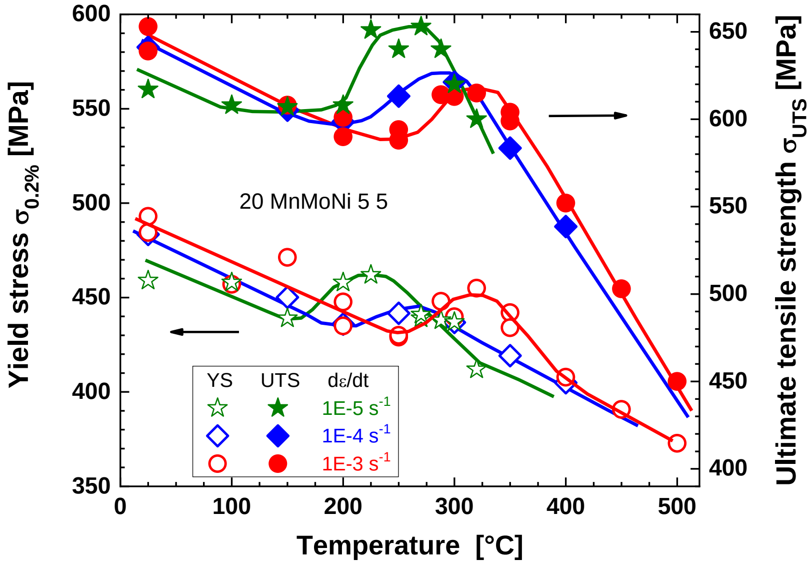

Figure 42: Shift of peak in yield stress (YS) and ultimate tensile strength (UTS) to higher temperatures with increasing strain rate.

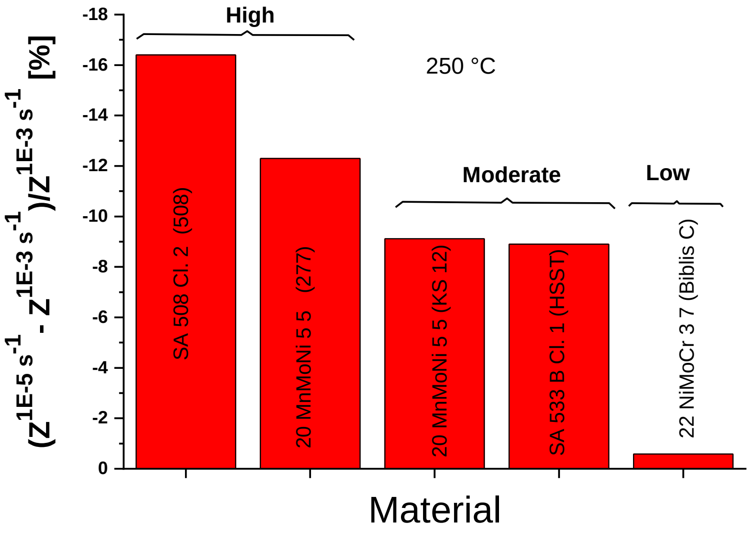

Figure 43: Ranking of RPV steels by DSA index.

2.1.2 Microstructure and heat treatments

The details of heat treatment process of each material are listed in Table 9. Apart from HT1, all the materials were in the quenched and tempered state with very similar heat treatment conditions. 508 steel had a 50 °C lower annealing temperature (600 vs. 650 °C) that results in a slightly higher free carbon concentration and smaller carbide precipitates. It explains the increased DSA susceptibility of 508 in spite of a low free nitrogen content. HT1 was fabricated from the Biblis C base metal through a specific two-step heat treatment with a higher austenitizing temperature of 1000 °C for grain growth and a shorter annealing time of 1 h at 650 °C. Some of the JRQ specimens went through a step-cooled (SC) [130] heat treatment for enhancing the phosphorus segregation at the GB (Table 9).

Table 9: Heat treatment of investigated steels.

Materials	Heat treatment
Biblis C BM	**A:** 890–900 °C/7 h/WQ & **T:** 640–650 °C/17 h/AC & **SR:** 540–555 °C/59 h/465 °C/590–610 °C/21 h/465 °C/590–605 °C/11.25 h/AC
HT 1	Like Biblis C BM & **A (CG):** 1000 °C/1 h/WQ & **T:** 625 °C/1 h/AC
277	**A:** 910–920 °C/6 h/WQ & **T:** 640–650 °C/9.5 h/FC
508	**A:** 900 °C/8 h/WQ & **T:** 600 °C/9 h/AC
HSST	**A:** 915 °C/12 h/AC/860 °C/12 h/WQ & **T:** 660 °C/12 h/FC & **SR:** 610 °C/40 h/FQ/550 °C/12 h/FQ 550 °C/12 h/FQ
KS 12	**A:** 900 °C/9 h/WQ & **T:** 650 °C/34 h/AC & **SR:** 550 °C/46.5 h/600 °C/8 h/AC
JRQ	**AS:** A: 900 °C; Q: 880 °C; T: 665 °C/12 h; SR: 620 °C/40 h **SC:** 593 °C/1 h/538 °C/15 h/524 °C/24 h/496 °C/48 h/468 °C/72 h/FC 315 °C (Argon)

(A: Austenitizing; WQ & T: water quenching & tempering; AC: air cooling; SR: stress relieving; FC: furnace cooling)

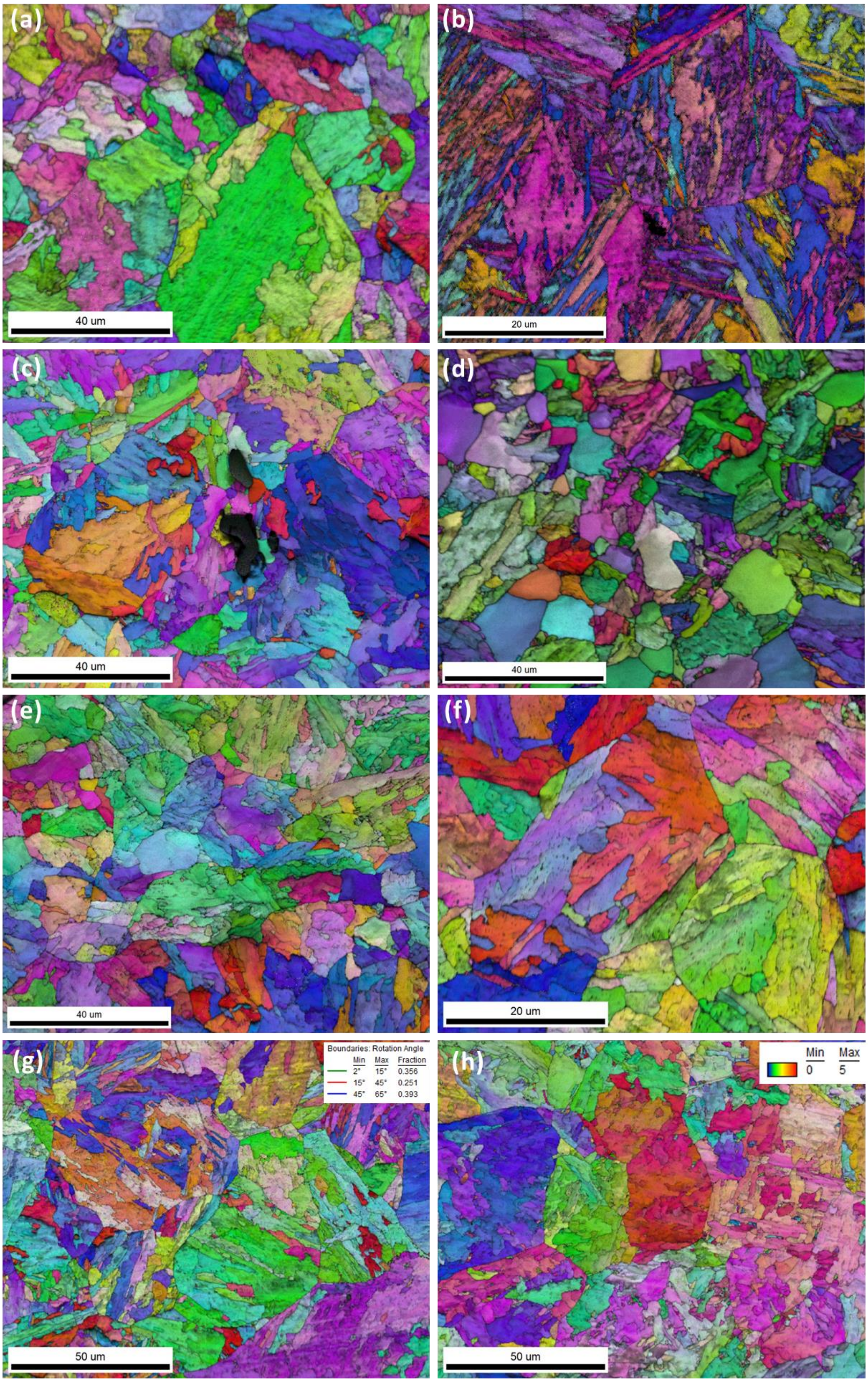
(a)
40 um
(b)
20 um
(c)
40 um
(d)
40 um
(e)
40 um
(f)
20 um
(g)
Boundaries: Rotation Angle
Min Max Fraction
2° 15° 0.356
15° 45° 0.251
45° 65° 0.393
50 um
(h)
Min Max
0 5
50 um

Figure 44: Inversed pole figures of as-received Biblis C (a), HT 1 (b), 277 (c), 508 (d), HSST (e), and KS12 (f), as-received (g) and step-cooled (h) JRQ material materials.

Figure 44 reveals the microstructure of the different materials in their as-received states. Biblis C, 277, HSST, KS12 and JRQ have a granular/upper bainitic microstructure with a mean prior-austenite grain size of 10 to 20 µm (Table 10). HT1 has an acicular tempered martensitic microstructure with the elongated laths oriented in various directions. Its PAGB size is roughly three times larger than in the corresponding Biblis C base metal. 508 has a mixed bainitic (lath) and ferritic-pearlitic (round) structure. The lath and complex sub-grain structure is shown with the inversed pole figures in Figure 44. The summary of prior-austenite grain size, bainite lath length and width of the seven materials are shown in Table 10. As shown in Figure 44 (g) and (h), after the SC heat treatment of JRQ, the ratio of low angle GB of JRQ material increased, indicating that the SC decreased the grain distortion, the deformation level and the dislocation density. The lower average image quality and higher kernel average misorientation (KAM) is in line with the slightly lower yield stress of the SC material. The results of tensile tests with as-received and SC JRQ materials with various loading rates at 288 °C are summarized in Figure 45. The SC material revealed a lower yield stress, UTS as well as uniform and fracture strain at all strain rates at 288 °C in tensile tests than the as-received steel.

Table 10: Grain morphology and lath dimension of the seven investigated materials.

Materials	**Microstructure**	**Prior-austenite grain size [µm]**		**Lath length [µm]**	**Lath width [µm]**
Biblis C	Granular, bainitic	12.5		6.6	5.0
HT 1	Tempered martensitic	40.4		21.2	1.8
277	Granular, bainitic	17.3		8.7	2.1
508	Bainitic/ferritic-pearlitic	Ferrite	9.4	12.2	4.1
		Bainite	20.1		
HSST	Granular, bainitic	15.7		9.7	6.8
KS12	Granular, bainitic	9.6		5.7	4.4
JRQ	Granular, bainitic	25.4		19.5	4.0

The quantitative characterization of the GB phosphorus segregation in the high-phosphorus steels JRQ and KS 12 is still pending. However, the segregation of phosphorus was indirectly demonstrated by the intergranular features on the fracture surface during air fatigue pre-cracking (Figure 46 and Figure 47), and post-test fracture after cooling in liquid nitrogen. The distribution of phosphorus seems to be rather inhomogeneous, as revealed by the strong specimen-to-specimen variation in the area share of intergranular features. Figure 46 illustrates the fatigue crack growth rate for each sequence of pre-cracking of the investigated steels in air. The air fatigue crack growth rate of high-phosphorus KS 12 was about two times higher than that of low-phosphorus HSST steel with similar sulphur content. Similarly, the SC JRQ material revealed a 40% higher fatigue crack growth rate than in the as-received state. Figure 47 shows the fracture features of HSST, KS12 and as-received and SC JRQ materials during fatigue pre-cracking in air. The HSST material shows the typical fatigue fracture surface with striations only, while in KS12 a relatively large amount of intergranular cracks was also observed. As shown in Figure 47 (g) to (l), a higher fraction of intergranular cracking was observed in SC than in as-received JRQ materials.

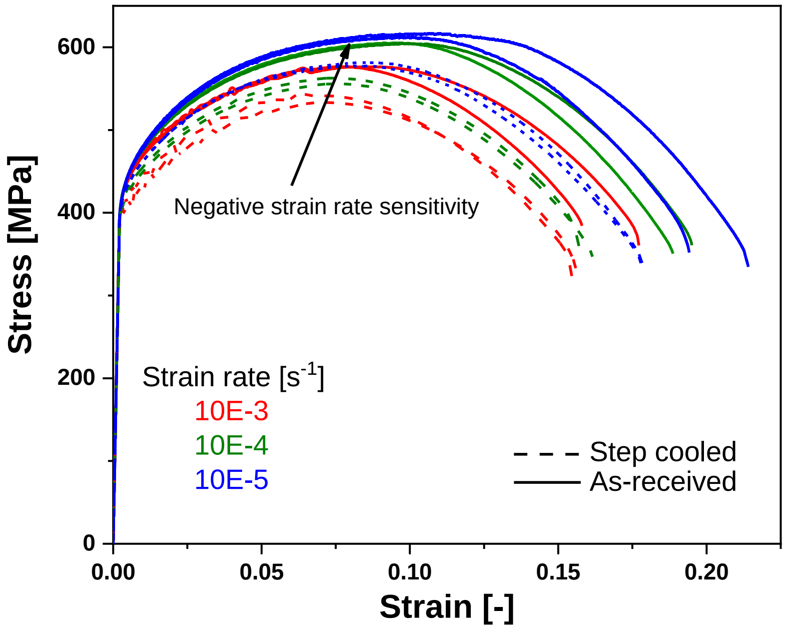

Figure 45: Tensile tests with as-received and step-cooled JRQ materials with various loading rates at 288 °C.

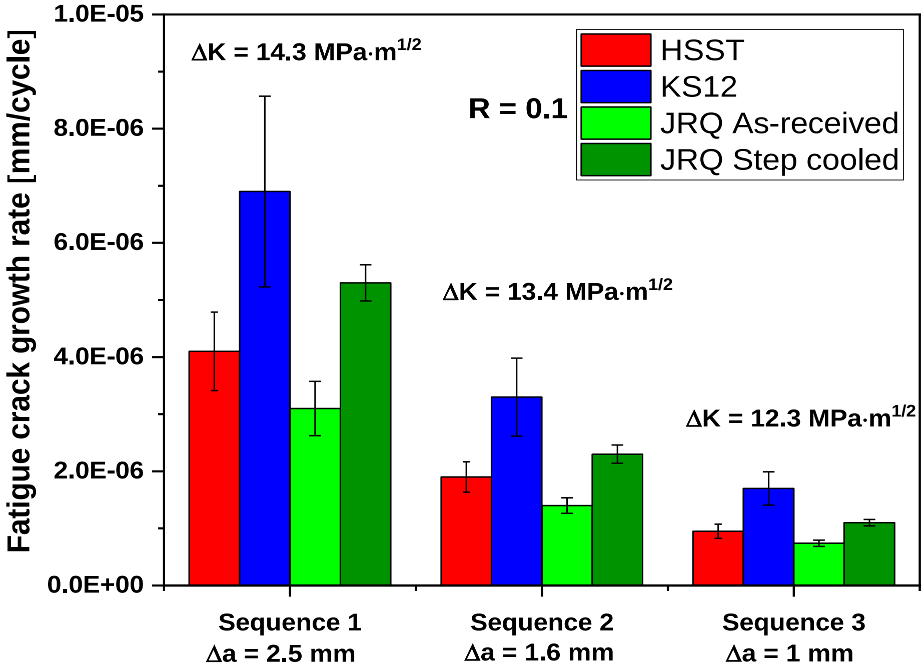

Figure 46: Fatigue crack growth rates for each pre-cracking sequence of the investigated RPV materials.

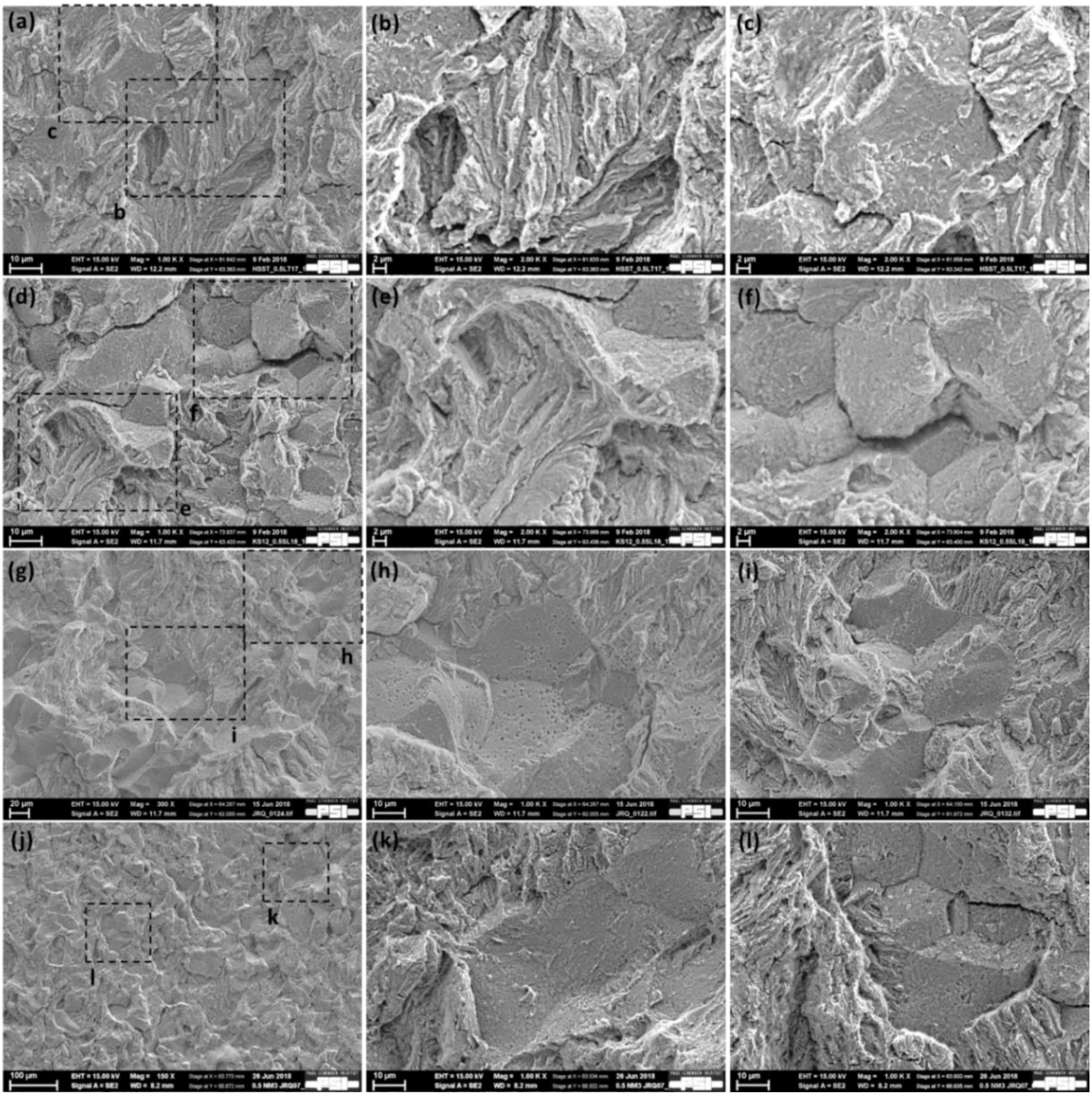
(a)
c
b
(b)
(c)
(d)
f
e
(e)
(f)
(g)
h
i
(h)
(i)
(j)
k
l
(k)
(l)
10 µm
2 µm
2 µm
10 µm
2 µm
2 µm
20 µm
10 µm
10 µm
100 µm
10 µm
10 µm

Figure 47: Fractography of pre-cracked fracture surface of HSST (a to c), KS12 (d to f), as-received (g to i) and step-cooled (j to l) JRQ materials.

2.1.3 Non-metallic inclusions analysis

The sulphur content of the steel as well as the size, type, morphology and spatial distribution of inclusions (especially MnS) are important material parameters, which have direct influence on corrosion process and fracture behaviour. Therefore, the inclusions in the as-received RPV steels investigated in this work were characterized with Scanning Electron Microscope (SEM) and Energy-Dispersive X-ray Spectroscopy (EDX). The main inclusions species include oxides (magnesium-aluminium spinel, magnesium oxide or aluminium oxide) and sulphides (MnS and CaS) and they often concomitted each other. Due to the low solubility of sulphur in both α- and γ-iron (about 0.02% and 0.001–0.007% at 900 °C, respectively), sulphur is mostly present as sulphide inclusions that are formed at PAGB. The Gibbs formation energy of various sulphides increases in the following sequence from CaS < MnS < NiS < FeS [159]. Therefore, MnS and CaS were formed preferentially.

The observed dimensions (1 to 20 µm) and morphologies of MnS inclusions may differ with different specimen orientations, positions in the plate and fabrication processes (hot rolling and forging), as shown in Table 11. The inclusions in the figures in Table 11 were all identified as MnS through EDX. Hot rolling elongates the MnS inclusions in the rolling directions, while forging produces more equiaxed inclusions. Most MnS inclusions were located at the PAGBs. It was found that the number density, but not the typical dimensions of MnS inclusions (1 to 20 µm) correlated well with the sulphur concentration in the steels [159]. In contrast to the other RPV steels, KS12 is very inhomogeneous and shows strong variations in through-thickness sulphur contents. Furthermore, in the high-sulphur steels HSST and KS12, some distinct clustering of large sulphides (ghost lines) with a length of a few hundreds of microns were also observed.

Table 11: Spatial distribution and morphology of the MnS inclusions in the investigated materials.

Material	Sulphur [%]	Orientation	Location	Shape	Dimension (mean) [µm]	Example
Biblis C	0.007	TL	PAGB	Clustering spherical	Diameter: ~ 7	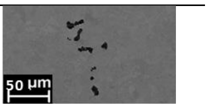
HT 1	0.007	TL		Clustering spherical	Diameter: ~ 11	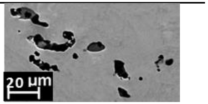
277	0.004	LT		Bands	Width: ~ 2 Length: ~ 9	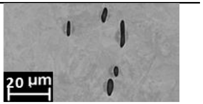
508	0.004	TL		Clustering spherical	Diameter: ~ 5	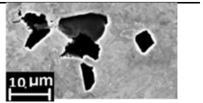
HSST	0.018	TL		Dispersed spherical/plates	Diameter: ~ 18	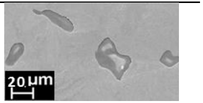
KS12	0.015	SL		Clustering bands	Width: ~ 3 Length: ~ 19	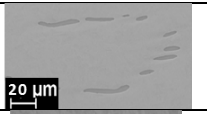
JRQ BM	0.004	TL		Plates	Width: ~ 1.5 Length: ~ 6	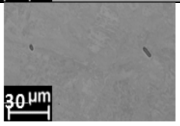

2.2 Experiments

2.2.1 High-temperature water loops

The EPFM tests in HTW were conducted in 10 or 5 L stainless steel autoclave systems (constant flow of 30 L/h) with integrated electro-mechanical loading devices. HTW loops [94] simulate the LWR coolant environment, as shown in Figure 48. During the experiments, all crucial mechanical parameters (such as load and pull rod stroke) and environmental parameters at inlet and outlet, such as the conductivity, temperature, pressure, DO and DH were monitored and recorded continuously. ECP of the specimens and the redox potential (platinum probe) were continuously monitored through a $Cu/Cu_2O/ZrO_2$-membrane reference electrode. The specimens were electrically insulated from the autoclave by Teflon and ZrO_2. The specimens were usually pre-oxidized for one week in the test environment before EPFM test, in order to establish a homogeneous oxide film. It enables hydrogen pick-up from the environment and corrosion reactions at a small constant pre-load with a stress intensity factor K_I between 2 and 18 MPa·m$^{1/2}$. A fully developed occluded crack crevice chemistry prevailed after the pre-oxidation period. In this work, the water conductivity and pH value at outlet gradually stabilized and normally were very similar to that of inlet at the end of the peroxidation period. After pre-oxidation, some of these EPFM tests started with an active growing SICC (by cyclic loading) or SCC cracking (chloride and constant load). The preceding EAC provides an aggressive occluded high-sulphur crack crevice chemistry and a high hydrogen uptake potential in the crack-tip process zone. The maximum K_I during these phases was 35 to 45 MPa·m$^{1/2}$ (corresponding to a low J of 5 to 10 kN/m).

EPFM tests with air fatigue pre-cracked and side-grooved C(T) specimens were conducted in HTW with different simulated LWR water chemistry environments. The different water chemistries and the resulting crack crevice conditions (that govern the hydrogen uptake in the process zone) are summarized in Table 12 and Table 13. Reducing BWR HWC was simulated by hydrogenated (DH content of 2 ppm) neutral high-purity water ($pH_{288°C}$ = 5.7, inlet conductivity = 0.055 µS/cm). The corresponding ECP of the specimens at 288 °C were –590 mV_{SHE} (HWC). PWR primary water was simulated by mildly alkaline borated and lithiated, hydrogenated high-purity water (1000 ppm boron as H_3BO_3, 2.3 ppm lithium as LiOH, $pH_{288\ °C}$ = 6.9, inlet conductivity of 24 µS/cm, DH content of 2.2 ppm). The corresponding ECP at 288 °C was –735 mV_{SHE}. Selected additional tests were performed in nitrogenated (oxygen- and hydrogen-free, –400 mV_{SHE})) or oxygenated (2 ppm DO), +100 mV_{SHE}) neutral high-purity water. As mentioned in Section 1.3.4.1, a moderate acidic pH shift of 1 to 1.5 units is possible in BWR, which led to the ΔECP shown in Table 13. To clearly elucidate the effect of hydrogen, the hydrogen concentration in the HWC tests was a magnitude higher than in the real BWR. The higher oxygen content was selected to simulate a realistic ECP on the RPV cladding. In some tests, 65 ppb of sulphate (H_2SO_4) or 50 ppb chloride (HCl) were added to produce a more aggressive occluded crevice chemistry or a growing EAC crack prior to the EPFM test.

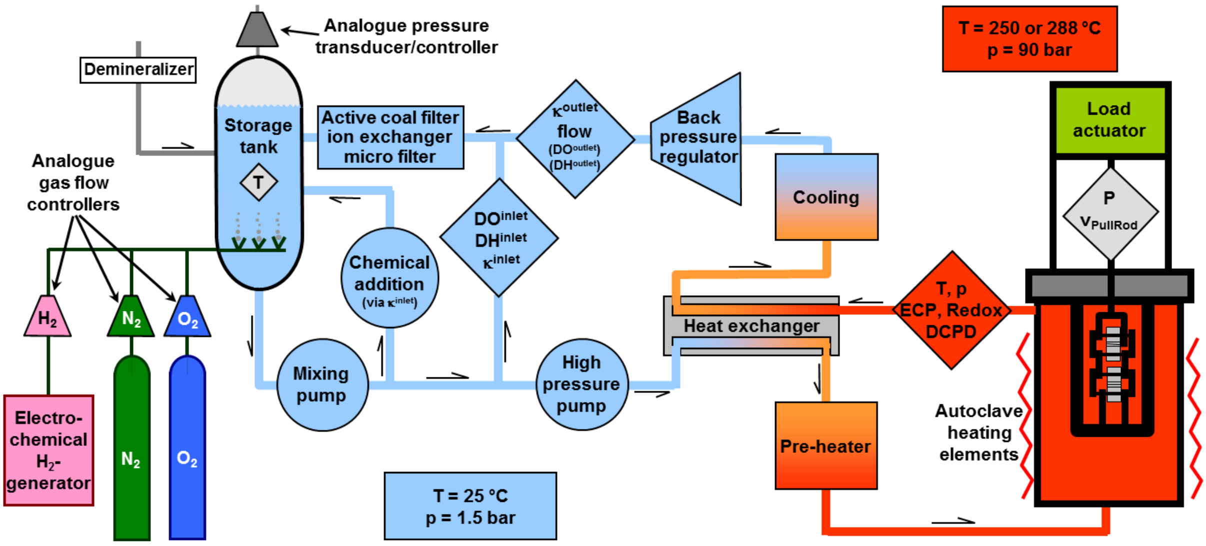
Analogue pressure transducer/controller
Demineralizer
Storage tank
T
Analogue gas flow controllers
H_2
N_2
O_2
Electro-chemical H_2-generator
N_2
O_2
Active coal filter ion exchanger micro filter
κ^{outlet} flow (DO^{outlet}) (DH^{outlet})
Back pressure regulator
Cooling
DO^{inlet} DH^{inlet} κ^{inlet}
Chemical addition (via κ^{inlet})
Mixing pump
High pressure pump
Heat exchanger
T, p ECP, Redox DCPD
Pre-heater
Autoclave heating elements
T = 25 °C p = 1.5 bar
T = 250 or 288 °C p = 90 bar
Load actuator
P $V_{PullRod}$

Figure 48: Illustration of HTW loop and autoclave systems for EPFM tests.

Table 12: Overview on investigated high-temperature water environments.

Environment		**Water chemistry**	**$pH_{288 °C}$**	**ECP [mV_{SHE}]**	**Dissolved oxygen [ppm]**	**Dissolved hydrogen [ppm]**
Pressurized water reactor (PWR)		Mildly alkaline borated and lithiated (1000 ppm B as H_3BO_3, 2.3 ppm Li as LiOH (inlet conductivity = 24 µS/cm)	7	–735	0	2.2
Boiling water reactor (BWR)	Normal water chemistry (NWC) oxygenated	Neutral high-purity water (inlet conductivity = 0.055 µS/cm)	5.7	+100	2	0
	Hydrogen water chemistry (HWC) hydrogenated			–590	0	2
	Nitrogenated			–400	0	0

The hydrogen uptake in the crack-tip process zone is governed by the local crevice conditions. As discussed in Sections 1.3.2 and 1.3.4, the crack-tip ECP is low and governed by the H_2/H_2O line in all environments and they mainly differ in their DH content and pH.

Hydrogen generation and pick-up occurs at the crack tip during pre-oxidation and the subsequent EPFM test. As discussed in Section 1.3.2, hydrogen concentration in the process zone for an EPFM test in HTW is dominated by the evolving occluded crack crevice chemistry and corrosion reactions at the plastically strained crack tip and the quasi-continuous oxide film rupture (depending on strain rate). Previous PSI investigations showed that pre-oxidation period (1 to 32 days) had no effect on the fracture behaviour in HTW [63]. Since hydrogen diffusion in RPV steels is very fast, the bulk hydrogen distribution is relatively homogeneous in the C(T) specimens. Based on Fick's second law of diffusion and a very conservative lower bound value of the diffusion coefficient of hydrogen at 300 °C (= 3×10^{-9} m^2/s), the hydrogen concentration at mid-thickness of a 1T-C(T) specimen reaches ~ 90% of the hydrogen concentration at the surface in 12 days at 288 °C [63]. The redistribution of hydrogen from the bulk material with low stress to the highly stressed crack tip with high hydrostatic, triaxial stress is also believed to be a minor contribution.

Table 13: Resulting approximate crack crevice conditions and potential gradient between crack-mouth and crack-tip ECP.

Environment	**Water chemistry**	**$pH_{288°C}$**	**Dissolved oxygen [ppm]**	**Dissolved hydrogen [ppm]**	**ECP [mV_{SHE}]**	**ΔECP [mV_{SHE}]**
Pressurized water reactor (PWR)	Mildly alkaline borated and lithiated (1000 ppm B as H_3BO_3, 2.3 ppm Li as LiOH	7	0	2.2	–735	~ 0
Boiling water reactor (BWR)	Normal water chemistry (NWC) oxygenated	~ 4.5 to 6	0	~ 0	~ –350 to –450	~ +450 to +550
	Hydrogen water chemistry (HWC) hydrogenated	~ 6	0	2	–590	~ 0
	Nitrogenated	~ 6	0	~ 0	~ –450	~ 0

2.2.2 Elastic-plastic fracture mechanics tests

2.2.2.1 Elastic-plastic fracture mechanics test details

EPFM tests according to ASTM E1820 [50] with air fatigue pre-cracked (crack length to width ratio $a_o/W \sim 0.5$) and side-grooved (a thickness reduction of 10% on each side of specimen to inhibit crack deflection and shear lip formation) C(T) specimens were conducted in different HTW environments and air. The reversed DCPD was used to monitor the crack advance during the EPFM tests. Due to load capacity limitations in some loops and the limited availability of some materials, both 25.0 mm thick 1T-C(T) (Biblis C, HT 1, 277 and 508) and 12.5 mm thick 0.5T-C(T) (HSST, JRQ and KS12) fracture mechanics specimens were used. The technical drawings of 0.5T- and 1T-C(T) fracture mechanics specimens with a sharp notch (notch radius R of 0.1 mm and notch depth to ligament width ratio a_o/W of 0.3) are shown in Figure 49 and Figure 50, respectively. The specimens were fabricated from the forged ingots or hot-rolled steel plates in different orientations according to ASTM E399 [51], with TL (Biblis C BM, HSST and 508), LT (277, 508) or SL (KS12) orientations, respectively. For a given material, the specimens had the same orientation and size and were usually tested in the same loading/autoclave system in air and HTW. The specimen size had no effect on the fracture initiation resistance and the variations were within the typical specimen-to-specimen scatter range. Specimen size and constraints are expected to have a stronger effect on the tearing resistance, but the differences were small as well. The designations of crack plane orientation and inclusion orientation are shown in Figure 51. The final $K_{I,\,max}$ during the final stage of pre-cracking was 14 and 21 MPa·m$^{1/2}$ for the 0.5T- and 1T-C(T) specimens, respectively.

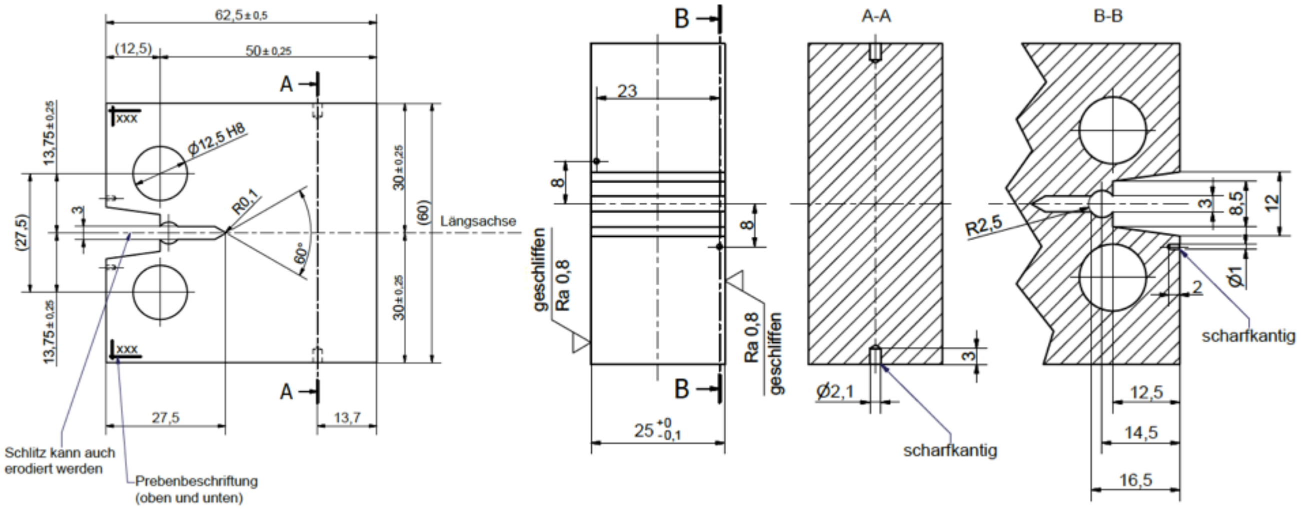
62,5±0,5
(12,5)
50±0,25
A
Ø12,5 H8
R0,1
60°
13,75±0,25
(27,5)
3
30±0,25
(60)
Längsachse
27,5
13,7
xxx
Schlitz kann auch erodiert werden
Prebenbeschriftung (oben und unten)
B
23
8
geschliffen Ra 0,8
25 +0 -0,1
A-A
Ø2,1
scharfkantig
B-B
R2,5
3
8,5
12
Ø1
2
scharfkantig
12,5
14,5
16,5

Figure 49: Configuration of 1T-C(T) specimens.

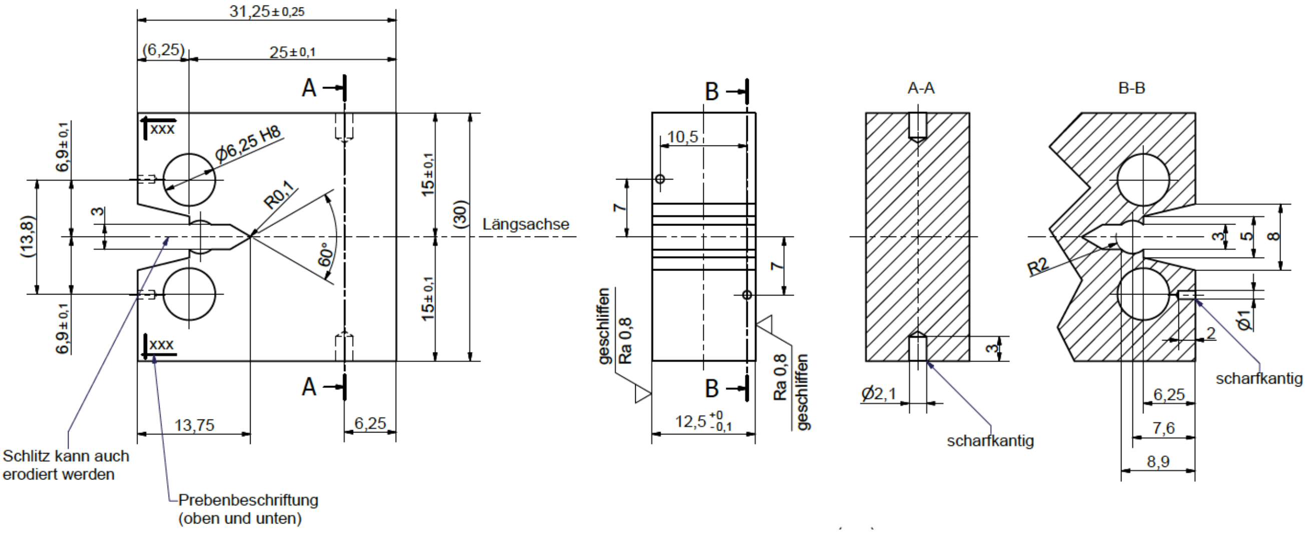
31,25±0,25
(6,25)
25±0,1
A
Ø6,25 H8
R0,1
60°
6,9±0,1
(13,8)
3
15±0,1
(30)
Längsachse
13,75
6,25
xxx
Schlitz kann auch erodiert werden
Prebenbeschriftung (oben und unten)
B
10,5
7
geschliffen Ra 0,8
12,5 +0 -0,1
A-A
Ø2,1
scharfkantig
B-B
R2
3
5
8
Ø1
2
scharfkantig
6,25
7,6
8,9

Figure 50: Configuration of 0.5T-C(T) specimens.

Due to the forming and heat treatment process, the top and bottom layers of the plates have a higher yield stress, but lower initial DBTT than the remaining part. From the ¼- to ¾-thickness position, there is little variation in toughness properties. The upper shelf toughness is affected by the non-metallic inclusions, in particular MnS. The upper shelf toughness can be significantly lower in segregation zones and show significant orientation dependence, in particular in high-sulphur steels. If possible, the specimens were machined from the ¼- to ¾-thickness position or the same location. Apart from KS 12, the other steels showed very similar upper shelf initiation resistance in air independent on thickness location and orientation.

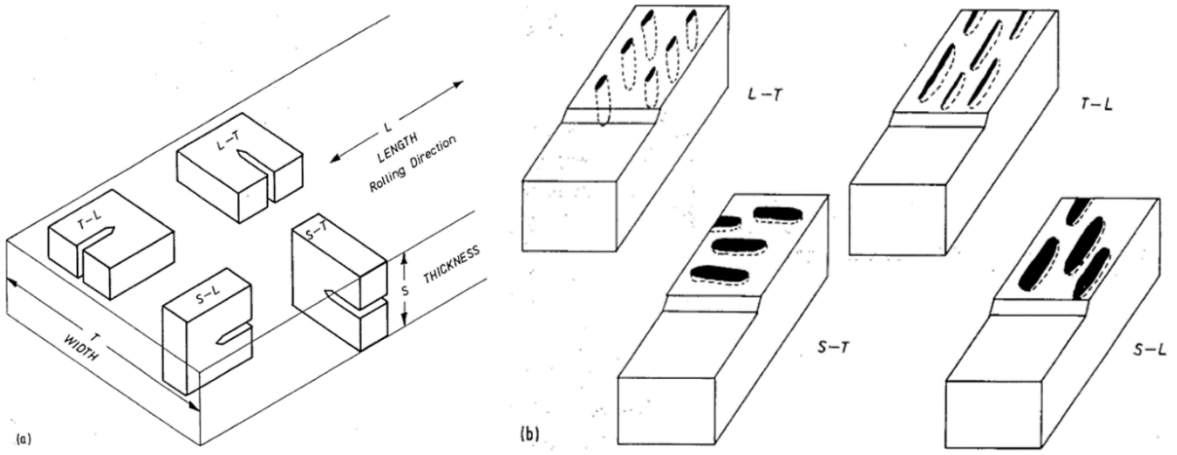

Figure 51: Schematic diagram of (a) crack plane orientation identification and (b) inclusion orientation in relation to specimen orientation: L = longitudinal; T = transverse; S = short transverse [160].

EPFM tests in both air and HTW environments at 25 to 320 °C were typically performed at a constant pull rod stroke rate with a standard crack opening displacement rate at load line ($dCOD_{LL}/dt$) of 0.25 and 0.35 mm/min for 0.5T and 1T-C(T) specimens, which resulted in an estimated crack-tip strain rate of 10^{-3} and 7×10^{-4} s^{-1} [11], respectively. Additionally, the loading rate and crack-tip strain rate were varied between 3×10^{-4} to 3 mm/min and 10^{-6} to 10^{-2} s^{-1}, as described in Table 14. The loading rate investigated in this work covers the strain rate for operational transients (10^{-6} to 10^{-4} s^{-1}) and during LOCA in nuclear power plants (10^{-4} to 10^{-2} s^{-1}).

Table 14: Crack opening displacement rates and corresponding crack-tip strain rates for CT specimens.

1T-C(T)	**$dCOD_{LL}/dt$ [µm/min]**	0.35	3.5	35	350	3500
	Crack-tip strain rate [s^{-1}]	7×10^{-7}	7×10^{-6}	7×10^{-5}	7×10^{-4}	7×10^{-3}
0.5 T-C(T)	**$dCOD_{LL}/dt$ [µm/min]**	0.25	2.5	25	250	2500
	Crack-tip strain rate [s^{-1}]	10^{-6}	10^{-5}	10^{-4}	10^{-3}	10^{-2}

2.2.2.2 Evaluation of elastic-plastic fracture mechanics tests

The details of the fracture resistance evaluation procedure are described in the previous works of PSI [14][63]. The determination of *J-R* curve was performed by the incremental method. EPFM tests in HTW in autoclaves are challenging and required some minor modifications with respect to the typical standard tests in air.

The *J-R* curves were calculated from the load-line displacement (LLD) curve of the increment *i*, at crack length *a (i)*, LLD *v (i)*, and load *P (i)*.

$$J_{(i)} = J_{el_{(i)}} + J_{pl_{(i)}} \tag{8}$$

$$J_{(i)} = \frac{(K_{(i)})^2(1-v^2)}{E} + J_{pl(i)} \tag{9}$$

where: J_{el} = elastic component of *J*, and J_{pl} = plastic component of *J*.

For the C (T) specimen at a force *P (i)*, $K_{(i)}$ is calculated as in Equations 10 and 11.

$$K_{(i)} = \frac{P_{(i)}}{(BB_N W)^{1/2}} f(\frac{a_i}{W}) \tag{10}$$

$$f\left(\frac{a_i}{W}\right) = \frac{\left\{\left(2+\frac{a_i}{W}\right)\left[0.886 + 4.64\left(\frac{a_i}{W}\right) - 13.32\left(\frac{a_i}{W}\right)^2 + 14.72\left(\frac{a_i}{W}\right)^3 - 5.6\left(\frac{a_i}{W}\right)^4\right]\right\}}{(1-\frac{a_i}{W})^{3/2}} \tag{11}$$

where *B* = sample thickness, B_N = net specimen thickness between the roots of the side grooves and *W* = sample width.

The plastic part of toughness $J_{pl\,(i)}$ is calculated as follows:

$$J_{pl(i)} = \left[J_{pl(i-1)} + \left(\frac{\eta_{pl(i-1)}}{b_{(i-1)}}\right)\frac{A_{pl(i)} - A_{pl(i-1)}}{B_N}\right]\left[1 - \gamma_{(i-1)}\left(\frac{a_{(i)} - a_{(i-1)}}{b_{(i-1)}}\right)\right] \tag{12}$$

$$\begin{gathered} \eta_{pl(i-1)} = 2.0 + 0.522\, b_{(i-1)}/W \\ \gamma_{(i-1)} = 1.0 + 0.76\, b_{(i-1)}/W \end{gathered} \tag{13}$$

The quantity $A_{pl(i)} - A_{pl(i-1)}$ is the increment of plastic area under the force versus plastic LLD record between lines of constant displacement spacing at points *i-1* and *i* (as shown in Figure 52). The quantity $J_{pl(i)}$ represents the total crack growth corrected plastic *J* at point *i* and is obtained in two steps, by first incrementing the existing $J_{pl(i-1)}$ and then by modifying the total accumulated result to account for the crack growth increment. Accurate evaluation of $J_{pl(i)}$ from the above relationship requires small and uniform crack growth increments consistent with the elastic compliance spacing, which are 0.05 and 0.1 mm for 0.5T- and 1T-C(T) in this work, respectively.

The quantity $A_{pl(i)}$ can be calculated from the following equation:

$$A_{pl(i)} = A_{pl(i-1)} + \frac{\left[P_{(i)} + P_{(i-1)}\right]\left[v_{pl(i)} - v_{pl(i-1)}\right]}{2} \tag{14}$$

where: $v_{pl(i)}$ = plastic part of the LLD, $v_i - P_{(i)}\, C_{LL\,(i)}$, and $C_{LL\,(i)}$ = experimental compliance, $(\Delta v/\Delta P)_i$, corresponding to the current crack size, a_i.

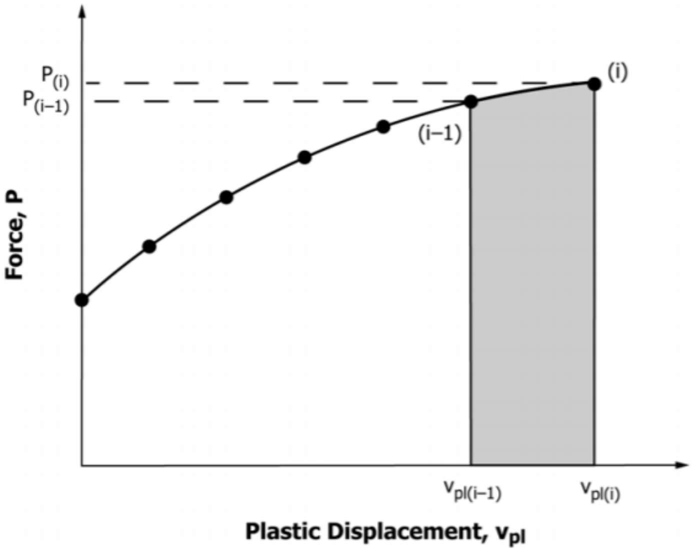

Figure 52: Definition of plastic area for resistance curve *J* calculation

Due to a lack of suitable displacement transducers for crack opening displacement measurements in EPFM tests in HTW, the pull rod stroke corrected by the elastic compliance of the load train was considered to be the LLD v_i of the specimen. This consideration was confirmed by control experiments with clip gauges in air that revealed only small differences (< 1.5% prior to the peak load and < 4% beyond the peak load). The uncertainties were further reduced by using the same load train for tests in air and HTW for a given material. The elastic compliance of the load train $C_{LT\,(i)}$ was calculated from the total elastic compliance $C_{tot\,(i)}$ by the specimen elastic compliance $C_{LL\,(i)}$.

$$C_{LT(i)} = C_{tot(i)} - C_{LL(i)} \tag{15}$$

$$\begin{aligned} C_{LL(i)} = \frac{1}{EB_e}\left(\frac{W + a_i}{W - a_i}\right)^2 \Bigg[2.0630 + 12.219\left(\frac{a_i}{W}\right) - 20.065\left(\frac{a_i}{W}\right)^2 \\ - 0.9925\left(\frac{a_i}{W}\right)^3 + 20.609\left(\frac{a_i}{W}\right)^4 - 9.9314\left(\frac{a_i}{W}\right)^5\Bigg] \end{aligned} \tag{16}$$

$$where\ B_e = B - \frac{(B - B_N)^2}{B}$$

The load train compliance $C_{LT\,(i)}$ was then used to calculate the crack opening displacement at load line v_i from the measured pull rod stroke v_{tot}.

$$v_i = v_{tot} - C_{LT(i)} P_{(i)} \tag{17}$$

The reversed DCPD technique (configuration of wire connections in Figure 53) was used for crack length monitoring. The crack length was calculated using the Johnson equation.

$$a = \frac{2W}{\pi} cos^{-1} \frac{\cosh(\pi y/2W)}{cosh\{(U/U_o)cosh^{-1}\left[\cosh\left(\frac{\pi y}{2W}\right)/\cos(\frac{\pi a_o}{2W})\right]\}} \tag{18}$$

where U and U_0 are the DCPD signal corresponding to the instantaneous crack length (a) and initial crack length (a_0) measured by post-test fractography, respectively. y is half of the distance between the DCPD potential measurement points (Figure 53) and W is the width of C(T) specimen.

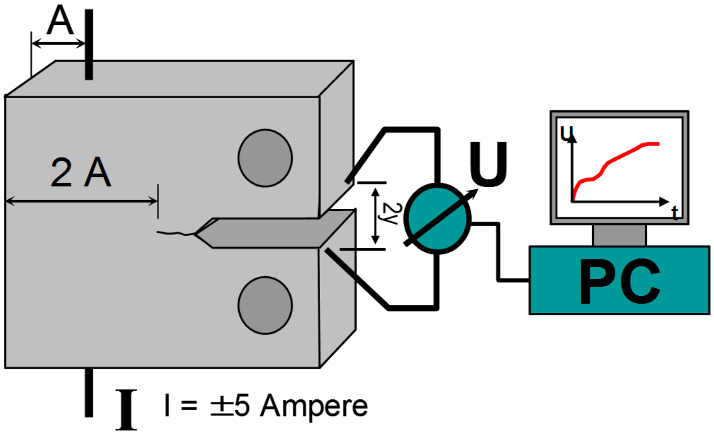

Figure 53: DCPD configuration.

The crack extension as calculated by DCPD was linearly corrected by the actual final crack extension measured by post-test fractography. The initial fatigue or CF pre-crack length a_0 from fractography was assigned to initiation of stable crack growth, as described in Figure 54. The crack extension measured by DCPD slightly overestimated the actual crack extension (from fractography) by ~ 5% and this accuracy was better than for the ULC method. The relative error of the corresponding crack lengths from the load line was much smaller (< 1%). The applied procedure for the detection of the onset of ductile crack growth was verified by qualification tests in air and HTW that were interrupted shortly after the onset of ductile crack growth. The difference between the small crack advances of 70 to 300 μm predicted by DCPD and measured by post-test fractography was less than 10%, confirming the adequacy of the selected approach (as requested by the ASTM E1820 standard).

The methods for the determination of the J-Δa curve, blunting line and J_{DCPD} at the onset of ductile crack growth are illustrated in Figure 54. The blunting line and apparent crack advance Δa_i due to blunting were calculated with J_{DCPD} and the flow stress σ_Y (Equation 19) at the corresponding temperature and strain rate (Equation 20).

$$\sigma_Y = \frac{\sigma_{YS} + \sigma_{UTS}}{2} \tag{19}$$

After onset of ductile crack growth, the *J* values were calculated with the load, LLD and corresponding crack length. The compliance change of the specimen with crack growth was considered during the calculation. *J*-Δa curves were plotted using the calculated *J* values, where $\Delta a = \Delta a_{DCPD} + \Delta a_i$. Δa_i is the increase in crack length during loading. *J*-Δa curve with all the exclusion lines, blunting line and the limits on *J* and Δa were calculated as specified in the ASTM standard.

$$\Delta a_i = \frac{J_{DCPD}}{2\sigma_Y} \tag{20}$$

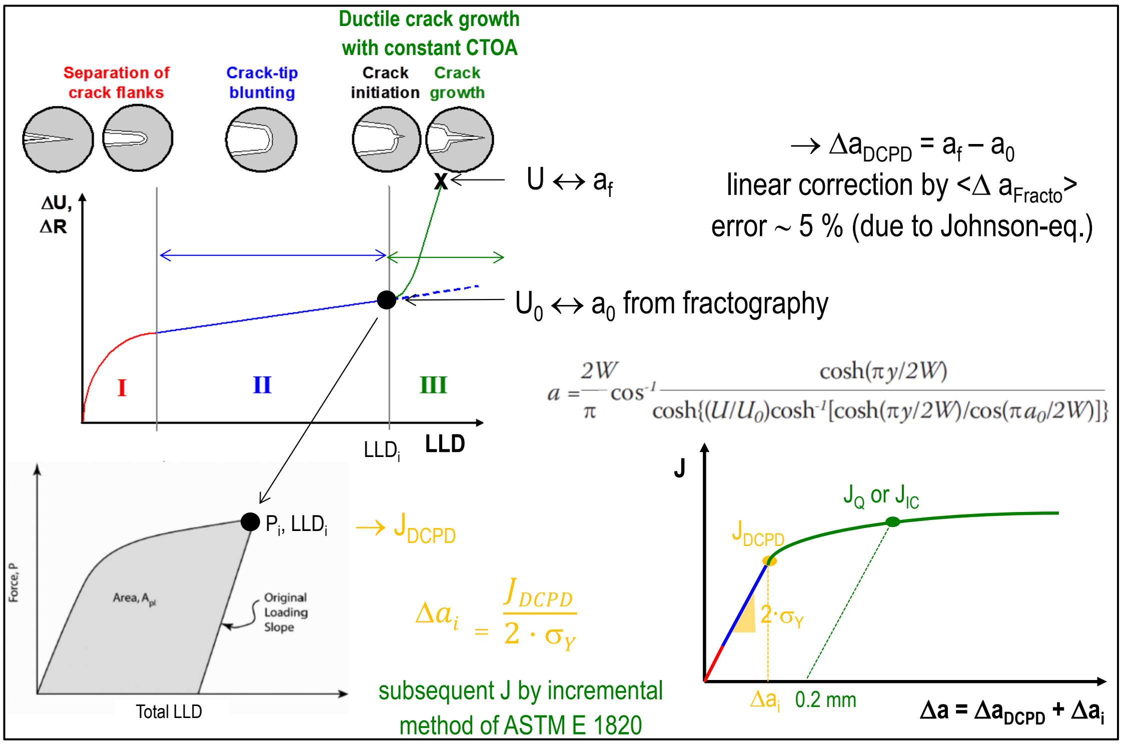
Ductile crack growth
with constant CTOA
Separation of crack flanks
Crack-tip blunting
Crack initiation
Crack growth
ΔU, ΔR
X
U ↔ a_f
→ Δa_DCPD = a_f – a_0
linear correction by <Δ a_Fracto>
error ~ 5 % (due to Johnson-eq.)
U_0 ↔ a_0 from fractography
I
II
III
LLD_i
LLD
a = 2W/π cos^-1 cosh(πy/2W) / cosh{(U/U_0)cosh^-1[cosh(πy/2W)/cos(πa_0/2W)]}
Force, P
Area, A_pl
Original Loading Slope
P_i, LLD_i
→ J_DCPD
Δa_i = J_DCPD / 2 · σ_Y
Total LLD
subsequent J by incremental
method of ASTM E 1820
J
J_Q or J_IC
J_DCPD
2·σ_Y
Δa_i
0.2 mm
Δa = Δa_DCPD + Δa_i

Figure 54: Applied procedure for development of *J*-Δa curve by the DCPD technique.

J integral values at initiation of stable crack growth were calculated as per the ASTM standard (J_Q) and at "physical initiation" (J_{DCPD}). J_Q is the J value corresponding to the intersection point between the regression line ($J = C_1 \cdot \Delta a^{C2}$) and the 0.2 mm exclusion line, which relates to a crack advance of ~ 200 µm. J_{DCPD} is calculated at the instant when the linear slope of DCPD potential drop vs. COD_{LL} curve starts to change and corresponds to a crack advance of ≤ ~ 50 µm. The J_{DCPD} values were usually ~ 35% (25 to 50%) smaller than the corresponding J_Q values. Additionally, the *J* integral $J_{\Delta a}$

at a specific crack advance of Δa was measured as the tearing resistance (e.g., $J_{0.1}$ at 0.1 inch = 2.54 mm). The magnitude of environmental reduction effects and parameter trends in HTW on J_Q and $J_{\Delta a}$ were very similar. Therefore, the focus in the results and discussion section is usually placed to J_Q only.

An example of DCPD and LLD recording and the evaluated *J-R* curve are shown in Figure 55. To qualify J_Q as J_{IC}, fifteen different criteria of ASTM E1820 have to be satisfied. Important small-scale yielding criteria were always satisfied, but other isolated criteria (e.g. straightness of crack front in case of preceding SICC) were not fulfilled occasionally in some tests. Therefore, J_Q is reported instead of J_{IC} in this paper.

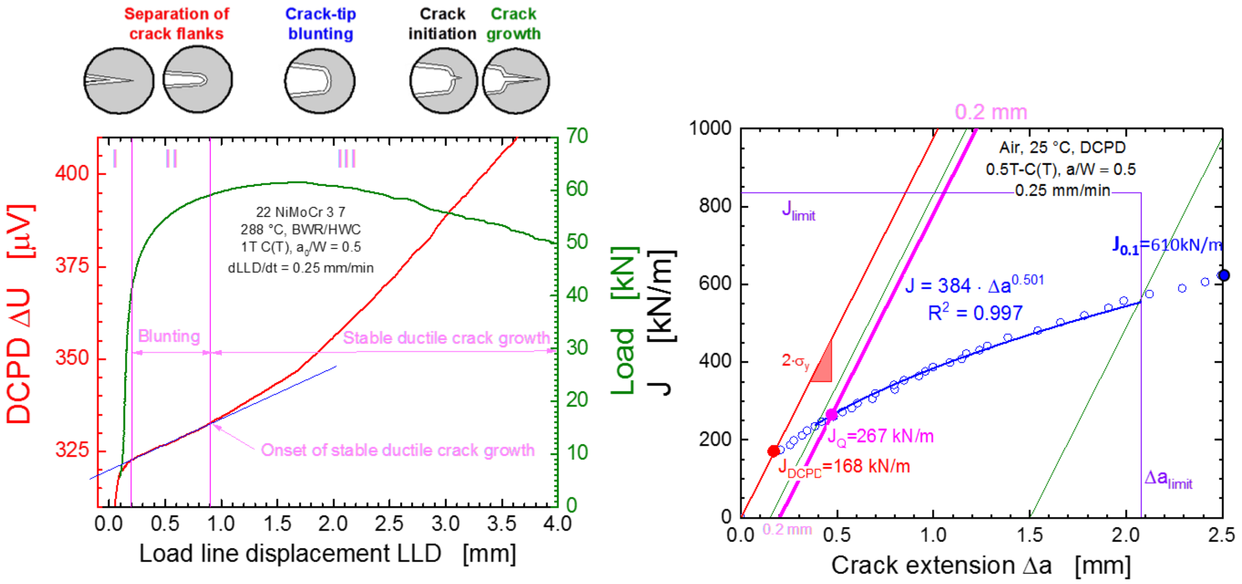

Figure 55: Example of load-line displacement, DCPD recording and the evaluated *J-R* curve.

Previous control tests in air with the conventional ULC and the DCPD method on the same load train revealed very similar J_Q and *J-R* curves, which were within the typical specimen-to-specimen scatter band for a given method. The crack length measurements by DCPD were much more reliable than with the ULC, in particular for small crack advances and in autoclaves with electrical isolations of the specimen by ZrO_2 rings in the pin holes of the load frame. Furthermore, unloading/reloading in ULC may affect the fracture behaviour in air and particular HTW. This was because of the modification of the crevice chemistry and closure effects (in case of high fracture surface roughness, slight out-of-midplane cracking or thick oxide film on the crack flanks). The *J-R* curves by DCPD method were validated with the comparison to normalization method [161] at PSI as well, which revealed the same results within the typical specimen to specimen scatter. Other methods like the measurement of stretch zone width for J_Q determination were not working well in HTW, since a clear stretch zone can not be observed in HTW (in particular at the lower loading rates). EPFM tests in air at FZ Rossendorf [162] with 1T-C(T) specimens with Biblis C material from a very close location as in this project, revealed the same J_Q values as at PSI. Therefore, there is sufficient confidence in the ability of the modified EPFM procedure to reveal potential HTW effects on the fracture resistance.

2.2.2.3 Tearing instabilities

In some EPFM tests, tearing instabilities with sudden large load drops and large crack advances were observed. They occurred normally beyond the peak load and after a certain preceding stable ductile crack growth in 0.5T- and 1T-C(T) specimens in both HTW and air. This phenomenon occurred particularly in HT1 and KS12 materials with lower tearing modulus, which may erroneously be interpreted as an unstable brittle crack extension (e.g., due to HE), but actually is a mechanical instability of the specimen/testing machine system and related to the low stiffness of the used loading machine. The tearing instability is related to the used specimen-loading system and not to an inherent unstable cracking behaviour of the material. In contrast to HT1, the instability phenomenon was not observed in the corresponding Biblis C base metal in spite of lower yield stress (and higher peak load to plastic limit load ratios).

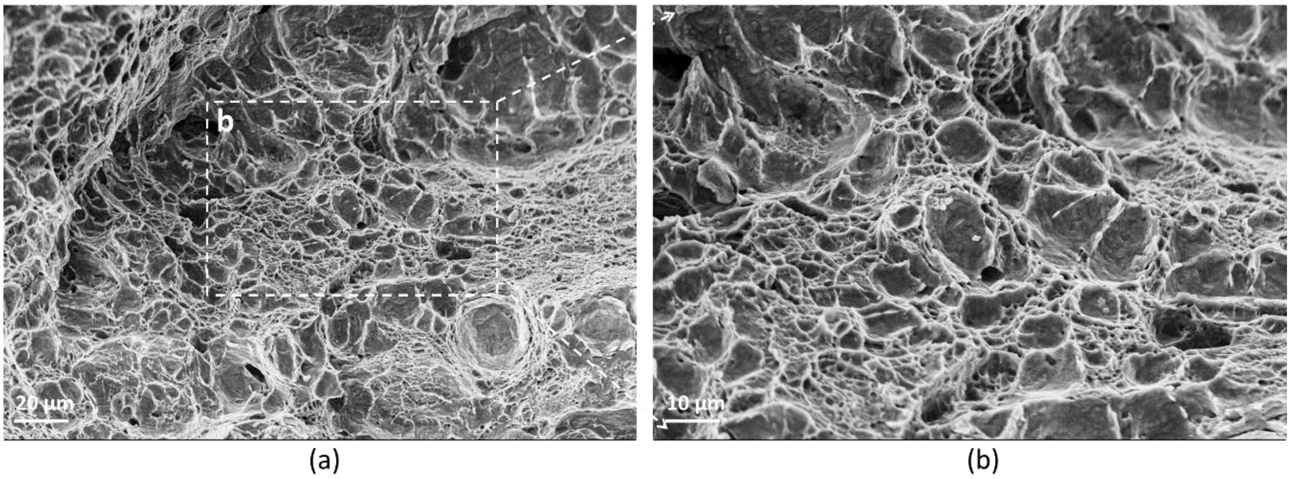

(a) (b)

Figure 56: (a) and (b) Fractographs showing ductile crack growth in CGHAZ material (HT1) during EPFM test in PWR HTW at 288 °C with a loading rate of 25 µm/min with sudden and large load drop.

Figure 56 shows a fractographic example of unstable crack extension in the CGHAZ material HT1. The fracture surface showed predominantly ductile crack growth (mainly MVC). There was no fractographic indication for macroscopic brittle cracking or sudden failure of un-cracked ligaments.

The J_Q values at initiation of ductile crack growth in these tests were not affected and were still valid. These load drops should be differentiated from smaller repetitive load drops (similar to serrations in tensile tests) that were sometimes observed beyond the peak load, in particular in steels with high DSA susceptibility in the DSA temperature-strain rate range (Figure 57 (a)).

To demonstrate the tearing instability, which resulted in the significant unstable rapid ductile crack extensions beyond the peak load, a non-dimensional quantity called tearing modulus, *T*, is introduced in Eq. (21) [163].

$$T = (E/\sigma_Y^2) \cdot (dJ/da) \tag{21}$$

where *E* is the Young's modulus and σ_Y the flow stress.

The material tearing resistance modulus T_{mat} is calculated by taking the slope dJ_R/da of the material J_I-R curve beyond J_{IC}. The applied tearing modulus T_{app} as crack driving force is calculated as the rate of change of the applied *J* ("non-linear" energy release rate) per unit crack extension $(dJ/da)_{\delta tot}$ at constant total displacement δ_{tot}. T_{app} depends on crack and specimen size/geometry, type of loading (displacement or load controlled), and the stiffness of the loading system. Tearing instability results from a lack of balance between the rate of increase of applied driving force and that of material resistance to crack growth. Tearing instability is not a material property, but also dependent on the used loading system/mode and specimen/crack configuration. Instability occurs, when the tearing resistance modulus T_{mat} of the material is smaller than the applied tearing modulus T_{app} as crack driving force [164],

$$T_{mat} < T_{app} \tag{22}$$

With the further refinement of theory, instability calculation criteria were simplified. Instability is reached, when Q ($Q = -\mathrm{d}P/\mathrm{d}\delta$) exceeds the stiffness of the whole loading system, K_M [165]:

$$Q = -\mathrm{d}P/\mathrm{d}v > K_M \tag{23}$$

(P = applied load and v = LLD of specimen)

The theory of tearing instability is based on the relationship between the loading system stiffness and the compliance of the specimen. Specimen compliance depends on strength level, specimen and pre-crack size. To verify the theory of tearing instability and its direct relation to the phenomenon with sudden load drop/DCPD potential increase/unstable crack growth, two experiments with HT1 material with and without load drops were analysed with the Q-K_M relation. Figure 57 (a), (b) and (c) show the load - pull rod stroke displacement curve, load - specimen LLD curve and the Q-K_M curve of 0.5T-C(T) specimen (B = 12.5 mm) with an air fatigue pre-crack length a_0 of 13.5 mm, where no instability was observed after reaching the peak load. Figure 57 (d), (e) and (f) show the corresponding curves for a specimen with an air fatigue pre-crack length a_0 of 13.2 mm with two instability sequences during the test. For the test with the longer pre-crack length, the Q value was always lower than the loading system stiffness. For the specimen with the shorter pre-crack and lower initial compliance, the two tearing instabilities exactly took place at the same time when the Q exceeded K_M. This analysis confirms that the phenomenon with sudden load drop/DCPD potential increase was related to tearing instabilities.

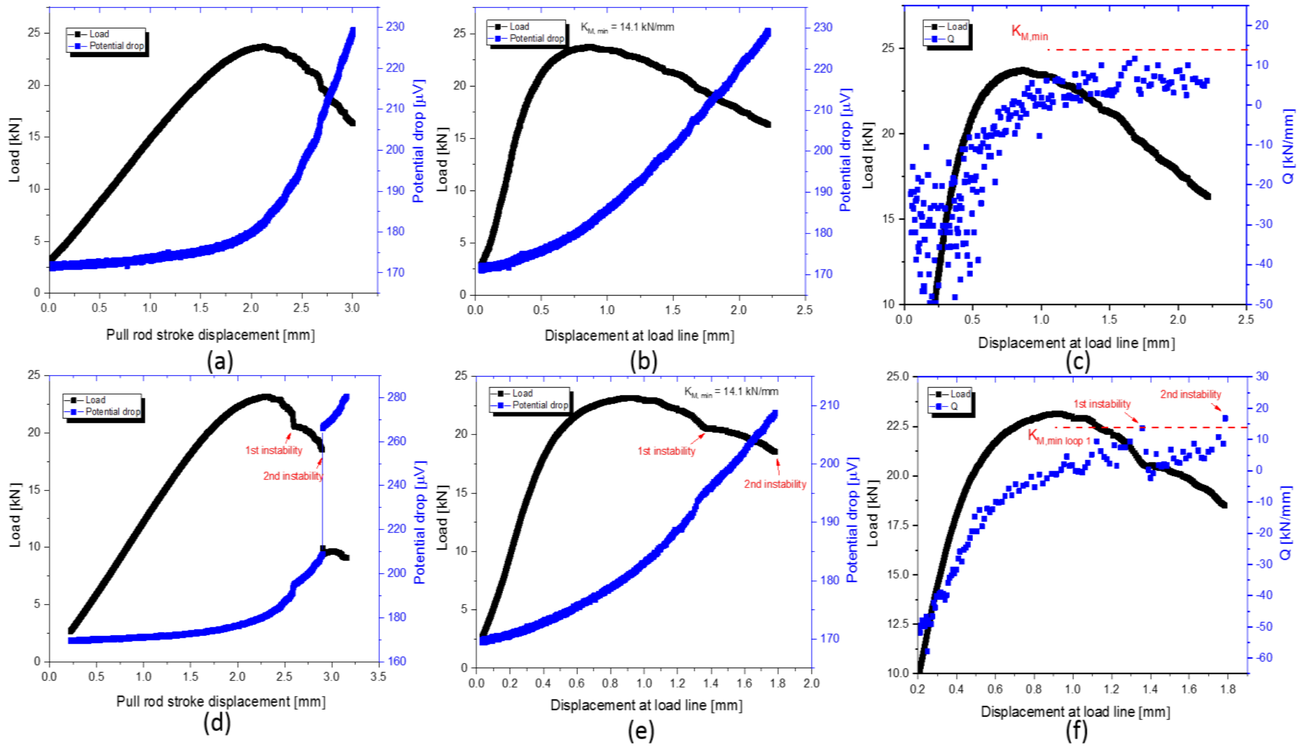

Figure 57: (a), (b) and (c) Load - pull rod stroke displacement curve, load - specimen load line displacement curve and the Q-K_M curve of HT1 material tested with a loading rate of 2.5 µm/min at 288 °C in PWR HTW (air fatigue pre-crack a_o = 13.5 mm) without tearing instabilities; (d), (e) and (f) the corresponding curves of HT1 material tested with loading rate of 2.5 µm/min at 288 °C in air (air fatigue pre-crack length a_o = 13.2 mm) with two instability sequences.

2.3 Post-test characterizations

The fracture mode/path and deformation mechanisms were systematically studied by optical light and various electron microscopy techniques. Additional techniques like instrumented nano-indentation, scanning transmission electron microscopy (TEM) or thermal desorption spectroscopy (TDS), partially in collaborations with external partners, were also used, but not covered in this manuscript.

At the beginning, the complete specimens were broken open by brittle fracture after cooling in liquid nitrogen for crack length measurements and fractographic investigations. The crack advance over the specimen surface was quite symmetrical to the specimen mid-plane. It usually had a straight or very slight thumbnail shape. Later on, all fracture mechanics samples were cut into two parts along the mid-plane using electrical discharge machining (EDM). One half was broken open along the crack propagation plane in liquid nitrogen and used for the crack size measurement to calculate fracture resistance. This part is used for the fractographic analysis on the fracture surface as well. The crack-tip region of the other half was machined out by EDM for crack-tip analysis using Electron Backscatter Diffraction (EBSD), Electron Channelling Contrast Imaging (ECCI) and EDX. Specimens were mechanically ground using water-proof SiC abrasive papers (Buehler CarbiMet^{TM}) with grit numbers of 1200, 2400 and 4000. The specimens were further polished with 3 μm, 1 μm (Buehler MetaDi^{TM}), 0.25 μm (Struers, DP) polishing suspension and 0.02 μm non-crystallizing amorphous colloidal silica suspension to ensure a deformation-free surface (Buehler MasterMet^{TM} 2). The specimens were carefully cleaned in the sequence of ethanol-acetone-ethanol before drying.

To reveal the micro-fracographic details, it was necessary to remove the oxide film grown during the HTW loop tests and/or deposits through the EDM process. Therefore, the oxide film were removed by galvanostatic reduction in an ENDOX bath, while the underlying metal matrix was cathodically protected. A constant current density of 0.15 A/cm^2 was used for an optimal performance. Upon immersing the samples into the ENDOX solution, a few drops of 5 to 10% Kodak Photo-Flo 200 solution was dipped on the samples as a wetting agent.

The SEM images were obtained from the Field Emission SEM - Zeiss ULTRA 55 in PSI. This SEM was equipped with EDX system using EDAX APOLLO XV Silicon Drift Detector (resolution: < 128 eV, 10 mm^2 SDD chip, elevation angle = 35°) and an EBSD system using EDAX Hikari Camera (450 Hz, 0.31 MPixel). With respect to TEM, ECCI and EBSD have much larger observation areas and simpler sample preparation and can work on bulk samples, but they have a lower spatial resolution. For post-characterization, ECCI and EBSD can be utilized to evaluate the fracture path, mode and site as well as dislocation density and dislocation arrangements at the crack tip of tested samples [166]. ECCI [167] is an imaging technique in SEM, based on the dependence of the backscatter electron signal on the orientation of crystal lattice planes with respect to incident electron beam due to electron channelling. It can be used for direct observation of lattice defects, such as dislocations, deformation twins and stacking faults, and their correlated quantitative characterization. The good ECCI image is obtained, when the matrix crystal is in Bragg condition. ECCI analyses were performed using solid-state four-quadrant detector (angular selective). ECCI was conducted at 15 to 25 kV acceleration voltage with working distance of 4 to 6 mm.

EBSD was carried out for the investigation of grain morphology and strain distribution [168]. It was conducted at 20 kV acceleration voltage with a 70^{o} tilting angle (120 μm aperture in high current mode) with the EDAX detector and TSL OIM Analysis 7 software. Two different options of the commercial EBSD strain analysis were used [169], grain reference orientation deviation (GROD) and KAM maps [170]. The KAM is a parameter that quantifies the average misorientation around a reference measurement point with respect to a defined set of nearest neighbour points. It has been suggested as a measure of the geometrically necessary dislocation density. Hence, it can qualitatively assess the local plastic strain related to deformation gradients. The GROD angle, which displays the misorientation angle of a point from the grain's average orientation, which helps to show areas in the deformed microstructure. EBSD is used for phase determination as well [171]. Austenite and ferrite can be easily distinguished by EBSD since they have different crystallographic structure. Ferrite/bainite/martensite can be distinguished with different image quality and different density of particular GBs. However, this method can not lead to unique phase discrimination because the image quality depend on additional factors as contamination, sample preparation or grain orientation.

EDX uses the characteristic X-rays that are emitted by the excitation of inner-shell atoms with the interaction of incident electrons. The photon energy and X-ray intensity curve (EDX spectrum) is obtained after an EDX analysis. This allows elemental analysis and chemical characterization through the peak location and energy in the curve, since each set of characteristic lines corresponds to a single element. In light of different experimental objectives, point analysis and elemental mapping can be applied to acquire the information on a specific point, or the distribution of the constituent element in a specific area. EDX was used here for the qualitative and semi-quantitative determinations of chemical compositions. It was conducted at an acceleration voltage of 20 kV with 120 μm aperture at working distance of 8 to 9.5 mm.

Chapter 3 Results and discussion

3.1 Fracture behaviour of RPV steels in air

In air, the upper shelf fracture initiation resistance J_Q shifted to higher temperatures with increasing loading rate for all RPV steels investigated in this work (Figure 58). J_Q slightly decreased with increasing temperature with a potential minimum at intermediate temperatures for the steels with high DSA susceptibility. This minimum occurred in the same region as the serrations and the maximum in negative strain rate sensitivity in tensile tests (Figure 59). At 250 and 288 °C, the fracture initiation resistance J_Q of all steels increased with decreasing loading rate due to DSA and the increase was slightly higher at 288 °C for the high DSA steels. Except for KS 12 (J_Q = 115 kN/m $\rightarrow$ K_{JC} = 156 MPa·m$^{1/2}$), the toughness of the different base metals was similar (J_Q = 320 kN/m ± 20% $\rightarrow$ K_{JC} = 260 MPa·m$^{1/2}$ ± 10% at 288 °C with the standard loading rates of 0.25 to 0.35 mm/min). The highest J_Q values were for the steels with high DSA susceptibility and low sulphur content. The simulated CGHAZ HT1 had a slightly lower toughness (J_Q = 228 kN/m $\rightarrow$ K_{JC} = 220 MPa·m$^{1/2}$) only. Serrations (small load drops) in load-COD curve above peak load were occasionally observed, in particular for the high DSA steels. The specimen size (0.5T vs. 1T C(T) specimens) and constraints had little effect on J_Q. The specimen-to-specimen variation in J_Q for given conditions for a given steel was in the range of ≤ ~ 10%. A significantly higher variation is expected for the inhomogeneous steel KS12 (~ 30%) and the simulated CGHAZ. The J_{DCPD} and the tearing resistance $J_{0.1}$ usually showed the same parameter trends as J_Q.

In all steels, fracture occurred by ductile transgranular tearing by MVC in the air. Apart from KS12, there was very little difference in the ductile fracture appearance between the different steels and under the investigated temperatures and strain rates. The crack path usually shares a zig-zag shape in all conditions.

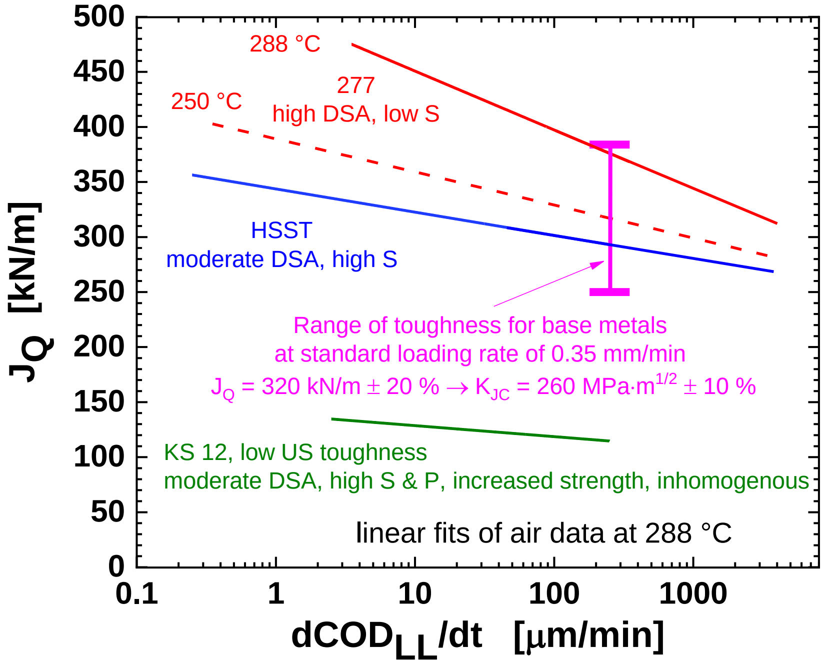

Figure 58: Effect of loading rate on fracture initiation resistance J_Q in air.

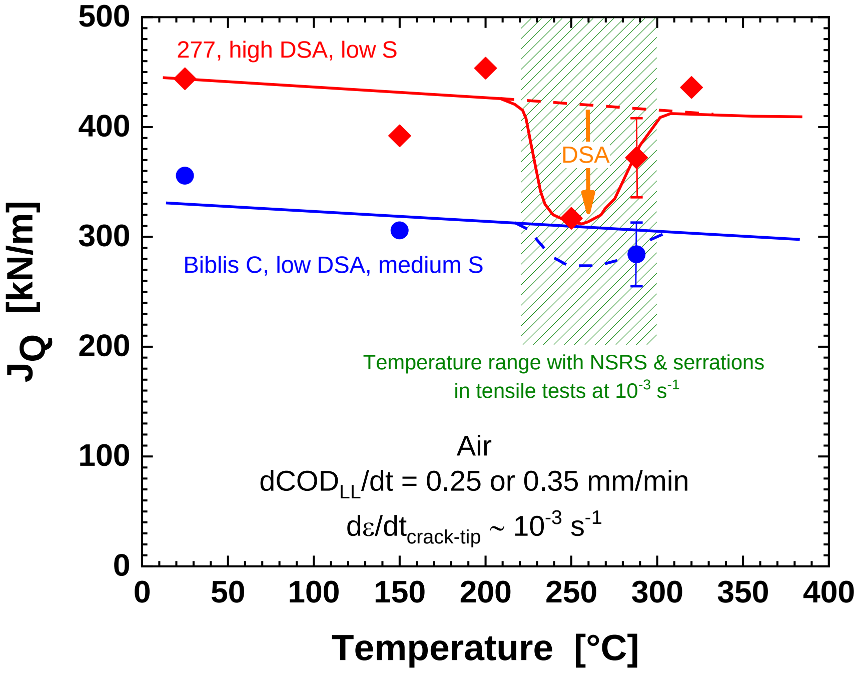

Figure 59: Effect of temperature on fracture initiation resistance J_Q in air.

3.2 Fracture behaviour of Biblis C steels as reference material

The fracture behaviour of Biblis C base metal with low sulphur content and low DSA and EAC susceptibilities in HTW was systematically characterized in a previous project at PSI and it is the reference material for this study. Exposure to HTW (BWR/HWC, PWR, BWR/NWC, nitrogenated HTW, 288 or 150 °C), or with additional electrochemical in-situ hydrogen charging (PWR) for 12 days (up to 32 days) did not reduce the fracture initiation and tearing resistance of the Biblis C base metal (Figure 60) in the investigated loading rate range. The fracture initiation resistance was within the typical specimen-to-specimen variation/scatter. However, a clear change in fracture morphology was observed that was very similar to that in EPFM and tensile tests in air after hydrogen pre-charging. This suggests that the hydrogen concentration in the crack-tip process zone was only slightly below the critical threshold for the onset of macroscopic effects in this material. Ductile fracture by MVC was observed for air tests without hydrogen charging. In contrast, tests in BWR and PWR environments resulted in higher roughness of the fracture surface than that after experiments in air due to formation of higher amounts of macro-voids, secondary cracks and QC facets on the fracture surface. In addition, pre-oxidation period (1 day up to 34 days) and loading type (constant or cyclic load with or without fatigue crack growth) during pre-oxidation phase had no impact.

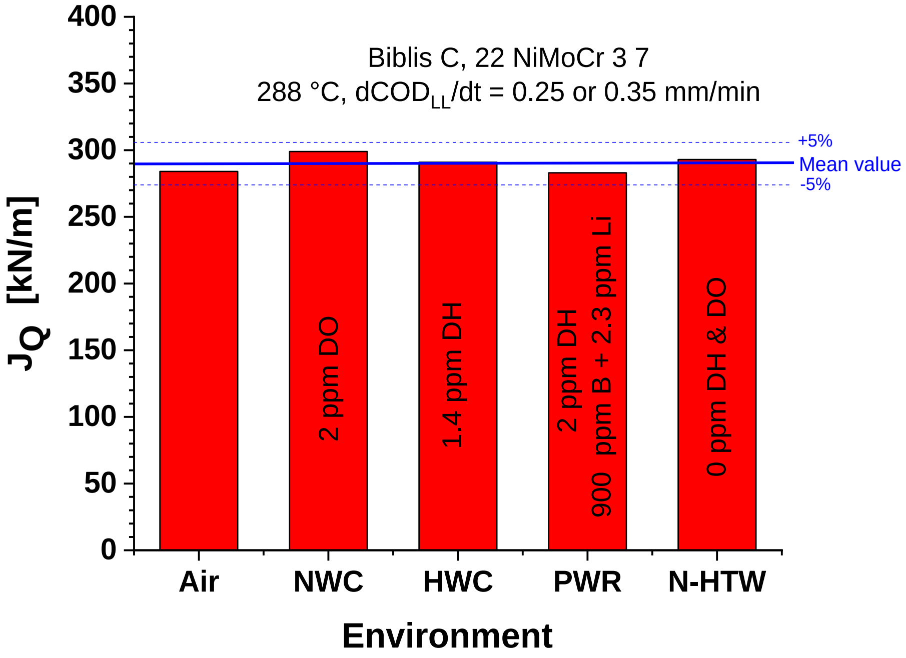

Figure 60: Fracture initiation resistance J_Q of Biblis C base metal in air and various HTW environments at 288 °C with a loading rate of 0.25 to 0.35 mm/min.

3.3 Effect of high yield stress

EPFM tests in HTW with the simulated CGHAZ of the Biblis C material with high yield stress at 288 °C indicated a moderate reduction of fracture initiation resistance (up to a maximum of 37%) in simulated PWR (Figure 61) and HWC environments (Figure 62) at slow loading rates. The environmental reduction increased with decreasing loading rates. The fracture initiation resistance in PWR or HWC environments was consistently lower than in the corresponding air tests, which is different from the test results of Biblis C base metal materials.

The increase of fracture initiation resistance with decreasing loading rate was similar for the Biblis C BM and simulated CGHAZ materials, which indicate a similar DSA susceptibility (Figure 63) in both structures. This suggests that the environmental reduction was mainly due to the effect of yield stress. Stronger effect in CGHAZ was also observed in tensile tests with hydrogen pre-charging (Figure 32 to Figure 34) [5]. The HE in tensile tests almost completely disappeared after annealing of the simulated CGHAZ material for 72 h at 625 °C (instead of 1 h), which reduced its yield stress from 740 to 460 MPa (similar level as in the unaffected base metal). This further confirmed that the HE in the CGHAZ is rather due to the higher yield stress than to the bigger prior-austenite grain size. As shown in Figure 62, the environmental reduction effect in HWC is higher than in NWC (low-sulphur crevice conditions prevails), which is due to higher DH and hydrogen availability in HWC.

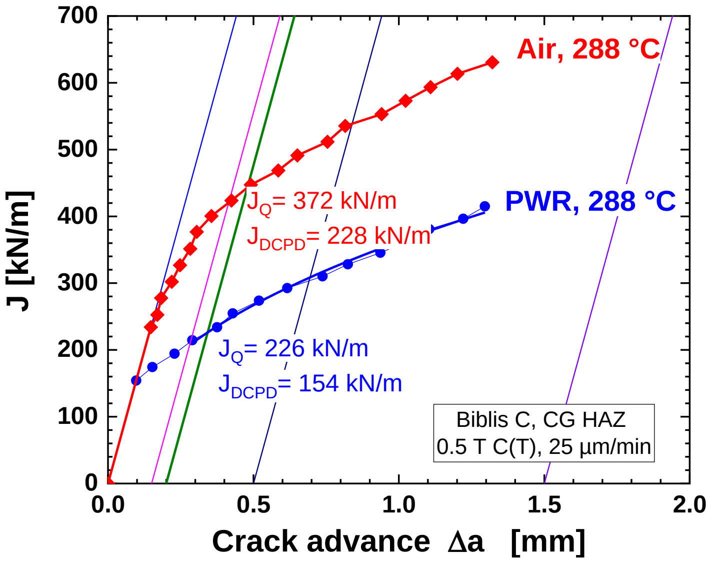

Figure 61: Example of fracture resistance curves of Biblis CGHAZ material in air and PWR environment at 288 °C. Reduction of fracture initiation resistance in PWR environment.

Since J_Q significantly increased with decreasing loading rate in air (due to DSA), the J_Q values with strongest reduction of fracture initiation resistance in HTW at very slow loading rates were still higher or in the range of the fracture initiation resistance in air at the standard loading rate of 0.25 to 0.35 mm/min. Therefore, the environmental reduction partially or fully compensated the increase of fracture initiation resistance by DSA in the investigated temperature-loading rate range. Nevertheless, the results clearly show that higher yield stress may result in stronger environmental effects. The higher yield stress results in a higher peak and hydrostatic stress ahead of crack tip and this favours the hydrogen enrichment in this region. Furthermore, due to the smaller plastic zone size, the available hydrogen is concentrated at a smaller volume and diffusion distances for hydrogen to the critical region in the process zone are smaller as well.

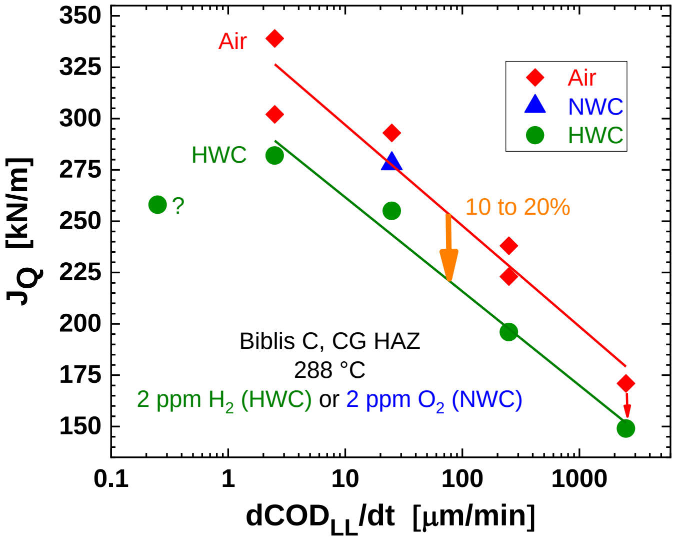

Figure 62: Moderate reduction in fracture initiation resistance in Biblis C CGHAZ in BWR/HWC environment at various loading rates.

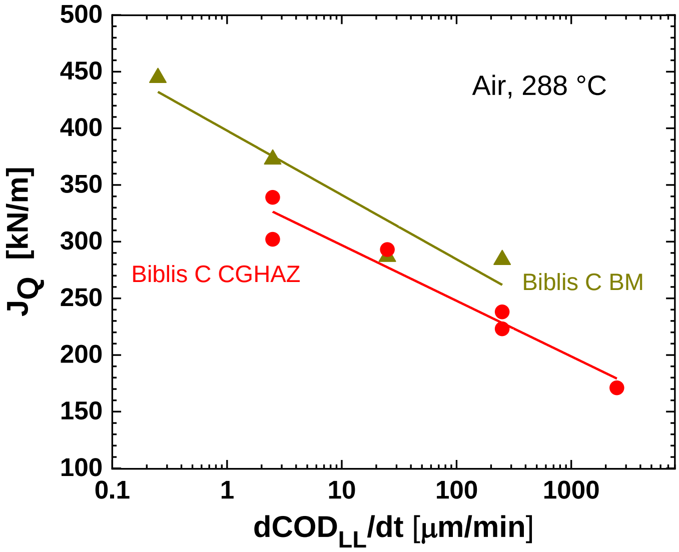

Figure 63: Effect of loading rate on fracture initiation resistance J_Q of Biblis C base metal and CGHAZ in air.

3.4 Effect of high dynamic strain aging susceptibility

Tensile tests in air with hydrogen pre-charging at PSI revealed a potential synergy between DSA and HE in RPV steel, probably due to the localization of plastic deformation (the combined effects of DSA and the shielding effect of hydrogen), as shown in Section 1.4. The strain rate range and amplitude of HE effects were significantly amplified by high DSA susceptibility in the DSA temperature-strain rate range. No effect of steel sulphur content (MnS inclusions as potential hydrogen traps) was observed in these tests. The HSST steel with high sulphur content of 0.018 wt.% and moderate DSA susceptibility only showed moderate HE, whereas the two RPV steels 277 and 508 with low sulphur content of 0.004 wt.%, but high DSA susceptibility, revealed significant HE. The HE degree and of hydrogen-induced softening correlated fairly well with the DSA susceptibility index (Figure 64). Furthermore, the limited data suggests that a high free interstitial nitrogen content (low aluminium and AlN content) may further increase the hydrogen effects at similar DSA susceptibilities.

The fracture behaviour of four RPV steels (Biblis C base metal, HSST, 277 and 508 with low, medium and high DSA susceptibilities, respectively) was investigated and compared in hydrogenated HTW at loading rates of 0.035 and 0.35 mm/min. As previously mentioned, the Biblis C base metal with low DSA susceptibility and low sulphur content did not reveal any environmental effects on fracture resistance (Figure 60). The environmental reduction of fracture initiation and tearing resistance was highest in the two RPV steels with high DSA susceptibility. This environmental reduction correlated fairly well with the different degrees of DSA susceptibility and the hydrogen-induced softening in tensile tests with hydrogen pre-charging (Figure 64 and Figure 65), although the effects on fracture resistance were smaller than anticipation based on the tensile tests. In contrast to oxidizing conditions (see Section 3.5), steel sulphur content played no role in hydrogenated HTW. To further elucidate the interaction of DSA with HTW and hydrogen effects and the underlying mechanisms, the fracture behaviour of the two RPV steels, 277 and 508, with high DSA susceptibility was therefore systematically studied at different loading rates, temperatures and water chemistries.

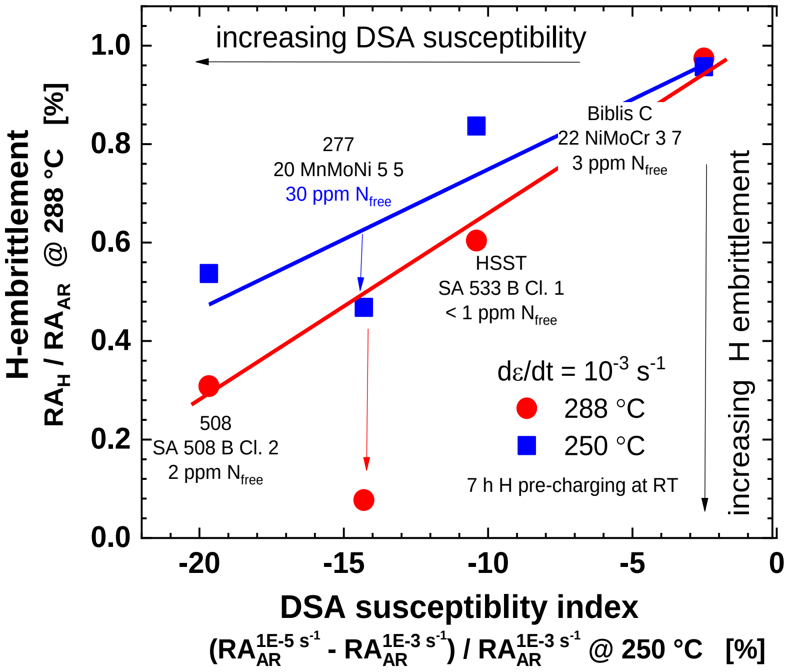

Figure 64: Correlation between hydrogen embrittlement and DSA susceptibility in tensile tests for the RPV steels investigated in this work.

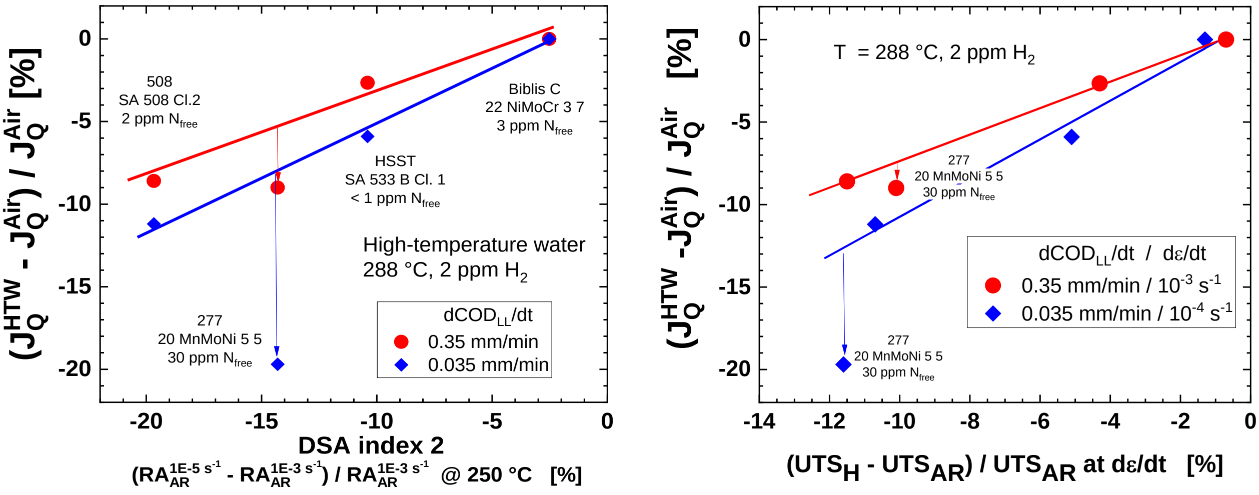

(a) (b)

Figure 65: (a) Correlation between environmental reduction of fracture initiation resistance and DSA susceptibility of different RPV steels in hydrogenated HTW; (b) correlation between environmental reduction of fracture initiation resistance in hydrogenated HTW and hydrogen-induced softening in tensile tests with hydrogen pre-charged specimens under identical (crack-tip) strain rate conditions.

3.4.1 Fracture behaviour of 277 material

Effect of loading rate

EPFM tests of 1T-C(T) 277 base metal specimens were performed in hydrogenated HTW and air with loading rates of 0.35, 35 and 3500 µm/min at 250 °C. In Figure 66 (a) and (c), the higher fracture initiation resistance at lower loading rates in air was due to the hardening and negative strain rate sensitivity by DSA. The higher fracture initiation resistance J_Q values hereby correlated very well with the higher peak loads in the corresponding load-displacement curves. In hydrogenated HTW, there was a clear reduction in fracture initiation (J_Q) and tearing resistance ($J_{0.1}$), where the reduction increased with the decreasing loading rate. The Biblis C base metal material with low DSA susceptibility, but otherwise similar bainitic microstructure and mechanical properties, did not reveal any environmental effects on fracture resistance under the identical conditions [63].

For all tests in air and the experiments in HWC with loading rates $\geq$ 35 µm/min at 250 °C, the fracture mode was mainly ductile by MVC (Figure 67 (a) and (b)). On the other hand, a very different fracture mode was observed in HWC at the very slow loading rate of 0.35 µm/min (Figure 67 (c)). Here the crack first initiated in a stable ductile mode by MVC (Figure 67 (d)) but then propagated by SICC (Figure 67 (e)) with “high-sulphur” EAC crack growth rate [92] at higher J levels. In the COD-load curve during the EPFM test, several small unloading can be seen particularly at the end of the test arising from fast local crack growth (retarded failure of large un-cracked ligaments, e.g., of large steps between the individual fan-shaped SICC cracks). These unloadings can result in a temporary drop of J and stop of SICC crack growth. Then the crack growth has to re-initiate by MVC, when J is increasing again.

The SICC crack growth rate and fractographic appearance was identical to those in slow rising load tests at the same loading rate in oxygenated HTW, where sub-critical SICC initiated at much lower K_I values (30 to 40 MPa·m$^{1/2}$ in oxygenated HTW vs. > 200 MPa·m$^{1/2}$ in HWC) [94], as shown in Figure 68 (a) and (b). The ductile crack growth rates in HWC were a factor of 1.13 higher than the ductile crack growth in air at 35 µm/min. Crack growth rate (including SICC) in HTW was a factor of ~ 2.5 higher than the ductile crack growth in air at 0.35 µm/min. The strong reduction in tearing resistance and increase in crack growth rate at the very slow loading rate of 0.35 µm/min is mainly caused by SICC crack growth by dissolution and not by a “physical” reduction of the fracture resistance. The fracture initiation J_Q value was still valid at 0.35 µm/min, since the crack initiated in a stable ductile manner. Fracture initiation and tearing resistance usually showed the same parameter trends and the relative environmental reduction in initiation and tearing resistance was similar. The environmental reduction of the tearing resistance $J_{\Delta a}$ only slightly increased with further crack advance Δa as long as no SICC occurred (Figure 69).

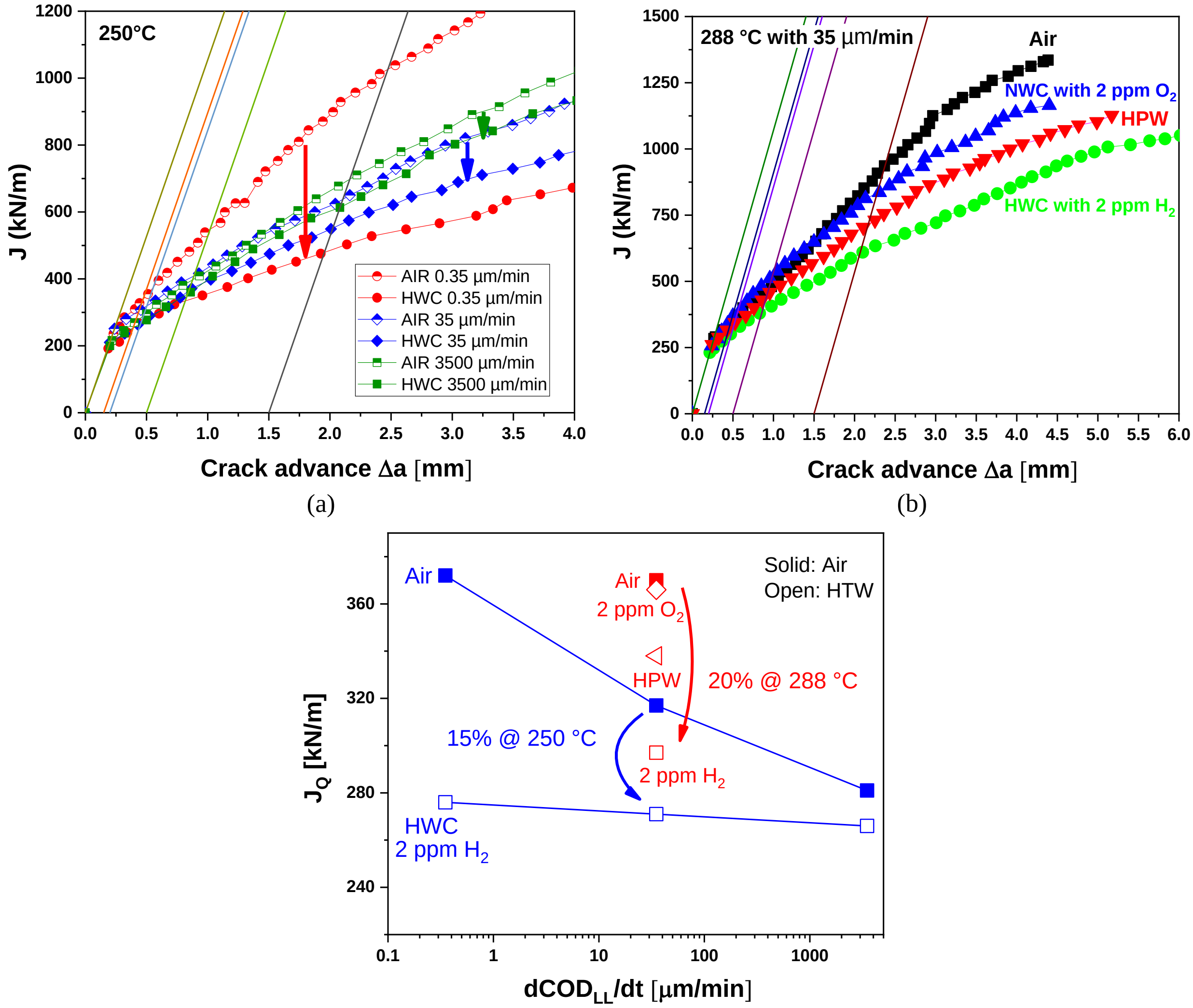

(a) (b)

(c)

Figure 66: (a) *J-R* curves of 277 material tested in hydrogenated high-temperature water and air at 250 °C with various loading rates (the arrows indicate the fracture resistance reduction from air to hydrogenated HTW); (b) *J-R* curves of 277 material tested in air and various HTW environments at 288 °C with 35 µm/min; (c) fracture initiation resistance of 277 in air and various HTW environments at 250 and 288 °C with various loading rates.

The observed behaviour is in line with EAC behaviour of RPV steels in HTW [28]. Sub-critical SICC may occur in RPV steels in HTW at slow crack-tip strain rates ≤ ~ 10^{-3} s^{-1} ($dCOD_{LL}/dt$ ≤ ~ 300 µm/min), if an aggressive occluded "high-sulphur" crack crevice chemistry is simultaneously established. The sulphides in the crack crevice environment strongly retard the repassivation after an oxide film rupture and increase the EAC crack advance by anodic dissolution. The “high-sulphur” crack crevice chemistry arises from the dissolution of the MnS inclusions that are intersected by the crack flanks and growing crack front or from the enrichment of sulphides and sulphate as impurities in the bulk environment. In oxygenated HTW, the sulphides are strongly enriched in the crack crevice environment by migration due to the potential gradient between the oxygenated crack mouth and oxygen-depleted crack tip (“anion pump”). The “high-sulphur” conditions are usually easily established in NWC.

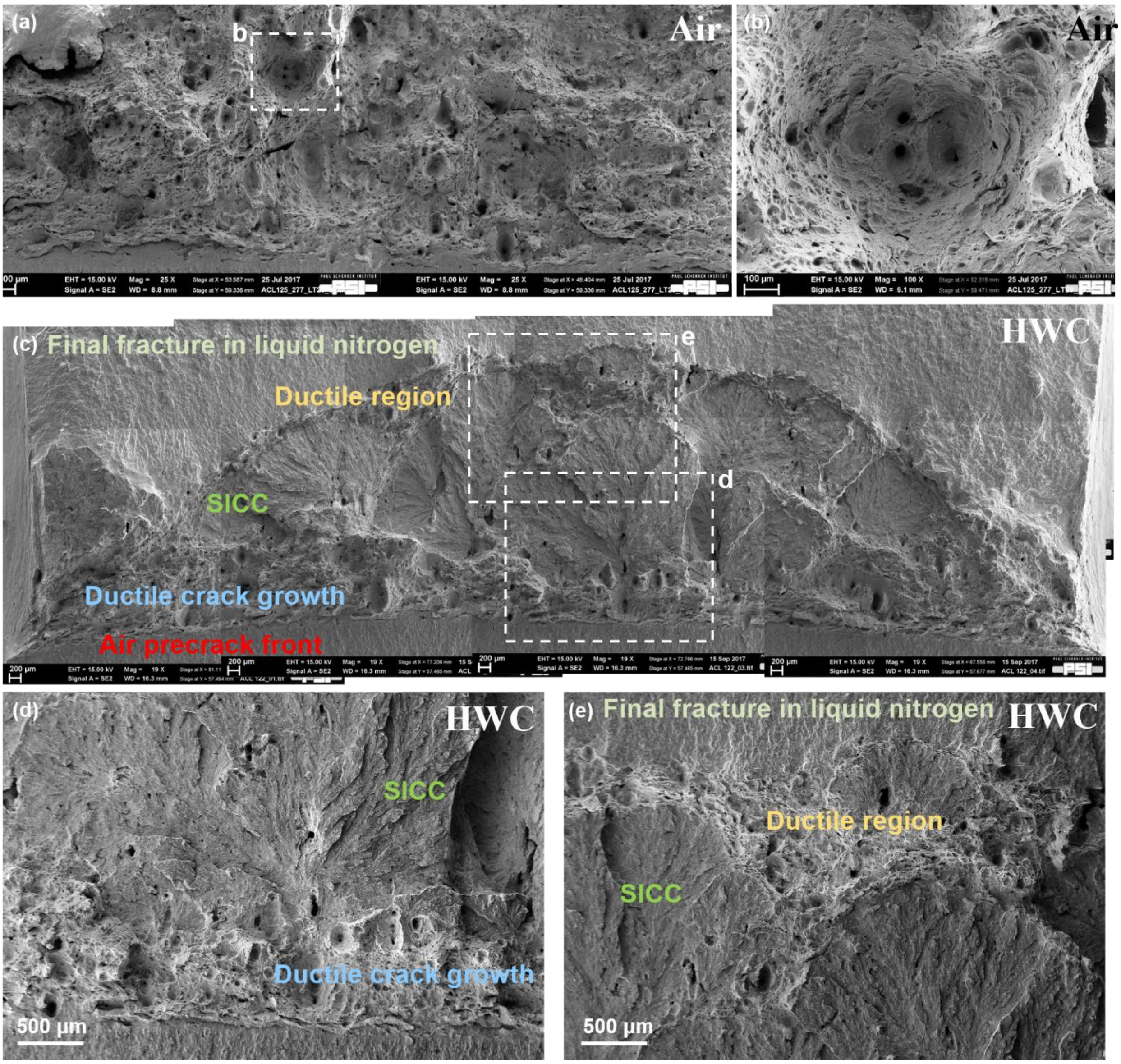
(a)
b
Air
(b)
Air
(c) Final fracture in liquid nitrogen
e
HWC
Ductile region
SICC
d
Ductile crack growth
Air precrack front
(d)
HWC
SICC
Ductile crack growth
500 µm
(e) Final fracture in liquid nitrogen
HWC
Ductile region
SICC
500 µm

Figure 67: (a) Fracture surface of 277 steel tested with 0.35 µm/min in air at 250 °C; (b) magnification of inset *b* in (a); (c) fracture surface of 277 steel tested with 0.35 µm/min in HTW with 2 ppm H_2 at 250 °C; (d) and (e) magnifications of insets *d* and *e* in (c).

Aggressive high-sulphur crevice conditions can also be achieved at low ECP in HWC environment (where the potential at crack mouth and crack tip are similar/low and migration is absent). The specific conditions can be achieved by the exposure and dissolution of fresh MnS inclusions and the slow transport of the sulphur anions out of the crack by diffusion, if the crack is growing with an adequately fast rate. Therefore, in hydrogenated water, ductile crack initiation and some ductile crack growth has to precede the onset of SICC to establish this dynamic equilibrium. A significantly higher *K* or *J* is necessary to achieve this situation at low ECP without sulphur-anion enrichment by the anion pump. However, if it is established, the same SICC crack growth rates are observed for the same crack-tip strain rates in oxygenated and hydrogenated HTW. Such a behaviour was also observed in cyclic loading tests, where "high-sulphur" CF crack growth rates can be established in high-purity water at low ECP, if loading frequency and crack growth were high and fast enough [92]. Above loading rates of 300 μm/min, the ductile crack growth rates and resulting crack-tip strain rates in HTW are too high for EAC to occur (and significantly larger than the maximum EAC rates of ~ 5×10^{-7} m/s) and to establish high-sulphur crack crevice conditions [92]. At extremely slow loading rates in hydrogenated HWC environment, the production rate of sulphides by the exposure and dissolution of MnS by the growing crack is much slower than their diffusion rate out of the crack enclave. Therefore, the "high-sulphur" conditions cannot be established in this case either.

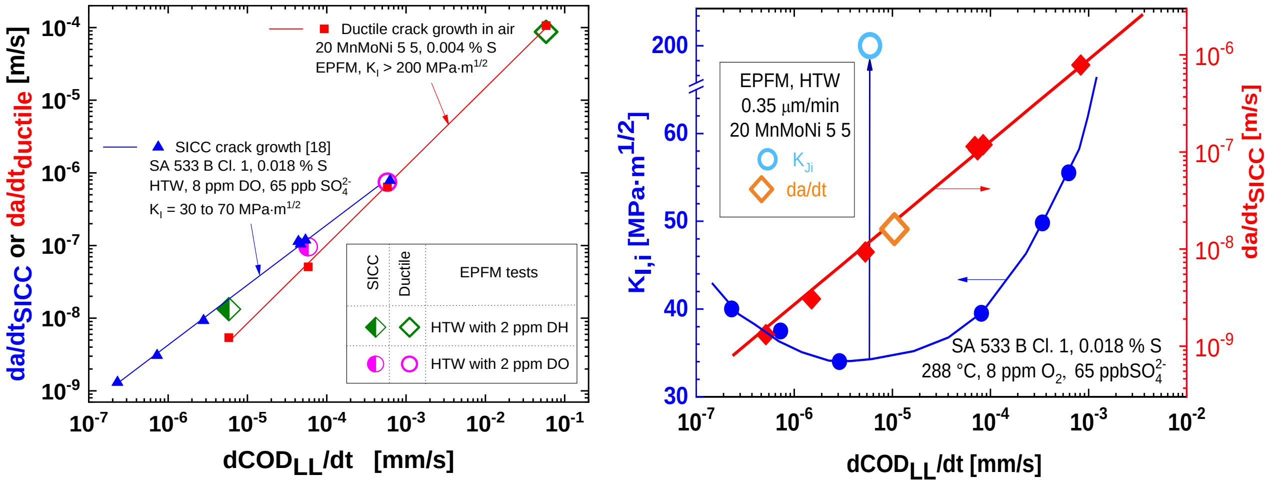

(a) (b)

Figure 68: (a) Comparison of ductile and SICC growth rates in EPFM and slow rising load tests under various conditions; (b) significantly higher K_J values at the onset of ductile fracture and subsequent SICC initiation in hydrogenated HTW than for SICC initiation in oxygenated HTW.

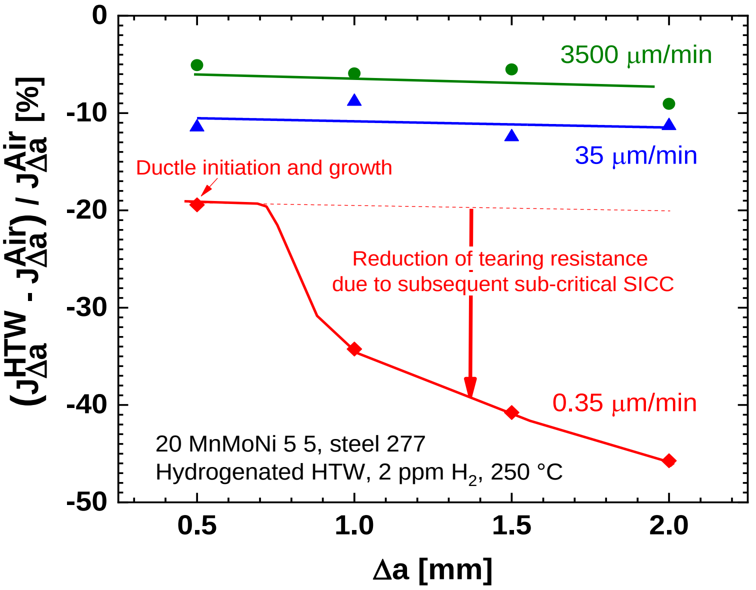

Figure 69: Relative reduction of tearing resistance $J_{\Delta a}$ for different crack advances Δ_a in the high DSA steel 277 in hydrogenated HTW at 250 °C with various loading rates. Onset of SICC at slowest loading rate of 0.35 μm/min after some preceding ductile crack growth.

Effect of water chemistry:

The effect of water chemistry was evaluated with EPFM tests in hydrogenated, oxygenated and nitrogenated HTW at 288 °C with loading rate of 35 μm/min, where the environmental reduction of fracture initiation resistance of 277 material was evident and SICC did not occur in all three HTW environments. As depicted in Figure 66 (b) and (c), all three HTW environments resulted in a reduction of fracture initiation and tearing resistance and an environmental acceleration of ductile crack growth rate compared to the EPFM test conducted in air, whereas the effects were most pronounced in the hydrogenated HTW. As indicated in Figure 70 (a), (b) and (c), the fracture morphology in oxygenated HTW resulted in lower roughness and smaller fraction of secondary cracks and QC facets (Figure 70 (e) to (g)) compared to the hydrogenated HTW, while the fracture surface after EPFM test in air was purely ductile (Figure 70 (d)). The fraction of secondary cracks, macro-void and QC facets for specimens tested in air, oxygenated and hydrogenated water was estimated to be 1.6, 1.8 and 2.5%, respectively.

In these three HTW environments, the crack crevice environments at the crack tip are all oxygen-free (since oxygen consumption on the crack flanks by corrosion is faster than its transport into the crack crevice by diffusion). The hydrogen concentration in the environment at the crack tip is similar or higher as in the bulk environment, since there is almost no consumption of hydrogen in the crack crevice and some hydrogen is produced by corrosion reactions. In hydrogenated HTW, the hydrogen content in the crack crevice is similar to that in the bulk environment and higher (two orders of magnitude or more) than in the oxygenated or nitrogenated HTW, where bulk environment is hydrogen-free. In the latter two cases, the crack crevice environment contains some hydrogen from local corrosion reactions and hydrolysis of metal cations. A slight acidification (slightly higher corrosion rate and increased hydrogen (H^+) content) may occur in oxygenated HTW by the sulphide enrichment by migration, but this effect is expected to be small for the low-sulphur steel 277. Nevertheless, the consistently lower environmental reduction of fracture resistance in oxygenated than in nitrogenated HTW is surprising in this context. The results suggested that the contribution from the DH in the crevice environment may be higher than that from the local corrosion reactions at the plastically strained crack tip in case of high hydrogen content in the bulk environment.

The results of EPFM tests in hydrogenated, oxygenated and nitrogenated HTW suggested that DSA effect dominates over crevice chemistry effect in the RPV steel with low sulphur content and high DSA susceptibility.

Effect of test temperature and pre-oxidation temperature:

The effect of temperature was investigated in hydrogenated HTW environment at a loading rate of 35 μm/min and temperature range of 150 to 320 °C (Figure 71). A moderate environmental reduction of fracture initiation (12 to 20%) and tearing resistance was observed in the whole temperature range. The 277 material showed a minimum in fracture initiation resistance in air and HTW at 250 °C and a maximum in environmental reduction of fracture initiation and tearing resistance at 288 °C under these conditions (Figure 71 (b) and (c)).

A maximum in negative strain rate sensitivity (and maximum in plastic strain localization tendency) due to DSA were observed in 277 material in tensile tests at this temperature range with strain rate of 10^{-4} s^{-1} in air [16]. Based on Sievert’s and Henry’s law [83][84], the absorbed hydrogen content in the bulk metal lattice at 150, 200, 250 and 320 °C is about 30, 50, 80 and 110% of that at 288 °C for a given DH concentration in the HTW. On the other hand, trapping efficiency strongly decreases with increasing temperature according to Arrhenius law and it is expected to become negligible above 350 to 400 °C. In combination with the DSA maximum at 250 to 288 °C at the tested loading rate, a potential peak of environmental effects around 290 °C is reasonable in this context.

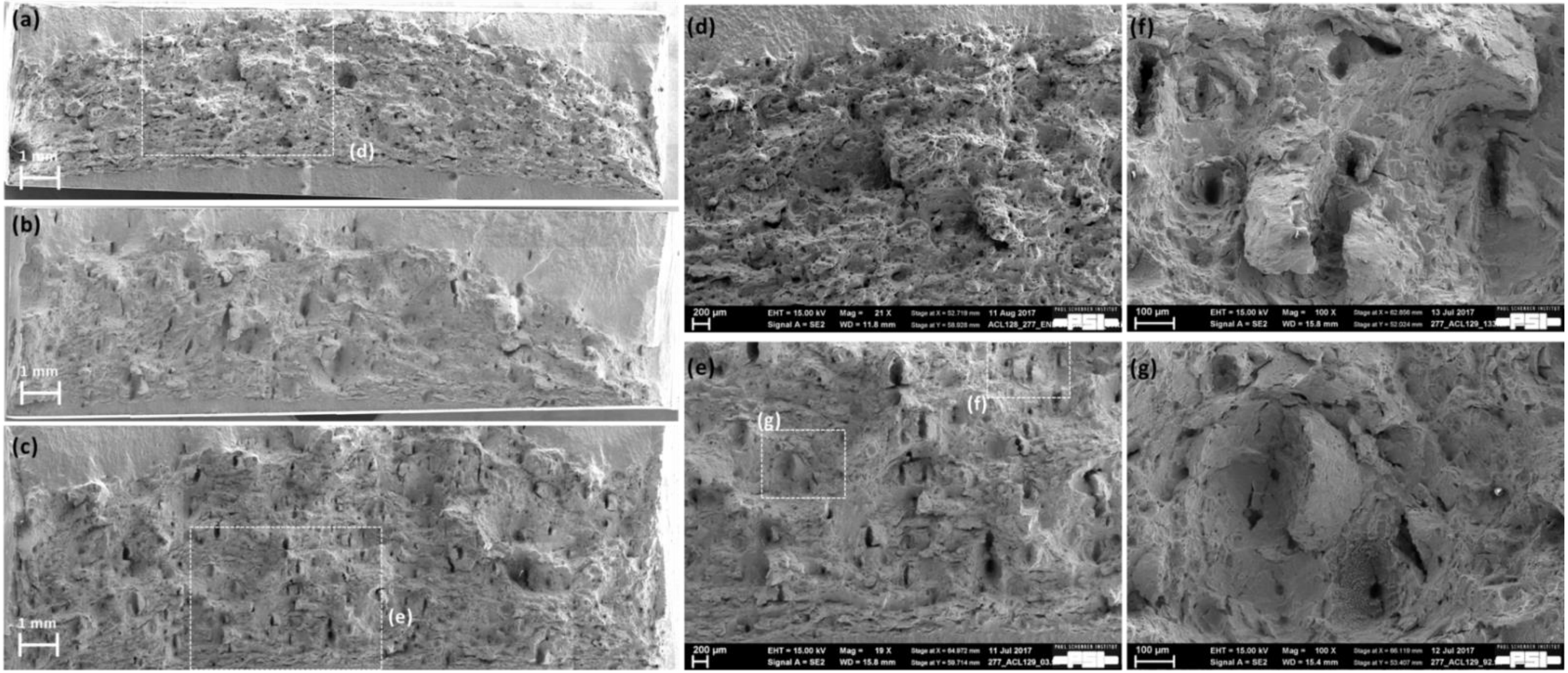
(a)
(d)
1 mm
(b)
1 mm
(c)
(e)
1 mm
(d)
200 µm
(f)
100 µm
(e)
(g)
(f)
200 µm
(g)
100 µm

Figure 70: Fracture surface of 277 steel tested with 35 µm/min at 288 °C in (a) air; (b) high-temperature water with 2 ppm O_2; (d) high-temperature water with 2 ppm H_2; (d) and (e) are magnifications of inset *d* and *e* in (a) and (c); (f) and (g) of inset *f* and *g* in (e).

In addition, the influence of pre-oxidation at 288 °C for one week on the fracture resistance in subsequent EPFM tests at lower temperatures of 200 and 250 °C was evaluated with a loading rate of 35 µm/min in hydrogenated HTW (Figure 71 (b)). The EPFM tests immediately started after the temperature was cooled down from 288 to 200 or 250 °C. A higher pre-oxidation temperature (288 °C) than in the subsequent EPFM test did not result in a change in the fracture initiation resistance and the environmental reduction of fracture initiation resistance, indicating that the evolving crack crevice chemistry during the EPFM test is the controlling factor in hydrogenated HTW.

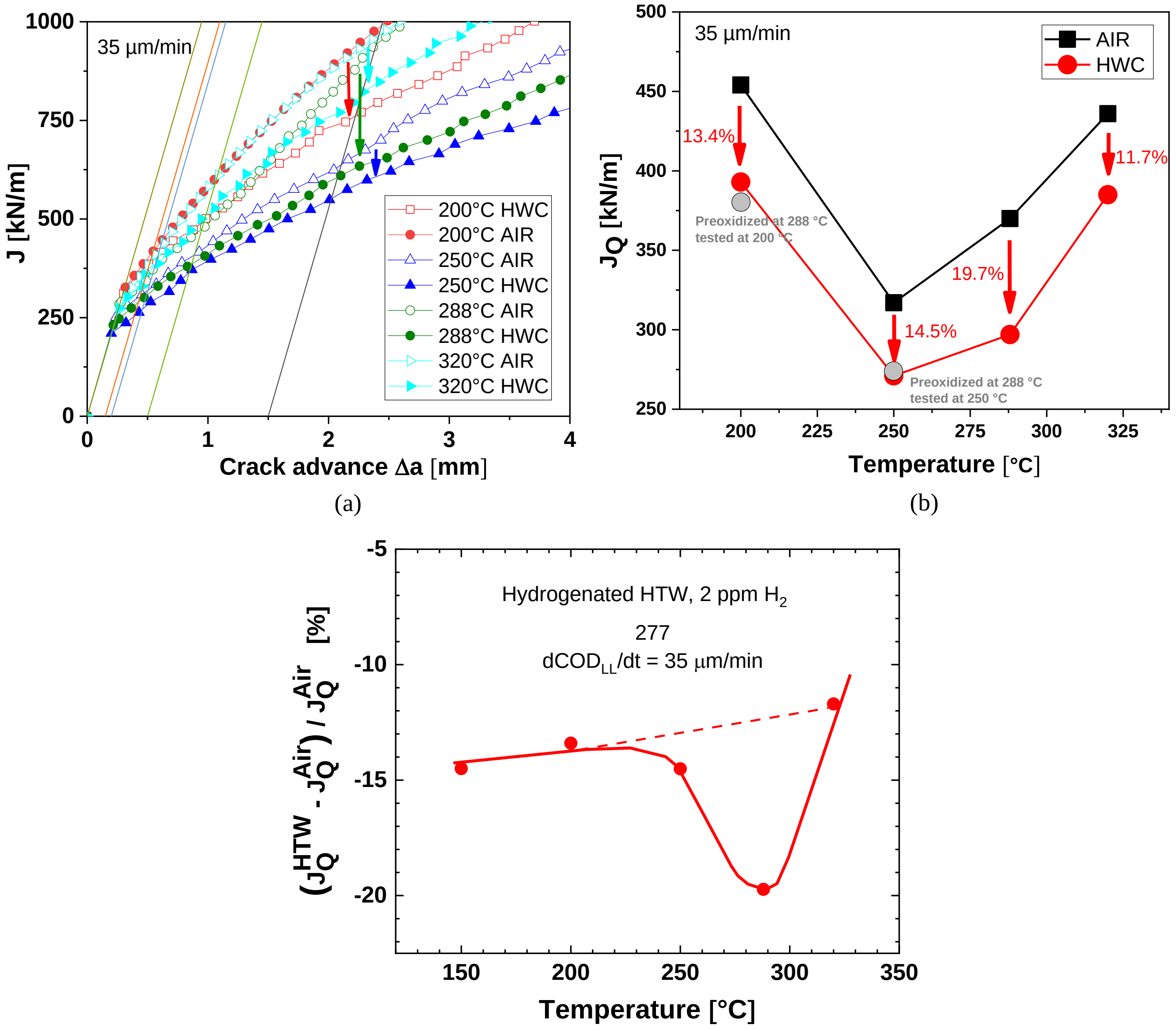

(a)

(b)

(c)

Figure 71: (a) *J-R* curves, (b) fracture initiation resistance and (c) relative reduction of fracture initiation resistance of 277 material tested in hydrogenated HTW and air at various temperatures with 35 µm/min.

3.4.2 Fracture behaviour of 508 material

EPFM tests with 508 steel with high DSA susceptibility were performed in various HTW environments and air (as depicted in Figure 72 (a)) with loading rates of 0.35 to 350 µm/min at 288°C. The 508 and 277 steels (with similar high DSA susceptibility and low sulphur content of 0.004 wt.%) consistently showed similar fracture behaviour in air and HTW in spite of the different microstructure (ferritic-bainitic vs. bainitic). The fracture initiation and tearing resistance in air and HTW increased with decreasing loading rate due to DSA. Environmental reductions in fracture initiation and tearing resistance were found in all three HTW environments with the highest and lowest reductions in hydrogenated HWC and oxygenated NWC environment, respectively. In all three environments, the environmental degradation increased with decreasing loading rate (due to DSA effect), but the lowest absolute value of fracture initiation resistance in HTW was still observed at the highest loading rate of 350 µm/min. The environmental degradation partially (NWC) or almost completely (HWC) compensated the increase of fracture initiation resistance in air due to DSA. These tests further confirmed the synergic effects of hydrogen and DSA on the environmental degradation especially at slower loading rates. This observed behaviour also suggests that DSA overwhelms possible crack crevice chemistry effects in these low-sulphur steels. The stronger effect in hydrogenated HTW is related to the higher hydrogen availability in the crack crevice environment.

Below a loading rate of ~ 10 µm/min, SICC was observed in oxygenated HTW environment in this steel. At a loading rate of 3.5 µm/min, crack growth initiated and further propagated by SICC without any ductile crack growth. The unexpected apparent low fracture initiation (Figure 72 (a)) and tearing resistance (Figure 72 (b)) and strong environmental acceleration of crack growth rate (Figure 72 (c)) in NWC at 3.5 µm/min were related to SICC and not to a real reduction in fracture initiation resistance. This loading rate boundary correlates fairly well with the strain rate threshold of 10^{-3} s^{-1} for SICC in SSRT with smooth tensile specimens in HTW. Above this threshold, SICC does not occur and the ductile crack growth rates are faster than the maximum SICC rates. SICC was not observed in the other HTW environments, even with lowest loading rates in this study (0.35 µm/min).

Figure 73 illustrates the representative fracture features of samples investigated in the tested environments at a loading rate of 3.5 µm/min. The predominant fracture mechanism was ductile MVC in all conditions (except in NWC). As shown in Figure 73 (a), (b) and (d), secondary cracks and macro-voids were observed along the whole fracture surface in specimen tested in HWC, while only ductile MVC was observed in specimens tested in nitrogenated high-purity water (HPW) and air. Figure 73 (c) clearly indicated higher fraction of secondary cracks and QC area along with the ductile crack growth in HWC compared to tests in air and HPW due to the higher DH concentration in the HTW. QC feature was found inside the secondary cracks or the macro-voids, where tear ridges were formed by ductile fracture. In oxygenated HTW, crack growth both initiated and further propagated by SICC as shown in Figure 73 (e). The SICC in NWC showed the typical fan shape appearance with feather morphology (Figure 73 (f)).

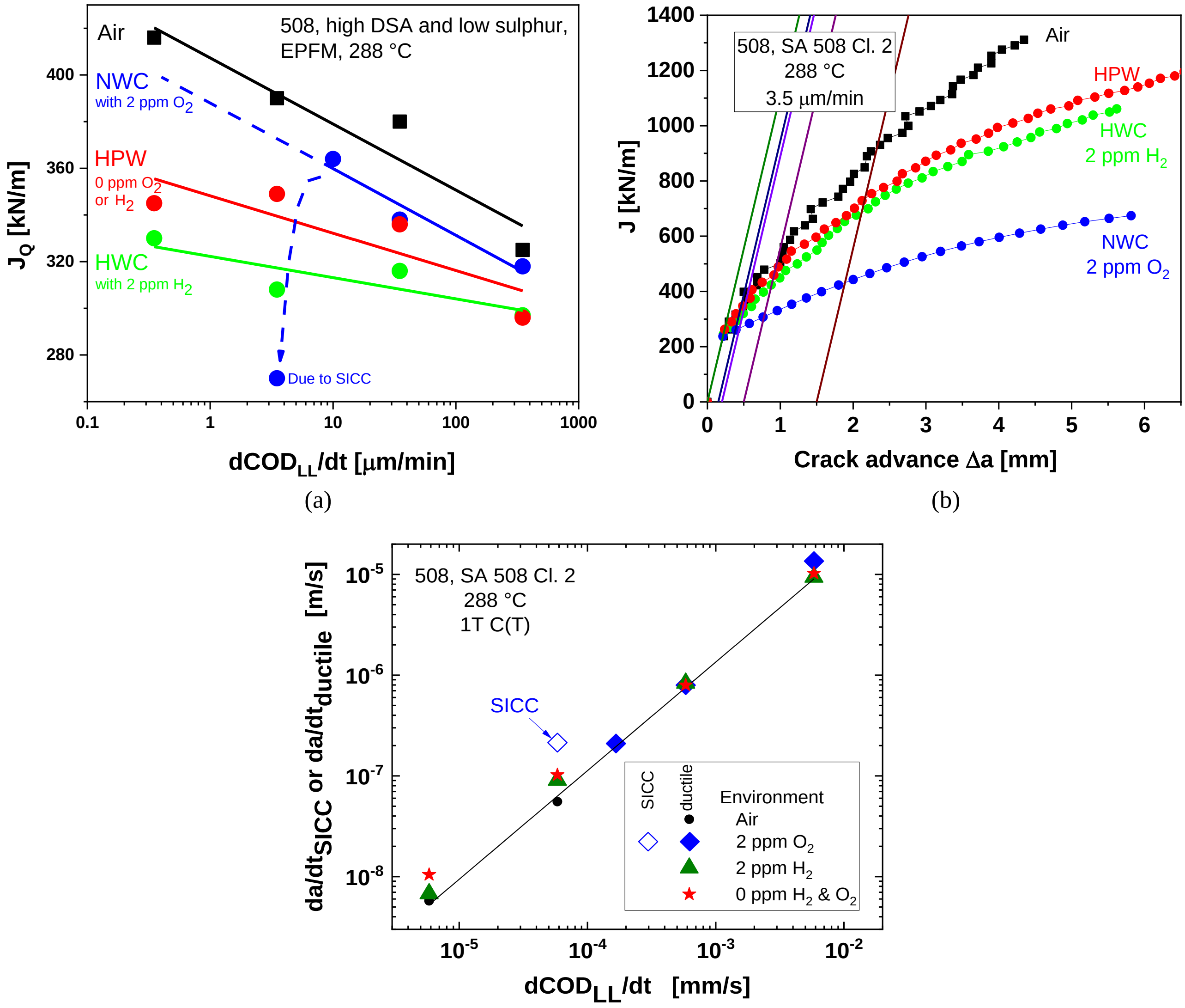

(a)

(b)

(c)

Figure 72: (a) Summary of fracture initiation resistance J_Q of 508 material in air and various HTW environments at 288 °C; (b) *J-R* curves of 508 material in air and various high-temperature water environments at 288 °C at 3.5 µm/min; (c) comparison of ductile and SICC growth rates in EPFM tests in different environments.

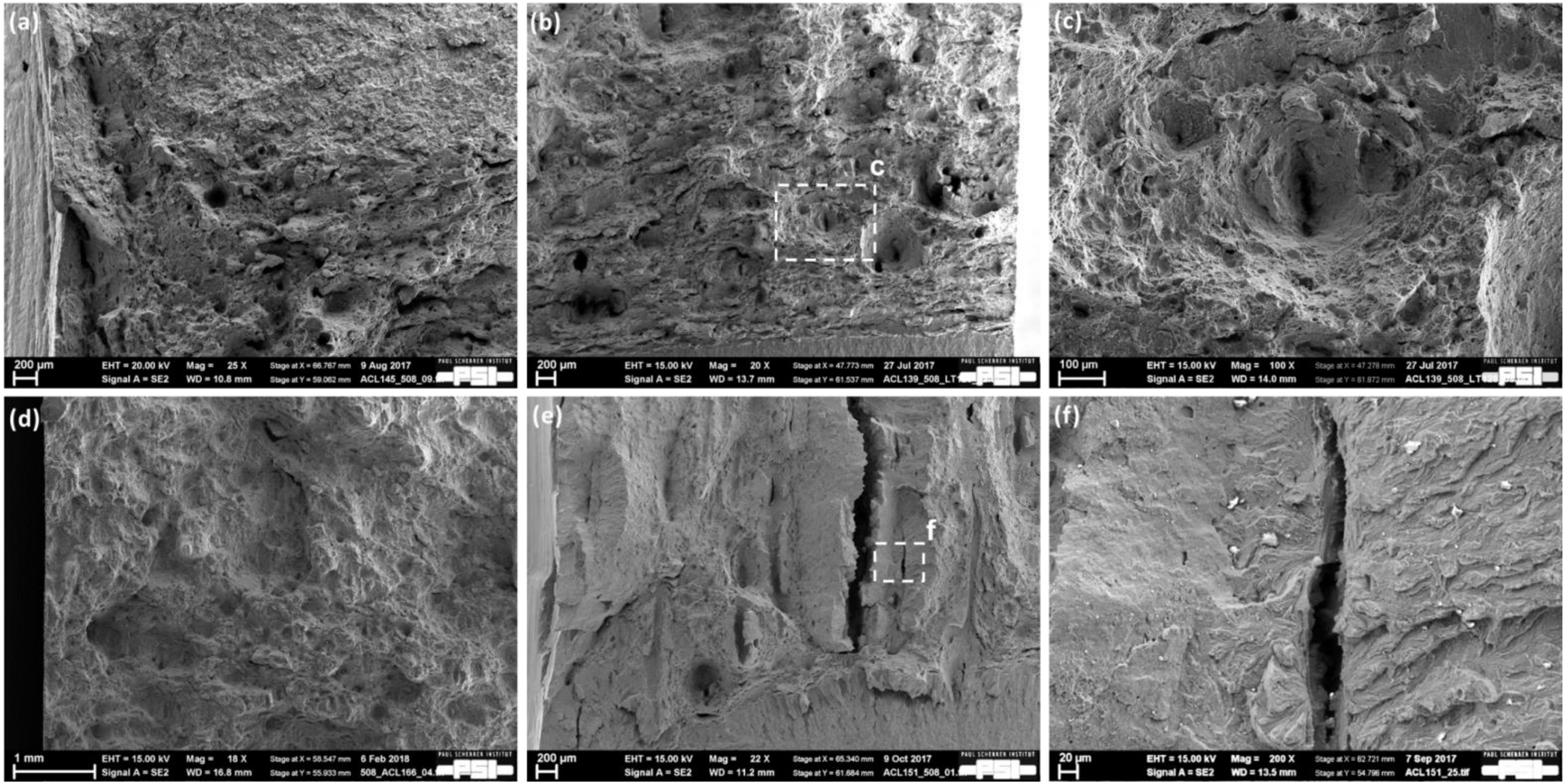
(a)
200 µm
EHT = 20.00 kV
Signal A = SE2
Mag = 25 X
WD = 10.8 mm
9 Aug 2017
ACL145_508_09.
(b)
c
200 µm
EHT = 15.00 kV
Signal A = SE2
Mag = 20 X
WD = 13.7 mm
27 Jul 2017
ACL139_508_LT
(c)
100 µm
EHT = 15.00 kV
Signal A = SE2
Mag = 100 X
WD = 14.0 mm
27 Jul 2017
ACL139_508_LT
(d)
1 mm
EHT = 15.00 kV
Signal A = SE2
Mag = 18 X
WD = 16.8 mm
6 Feb 2018
508_ACL166_04.
(e)
f
200 µm
EHT = 15.00 kV
Signal A = SE2
Mag = 22 X
WD = 11.2 mm
9 Oct 2017
ACL151_508_01.
(f)
20 µm
EHT = 15.00 kV
Signal A = SE2
Mag = 200 X
WD = 13.5 mm
7 Sep 2017
ACL151_25.tif
PAUL SCHERRER INSTITUT
PSI

Figure 73: Fracture surface of 508 steel tested with 3.5 µm/min at 288 °C in (a) air; (b) to (c) hydrogenated HTW with 2 ppm H_2; (d) nitrogenated high-purity water; (e) to (f) oxygenated HTW with 2 ppm O_2.

If this kind of SICC initiation at the high J value with significant plastic yielding should be rather regarded as sub-critical crack growth or as “rapid and critical” environmental fracture is unclear. This transition is rather gradual and is ambiguous to some extent (Figure 74 (a)). SICC and dissolution can affect the environmental fracture behaviour at slow strain rates both by the crack growth and the production of an occluded crack crevice chemistry, as shown by this work. However, this should be clearly separated from conventional sub-critical SICC that occurs under LEFM conditions in highly oxidizing conditions.

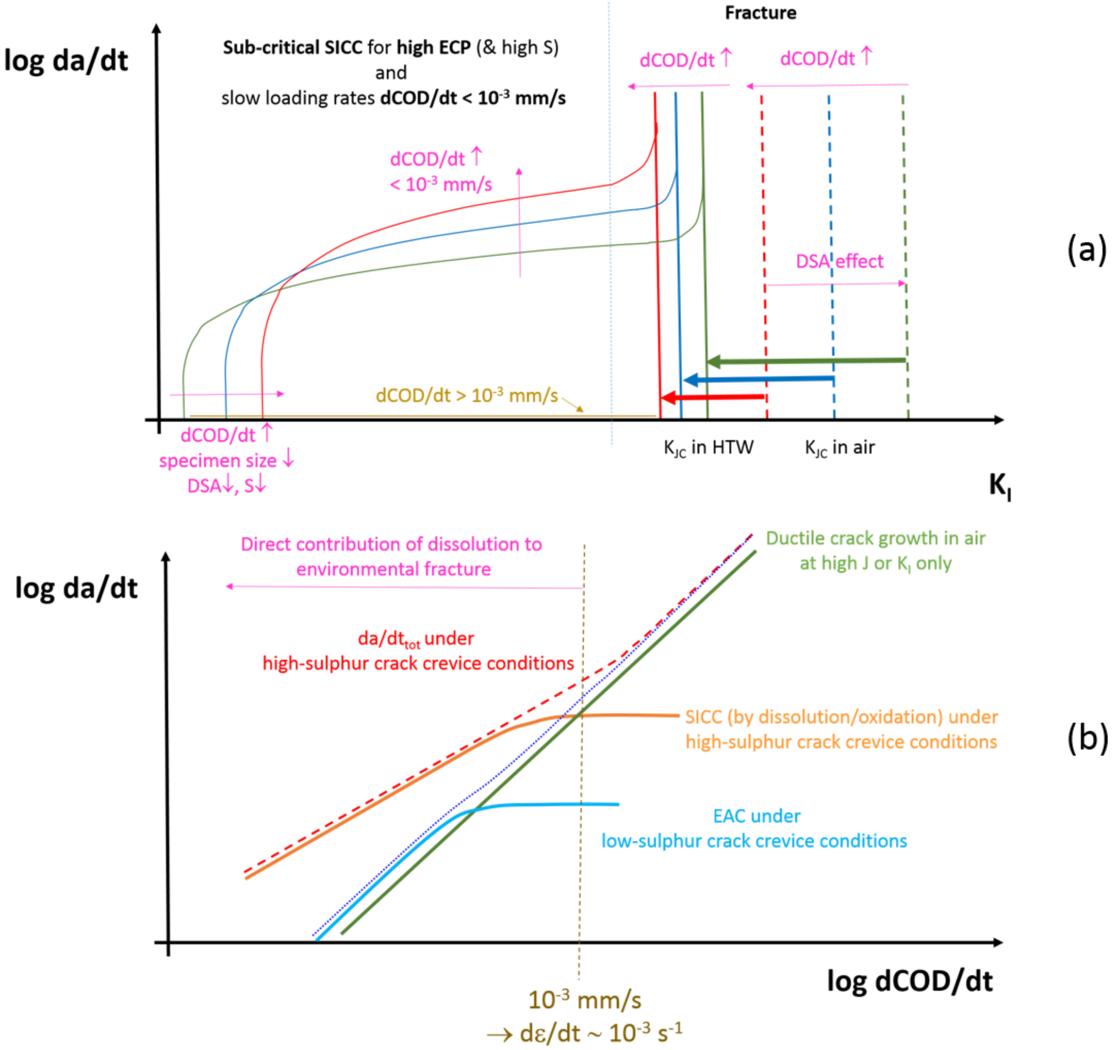
Fracture
log da/dt
Sub-critical SICC for high ECP (& high S)
and
slow loading rates dCOD/dt < 10^{-3} mm/s
dCOD/dt ↑
dCOD/dt ↑
dCOD/dt ↑
< 10^{-3} mm/s
DSA effect
(a)
dCOD/dt > 10^{-3} mm/s
dCOD/dt ↑
specimen size ↓
DSA↓, S↓
K_{JC} in HTW
K_{JC} in air
K_I
Direct contribution of dissolution to
environmental fracture
log da/dt
Ductile crack growth in air
at high J or K_I only
da/dt_{tot} under
high-sulphur crack crevice conditions
SICC (by dissolution/oxidation) under
high-sulphur crack crevice conditions
(b)
EAC under
low-sulphur crack crevice conditions
log dCOD/dt
10^{-3} mm/s
→ dε/dt ~ 10^{-3} s^{-1}

Figure 74: The relation of crack growth rate with (a) K_I and (b) crack opening displacement rate under different conditions.

Under highly oxidizing conditions (high ECP > 0 mV_{SHE}), onset of sub-critical SICC may occur in high-sulphur steels in high-purity water at low K_I values of 20 to 40 $\text{MPa·m}^{1/2}$ with pre-cracked specimens in slow rising load tests with constant displacement rate at very slow loading rates of less than 10^{-3} mm/s [64] (Figure 68 (b)). This K_I threshold for SICC is shifted to higher values with increasing loading rates. Above a displacement rate of 10^{-3} mm/s, no onset of SICC is observed. The subsequent constant SICC rates increase with increasing loading rate according to a power law (with an exponent of 0.8 (slightly lower than linear) up to an upper threshold SICC rate of 10^{-7} to 10^{-6} m/s (corresponding to continuous anodic dissolution under high-sulphur crack crevice conditions) with only a very weak K_I dependence [28]. Above a loading rate of 10^{-3} mm/s, SICC rates by anodic dissolution become smaller than the ductile growth rates at high K_I values and the resulting crack advances by SICC/dissolution are insignificant at high loading rates (Figure 74 (b)). A growing sharp SICC crack at slow loading rates will transform to a blunting crack, when the displacement rate is shifted well above the threshold displacement rate for SICC. The threshold K_I for the onset of SICC is shifted to lower values with increasing steel sulphur content, ECP, DSA susceptibility, yield stress and specimen size, but these parameters have little effect on the subsequent SICC rates [28][100]. In hydrogenated high-purity water, no SICC was observed in such tests up to K_I values of 80 MPa·$m^{1/2}$. Onset of slow low-sulphur SICC at much higher K_I values is not completely excluded, but not confirmed by our tests in HWC, where SICC only occurred after some preceding ductile crack growth (see Figure 67 and Section 3.4.1).

A pseudo fracture resistance *J-R* curve can be derived from tests with sub-critical SICC according to the evaluation of an EPFM experiment. This would indicate a huge safety concern due to the extremely low fracture initiation and tearing resistance. This clearly is not an environmental reduction of the fracture resistance, but sub-critical SICC. In fact, the specimens fail at much higher K_I or J values (in particular in bigger specimens) than predicted based on such a pseudo fracture resistance curve. It should always be checked, if the fracture test results were possibly affected by sub-critical SICC by careful post-test fractography, in particular under highly oxidizing conditions. SICC is restricted to oxidizing conditions and slow strain rates as shown by lab and service experience [28]. Cracks can be formed and sub-critically grow by SICC until they reach a critical size (leak, ductile or brittle fracture, plastic collapse). SICC and dissolution can affect the environmental fracture behaviour at slow strain rates. However, the bigger practical concern of SICC with regard to final fracture/failure of components probably is that the shorter time interval between leak and break due to the high SICC rates. Under such conditions, the benefit of leak before break behaviour is lost.

The observed fracture behaviour of the two high-DSA steels 277 and 508 in HTW (effects of temperature and loading rate) and the good correlation between DSA susceptibility and the environmental reduction of fracture resistance in HWC (Figure 65), strongly suggest some synergy effects between hydrogen and DSA. The relative reduction in fracture initiation resistance was hereby in the same range as the softening of UTS in tensile tests in air with hydrogen pre-charged specimens under comparable strain rate conditions (Figure 65 (b)). The effects were more pronounced in the RPV steel 277 (with the highest free nitrogen content), which had a slightly lower DSA susceptibility in air than the steel 508. The 508 material has a mixed bainitic-ferritic structure and a higher DSA susceptibility, but slightly lower HE susceptibility as shown in tensile tests (Figure 64 (b)). 508 steel revealed a smaller environmental reduction in fracture initiation resistance in HTW than the 277 steel. The 277 steel revealed a more pronounced environmental reduction effect of fracture resistance in HTW than anticipated based on the DSA susceptibility in tensile tests in air and on the general DSA trend in Figure 65. However, the environmental reduction effect of fracture resistance of 277 steel in hydrogenated HTW is in excellent accordance with the HE susceptibility of the different steels in tensile tests with hydrogen pre-charging. 277 material also showed slightly stronger localization of plastic deformation and higher amount of secondary cracking in HTW than the 508 steel. The only major difference to the other steels in this context was the free nitrogen content in 277 steel that was a magnitude higher. This would imply a different effect of free carbon and nitrogen on plasticity (which was reported for fcc steels [172]) and/or their interactions with hydrogen. If the difference of the environmental reduction of fracture initiation resistance and HE susceptibility is solely related to different free carbon and nitrogen contents or to other different microstructural features that affect the plastic deformation and hydrogen trapping behaviour (e.g., higher amount of lath, packet and prior-austenite grain boundaries in the 277 steels as barriers) currently remains unclear.

3.4.3 Discussion on the effect of dynamic strain aging

For RPV steels with high DSA susceptibility in the DSA temperature-strain rate range, there is direct evidence of moderate environmental reduction of fracture initiation resistance and moderate environmental acceleration of ductile crack growth rate in hydrogenated HTW environment. The fracture was dominated by ductile MVC with small amounts of secondary cracking and QC. The area share of the secondary cracking and QC increased with the environmental reduction of fracture initiation resistance. The underlying mechanisms, which lead to the microscopic plastic deformation and the moderate macroscopic change of the fractographic features, are discussed in this chapter.

Secondary crack formation:

Smaller amounts of secondary cracks and QC facets were observed on the fracture surface in NWC than in HWC environment, while for tests in air the fracture surface was fully ductile in both 277 and 508 materials. To study the formation mechanism of the secondary cracks and the potential relationship between secondary cracks and environmental degradation effects, metallographic cross-sections of a 277 specimen tested at 288 °C with 35 µm/min in HWC environment were cut with EDM (the cutting plane perpendicular to the fracture surface and at the position of secondary cracks). These cross-sections were fine polished to 0.02 µm and further investigated with EDX.

On the cross section of the cut specimen, deep cracks with lengths of roughly 0.5 to 1.5 mm were always found right beneath the position of secondary cracks on the fracture surface, with an example shown in Figure 75 (a). In Figure 75 (b), the EDX area mapping at the tip of the crack on cross section is shown, which indicates the existence of some remaining inclusions like Al_2O_3 and MnS/CaS. The element mapping showed that the matrix was partially dissolved and some cavities were formed. Besides, the traces of oxides were also discovered around the secondary crack tip. It reveals that oxidation and corrosion reaction occurred up to the secondary crack tip, showing strong evidence of the promoting effects of inclusions on the secondary crack formation. EDX point scanning was carried out on the matrix and inside the dissolved cavities, which were marked with *A* (matrix), *B* and *C* (inside the dissolved region of cavities), respectively, as shown in Figure 75 (c) and (d). The major peaks in spectrum of point *A* were mainly from iron, while *B* and *C* showed remaining peaks of sulphur, calcium and manganese, which indicated that the dissolved region in the cavities was composed of MnS/CaS inclusions before the corrosion/oxidation occurred. It demonstrated that the secondary crack formation was facilitated by the dissolution of sulphides and the enhanced corrosion reaction or oxidation beneath the fracture surface. During EPFM tests, the generated secondary cracks were under bending situation with the external loading. Therefore, the oxide film were ruptured under the bending stress and the anodic dissolution of the matrix metal occurred until full repassivation. This (repetitive) process provided an additional source of hydrogen that enhanced the local hydrogen uptake to the metal lattice. Additionally, the undissolved MnS inclusions ahead of crack tip may also act as strong hydrogen traps and crack initiation sites.

The fracture appearance inside the secondary cracks had a QC feature, exhibiting the characteristics of both cleavage and plastic micro-voids. These cracks normally initiated at the central cleavage facets and as the crack spread, the cleavage facets blended into areas of ductile fracture. The cleavage steps then became tear ridges with small and fine-dispersed dimples. The region outside the tearing ridges was fully ductile by MVC. Although the appearance of QC (as one of the microstructural symbols of HE) was discovered along with secondary cracks, the stable ductile transgranular tearing by MVC still dominates on the whole fracture surface. The low area share (2 to 3%) of secondary cracks with QC on the fracture surface cannot fully explain the 20% reduction of fracture initiation resistance in HWC at 288 °C. In contrast, the indirect contribution of the secondary cracks by the increase in local hydrogen uptake may eventually be more effective.

A more significant role of MnS inclusions on HE susceptibility might be anticipated [8], since MnS inclusions are strong hydrogen traps and might act as preferred initiation sites for (hydrogen-induced) “brittle” micro-crack or ductile micro-void formation. In addition, the dissolution of MnS inclusions can produce an aggressive sulphide-rich crack crevice environment. But this was finally not confirmed in this study in hydrogenated HTW, where low-sulphur crack crevice chemistry conditions are expected to prevail. Apart from very slow loading rates with sub-critical SICC, no QC features were found around the MnS inclusions in both hydrogenated and oxygenated HTW as well as in tensile test in air with hydrogen precharging in all materials. There was no microscopic evidence for hydrogen-induced micro-crack formation at MnS inclusions, e.g. ahead of the main EPFM crack tip with linking to the main crack in both low- and high-sulphur steels. The effects of steel sulphur content and MnS inclusions on environmental reduction in fracture resistance in EPFM tests are mainly caused due to the possibility of the formation of a sulphur-rich crevice environment and increase in hydrogen uptake, which is favoured by a high dissolved oxygen and high steel sulphur contents. In hydrogenated HTW, low-sulphur crevice chemistry conditions usually prevail in both low-sulphur and high-sulphur steels in EPFM tests, which explains the dominance of the DSA effect. The higher share of secondary cracks and stronger reduction of fracture resistance in HWC in the low-sulphur steels with high DSA susceptibility further confirms the limited role of MnS inclusions in hydrogenated HTW. These observations also confirm the synergic contribution of plastic strain localization by DSA and hydrogen for the secondary crack formation.

Interaction of hydrogen and DSA:

For studying the underlying mechanism of potential synergic effects of DSA and hydrogen, EBSD mapping was performed at crack tips of 277 specimens tested in air ($J_{Q, AIR}$ = 370 kN/m) and HWC ($J_{Q, HWC}$ = 297 kN/m) at 288 °C with 35 µm/min, as shown in Figure 76 (a) and (d), respectively. In the 277 material with high DSA susceptibility, stronger localized deformation was discovered at the crack tip in HWC than in air. At the region up to 20 µm ahead of the crack tip, tiny grains with slight orientation difference were clearly observed in the specimen tested in HWC. These tiny grains indicated a higher distortion and more localized plastic deformation at the crack-tip region despite of the lower peak load of the EPFM test and lower J_Q in HWC than in air.

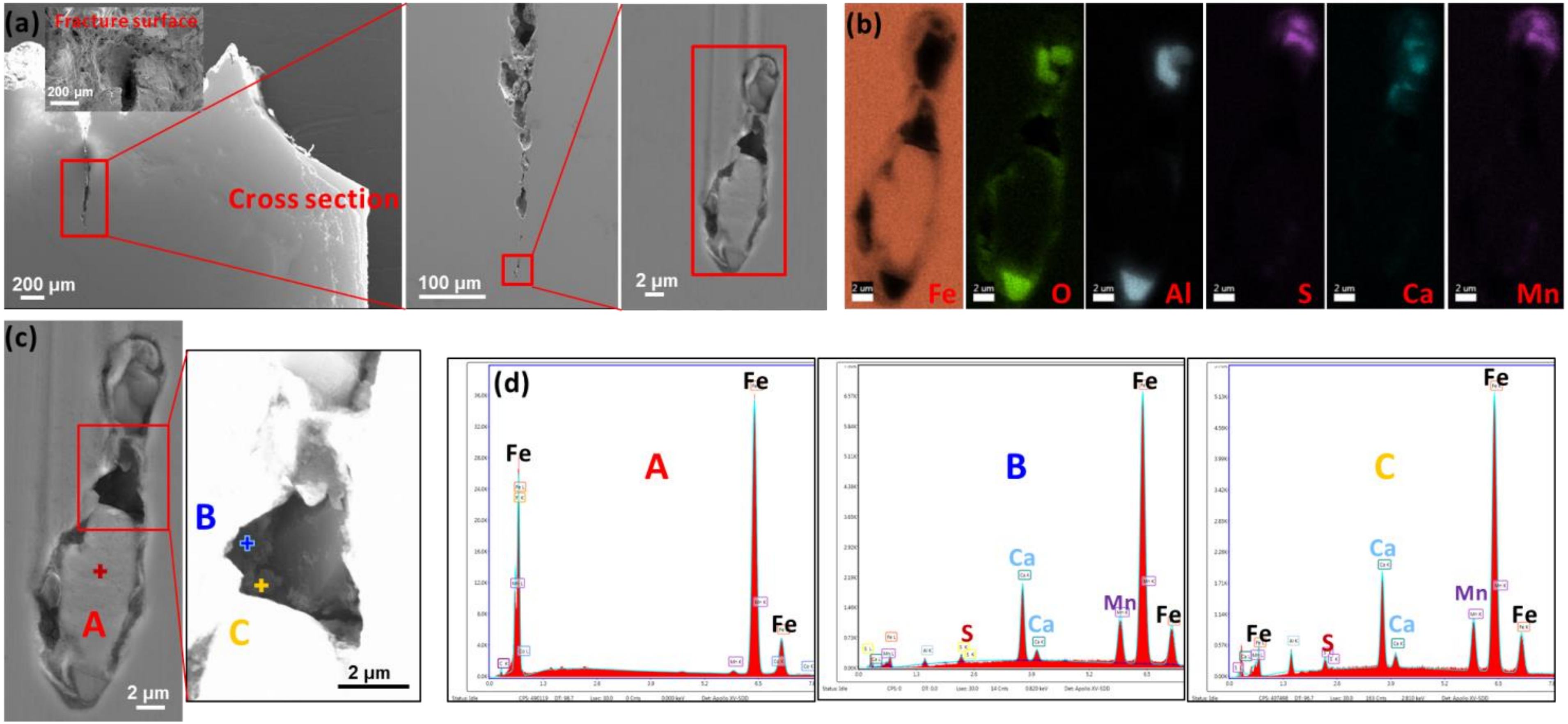

Figure 75: SEM and EDX investigations on secondary cracks of 277 specimen tested at 288 °C with 35 µm/min in hydrogenated HTW. (a) SEM images showing a deep crack on the cross section beneath the secondary crack on the fracture surface; (b) EDX area mapping of marked area in (a); (c) SEM images showing the dissolved cavity at the crack tip on cross section; (d) EDX point scanning of spot *A*, *B* and *C* in (c).

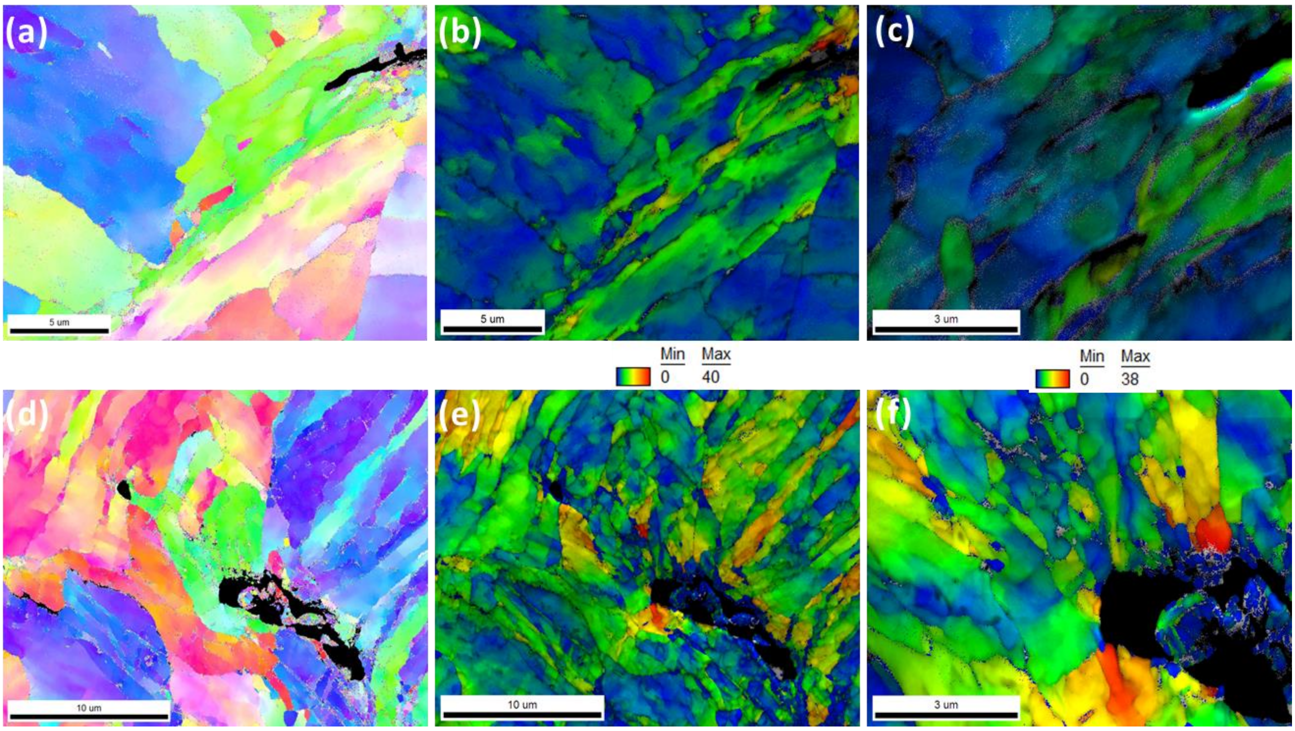
(a)
5 um
(b)
5 um
(c)
3 um
Min Max
0 40
Min Max
0 38
(d)
10 um
(e)
10 um
(f)
3 um

Figure 76: EBSD maps at crack tips of 277 material tested in air ($J_{Q, AIR}$ = 370 kN/m) (a–c) and hydrogenated HTW ($J_{Q, HWC}$ = 297 kN/m) (d–f) at 288 °C with 35 μm/min, respectively. ((b) and (e) show grain reference orientation deviation mapping with an angle range of 0^o to 40^o, while (c) and (d) show grain reference orientation deviation mapping with an angle range of 0^o to 38^o).

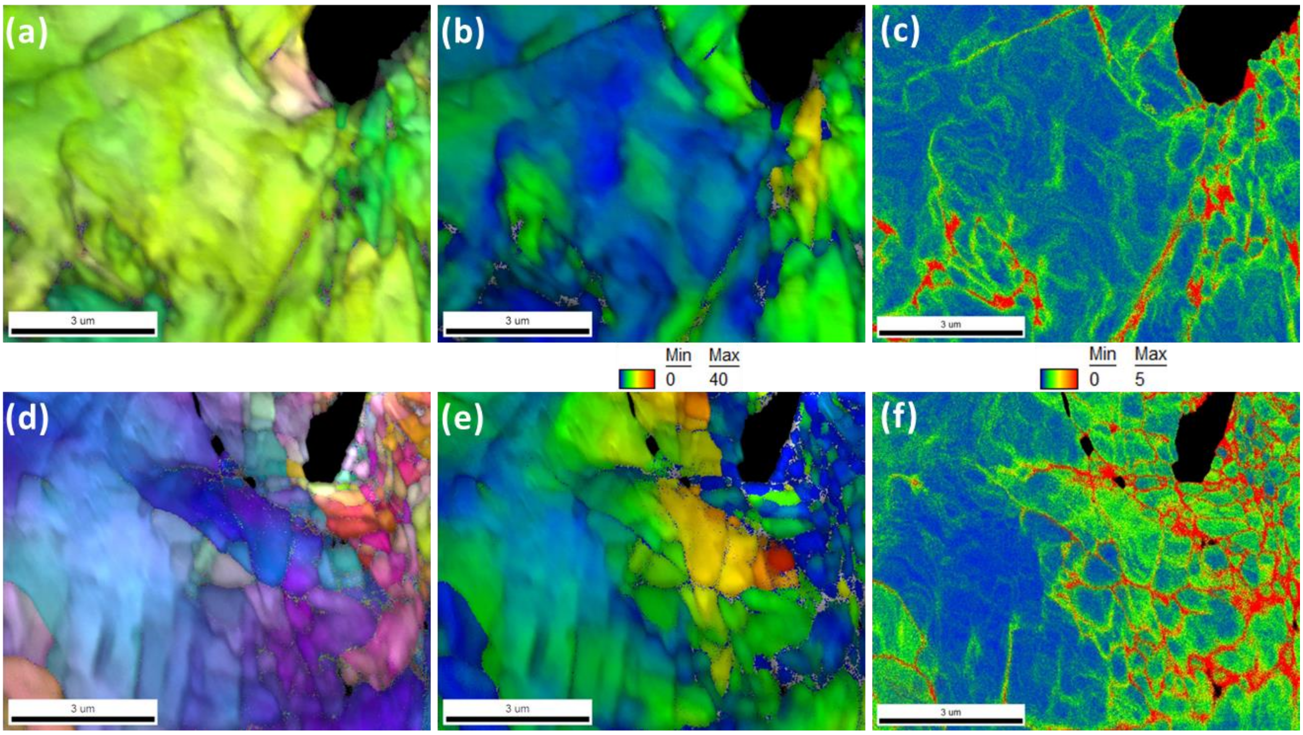
(a)
3 um
(b)
3 um
(c)
3 um
Min Max
0 40
Min Max
0 5
(d)
3 um
(e)
3 um
(f)
3 um

Figure 77: EBSD maps at crack tips of 508 material tested in air ($J_{Q, AIR}$ = 380 kN/m) (a–c) and hydrogenated HTW ($J_{Q, HWC}$ = 316 kN/m) (d–f) at 288 °C with 35 μm/min, respectively. ((b) and (e) show grain reference orientation deviation mapping with an angle range of 0^o to 40^o, while (c) and (f) show kernel average misorientation mapping with a misorientation range of 0^o to 5^o).

Stronger localized deformation at the crack tip in HWC compared to air was discovered for 508 material as well, which is shown in Figure 77. As depicted in GROD and KAM maps, the local orientation deviation and KAM are higher in HWC than in air environment. Therefore, the higher level of localization of plastic deformation in hydrogenated HTW than in air was well confirmed with the GROD and KAM mapping. The localized deformation favours local hydrogen enrichment above the critical threshold concentration and leads to the change of macroscopic fractographic features by influencing the microscopic plastic deformation process. Therefore, similar synergic effects of DSA with hydrogen on the fracture behaviour and the reduction of fracture initiation resistance in HWC were confirmed for both 277 and 508 materials.

DSA results in plastic deformation localization due to the negative strain rate sensitivity. These localized deformation regions facilitate hydrogen enrichment and accumulation. Therefore, available hydrogen can be concentrated in smaller process zone volume with short diffusion distances so that local hydrogen concentration may reach the critical content. The localization of plastic deformation favours rupture of the protecting oxide film, subsequent anodic dissolution and further hydrogen uptake. Higher level of localization of plastic deformation and higher dislocation density were observed (Figure 77 (e) and (f)), which confirmed the above hypothesis.

Secondary crack formation due to corrosion reaction beneath the fracture surface can enhance the local hydrogen uptake and act as the starting point of fracture process zone by localized plastic deformation, but it cannot completely explain the reduction of fracture initiation resistance in HWC at 288 °C. Stronger localized deformation at the crack tip in HWC with interaction of DSA and hydrogen compared to air was the main reason for the environmental reduction in 277 steel.

Failure occurred by stable ductile tearing by micro-void formation and coalescence with additional, small amounts (a few %) of secondary cracks and QC facets. Micro-void formation is facilitated by a high hydrostatic, triaxial stress and large inclusion particles with weak bonding strength to the matrix. The RPV steels contain both large MnS inclusions (1 to 100 µm) with weak bonding and fine dispersed carbide (or carbonitride) particles like Fe_3C (0.1 to 1 µm) with stronger bonding to the matrix, respectively. The size of the MnS inclusions is one or two orders of magnitude bigger than the carbide particles, but their particle density is several orders of magnitude lower. However, the density of MnS inclusions is still sufficiently high to act as preferred nucleation sites for micro-void formation in the plastic zone at the crack tip. Therefore, the micro-void formation usually starts at the large MnS inclusions in the peak hydrostatic stress region. The lower upper shelf toughness of RPV steels with high sulphur content is a direct consequence of this.

After some void growth, stress and plastic strain localization takes place in the inter-void regions. The higher local plastic strain in these regions results in micro-void formation at carbide particles with stronger bonding and leads to crack growth by MVC. Hydrogen trapping at the interface between the MnS inclusions and carbide particles can facilitate micro-void formation by decohesion that may start at lower strains. Furthermore, hydrogen (by HELP) and DSA (due to negative strain rate sensitivity) can further amplify the strain localization in the inter-void region and facilitate both the micro-void formation (at smaller particles) and the coalescence of the micro-voids.

The bonding of the MnS inclusions to the matrix is very weak and hydrogen does not further weaken the bonding here. Therefore, the major effect of hydrogen is rather on the inter-void strain localization and micro-void formation at small particles. The effect of hydrogen in tensile test in air with hydrogen pre-charging was most pronounced on the fracture strain and, in particular, the reduction of area, which supports the idea of hydrogen effects on inter-void strain localization. The hydrogen effects were strongest in the post-necking region on tensile specimens. Micro-void formation starts briefly before reaching the UTS under uniform strain, whereas coalescence is dominating after the onset of necking. Macroscopically, DSA increases the yield stress, UTS, strain hardening (higher peak load in EPFM tests), peak and hydrostatic stress at the crack tip, which favour both the hydrogen enrichment in this zone as well as micro-void formation at inclusions. However, its effect is believed to be small due to the small increase in strength. Microscopically, on the other hand, DSA results in strain localization due to the negative strain rate sensitivity, which amplifies the inter-void strain localization and void formation. With the negative strain rate sensitivity, the flow stress decreases with increasing strain rate. Regions with higher local strain give a higher strain rate for a given loading rate and lower flow stress, which tends to further increase the plastic deformation in these regions (self-amplifying, positive feedback effect).

The reduction effects were limited and moderate in this study due to the low hydrogen availability in HTW in connection with high density of fine-dispersed hydrogen traps in RPV steels. There is much higher free hydrogen in the bulk lattice in the tensile tests that may strongly amplify the inter-void strain localization by HELP and DSA. In addition, the reduction in fracture resistance tended to increase with decreasing loading rate, but since fracture resistance also significantly increased with decreasing loading rate in air due to DSA, the reduced toughness values at slow loading rates were still higher than those under standard loading rate conditions (0.25 to 0.35 mm/min). The environmental reduction and softening by synergic effects of hydrogen and DSA in hydrogenated HTW partially compensated the toughness increase by negative strain rate sensitivity and hardening due to DSA in air.

3.5 Effect of high environmentally-assisted cracking and high temper embrittlement susceptibilities

An overview on the correlation between the fracture initiation resistance reduction and DSA susceptibility or steel sulphur content in hydrogenated and oxygenated HTW at 288 °C at a standard loading rate of 0.25 to 0.35 mm/min is shown in Figure 78 and Figure 79, respectively. In the Biblis C steel with low sulphur and phosphorus contents and low DSA, EAC and TE susceptibilities, environmental effects on fracture initiation resistance seem to be absent or marginal in both oxygenated and hydrogenated HTW. In hydrogenated HTW, a good correlation between relative reduction in fracture initiation resistance in HTW with DSA susceptibility (or hydrogen-induced softening) in tensile tests in air was observed, and sulphur content played a minor role only. In the low-sulphur steels with high DSA susceptibility, the environmental reduction of fracture initiation resistance was higher in hydrogenated than in oxygenated HTW. The relative reduction in fracture initiation resistance seemed to be most pronounced in the RPV steel with the high free nitrogen content. In oxygenated HTW, on the other hand, the steel sulphur content seems to play a more important role in addition to the DSA susceptibility. The RPV steels with high sulphur content and moderate DSA susceptibility showed a stronger reduction in fracture initiation resistance in oxygenated HTW. The environmental reduction of J_Q in NWC increased with increasing steel sulphur content for low and moderate DSA steels (Biblis C, HSST and KS 12) with the exception that the high DSA steel 277 with high free nitrogen content and JRQ steel with high TE also showed a high reduction in NWC environment. The evolution of an aggressive occluded high-sulphur crack crevice chemistry with high hydrogen uptake potential is facilitated by a high sulphur content of steel.

To fully elucidate the potential interactions of hydrogen/HTW effects with EAC and/or TE susceptibility, the fracture behaviour of RPV steels with high sulphur and/or phosphorus contents is systematically discussed in the following sections.

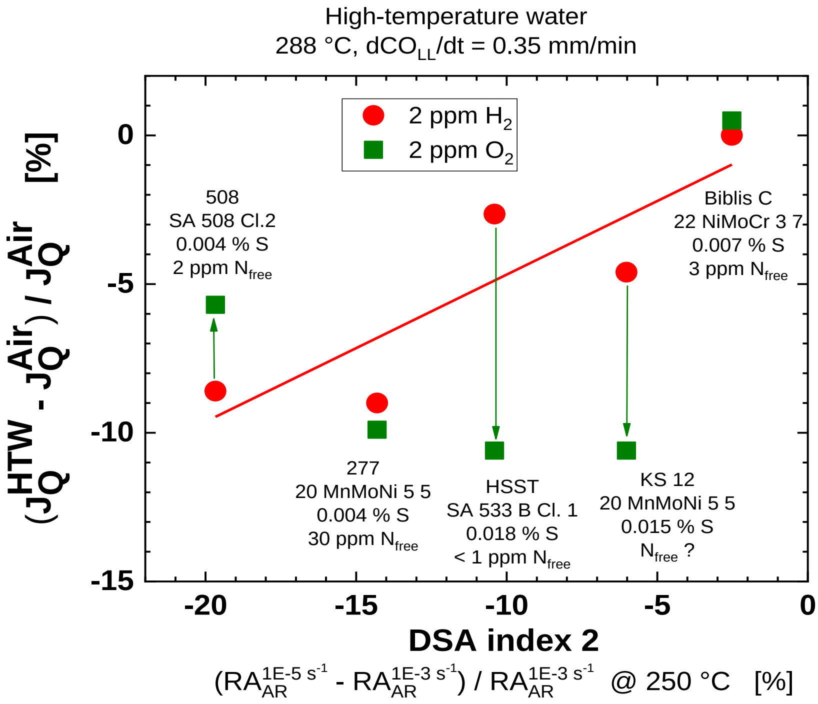

Figure 78: Correlation between environmental reduction of fracture initiation resistance and DSA susceptibility and steel sulphur content in hydrogenated and oxygenated HTW. A good correlation is observed with DSA susceptibility in hydrogenated HTW.

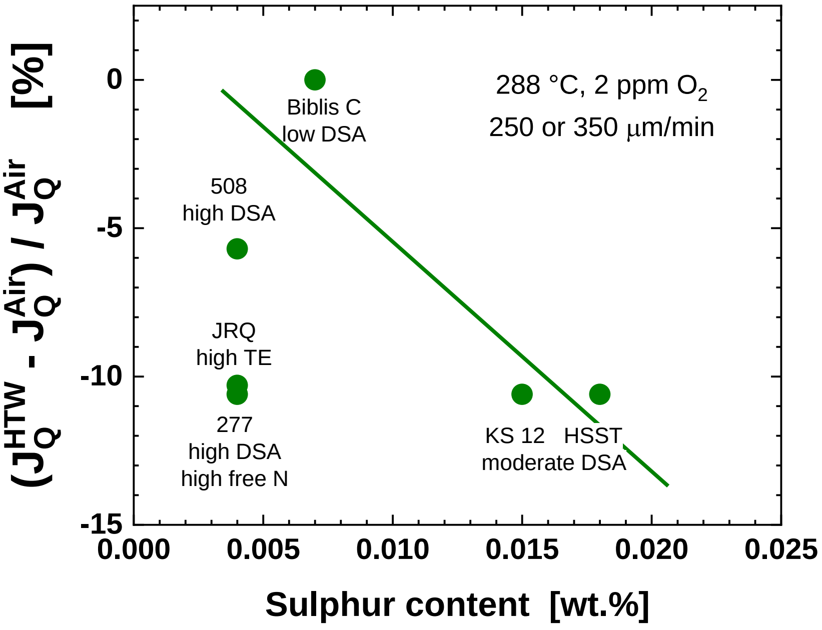

Figure 79: Effect of steel sulphur content on the environmental reduction of fracture initiation resistance in oxygenated HTW. In oxygenated HTW, the steel sulphur content seems to play a more important role.

3.5.1 Fracture behaviour of HSST material with high sulphur and EAC susceptibility

EPFM tests of the HSST material with high sulphur and low phosphorus contents and with high EAC and moderate DSA susceptibilities were performed in various HTW environments and in air (as depicted in Figure 80) with loading rates of 0.25 to 250 µm/min at 288 °C. A reduction in fracture initiation resistance was found in both hydrogenated and oxygenated HTW environments and this degradation slightly increased with decreasing loading rate (due to moderate DSA effect). In contrast to the low-sulphur steels with high DSA susceptibility [5][64], the HSST material with high sulphur content and moderate DSA susceptibility revealed a stronger environmental reduction of fracture initiation resistance in oxygenated (NWC with 2 ppm O_2) than in hydrogenated HTW (HWC with 2 ppm H_2) at loading rates of 25 to 250 µm/min (where SICC is absent). For high-sulphur steels, there is a more pronounced effect of steel sulphur content and stronger reduction of fracture initiation resistance in the oxygenated HTW. It was related to the sulphide enrichment in the crack crevice environment by migration due to the potential gradient in the crack-mouth region in NWC. This produces an aggressive, sulphide-rich crevice environment with high hydrogen uptake potential in the crack-tip process zone (see Sections 1.3.2 and 1.3.4.1). The DH content of the bulk environment only plays a minor role here.

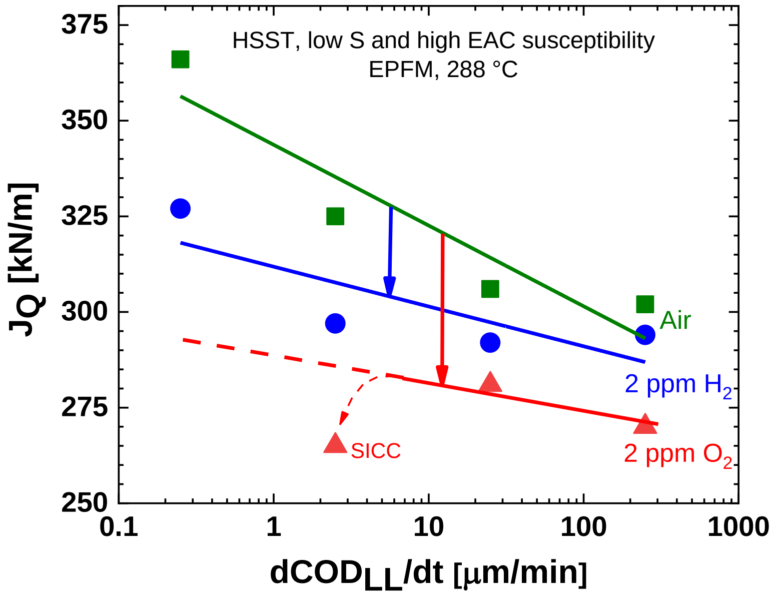

Figure 80: Effect of loading rate and water chemistry on fracture initiation resistance of high-sulphur steel HSST.

The reduction of fracture initiation resistance tended to slightly increase with decreasing loading rate. However, since fracture initiation resistance in air increased with decreasing loading rate (DSA effect), the J_Q values at slow loading rates were still higher than those under standard loading rates (0.25 to 0.35 mm/min). Therefore, HTW effects seem just to (partially or fully) compensate the increase of fracture initiation resistance by DSA. Furthermore, slow plant transients usually result in relatively small peak K_I values at crack tip and are less critical than it may appear at a first glance due to the potentially stronger environmental effects.

At slow loading rates < 10 μm/min, SICC was occasionally observed in this work, in particular in oxygenated HTW and the high-sulphur steels. In oxygenated HTW, the cracks can even initiate by SICC, whereas in hydrogenated water, ductile crack initiation and some ductile crack growth was preceding the onset of SICC. The strong reduction on the fracture initiation and tearing resistance in HTW with these very slow loading rates was due to the SICC crack growth.

Some of the EPFM tests with the high-sulphur steel HSST started with an active growing SICC crack at low K_I values (by suitable cyclic loading). It results in an aggressive occluded high-sulphur crack crevice chemistry and a very high hydrogen uptake potential in the crack-tip process zone. Furthermore, in some tests, 50 ppb of chloride (as HCl) was additionally added to produce a very aggressive crevice chemistry with an active growing SCC cracking under constant load prior to the EPFM test. The effects of crevice chemistry and preceding EAC crack growth on the fracture behaviour of HSST material are summarized in Figure 81 for standard loading rates of 0.25 mm/min (where SICC is absent). A preceding SICC crack growth at low K_I values further reduced the fracture initiation resistance in the subsequent EPFM test in both oxygenated and hydrogenated HTW. The fracture initiation resistance value with preceding SICC crack growth in hydrogenated HTW approximately reached that in oxygenated water without prior SICC growth. The addition of 50 ppb of chloride further reduced the fracture initiation resistance slightly in oxygenated HTW. These preliminary test results revealed a moderate, but clear reduction of the fracture initiation resistance with aggressive occluded crevice environment and with preceding fast high-sulphur EAC crack growth (favoured by, e.g., a high steel sulphur content, high ECP or chloride impurities).

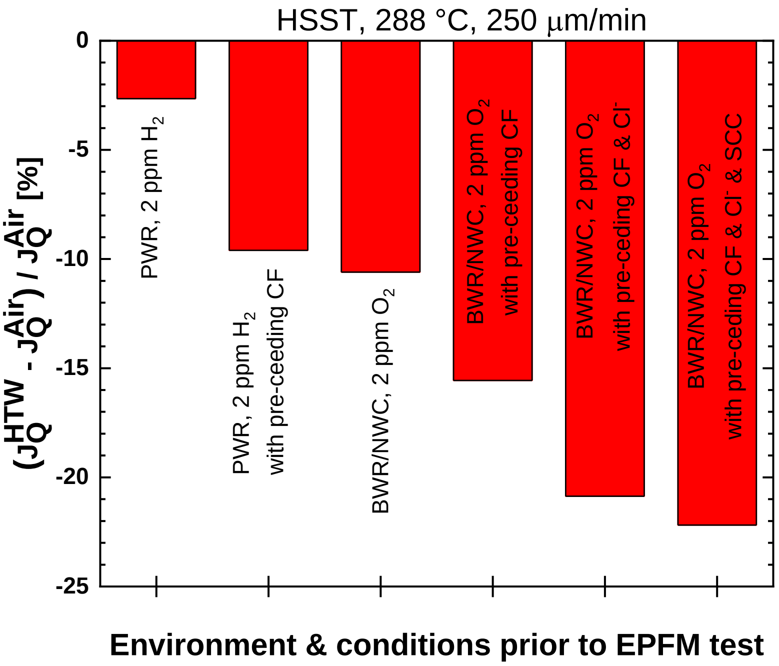

Figure 81: Effect of water chemistries and preceding EAC crack growth on reduction in fracture initiation resistance of high-sulphur steel HSST.

Figure 82 illustrates the representative fracture features of HSST samples investigated in all environments. The predominant fracture mechanism was ductile MVC and the crack path had a zig-zag shape in all conditions. Larger quantities of secondary cracks, QC and macro-voids were observed in samples tested in NWC than in HWC and in air. With preceding fast high-sulphur EAC crack growth, higher fraction of macro-voids and secondary cracks were observed with SEM. It is stressed that the area fractions of these features were relatively low (a few percents at maximum) and cannot solely explain the observed reduction of fracture resistance in HTW (up to 25%).

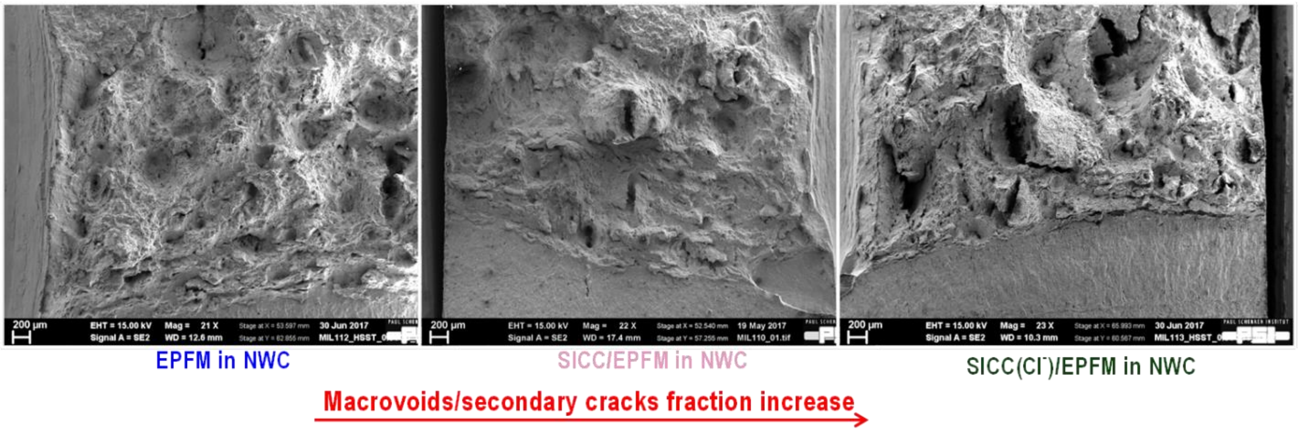

Figure 82: Fracture surface of high-sulphur steel HSST after EPFM tests in oxygenated HTW at 288 °C with a loading rate of 250 μm/min in a standard test (left), with preceding SICC growth (middle) and preceding SICC and chloride addition (right).

3.5.2 Fracture behaviour of JRQ material with high phosphorus content and TE susceptibility

The potential interactions of hydrogen/HTW effects with TE susceptibility was investigated by the EPFM tests on the RPV steel with high phosphorus content, which is systematically discussed in the following section. The JRQ material has high phosphorus and low sulphur contents as well as high TE, low DSA and EAC susceptibilities. The TE susceptibility was further increased by SC heat treatment. EPFM tests of as-received and SC JRQ specimens were performed at 288 °C in hydrogenated and oxygenated HTW (2.5 to 25 µm/min) and in air (0.25 to 250 µm/min), which are summarized in Figure 83. The higher fracture initiation resistance for both as-received and SC JRQ materials at lower loading rates in air were due to DSA. The SC material with enhanced phosphorus GB segregation consistently showed a lower fracture initiation resistance than the as-received steel under all conditions, which is in line with its lower UTS and fracture strain in tensile tests in air. In good agreement with the low-sulphur steels with high DSA susceptibility [64][173], both the SC and as-received JRQ materials showed higher environmental reduction of fracture initiation resistance in hydrogenated than oxygenated HTW as depicted in Figure 83 and Figure 84. The environmental reduction in fracture initiation resistance in the JRQ material in hydrogenated and oxygenated HTW was significantly higher than what can be expected based on its low DSA susceptibility and sulphur content (Figure 85). All these observations very clearly indicate some potential synergies between hydrogen/HTW effects and TE susceptibility. Although a stronger environmental reduction of the fracture initiation resistance may be expected for the SC material, both heat treatment conditions revealed similar environmental reduction effects.

In air and HTW, stable ductile tearing by MVC was the dominating fracture mode in the JRQ material. Additionally varying amounts of QC regions and secondary cracking at inclusions and along the PAGBs were present in HTW as well. As indicated in Figure 86, the fracture surface of both SC and as-received JRQ material in oxygenated HTW had a lower roughness and smaller amount of secondary cracks and QC facets than in hydrogenated HTW, while the fracture surface after the EPFM test in air was purely ductile by MVC**.** As shown in the fractography, the secondary cracks in JRQ material have a more inhomogeneous distribution than in the other RPV steels. As expected, the fracture surface of SC specimens revealed a higher fraction of intergranular features, which was due to the weakening of the GBs by decohesion related to the phosphorus segregation. The intergranular features in JRQ material have a higher area fraction than in the other RPV steels. However, the absolute intergranular fraction was still low. In addition, there was no distinct difference between the intergranular fraction on fracture surface tested in HTW and in air.

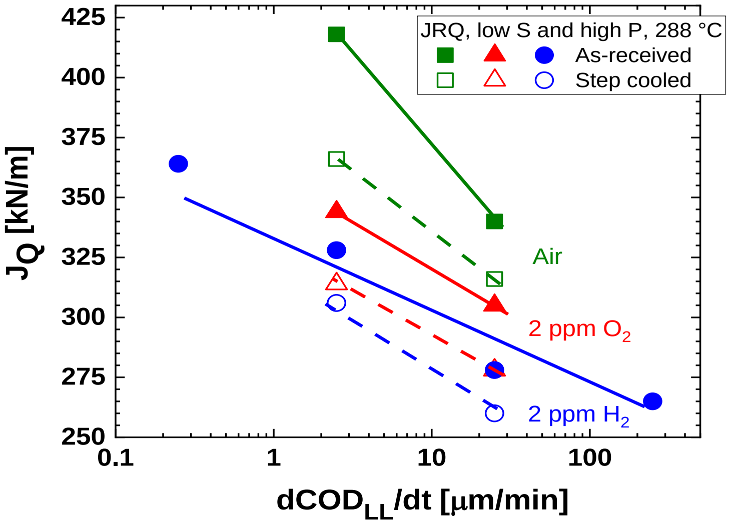

Figure 83: Fracture initiation resistance of as-received and step-cooled JRQ material in air, hydrogenated and oxygenated HTW at 288 °C with various loading rates.

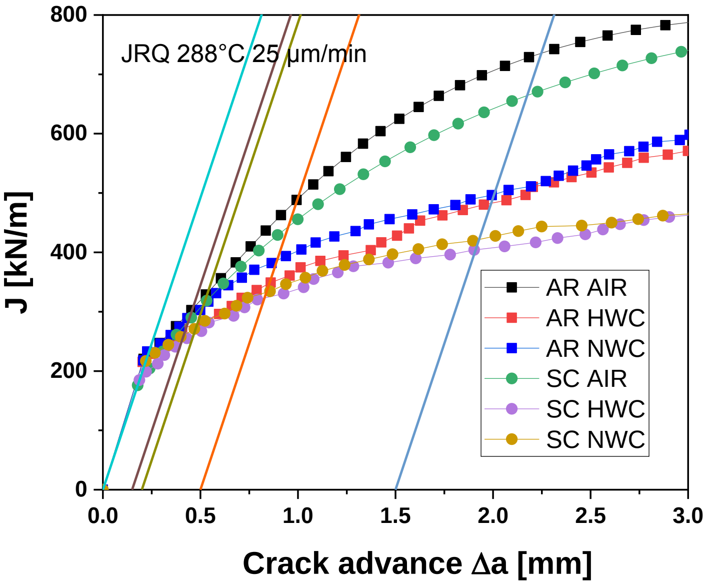

Figure 84: J-*R* curves of as-received and step-cooled JRQ material tested in air, hydrogenated and oxygenated HTW environments at 288 °C with 25 µm/min.

Furthermore, a few regions with very localized SICC features were observed in both SC and as-received materials in oxygenated and hydrogenated HTW (Figure 87) at loading rates of 2.5 and 25 µm/min. The local SICC features (in particular in hydrogenated HTW at the higher loading rate of 25 µm/min) indicate a potentially higher corrosion activity and increased local hydrogen content of regions with very high phosphorus enrichment (GB corrosion in TE is, e.g., observed in acidic solution at room temperature). These local SICC features also were significantly different from the occasionally observed macroscopic SICC in other materials at very slow loading rates (e.g., HSST, KS12 and 508 in oxygenated HTW or 277 in hydrogenated HTW). The EAC behaviour of LAS in HTW is dominated by the sulphur content and sulphides that are formed by the dissolution of MnS inclusions. Phosphorus content usually has no effect on macroscopic transgranular EAC growth rates and susceptibility. In the EAC tests at PSI with the high-phosphorus steel KS12, isolated local intergranular regions were sometimes observed, but their share was too low to significantly affect the macroscopic crack growth rate.

The reduction of fracture initiation resistance in hydrogenated and oxygenated HTW is higher than it was anticipated based on the ductility reduction in tensile tests in air with hydrogen pre-charged specimens (see Figure 37). Furthermore, the tensile specimens revealed no intergranular features. The reason for this is probably due to the much higher hydrostatic stress at the crack tip (about three times the yield stress) than in a tensile specimen with moderate necking and slight stress concentration, in addition to the increased local corrosion activity in phosphorus-enriched regions in HTW.

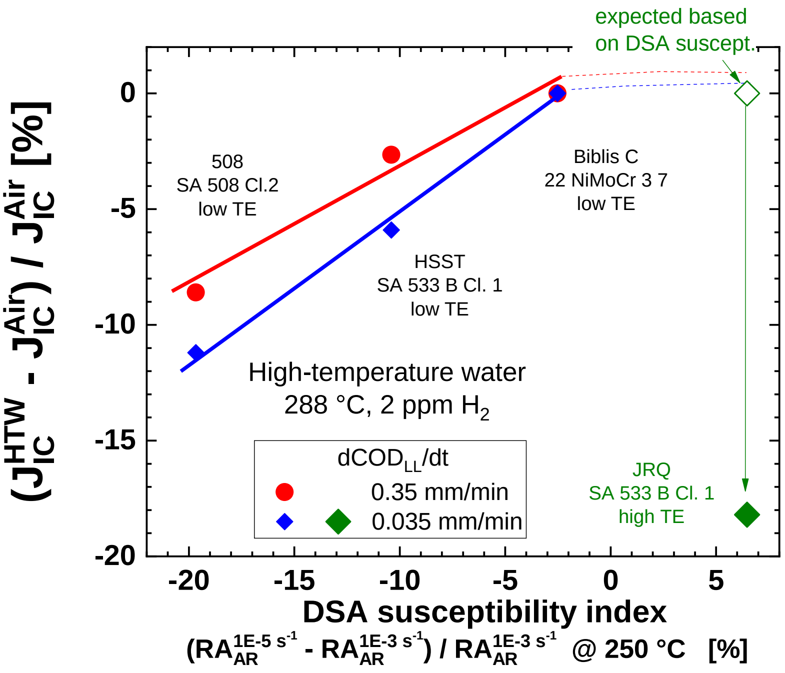

Figure 85: Correlation between environmental reduction of fracture initiation resistance and DSA susceptibility of different RPV steels in hydrogenated HTW. The JRQ steel shows a stronger reduction than it may be expected on its DSA susceptibility.

The low intergranular fraction is probably related to the low phosphorus content for TE (strong effects are usually observed above 0.03 wt.% phosphorus) and the low hydrogen availability and hydrogen trapping efficiency at GBs at 288 °C (see Figure 12 with trap binding energy of 58 kJ/mol). The very inhomogeneous phosphorus distribution (macro-segregation), the fine grain size (and large GB area), the increased temperature of 288 °C and the moderate (matrix) strength level of the RPV steels impede intergranular cleavage fracture along the PAGBs and the exceedance of the intergranular fracture stress (see Figure 7). At these temperature and strength levels, micro-void formation in the matrix is still the dominant fracture mechanism. The phosphorus enrichment around carbide particles in high-phosphorus steels due to carbide precipitation (extremely low phosphorus solubility in Fe_3C) and coarsening during tempering or long-term thermal ageing can weaken the interface between the carbide particle and matrix by decohesion. The weakening of boundaries can be in synergy with trapped hydrogen and potentially increased local corrosion rates in the phosphorus-enriched regions and facilitate micro-void formation.

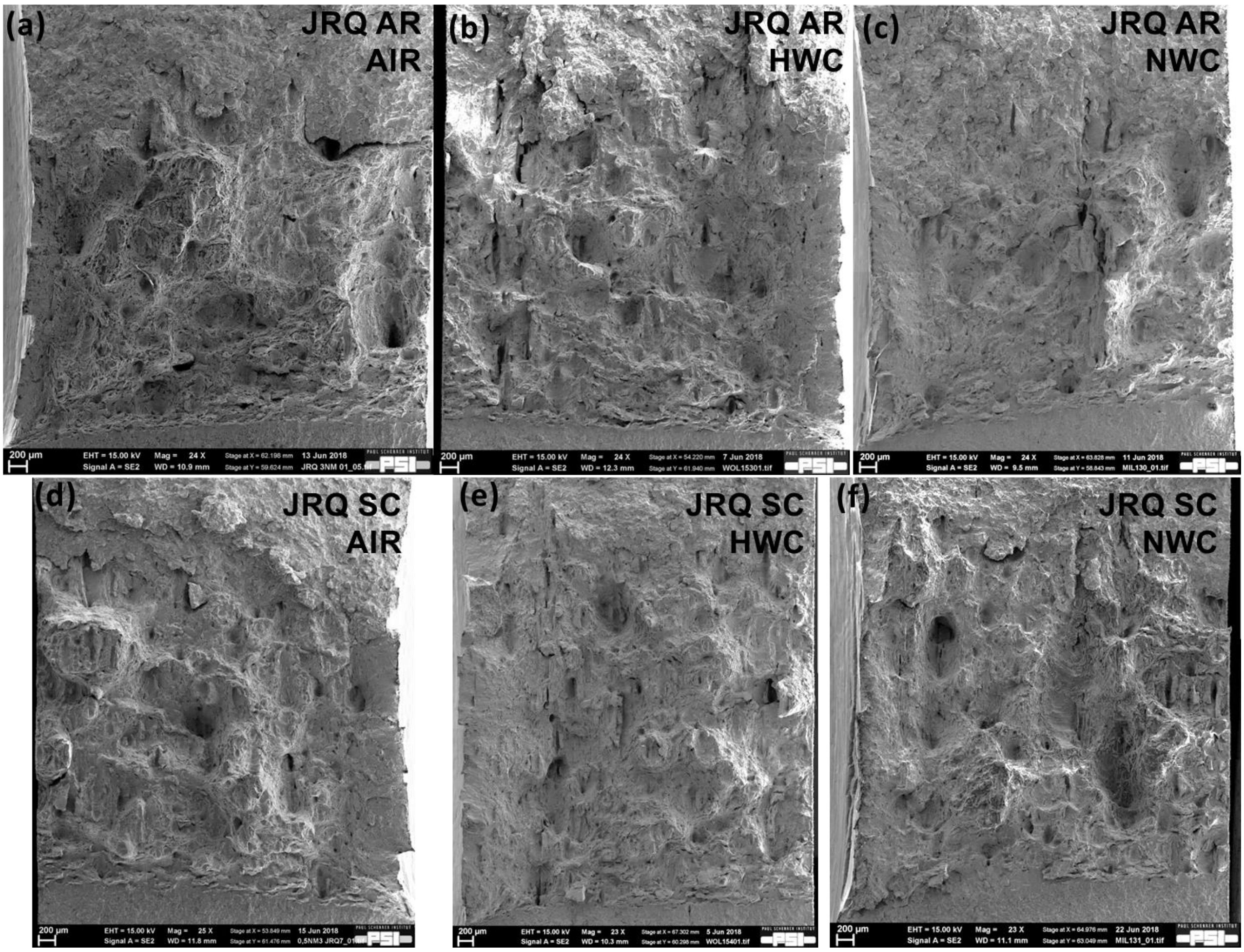

Figure 86: Fracture surface of as-received JRQ material tested with 25 µm/min at 288 °C in (a) air, (b) HWC and (c) NWC; fracture surface of step-cooled JRQ material tested with 25 µm/min at 288 °C in (d) air, (e) HWC and (f) NWC. The fracture surface of both step-cooled and as-received JRQ material in NWC had a smaller amount of secondary cracks and quasi-cleavage facets than in HWC, while the fracture surface after the EPFM test in air was mainly MVC.

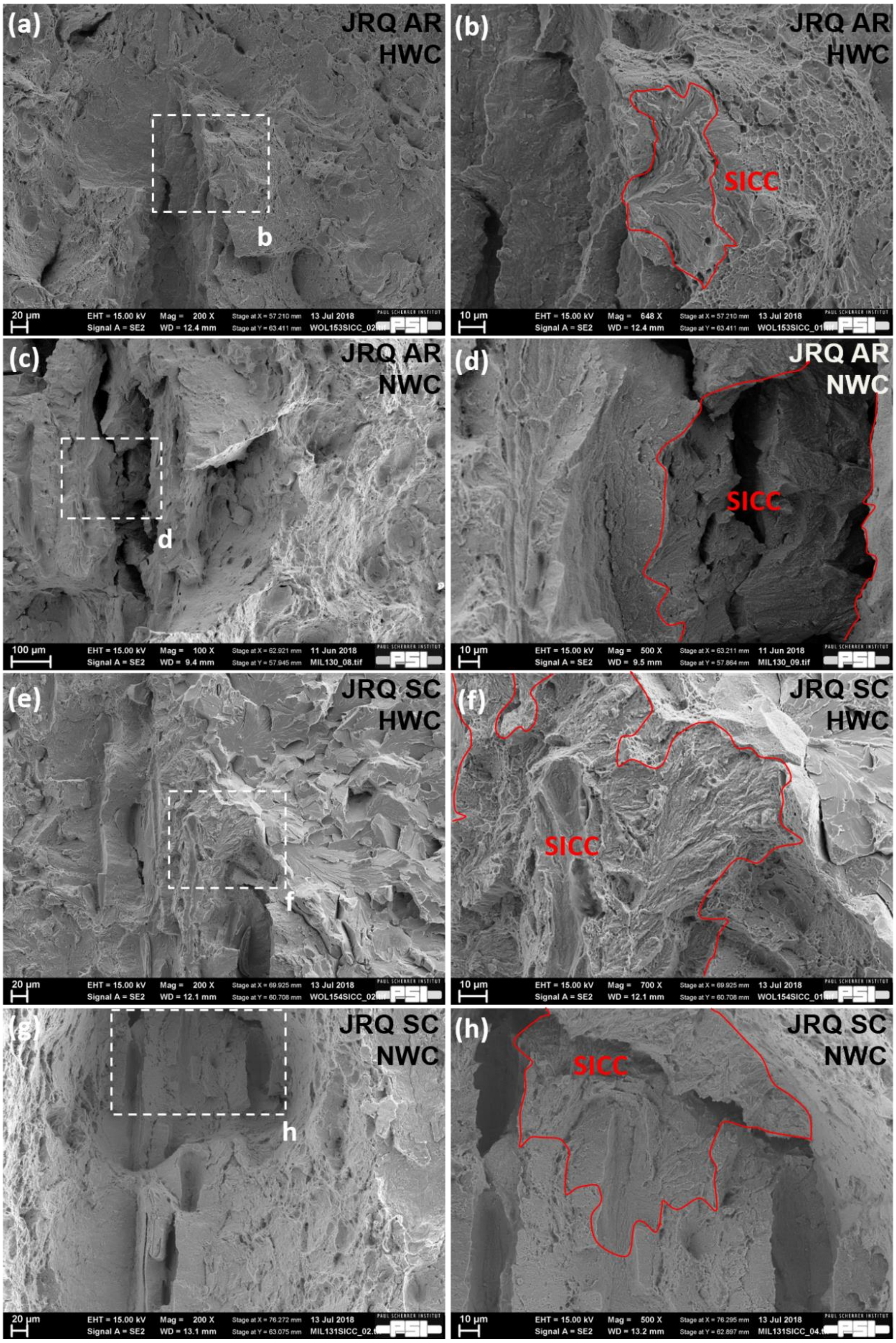
(a)
JRQ AR
HWC
b
20 µm
(b)
JRQ AR
HWC
SICC
10 µm
(c)
JRQ AR
NWC
d
100 µm
(d)
JRQ AR
NWC
SICC
10 µm
(e)
JRQ SC
HWC
f
20 µm
(f)
JRQ SC
HWC
SICC
10 µm
(g)
JRQ SC
NWC
h
20 µm
(h)
JRQ SC
NWC
SICC
10 µm

Figure 87: Fracture surface of as-received JRQ material tested with 25 µm/min at 288 °C in (a)–(b): HTW with 2 ppm H_2 and (c)–(d) HTW with 2 ppm O_2; fracture surface of step-cooled JRQ material tested with 25 µm/min at 288 °C in (e)–(f) HTW with 2 ppm H_2 and (g)–(h) HTW with 2 ppm O_2. Regions with limited and localized SICC features were observed in both step-cooled and as-received materials in oxygenated and hydrogenated HTW.

Efficient hydrogen trapping at the interface of (large) Fe_3C carbide particles is expected to be still effective at 288 °C due to the high trap binding energy of (large) Fe_3C carbides of about 84 kJ/mol (see Figure 12 and Table 4) vs. 58 kJ/mol for GBs. Therefore, TE can also facilitate transgranular fracture by MVC or fracture along the lath boundaries with the carbide precipitates. At lower temperatures, e.g., for the post-test fracture in liquid nitrogen, a higher share of intergranular cracking was observed, which supports the above-mentioned ideas.

The results suggested that the contribution from the DH in the crevice environment can be higher than that from the local corrosion reactions at the plastically strained crack tip in case of high hydrogen contents in the bulk environment for JRQ material. The EPFM test results in various HTW environments also suggest that TE effect dominates over crevice chemistry effect in low-sulphur and high-TE RPV steel, where low-sulphur crevice chemistry conditions are expected to prevail.

3.5.3 Fracture behaviour of KS12 material with high sulphur and high phosphorus contents

The KS12 steel has high sulphur and phosphorus contents and high EAC and TE susceptibilities as well as a low upper shelf toughness and a very inhomogeneous distribution of phosphorus and MnS inclusions (with clusters and segregation lines). The inhomogeneous phosphorus distribution was confirmed by previous EAC tests with this material in oxygenated HTW. These tests revealed a strong specimen-to-specimen variation in crack paths from almost purely transgranular to partially intergranular with little variation in EAC growth rates under identical test conditions.

EPFM tests were performed with this material in oxygenated and hydrogenated HTW with loading rates from 2.5 to 250 μm/min at 288 °C including tests with preceding SICC or SCC cracking growth (chloride addition). Based on the previously described interactions between EAC and TE susceptibilities with hydrogen and HTW effects on the fracture initiation resistance of the HSST and JRQ steels, particularly strong environmental effects were expected for the KS12 material. However, due to the limited amount of specimens and very strong specimen-to-specimen variation in upper shelf fracture initiation resistance (30% or more), no clear conclusions can be derived with regard to the environmental degradation effects in this steel. In some cases, e.g., at the standard loading rate of 250 μm/min, the fracture initiation resistance in oxygenated HTW (where moderate environmental effects are expected) was almost 30% higher than in air. The frequent occurrence of SICC in tests with slow loading rates and tearing instabilities after reaching the peak load in EPFM tests further complicated the identification of environmental effects. Qualitatively, similar trends were observed in the tests on KS12 material as on the high-sulphur HSST steel for the slow loading rates of 2.5 μm/min (Figure 88) and 25 μm/min. Such an inhomogeneous material requires a large number of tests to derive statistically accurate conclusions and the careful selection of specimen from the same locations with similar microstructure.

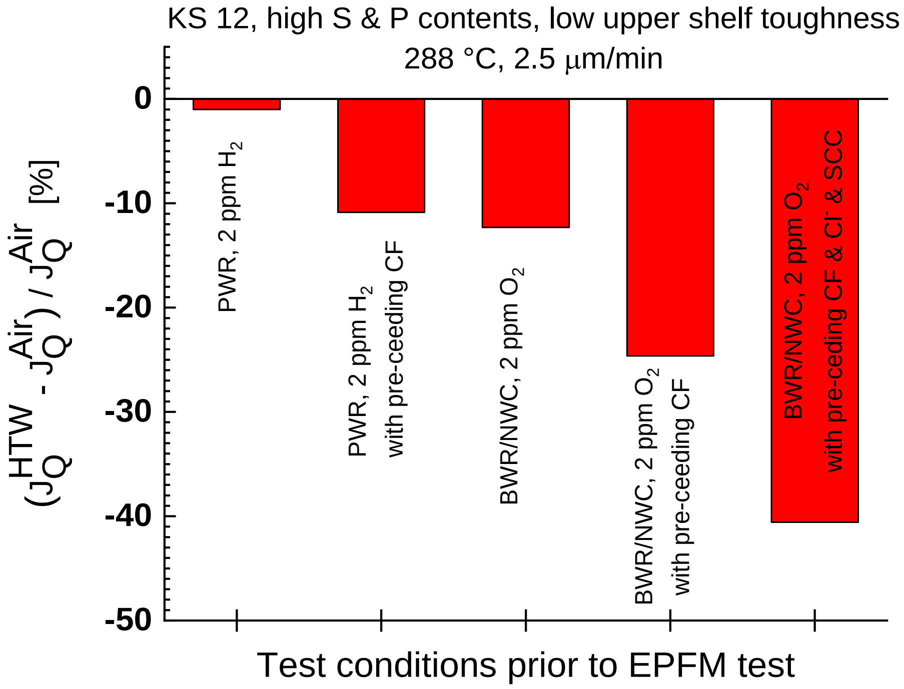

Figure 88: Effect of water chemistries and preceding EAC crack growth on the reduction in fracture initiation resistance of KS12 steel with loading rate of 2.5 µm/min. Similar effects as for the high-sulphur steel HSST (Figure 81).

Although clear conclusions can not be drawn due to the scatter issue, some fractographic observations support the evidence of environmental effects. Interestingly, in contrast to the high-phosphorus JRQ steel with high TE susceptibility, almost no intergranular cracking was observed in the KS12 material, but this can be partially related to the very inhomogeneous phosphorus distribution and strong aggregates of sulphide inclusions in this steel. The general fracture surface appearance was also quite different from that in the HSST material, which has a similar high sulphur content and high EAC susceptibility. The surface roughness was very high for all specimens of KS12 tested in air and the various HTW environments. The fracture appearance had a terrace-like structure with higher and lower plateaus as well as a mixed mode of QC and ductile features, as shown in Figure 89. The deep plateaus or macro-cavities were usually related to clusters of sulphide inclusions. Such plateaus were observed for KS12 both in air and HTW, but not for the high-sulphur HSST steel with more homogeneous sulphide distribution. EDX mapping of polished cross section perpendicular to the crack plane and growth direction confirmed that the remaining inclusions were mainly sulphides (MnS or CaS) (Figure 90). In oxygenated and hydrogenated HTW, many secondary cracks were found right beneath the position of plateaus with sulphide clusters, which was not the case in the corresponding air tests. The secondary crack formation is an indirect evidence for the environmental effects on the fracture initiation resistance in KS12 steel.

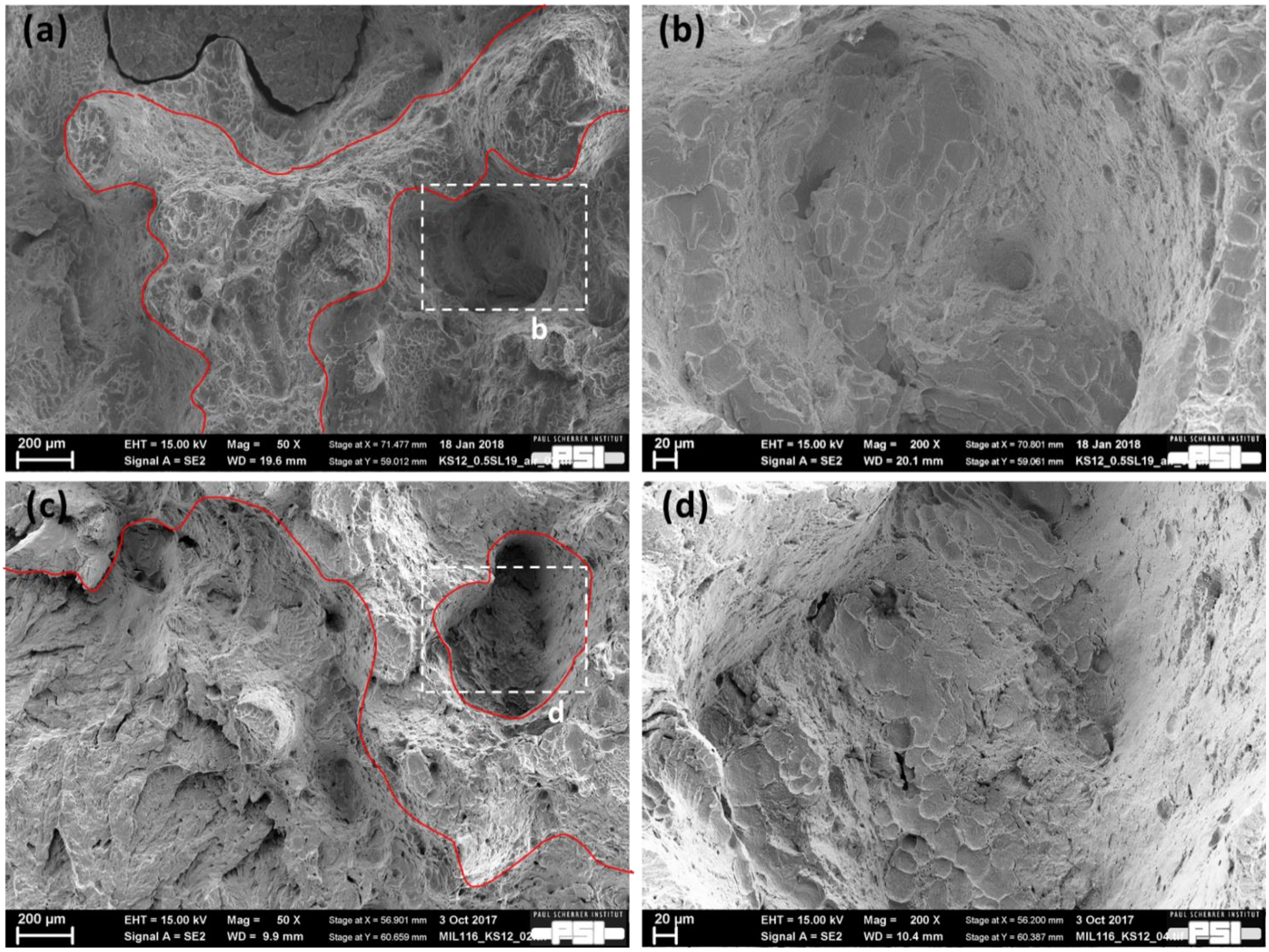
(a)
b
200 µm
EHT = 15.00 kV
Mag = 50 X
Signal A = SE2
WD = 19.6 mm
Stage at X = 71.477 mm
Stage at Y = 59.012 mm
18 Jan 2018
(b)
20 µm
EHT = 15.00 kV
Mag = 200 X
Signal A = SE2
WD = 20.1 mm
Stage at X = 70.801 mm
Stage at Y = 59.061 mm
18 Jan 2018
(c)
d
200 µm
EHT = 15.00 kV
Mag = 50 X
Signal A = SE2
WD = 9.9 mm
Stage at X = 56.901 mm
Stage at Y = 60.659 mm
3 Oct 2017
(d)
20 µm
EHT = 15.00 kV
Mag = 200 X
Signal A = SE2
WD = 10.4 mm
Stage at X = 56.200 mm
Stage at Y = 60.387 mm
3 Oct 2017
PAUL SCHERRER INSTITUT
PSI

Figure 89: Fracture surface of KS12 steel tested with 25 µm/min at 288 °C in air (a to b) and in oxygenated HTW with 2 ppm O_2 (c to d).

EDX mapping at the tip of these deep secondary cracks indicated the existence of some remaining sulphide inclusions. The matrix material was partially dissolved and some cavities/crevices were formed. Besides, the traces of iron oxide precipitates or oxide film were discovered around the secondary crack tip, revealing that oxidation or corrosion reactions took place up to several millimetres below the plateau on the fracture surface. These distinct secondary cracks were strongly promoted by the sulphide inclusions, but were not observed in previous EAC tests at lower K_I values. The secondary cracks have been formed by HAEAC and/or dissolution. During the EPFM tests, the generated secondary cracks were under bending stress and Mode-I crack opening in the C(T) specimens. Therefore, the oxide film were ruptured under the bending stress and the anodic dissolution of the metal matrix occurred until a new protective oxide film formed. This process provided an additional source of hydrogen that facilitated the hydrogen uptake to the metal lattice and HAEAC. Additionally, the undissolved MnS inclusions ahead of crack tip may also act as strong hydrogen traps and HAEAC initiation sites. The formation of the secondary cracks makes the crevice chemistry of the main crack more aggressive, increases the local content of sulphur anions and hydrogen concentration and can finally assist in reducing the fracture initiation resistance in HTW.

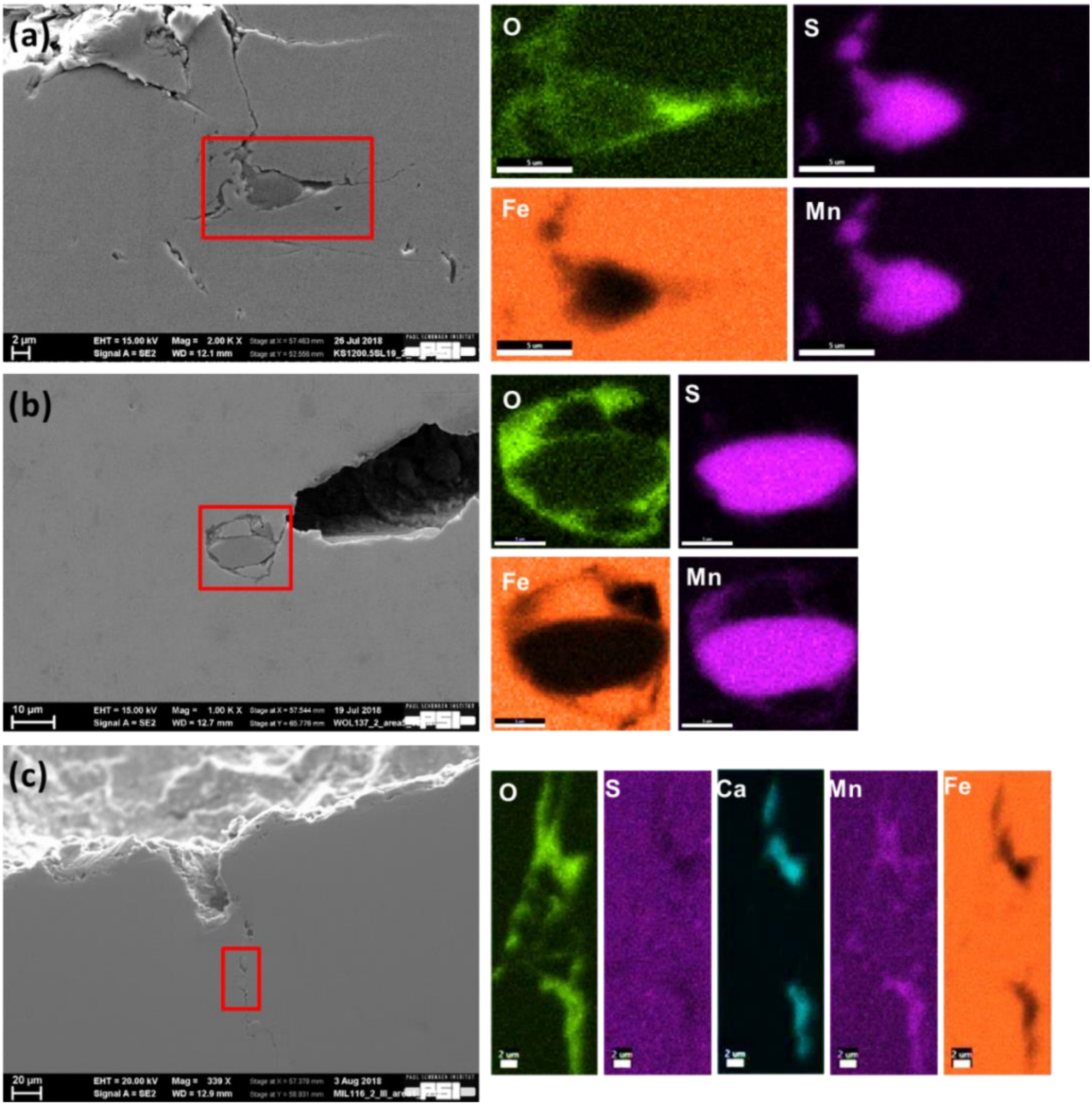
(a)
O
S
Fe
Mn
2 µm
EHT = 15.00 kV
Signal A = SE2
Mag = 2.00 K X
WD = 12.1 mm
26 Jul 2018
(b)
O
S
Fe
Mn
10 µm
EHT = 15.00 kV
Signal A = SE2
Mag = 1.00 K X
WD = 12.7 mm
19 Jul 2018
(c)
O
S
Ca
Mn
Fe
20 µm
EHT = 20.00 kV
Signal A = SE2
Mag = 339 X
WD = 12.9 mm
3 Aug 2018
2 µm
PSI

Figure 90: SEM and EDX investigations on secondary cracks of KS12 specimens tested at 288 °C with 25 µm/min in (a) air, (b) hydrogenated HTW and (c) oxygenated HTW.

3.5.4 Discussion of the effect of EAC and TE susceptibility

In the Biblis C base metal material with low sulphur and phosphorus contents and low DSA, EAC and TE susceptibilities, environmental effects on fracture initiation resistance were absent or marginal in both oxygenated and hydrogenated HTW [5][63]. The HSST steel with high sulphur content and high EAC, but low and moderate TE and DSA susceptibilities, showed environmental reduction of fracture resistance in both environments. The environmental effects were more pronounced in oxygenated HTW. In the JRQ material with high phosphorus and low sulphur contents and high TE, but low EAC and DSA susceptibilities, the environmental reduction effects were more pronounced in hydrogenated HTW. Additionally, low-sulphur steels with high DSA susceptibility also revealed stronger effects in hydrogenated HTW [5][173].

In the high-sulphur HSST steel, the more pronounced effect of steel sulphur content and stronger reduction in oxygenated HTW was related to the sulphide enrichment in the crack crevice environment. Sulphide enrichment by migration is due to the potential gradient in the crack-mouth region in oxygenated water as described in Section 1.3.4. This produces an aggressive high-sulphur crevice environment with high hydrogen uptake potential in the steel. DH content of the bulk environment only plays a secondary role here. Furthermore, the MnS inclusions may act as strong hydrogen traps in the process zone at the crack tip. However, this trapping effect can be less important as suggested by the moderate ductility reduction in tensile tests on HSST in air with hydrogen pre-charging [5]. A stronger localized deformation at the crack tip was discovered for HSST material in oxygenated than in hydrogenated HTW or air, as shown in Figure 91. Tiny grains formed by severe localized plastic deformation were observed at the crack tip after tests in oxygenated HTW. In contrast, grains with cell-like structure were observed in hydrogenated HTW. As depicted in the GROD maps, the local orientation deviations are higher in the case of NWC environment, which indicates a higher level of localization of plastic deformation. Therefore, a considerable amount of dislocations moved and piled-up in the front of the crack tip in NWC, as indicated in the GROD mapping in Figure 91 (c), (f) and (i). The aggressive occluded crack crevice chemistry increases the hydrogen availability and uptake potential, which results in higher level of localization of plastic deformation at crack tip. The localization of plastic deformation can be explained by the HELP mechanism, where hydrogen may form Cottrell atmospheres around dislocation cores that decrease dislocation-dislocation and dislocation-obstacle interactions (shielding effect).

As revealed by the EPFM tests with the JRQ material, there is a potential interaction of hydrogen and TE susceptibility in environmental reduction of fracture initiation resistance. In line with the other low-sulphur steels, the environmental reduction of fracture initiation resistance was higher in hydrogenated HTW. Both in oxygenated and hydrogenated HTW, the effects were higher than it may be expected based on the low sulphur content and DSA susceptibility, indicating the TE effect. The failure mode was not intergranular, but still transgranular dominated by ductile MVC with additional small amounts of secondary cracking, macro-voids, QC, intergranular cracking and local SICC in HTW. The intergranular cracking fraction in the SC conditions was higher than in the as-received conditions or than in the other RPV materials. The environmental reduction of the fracture initiation resistance of JRQ material in hydrogenated HTW at a loading rate of 25 μm/min is 18%. This value was significantly higher than in the other steels with comparable low DSA susceptibility. The environmental reduction is 1% (Biblis C, low sulphur) and 4% (HSST, high sulphur) under the identical conditions. This value is also slightly higher than the environmental reduction of 15 to 16% in the two low-sulphur steels with high DSA susceptibility. Together with the lower fracture initiation resistance of the SC material in both air and HTW, this suggests that TE may play a role in spite of the low intergranular cracking fraction.

The interaction of weakened GBs by HEDE and TE (phosphorus segregation to GBs), and localized deformation (by HELP and DSA) may result in local intergranular cracking at lower stresses/strains than without hydrogen. The intergranular cracking is rather caused by the described mechanical effect that may be further amplified by the potentially increased corrosion rates of the phosphorus-enriched GBs. The relatively low area fraction of intergranular cracking can be related to several reasons. The high TE susceptibility of the JRQ steel in this context is just a relative ranking among the investigated RPV materials and with respect to (modern) Western RPV steels. The TE susceptibility of JRQ material is still moderate. The hydrogen availability in HTW and hydrogen trapping efficiency at GBs at 288 °C are too low for significant GB embrittlement by the HEDE mechanism. The moderate matrix strength with a yield stress of about 400 MPa is not favouring HE. The TE and weakening of GBs increase with phosphorus and impurity contents, larger grain size CGHAZ or increased strength and can be further enhanced by irradiation enhanced diffusion. A larger grain size and higher strength also increase the HE susceptibility. Intergranular cracking in the EPFM tests is dependent on the local stress and strength ratios between the GB and intra-grain region. The intergranular cleavage stress is only slightly dependent on temperature and it decreases with phosphorus content on the GBs. In contrast, the yield stress in bcc alloys strongly increases at low temperatures, but is hardly influenced by the phosphorus content. This favours the intergranular cleavage at low temperatures and seems to be confirmed by the higher intergranular cracking fraction in the post-test fracture at liquid nitrogen temperature. The phosphorus enrichment around carbide particles in high-phosphorus steels due to carbide precipitation (extremely low phosphorus solubility in Fe_3C) and coarsening during tempering or long-term thermal ageing can weaken the interface between the carbide particle and matrix by decohesion, eventually in synergy with trapped hydrogen and increased local corrosion rates, and facilitate micro-void formation. Therefore, TE can also facilitate transgranular fracture by MVC or fracture along the lath boundaries with the carbide precipitates. The interaction of TE with hydrogen and HTW on fracture initiation resistance is a bigger concern for LAS turbine discs or bolt steels with high strength or for RPV steels after irradiation. The CGHAZ of the pressurizer welds (with less stringent limits for phosphorus content than for the core beltline region of RPVs and potentially higher bulk phosphorus contents) with higher operating temperatures around 350 °C may show the highest TE potential during service and long-term operation.

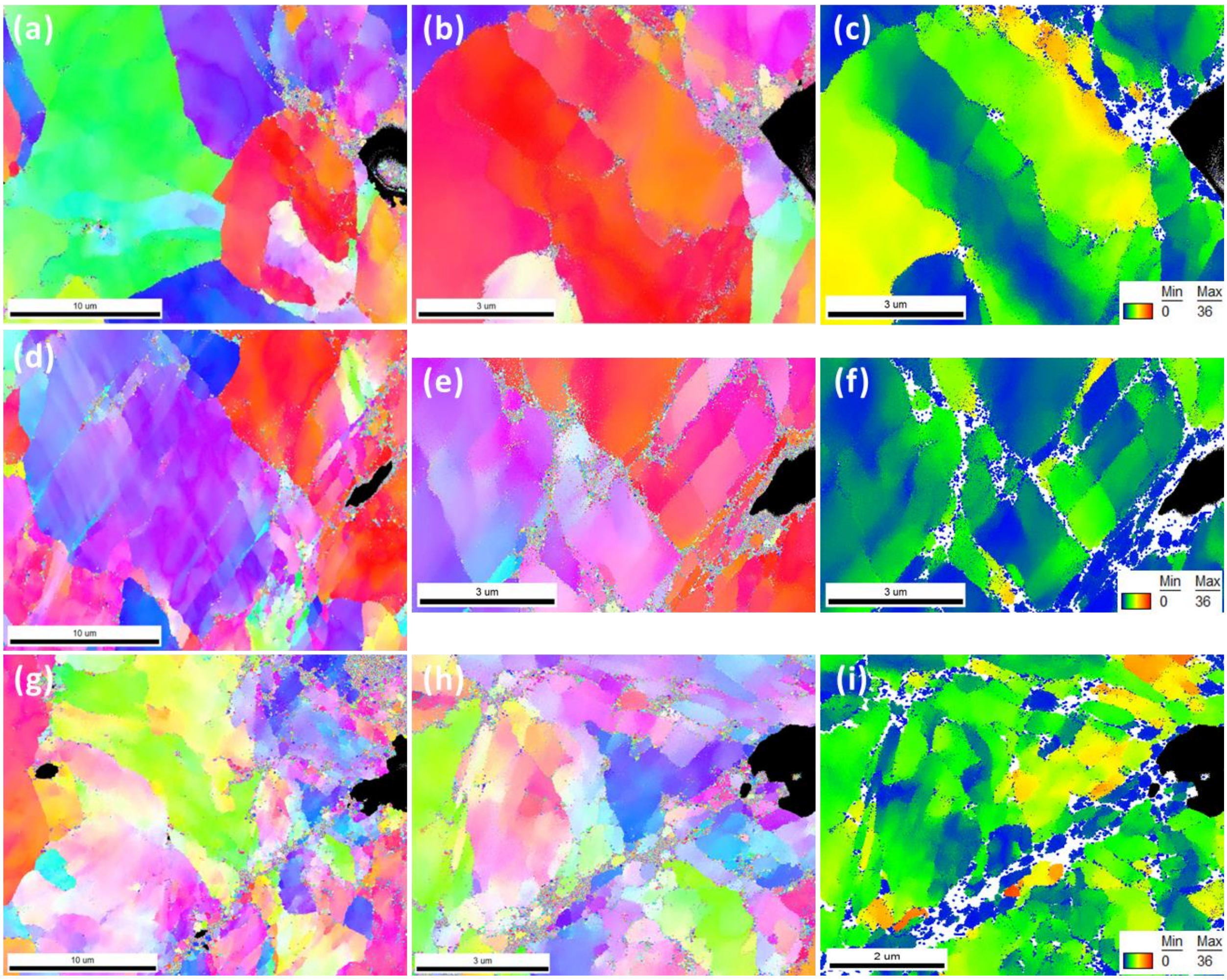

Figure 91: (a) to (c), (d) to (f) and (g) to (i) EBSD maps at crack tips of HSST material tested in air ($J_{Q, AIR}$ = 302 kN/m), hydrogenated HTW ($J_{Q, HWC}$ = 273 kN/m) and oxygenated HTW ($J_{Q, NWC}$ = 235 kN/m) at 288 °C with 250 μm/min, respectively. ((c), (f) and (i) show grain reference orientation deviation mapping with an angle range of 0^o to 36^o).

The observed void formation and QC crack growth occur at lower strains/stresses in HTW than in air or hydrogen-free conditions. The inter-void strain localization and accumulation of hydrogen in these zones increased localized plastic strain (HELP) and/or the early formation and growth of micro-voids at carbide particles by the HELP, TE and HESIV mechanisms. The localized deformation areas are preferred regions for hydrogen enrichment and accumulation, which further amplifies the localization of plastic deformation by hydrogen with autocatalytic positive feedback effects. The observed fracture behaviour of RPV steels with either high sulphur or high phosphorus contents in this study suggests a combination of the HESIV and HELP mechanisms together with minor contributions of HEDE. HESIV and HELP are enhancing ductile failure by MVC, but also facilitating brittle cleavage or QC cracking. The similarities of the fracture morphologies in HTW and hydrogen pre-charged specimens in air (Figure 38) with the same RPV steels [5] further confirmed that hydrogen is the main reason for the environmental reduction of fracture initiation resistance in HTW. There is clear evidence of moderate reduction in fracture initiation resistance in HTW in RPV steels with high EAC and TE susceptibilities, which demonstrated the synergies of HTW/hydrogen with DSA, EAC and TE effects.

3.6 Fracture mode and mechanisms

The fracture and deformation mechanism were studied by various techniques like SEM/EDX/EBSD/ECCI/STEM as well as by nano-indentation, TDS and micro-hardness measurements. The TDS, nano-indentation and micro-hardness measurements are still ongoing and not yet fully evaluated, but the following preliminary conclusions can be summarized as follows:

The tensile tests in air with hydrogen pre-charged specimens revealed a clear change in macroscopic fracture mode from the classical cup and cone fracture with ductile dimples to a shear-dominated fracture with shear dimples that was inclined at 45 ° angle (Figure 38). This change was not observed in tensile tests in hydrogenated HTW with smooth or notched specimens. In addition, additional and varying, but small amounts of secondary cracking, macro-voids, QC and intergranular cracking were observed in hydrogen pre-charged specimens and tests in HTW (Figure 39). Their relative share on the fracture surface was much higher in the hydrogen pre-charged specimens with higher hydrogen content, which is in good agreement with the higher degree of HE (with the exception of JRQ material).

The failure mode in EPFM tests in air with un-charged specimens was always pure ductile MVC. The fracture surface of the corresponding tests in HTW and with hydrogen pre-charged specimens always had a significantly rougher surface and contained additionally small and varying amounts of secondary cracking, macro-voids and QC (typically a very few % in total) as shown in Figure 92 to Figure 95. Apart from the higher roughness and presence of some macro-voids, the ductile part (shape, number and size distribution of voids) in specimens tested in HTW and air was very similar, which does not imply the absence of hydrogen effects. Some steels (e.g., KS12, HSST) sometimes also contained some very localized intergranular cracking features with a very low total area share on the fracture surface. The JRQ steel with high phosphorus content and high TE susceptibility showed a significantly higher share of intergranular fracture than the other RPV steels, but the absolute value was still small. The total area share of all these features on the fracture surface was typically a magnitude lower than the observed reduction in fracture initiation resistance in HTW. Therefore, these fractographic features are not the sole or main reason for the environmental reduction in fracture initiation resistance. Both in air and HTW, the crack path had the typical zig-zag shape of ductile fracture (see Section 1.2.1).

Macro-voids (Figure 92) and secondary cracks (Figure 93) were often related to inclusions like MnS and Al_2O_3 and clusters of them, but not exclusively. They are known to be strong traps for hydrogen and to be preferred initiation sites for both brittle micro-crack initiation and micro-void nucleation. This also applies to the smaller carbide precipitates. Furthermore, the dissolution of MnS (locally) increases the hydrogen uptake and they are the typical initiation sites for EAC with the typical fan-shaped SICC features with feather morphology. Relatively flat local QC features with plastic tear ridges at their borders were observed, often in connection with inclusions (Figure 94). Some of them resembled hydrogen flakes, but there was a strong variation in their appearance. At higher magnification, some of the QC features and the intergranular cracks (Figure 95) contained some nano-sized features, which eventually can be caused by the very fine precipitates, GB segregation or nano-voids (Figure 95).

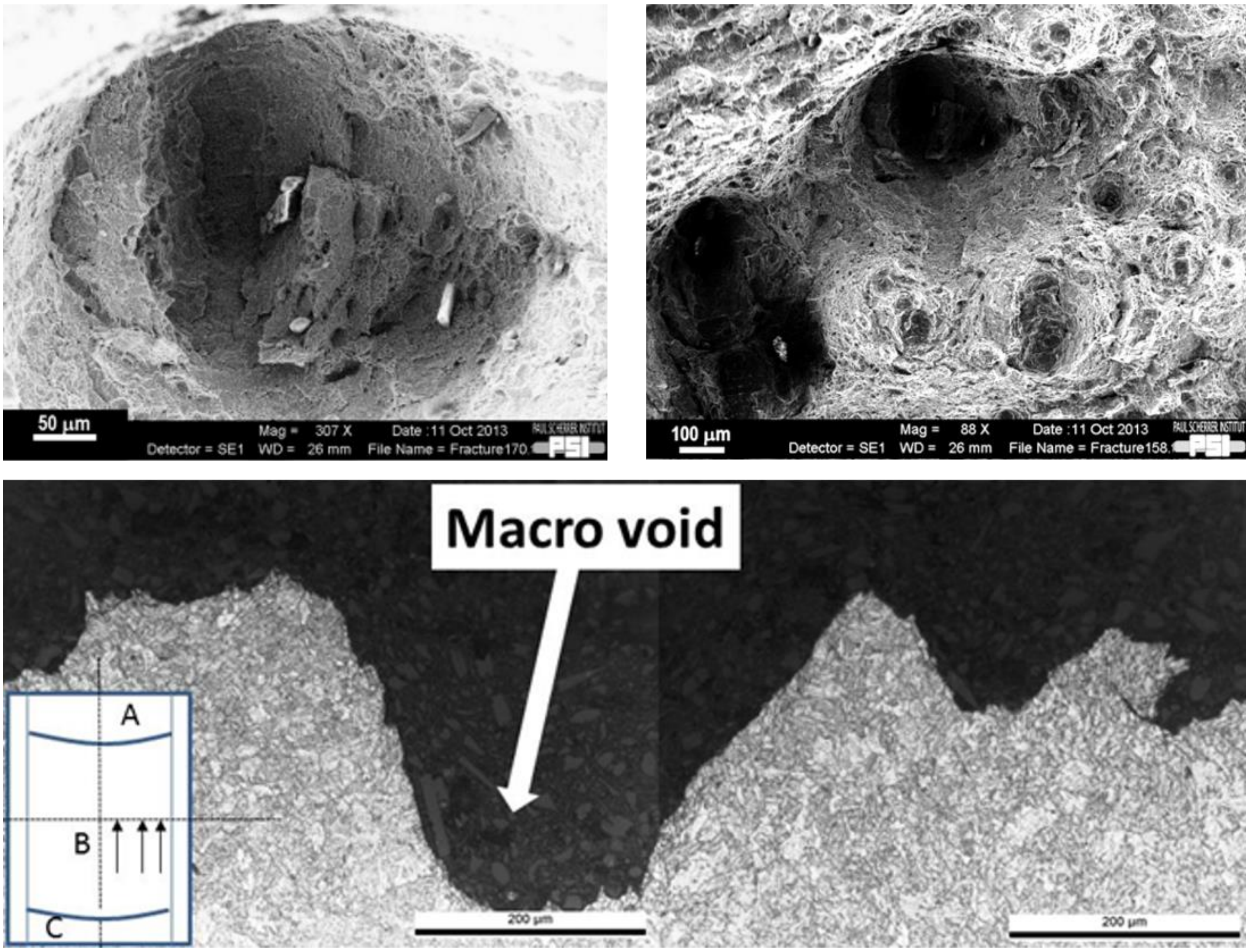
50 µm
Mag = 307 X
Date :11 Oct 2013
Detector = SE1
WD = 26 mm
File Name = Fracture170
PSI
100 µm
Mag = 88 X
Date :11 Oct 2013
Detector = SE1
WD = 26 mm
File Name = Fracture158
PSI
Macro void
A
B
C
200 µm
200 µm

Figure 92: Examples of macro-voids after EPFM tests in HTW. (*A*: pre-crack by fatigue in air; *B*: cross section of crack propagation path; *C*: end of EPFM test).

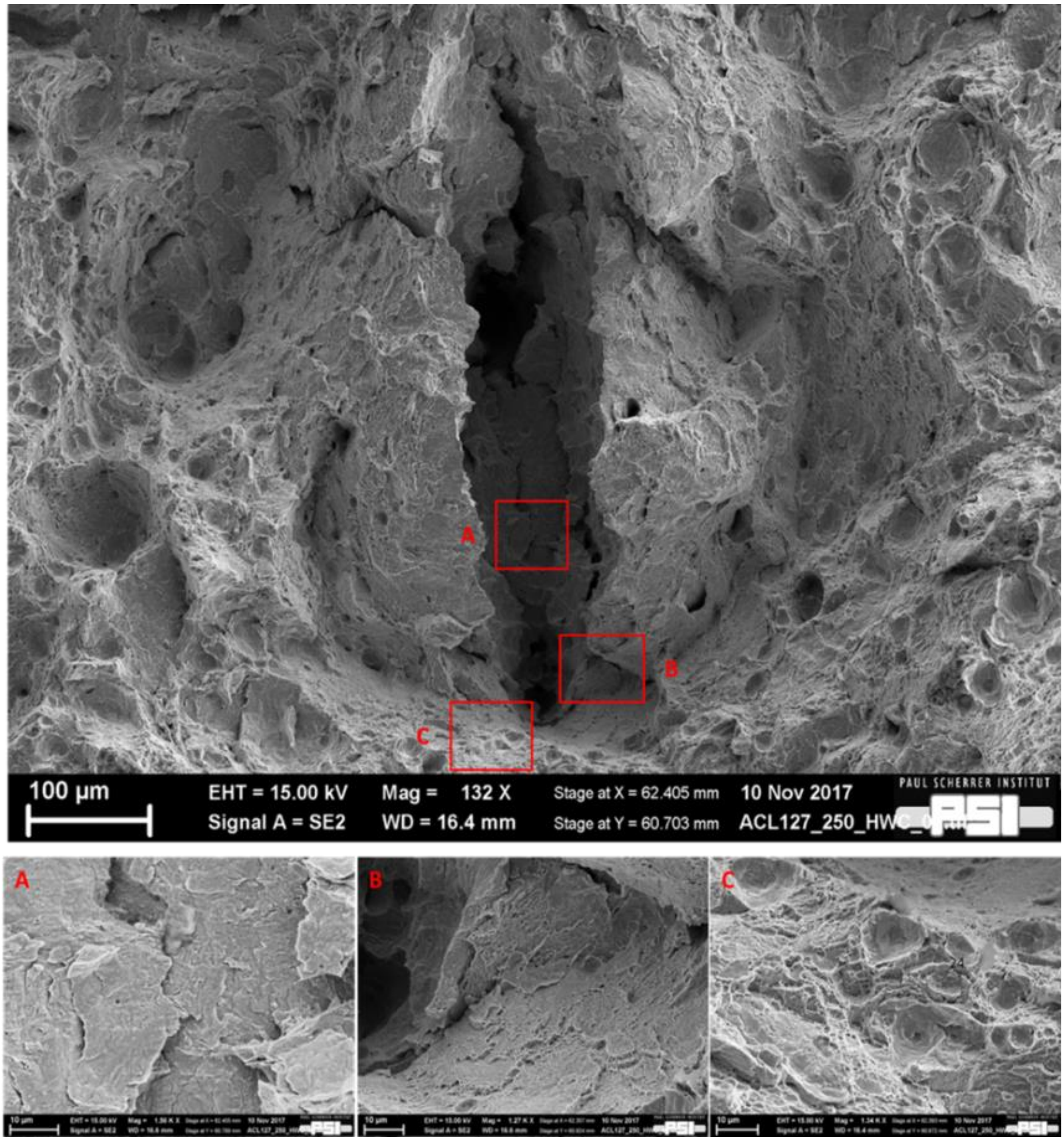
A
B
C
100 µm
EHT = 15.00 kV
Signal A = SE2
Mag = 132 X
WD = 16.4 mm
Stage at X = 62.405 mm
Stage at Y = 60.703 mm
10 Nov 2017
ACL127_250_HW
PAUL SCHERRER INSTITUT
PSI
A
B
C

Figure 93: Example of secondary crack with "brittle" quasi-cleavage features (*A* and *B*) and ductile micro-voids at the border of the cavity (*C*).

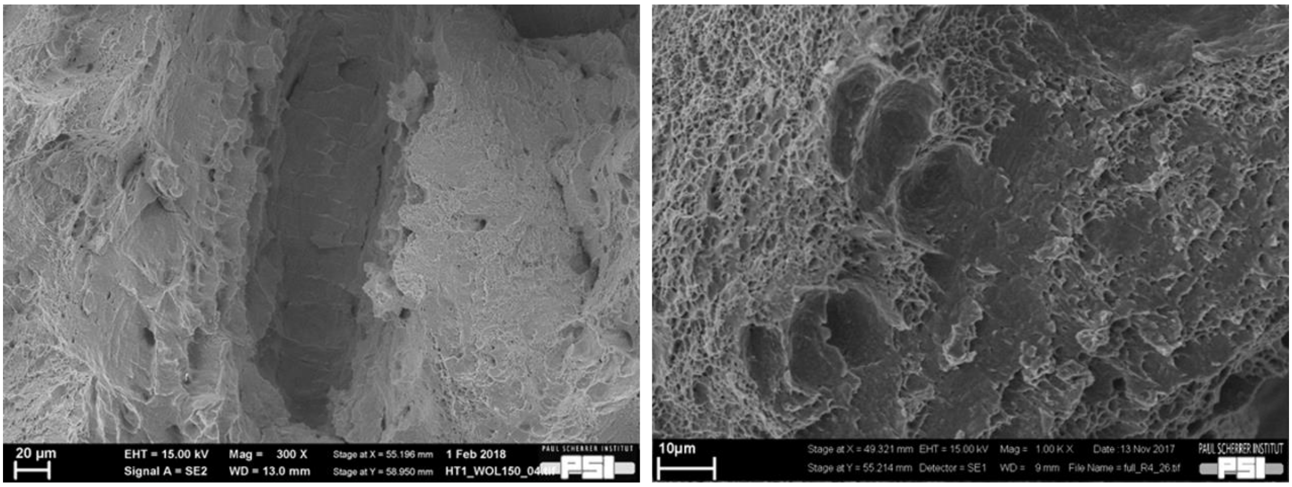
20 µm
EHT = 15.00 kV
Mag = 300 X
Stage at X = 55.196 mm
1 Feb 2018
Signal A = SE2
WD = 13.0 mm
Stage at Y = 58.950 mm
PAUL SCHERRER INSTITUT
PSI
10µm
Stage at X = 49.321 mm
EHT = 15.00 kV
Mag = 1.00 K X
Date :13 Nov 2017
Stage at Y = 55.214 mm
Detector = SE1
WD = 9 mm
File Name = full_R4_26.tif
PAUL SCHERRER INSTITUT
PSI

Figure 94: Examples of various local "brittle" and relatively flat quasi-cleavage features on the fracture surface after EPFM tests in HTW or tensile tests after hydrogen pre-charging.

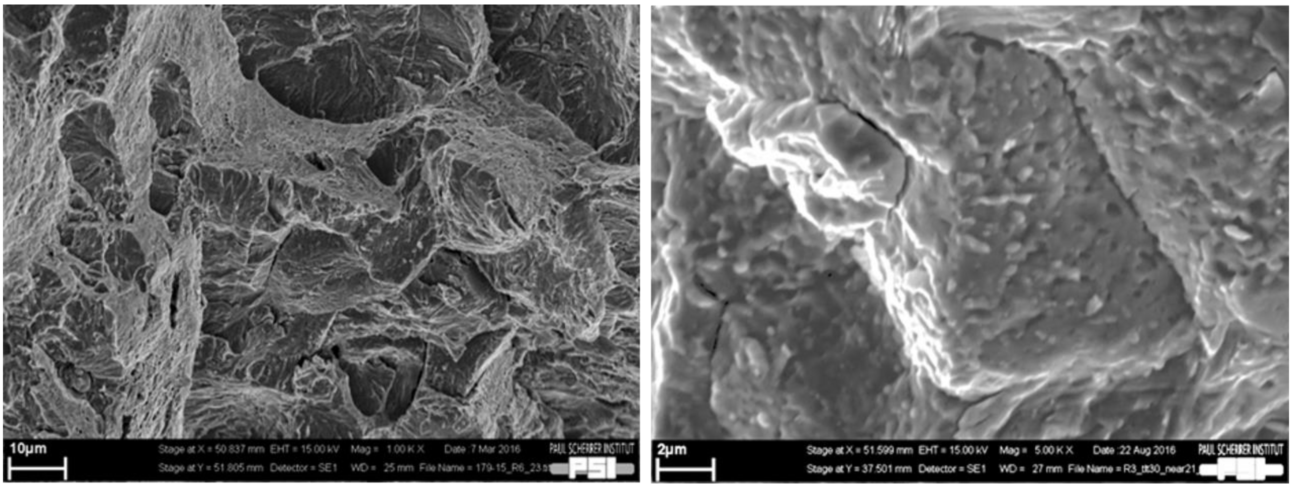
10µm
Stage at X = 50.837 mm
EHT = 15.00 kV
Mag = 1.00 K X
Date :7 Mar 2016
Stage at Y = 51.805 mm
Detector = SE1
WD = 25 mm
PAUL SCHERRER INSTITUT
PSI
2µm
Stage at X = 51.599 mm
EHT = 15.00 kV
Mag = 5.00 K X
Date :22 Aug 2016
Stage at Y = 37.501 mm
Detector = SE1
WD = 27 mm
PAUL SCHERRER INSTITUT
PSI

Figure 95: Examples of intergranular fracture features after tensile testing with hydrogen pre-charged specimens in air with grain boundary precipitates and/or nano-void features.

The similarities of the fracture modes in HTW and hydrogen pre-charged specimens and the similar parameter effects suggest that hydrogen is the main reason for the environmental reduction of fracture initiation resistance in HTW. Significant plastic straining and high plastic strains are necessary for distinct HE effects at temperatures of 150 to 300 °C, which further indicates that hydrogen-dislocation and hydrogen-vacancy interactions play a central role. The observed behaviour suggests a combination of plastic strain localization by the HELP mechanism, in synergy with DSA and HESIV mechanisms with additional minor contributions of HEDE. HESIV (and HEDE and TE) facilitates micro-void formation that occurs at lower strains/stresses than without hydrogen. HELP and DSA may further facilitate the inter-void strain localization and micro-void formation at smaller particles in these regions. Both together can result in a completely ductile failure mode as in air without hydrogen! HEDE promotes micro-crack formation at inclusions or intergranular cracking. The interaction of localized deformation regions (by HELP) with weakened grain and phase (MnS, Al_2O_3, carbides) boundaries (through HEDE/TE) can cause brittle cracking at lower stresses/strains than without hydrogen. These effects are linked, since plastic deformation inevitably produces a large amount of extra vacancies by dislocation interactions. Anodic dissolution at the bare crack tip also produces some extra vacancies in the steel. Vacancies and their clusters in turn affect the movement of dislocations. An increased vacancy cluster concentration in the presence of hydrogen was confirmed by unpublished Positron Annihilation Spectroscopy measurements at PSI.

The deformation structures in the bulk and at crack tips were therefore characterized by STEM. The complex fine-grained bainitic microstructure with high density of fine-dispersed, various carbide precipitates and high dislocation density in the undeformed state make such evaluations rather challenging and our preliminary conclusions are described as below. STEM investigations were performed on fracture mechanics specimens of 277 material with high DSA susceptibility, which were tested at 288 °C with 35 µm/min in air and in hydrogenated HTW, respectively. The environmental reduction of fracture initiation resistance in hydrogenated HTW from that in air was around 15%. As shown by the STEM investigations in Figure 96, more regions with a high degree of strain localization were observed in specimens tested in HWC. Hydrogen may impede cross slip of dislocations and favour planar and coarse slip, resulting in stronger localization of plastic deformation in synergy with DSA effect. Such localized plastic deformation regions with high strain concentration may become preferred sites for further hydrogen accumulation and void nucleation. At a higher magnification, well-developed 3D dislocation cell structures were observed in the specimens tested in hydrogenated HTW, which implies the dislocation movement by cross slip and climb. For specimens tested in air, such a clear cell structure was not observed and they had a dislocation structure of tangled appearance.

The ongoing EBSD, ECCI and STEM investigations of crack-tips from EPFM tests in air and HTW did not reveal any macroscopic shear band formation (as it is typically observed in static strain ageing, e.g., Lüders bands). The localization of plastic deformation was restricted to the direct vicinity of the crack tip, which is the region with the highest equivalent plastic strain and hydrogen content, since a second hydrogen accumulation peak is expected at the peak hydrostatic stress region at the distance of about one CTOD from the crack tip. In RPV steels with high DSA susceptibility, clear indications for more pronounced plastic strain localization and sub-grain formation was revealed by EBSD in the specimens tested in hydrogenated HTW (Figure 77). A similar plastic strain localization was observed in the high-sulphur steels in oxygenated HTW (Figure 91). These evidences support the strain localization hypothesis by the HELP mechanism.

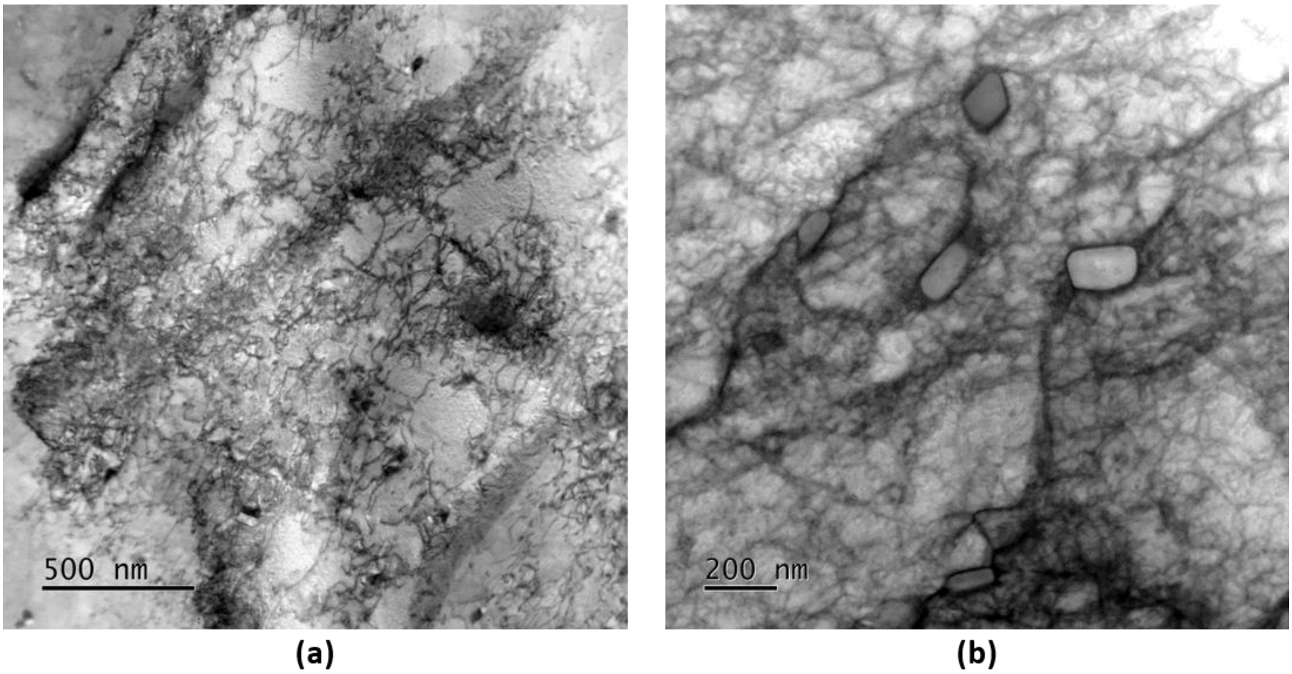

Figure 96: Dislocation structure in 277 steel after fracture mechanics test at 288 °C and strain rate of 10^{-3} s^{-1} in hydrogenated HTW (a) and in air (b).

The moderate environmental effects, the complex hydrogen-plastic deformation interactions and their very localized nature, the different potential fracture processes and interactions with other embrittling effects (DSA, TE, EAC) as well the complex upper bainitic microstructure make a clear identification of the underlying mechanisms for the environmental reduction in fracture initiation resistance very difficult. The suggested ideas remain speculative to some extent.

3.7 Final thoughts

Overall, the observed reductions of fracture resistance in HTW, in particular at standard loading rates of 250 to 350 μm/min (LOCAs), were only very moderate. The stronger environmental reduction of fracture resistance in HTW at slower loading rates was compensated by the increase of fracture resistance with decreasing loading rate in air by DSA. The strong apparent reduction of fracture initiation and tearing resistance in HTW at very slow loading rates, in particular in high-sulphur steels and in NWC, was due to SICC. Nevertheless, tensile tests in air with hydrogen pre-charging on some RPV steels with high DSA or high yield stress revealed strong HE, if sufficient hydrogen (a few wppm) is present in the material [5]. Only marginal environmental effects were observed on strength and ductility in smooth tensile samples in SSRT in HWC due to the limited hydrogen availability. However, a sharp notch significantly enhanced the reduction of ductility [5].

The main reason for the moderate degradation effects is the low hydrogen availability in HTW in connection with a very high density of various (fine-dispersed and strong) hydrogen traps in RPV steels [174]. The very fast hydrogen diffusion, permeation rates and low trapping efficiency at higher temperatures limit the hydrogen enrichment. The hydrogen concentration in the bulk lattice is usually governed by the low DH content in the water. The high exchange current density of the H_2O/H_2 reaction with regard to typical corrosion rates and the high ohmic resistance of the water strongly limit (local) cathodic overpotentials, polarization and hydrogen uptake by (local) corrosion reactions. The H_2O/H_2 and Fe/Fe_3O_4 lines are parallel in the Pourbaix diagram. Acidic pH shifts just give a higher H^+ availability. Acidic pH shifts in the occluded crack crevice environment are strongly limited in HTW under typical LWR conditions. Furthermore, factors that can amplify the HTW effects on fracture resistance like DSA and TE susceptibilities or strength level were moderate only.

Unfavourable combinations of high sulphur content, increased strength, and high EAC, TE and DSA susceptibilities can produce effects that are more significant. Irradiation, e.g., may increase the strength and TE susceptibility, but also produces a high density of fine-dispersed defects that may act as strong hydrogen traps. The effect of irradiation in this context is still an open issue and will be investigated in a new project at PSI. Stronger HE can be anticipated at temperatures below 150 °C due to the stronger trapping efficiency, but this is partially counteracted by the lower hydrogen availability (lower Sievert’s constant, solubility and corrosion rates) for a given DH concentration in HTW.

Chapter 4 Conclusions and outlook

4.1 Conclusions

The fracture behaviour in the upper shelf region of low-alloy reactor pressure vessel (RPV) steels with various sulphur and phosphorus contents and different environmentally-assisted cracking (EAC), temper embrittlement (TE) and dynamic strain aging (DSA) susceptibilities in different simulated light water reactor (LWR) environments was evaluated by elastic-plastic fracture mechanics (EPFM) tests. These tests were performed at different temperatures and strain rates and were analysed by fractographic post-test evaluations. Stable ductile transgranular tearing by micro-void coalescence (MVC) dominates in air and high-temperature water (HTW) with additional and varying, but small amounts (a few %) of secondary cracking, macro-voids, quasi-cleavage and intergranular cracking in HTW. No unstable cracking and no change in the dominant fracture mechanism and only moderate reductions (< 25%) in fracture initiation and tearing resistance were observed in both pressurized water reactor (PWR) and boiling water reactor (BWR) environments. The main results can be summarized as follows:

Reference material Biblis C

- In steels with low sulphur and low phosphorus contents and low DSA susceptibility, environmental effects on fracture resistance are absent or marginal in both oxygenated and hydrogenated HTW.

Simulated coarse-grain heat-affected zone of Biblis C material with higher yield stress

- Higher yield stress may result in stronger environmental effects, as expected. The higher yield stress results in a higher peak and hydrostatic stress ahead of crack tip and this favours the hydrogen enrichment in this region. Furthermore, due to the smaller plastic zone size, the available hydrogen is concentrated at a smaller volume and diffusion distances for hydrogen to the critical region in the process zone are smaller.

Steels with low sulphur content, but high DSA susceptibility

- The two steels with low sulphur content, but high DSA susceptibility showed clear effects in both environments, although the effects generally were more pronounced in hydrogenated HTW. The reduction of fracture initiation and tearing resistance increased with decreasing loading rate in the DSA temperature-strain rate range and was most pronounced in hydrogenated HTW and at 288 °C. In hydrogenated HTW, the toughness reduction correlated fairly well with the DSA susceptibility of the different steels and sulphur content played no or only a very minor role. Therefore, in hydrogenated HTW, DSA effects seem to dominate over effects of occluded crevice chemistry.

- Although the environmental reduction in fracture initiation resistance increased with decreasing loading rate, the lowest fracture initiation resistance in hydrogenated HTW was measured at 250 °C and highest loading rates, because of the minimum in toughness at 250 °C and negative strain rate sensitivity in air due to DSA in these steels. The environmental reduction and softening by hydrogen/HTW partially (or at maximum fully) compensated the toughness increase by hardening due to DSA in air.

- Stronger reductions of fracture resistance were observed at slow loading rates, in particular in oxygenated HTW. This is due to strain-induced corrosion cracking.

- The more significant fracture resistance reduction in hydrogenated HTW may be due to the synergy between DSA and hydrogen effects, resulting in localization of plastic deformation. This was verified by EBSD investigations at the crack tips.

Steels with high sulphur and/or high phosphorus contents and high EAC and/or high TE susceptibility

- In low-alloy RPV materials with high phosphorus and low sulphur contents and high TE and moderate DSA susceptibility, TE effect dominates over effects of occluded crevice chemistry. The reduction of fracture initiation and tearing resistance was most pronounced in hydrogenated HTW.

- For high-sulphur steels with high EAC susceptibility, the strongest environmental reduction occurred in aggressive occluded crevice environment (oxygenated HTW with addition of impurities) with preceding EAC crack growth, accompanied with higher macro-voids and secondary crack fraction on the fracture surface. The aggressive occluded crack crevice chemistry increases the hydrogen availability and uptake potential, which resulted in higher level of localization of plastic deformation at the crack tip.

HELP and HESIV with minor contributions by HEDE are the most probable HE mechanisms in this context. The observed behaviour (parameter effects and the fracture modes/morphologies) suggests a combination of plastic strain localization by the HELP mechanism, in synergy with DSA, and HESIV mechanisms with additional minor contributions of HEDE (e.g., for micro-crack formation at inclusions).

The main reason for the moderate degradation effects is the low hydrogen availability in HTW in connection with a very high density of various (fine-dispersed and strong) hydrogen traps in RPV steels. In addition, the environmental reduction and softening by hydrogen/HTW only partially compensated the toughness increase by hardening due to the DSA susceptibility of the investigated RPV steels.

Although the environmental effects appear as very moderate at the present stage, materials with low initial upper shelf toughness (e.g., high-sulphur RPV steels) and/or with unfavourable combinations of high sulphur content, increased strength, high EAC, TE and DSA susceptibility can be particularly critical in this context.

The investigated materials conservatively cover the Swiss RPV steels. The absence of strong HTW effects on the fracture resistance in un-irradiated RPV steels in the temperature range from 150 to 300 °C in PWR and BWR environments is well validated by a large number (~ 200) of EPFM tests in HTW with various RPV steels over a broad range of conditions and there is solid confidence in this observation. This statement is believed to be valid for the RPV parts outside the core belt region and is finally the major and most important practical outcome of this PhD project for the Swiss Federal Nuclear Safety Inspectorate ENSI (funding agency of this project) and utilities. Some concerns remain with regard to lower temperatures < 150 °C, unfavourable combinations of material parameters that can increase HTW effects on fracture resistance, and in particular, the behaviour of irradiated RPV steels. In old plants with small margins with regard to irradiation embrittlement, even small environmental effects can be significant and critical and there is a need to verify this observation for irradiated RPV steels also.

4.2 Outlook

From a practical point of view, the observed fracture behaviour in HTW should be verified with irradiated RPV steels, which currently is the major pending issue. The irradiation hardening, e.g., may further increase the HE and HTW effects on fracture resistance, although only moderate effects are anticipated based on this work (e.g., based on the CGHAZ results). Furthermore, the fracture behaviour at lower temperatures < 150 °C, e.g., with CGHAZ material with high strength or materials with high TE susceptibility, should also be further evaluated for a comprehensive and complete view. In particular, it should be checked, if HTW can shift the DBTT to higher temperatures in the upper transition region. Tests should also include materials with unfavourable combinations of parameters (high DSA and TE susceptibilities, increased strength and high sulphur content) that may enhance HTW effects on the fracture resistance. However, the availability of such materials is quite limited. Conditions that may result in a higher hydrogen content in the material, e.g., during prolonged PWR shut-down (oxygenated, borated water with low pH in combination with unclad regions or cladding defects) or during flow-accelerated corrosion (only relevant for carbon steel piping and vessels) are of minor concern.

The underlying mechanism of environmental reduction in fracture resistance in HTW remains an open issue. The weak (or moderate) effects, the manifold and complex hydrogen-plastic deformation interactions and their very localized nature, the different potential fracture processes and interactions with other embrittling effects (DSA, TE, EAC) as well the complex upper bainitic microstructure finally make a clear identification of the underlying mechanisms almost impossible. Such investigations should be performed under conditions that correspond to those in the process zone under dynamic crack-tip plasticity in an evolving occluded crevice environment during an EPFM test or fracture. First attempts to verify some hypothesis by TEM and ECCI (e.g., HELP), Positron Annihilation Spectroscopy (HESIV) or TDS (hydrogen trapping at different temperatures) or Nano-indentation (localization of plastic deformation) were not yet successful and their interpretation is highly complex. In-situ mechanical testing (e.g., X-ray Tomography, Neutron Tomography, Small-Angle X-ray Scattering or Small-angle Neutron Scattering for void formation at Swiss Light Source and Swiss Spallation Neutron Source at PSI), microscopic Digital Image Correlation (strain localization) or Internal Friction (DSA, interstitial carbon, nitrogen and hydrogen) are also challenging, in particular at higher temperatures. Further mechanistic investigations probably require an amplification of the hydrogen effects by significantly higher hydrogen contents in the material (well beyond the conditions that can be regarded as plant relevant). This can be only achieved by electrochemical hydrogen pre-charging. In-situ electrochemical or chemical charging at higher temperatures > 100 °C is hardly possible and charging in hydrogen gas atmospheres requires very high hydrogen gas partial pressures. Interactions of DSA and HE (or TE and HE) can be better studied by a silicon-killed carbon steel with high free nitrogen content or high-strength bainitic turbine disc steel with higher phosphorus content, respectively, which have many similarities and commonalities with RPV steels.

References

[1] W.L. Server, R.K. Nanstad, 1 - Reactor pressure vessel (RPV) design and fabrication: the case of the USA, in: N. Soneda (Ed.), Irradiation Embrittlement of Reactor Pressure Vessels (RPVs) in Nuclear Power Plants, Woodhead Publishing Series in Energy 2015, pp. 3–25.

[2] Y. Tanaka, 2 - Reactor pressure vessel (RPV) components: processing and properties, in: N. Soneda (Ed.), Irradiation Embrittlement of Reactor Pressure Vessels (RPVs), Woodhead Publishing Series in Energy 2015, pp. 26–43.

[3] I.A. Vatter, C.A. Hippsley, S.G. Druce, Review of thermal ageing data and its application to operation reactor pressure vessels, International Journal of Pressure Vessels and Piping 54(1–2) (1993) 31–48.

[4] W.L. Server, R.K. Nanstad, 6 - Integrity and embrittlement management of reactor pressure vessels (RPVs) in light-water reactors, in: N. Soneda (Ed.), Irradiation Embrittlement of Reactor Pressure Vessels (RPVs) in Nuclear Power Plants, Woodhead Publishing Series in Energy 2015, pp. 132–155.

[5] H.P. Seifert, S. Ritter, P. Spätig, J. Bai, W. Chen, G.S. Rao, Z. Que, Safe long-term operation in the context of environmental effects on fracture, fatigue and environmentally-assisted cracking - Final report of the SAFE-II project, Paul Scherrer Institut, PSI Report No. 18–03, Villigen, Switzerland, ISSN 1019–0643, 2018.

[6] J. Hickling, D. Blind, Strain-induced corrosion cracking of low-alloy steels in LWR systems - case histories and identification of conditions leading to susceptibility, Nuclear Engineering and Design 91(3) (1986) 305–330.

[7] P.L. Andresen, Emerging Issues and fundamental processes in environmental cracking in hot water, Corrosion 64(5) (2008) 439–464.

[8] H.P. Seifert, J. Hickling, D. Lister, Corrosion and environmentally-assisted cracking of carbon and low-alloy steels, Comprehensive Nuclear Materials, Elsevier, Oxford, UK, 2012, pp. 105–142.

[9] A. Kimura, M. Shibata, R. Kasada, H. Nakata, K. Fujii, K. Fukuya, Grain boundary phosphorous segregation and its influence on the ductile brittle transition temperature in reactor pressure vessel steels, Journal of ASTM International 1(9) (2004) 1–14.

[10] S.G. Druce, G. Gage, G. Jordan, Effect of ageing on properties of pressure vessel steels, Acta Metallurgica 34(4) (1986) 641–652.

[11] J.H. Yoon, B.S. Lee, Y.J. Oh, J.H. Hong, Effects of loading rate and temperature on J-R fracture resistance of an SA516-Gr.70 steel for nuclear piping, International Journal of Pressure Vessels and Piping 76(9) (1999) 663–670.

[12] H. Hänninen, H.P. Seifert, Y. Yagodzinsky, U. Ehrnstén, O. Tarasenko, P. Aaltonen, Effects of dynamic strain ageing on environment-assisted cracking of low alloy pressure vessel and piping steels, 10th Int. Conf. on Environmental Degradation of Materials in Nuclear Power Systems - Water Reactors, Lake Tahoe, Nevada, USA, 2001.

[13] L.A. James, W.C. Porr, The effect of an elevated temperature aqueous environment upon the J-controlled tearing of a low-alloy steel, International Journal of Pressure Vessels and Piping 76(11) (1999) 769–779.

[14] H.P. Seifert, S. Ritter, P. Spätig, J. Bai, S. Roychowdhury, Safe long-term operation in the context of environmental effects on fracture, fatigue and environmentally-assisted cracking, Paul Scherrer Institut, PSI Report No. 15–03, Villigen, Switzerland, ISSN 1019-0643, 2015.

[15] R. Schellenberger, P. Deimel, JR curves of the low alloy steel 20 MnMoNi 5 5 with two different sulphur contents in oxygen-containing high temperature water at 240 °C, Nuclear Engineering and Design 151(2–3) (1994) 449–461.

[16] G.S. Rao, H.P. Seifert, S. Ritter, P. Spätig, Z. Que, Effect of hydrogen on tensile behavior of low alloy steel in the regime of dynamic strain ageing, Procedia Structural Integrity 2(2016) (2016) 3399-3406.

[17] Nuclear Power Reactors in the World, International Atomic Energy Agency, 0700-Nuclear power, Vienna, Austria, 2017.

[18] Light water reactor, European Nuclear Society, 2009.

[19] K. Fukuya, Current understanding of radiation-induced degradation in light water reactor structural materials, Journal of Nuclear Science and Technology 50(3) (2013) 213–254.

[20] T. Allen, J. Busby, M. Meyer, D. Petti, Materials challenges for nuclear systems, Materials Today 13(12) (2010) 14–23.

[21] Assessment and management of ageing of major nuclear power plant components important to safety: PWR pressure vessels, International Atomic Energy Agency, 2007.

[22] H. Wolfgang, Material for Nuclear Plants: From safe design to residual life assessment, Springer-Verlag London 2013.

[23] L. Oliver, B. Helmersson, E. Fredriksson, G. Ledergerber, W. Kaufmann, G. Wikmark, B. Cheng, A. Kucuk, Review of water chemistry and corrosion products in a NWC plant transitioned to hydrogen injection and OLNC, Nuclear power plant conference 2010 (NPC 2010), Toronto, Ontario, Canada, 2010.

[24] Reactor pressure vessel head degradation and reactor coolant pressure boundary integrity, United States Nuclear Regulatory Commission, Bulletin 2002–01, 2002.

[25] Integrity of reactor pressure vessels in nuclear power plants: assessment of irradiation embrittlement effects in reactor pressure vessel steels, International Atomic Energy Agency, 2009.

[26] D.T. Blagoeva, L. Debarberis, M. Jong, Stability of ferritic steel to higher doses: Survey of reactor pressure vessel steel data and comparison with candidate materials for future nuclear systems, International Journal of Pressure Vessels and Piping 122 (2014) 1–5.

[27] Materials handbook for nulcear plant pressure-boundary components, Electric Power Research Institute, EPRI 1002792, Palo Alto, CA, 2002.

[28] H.P. Seifert, S. Ritter, Strain-induced corrosion cracking behaviour of low-alloy steels under boiling water reactor conditions, Journal of Nuclear Materials 378(3) (2008) 312–326.

[29] K.H. Lee, S.G. Park, M.C. Kim, Characterization of transition behavior in SA508 Gr.4N Ni-Cr-Mo low alloy steels with microstructural alteration by Ni and Cr contents, Materials Science and Engineering A 529 (2011) 156–163.

[30] D.R. Askeland, F. Haddleton, P. Green, H. Robertson, The science and engineering of materials, Springer US 1996.

[31] J. Roesler, H. Harders, M. Baeker, Mechanical behaviour of engineering materials: metals, ceramics, polymers, and composites, Springer-Verlag Berlin Heidelberg 2007.

[32] D. François, Ductile fracture, in: D. François, A. Pineau, A. Zaoui (Eds.), Mechanical Behaviour of Materials: Volume II: Fracture Mechanics and Damage, Springer Netherlands 2013, pp. 193–264.

[33] A.S. Argon, Formation of cavities from nondeformable second-phase particles in low temperature ductile fracture, Journal of Engineering Materials & Technology 98(1) (1976) 24–27.

[34] A.S. Argon, J. Im, R. Safoglu, Cavity formation from inclusions in ductile fracture, Metallurgical & Materials Transactions A 6(6) (1975) 825–837.

[35] M.J. Worswick, R.J. Pick, Void growth and constitutive softening in a periodically voided solid, Journal of the Mechanics & Physics of Solids 38(5) (1990) 601–625.

[36] T.B. Cox, J.R. Low, An investigation of the plastic fracture of AISI 4340 and 18 nickel-200 grade maraging steels, Metallurgical and Materials Transactions A 5(6) (1974) 1457–1470.

[37] G. Lange, M. Pohl, Systematische Beurteilung technischer Schadensfälle, Wiley-VCH 2014.

[38] Z.L. Zhang, C. Thaulow, J. Ødegård, A complete Gurson model approach for ductile fracture, Engineering Fracture Mechanics 67(2) (2000) 155–168.

[39] J. Pokluda, P. Šandera, Brittle and ductile fracture, Micromechanisms of Fracture and Fatigue: In a Multiscale Context, Springer-Verlag London 2010, pp. 69–123.

[40] Metals handbook, ASM International 1998.

[41] C. Beachem, R. Pelloux, Electron fractography: a tool for the study of micromechanisms of fracturing processes, Fracture Toughness Testing and its Applications, STP381-EB, ASTM Committee E-24, ASTM International, West Conshohocken, PA, 1965.

[42] A.A. Griffith, The phenomena of rupture and flow in solids, Philosophical Transactions of the Royal Society A, 221 (1921) 582–593.

[43] K. Wallin, A simple theoretical Charpy-V - KC Correlation for irradiation embrittlement, Pressure Vessels and Piping, ASME, 1989, pp. 93–100.

[44] F.R. Stonsifer, R.W. Amstrong, Effect of prior austenite grain size on fracture toughness properties of A533 B steel, in: D.M.R. Taplin (Ed.), Fracture, Pergamon Press 1977, pp. 1–6.

[45] P. Deimel, E. Sattler, Non-metallic inclusions and their relation to the J-integral, Ji phys, at physical crack initiation for different steels and weld metals, Journal of Materials Science 33 (1998) 1723–1736.

[46] C.J. McMahon, Intergranular fracture in steels, Materials Science and Engineering 25 (1976) 233–239.

[47] P.E. Soulat, B. Houssin, P. Bocquet, M. Bethmont, Analysis of radiation embrittlement results from a French Forging examined in the second phase of an IAEA-cooridinated research program, in: L. Steele (Ed.) Radiation Embrittlement of Nuclear Reactor Pressure Vessel Steels: An international Review (Fourth Volume), ASTM International, West Conshohocken, PA, 1993, pp. 249–265.

[48] X.K. Zhu, J.A. Joyce, Review of fracture toughness (G, K, J, CTOD, CTOA) testing and standardization, Engineering Fracture Mechanics 85 (2012) 1–46.

[49] American Society for Testing and Materials, E399 Standard Test Method for Linear-Elastic Plane-Strain Fracture Toughness KIc of Metallic Materials, 2017

[50] American Society for Testing and Materials, E1820 Standard test method for measurement of fracture toughness, 2013

[51] American Society for Testing and Materials, E1921 Standard test method for determination of reference temperature, To, for ferritic steels in the transition range, 2018

[52] M.E. Orazem, W. Ruch, An improved analysis of the potential drop method for measuring crack lengths in compact tension specimens, International Journal of Fracture 31 (1986) 245–258.

[53] S. Bhowmik, S.K. Acharyya, P. Sahoo, Estimation and comparative study of JIC using different methods for 20MnMoNi55 steel, Materials and Design 46 (2013) 680–687.

[54] X.K. Zhu, J.A. Joyce, J-Resistance curve testing of HY80 steel using SE(B) specimens and normalization method, Engineering Fracture Mechanics 74 (2007) 2263–2281.

[55] J. Chêne, L'hydrogène dans les matériaux métalliques en relation avec les interactions plasticité-environnement, PlastOx 2007 (2009) 131–145.

[56] J.P. Hirth, Effects of hydrogen on the properties of iron and steel, Metallurgical Transactions A 11(6) (1980) 861–890.

[57] R.A. Oriani, The physical and metallurgical aspects of hydrogen in metals., in: L. Maui (Ed.) Fourth International Conference on Cold Fusion, Electric Power Research Institute, Palo Alto, CA, 1993.

[58] R. Kirchheim, A. Pundt, Hydrogen in Metals, in: D.E. Laughlin, K. Hono (Eds.), Physical Metallurgy, Elsevier 2014, pp. 2597–2705.

[59] I.M. Robertson, The effect of hydrogen on dislocation dynamics, Engineering fracture mechanics 64(5) (1999) 649–673.

[60] N. Bandopadhyay, Hydrogen-induced cracking in 4340-type steel: Effects of composition, yield strength, and H2 pressure, Metallurgical Transactions A 14(4) (1983) 881–888.

[61] C.D. Beachem, New model for hydrogen-assisted cracking (hydrogen embrittlement), Metallurgical and Materials Transactions B 3(2) (1972) 441–455.

[62] H. Hänninen, Conjoint actions of hydrogen and irradiation embrittlement on the pressure vessel steel of nuclear power plants, VTT-MET C-209, Espoo, 1992.

[63] S. Roychowdhury, H.P. Seifert, P. Spätig, Z. Que, Effect of high-temperature water and hydrogen on the fracture behavior of a low-alloy reactor pressure vessel steel, Journal of Nuclear Materials 478 (2016) 343–364.

[64] Z. Que, H.P. Seifert, P. Spätig, G.S. Rao, S. Ritter, Effect of high-temperature water environment on the fracture behaviour of low-alloy RPV steels, Proceedings of the 18th International Conference on Environmental Degradation of Materials in Nuclear Power Systems - Water Reactors, Portland, USA, 2017.

[65] G.H. Broomfield, Hydrogen effects in an irradiated 1% Cr, 12% Mo PWR pressure vessel steel, Journal of Nuclear Materials 16(3) (1965) 249–259.

[66] J.K. Chakravartty, G.E. Prasad, T.K. Sinha, M.K. Asundi, Hydrogen embrittlement of ASTM A 203 D nuclear structural steel, Journal of Nuclear Materials 138(1) (1986) 107–116.

[67] M. Ruščák, A. Brožova, J. Otruba, K. Šplíchal, J. Žd'árek, P. Sajdl, Hydrogen induced embrittlement and fracture toughness of reactor pressure vessel steel, Proc. IAEA Specialists' Meeting on Subcritical Crack Growth, NUREG/CP-0112, 1990, pp. 27–35.

[68] R.E. Mazel, F.A. Khromchenko, V.G. Grinenko, T.P. Kuznetsova, Investigation of the susceptibility of reactor vessel welds to hydrogen-induced brittle failure, International Institute of Welding, XXXI Congress IIW, Document No. X-889-78, 1978.

[69] C.R. Brinkman, J.M. Beeston, The effect of hydrogen on the ductile properties of irradiated pressure vessel steels, in: A. Bement (Ed.) Irradiation Effects on Structural Alloys for Nuclear Reactor Applications, STP484-EB, ASTM International, West Conshohocken, PA, 1970, pp. 42–72.

[70] R.A. Cottis, 2.10 - Hydrogen embrittlement, in: B. Cottis, M. Graham, R. Lindsay, S. Lyon, T. Richardson, D. Scantlebury, H. Stott (Eds.), Shreir's Corrosion, Elsevier 2010, pp. 902–922.

[71] H. Wipf, Solubility and diffusion of hydrogen in pure metals and alloys, Physica Scripta 94 (2001) 43–51.

[72] T. Michler, J. Naumann, Microstructural aspects upon hydrogen environment embrittlement of various bcc steels, International Journal of Hydrogen Energy 35(2) (2010) 821–832.

[73] Hydrogen effects in metals, in: A.W. Thompson, I.M. Bernstein (Eds.) Third International Conference on Effect of Hydrogen on Behavior of Materials, Metallurgical Society of AIME, Warrendale, PA, CA, 1980.

[74] T. Doshida, K. Takai, Dependence of hydrogen-induced lattice defects and hydrogen embrittlement of cold-drawn pearlitic steels on hydrogen trap state, temperature, strain rate and hydrogen content, Acta Materialia 79 (2014) 93–107.

[75] S.Y. Lynch, 2 - Hydrogen embrittlement phenomena and mechanisms, in: V.S. Raja, T. Shoji (Eds.), Stress Corrosion Cracking: Theory and Practice, Woodhead Publishing Series in Metals and Surface Engineering 2011, pp. 90–130.

[76] J.A. Lee, Hydrogen-induced toughness drop in weld coarse-grained heat-affected zones of linepipe steel, Materials Characterization 82 (2013) 17–22.

[77] R.P. Gangloff, B. Somerday, Gaseous hydrogen embrittlement of materials in energy technologies, Woodhead Publishing 2012.

[78] D.J. Kim, W.J. Lee, B.H. Kim, Hydrogen attack on simulated weld heat affected zone of 3Cr-1Mo-0.25V steel, Science and Technology of Welding and Joining 6(6) (2001) 402–404.

[79] M. Nagumo, Fundamentals of hydrogen embrittlement, Springer Singapore 2016.

[80] Z. Huang, Q. Shi, F. Chen, Y. Shi, FEM simulation of the hydrogen diffusion in X80 pipeline steel during stacking for slow cooling, Acta Metallurgica Sinica 27(3) (2014) 416–421.

[81] A.R. Troiano, The role of hydrogen and other interstitials in the mechanical behavior of metals, Metallography, Microstructure, and Analysis 5(6) (2016) 557–569.

[82] Z. Que, H.P. Seifert, P. Spätig, S. Ritter, G.S. Rao, High-temperature water effects on the fracture behaviour of low-alloy RPV steels, The European Corrosion Congress, Montpellier, France, 2016.

[83] A. Turnbull, Hydrogen diffusion and trapping in metals, in: R.P. Gangloff, B.P. Somerday (Eds.), Gaseous Hydrogen Embrittlement of Materials in Energy Technologies: Mechanisms, Modelling and Future Developments, Woodhead 2012, pp. 89–128.

[84] R.F. Prini, Evaluation of data on solubility of simple apolar gases in light and heavy water at high temperature, Journal of Physical and Chemical Reference Data 18(3) (2009) 1231–1243.

[85] M. Nagumo, H. Yoshida, Y. Shimomura, T. Kadokura, Ductile crack growth resistance in hydrogen-charged steels, Materials Transactions 42(1) (2001) 132–137.

[86] M.B. Djukic, V.S. Zeravcic, G. Bakic, Hydrogen embrittlement of low carbon structural steel, in: Z.L. Zhang, B. Skallerud, C. Thaulow (Eds.) 20th European Conference on Fracture (ECF20), 2014, pp. 1167–1172.

[87] H. Momida, Y. Asari, Y. Nakamura, Hydrogen-enhanced vacancy embrittlement of grain boundaries in iron, Physical Review B 88(14) (2013) 1–13.

[88] X.Q. Wu, I.S. Kim, Effects of strain rate and temperature on tensile behavior of hydrogen-charged SA508 Cl.3 pressure vessel steel, Materials Science and Engineering A 348(1–2) (2003) 309–318.

[89] H. Cho, I.S. Kim, Effects of hydrogen on tensile properties of SA508 Cl.3 reactor pressure vessel steel at high temperature, Material Science Forum 475–479 (2005) 4121–4124.

[90] K. Šplíchal, Combination of radiation and hydrogen damage of reactor pressure vessel materials, International Journal of Pressure Vessel Piping 55 (1993) 361–373.

[91] H. Hänninen, K. Törönnen, W.H. Cullen, Comparison of proposed cyclic crack growth mechanisms of low-alloy steels in LWR environments, 2nd Int. IAEA Specialist's Meeting on Sub-Critical Crack Growth, Sendai, Japan, 1985.

[92] H.P. Seifert, S. Ritter, Corrosion fatigue crack growth behaviour of low-alloy reactor pressure vessel steels under boiling water reactor conditions, Corrosion Science 50(7) (2008) 1884–1899.

[93] H. Hänninen, On the mechanisms of environment sensitive cyclic crack growth of nuclear reactor pressure vessel steels, Corrosion Science 23(6) (1983) 663–679.

[94] H.P. Seifert, S. Ritter, Stress corrosion cracking of low-alloy reactor pressure vessel steels under boiling water reactor conditions, Journal of Nuclear Materials 372(1) (2008) 114–132.

[95] R.P. Gangloff, 6.02 - Hydrogen-assisted cracking in: I. Milne, R.O. Ritchie, B. Karihaloo (Eds.), Reference Module in Materials Science and Materials Engineering - Comprehensive Structural Integrity, Oxford, Pergamon, 2003, pp. 31–101.

[96] H.P. Seifert, Literature survey on the stress corrosion cracking of low-alloy steels in high-temperature water, Paul Scherrer Institut, PSI Report No. 02–06, Villigen, Switzerland, ISSN 1019–0643, 2002.

[97] N. Taylor, H.M. Nykyforchyn, O.T. Tsyrulnyk, Effect of hydrogenation on the fracture mode of a reactor pressure-vessel steel, Material Science 45(5) (2009) 613–625.

[98] K. Fruzzetti, 2005 interim review of the pressurized water reactor primary water chemistry guidelines - revision 5, EPRI, Palo Alto, CA, 1009933, 2005.

[99] K. Wolski, 5 - Environmentally assisted cracking (EAC) in nuclear reactor systems and components, in: D. Féron (Ed.), Nuclear Corrosion Science and Engineering, Woodhead Publishing Series in Energy 2012, pp. 104–130.

[100] H.P. Seifert, S. Ritter, Research and service experience with environmentally-assisted cracking in carbon and low-alloy steels in high-temperature water, SKI, SKI Report 2005:60, Stockholm, Sweden, ISSN 1104–1374, 2005.

[101] R. Kilian, A. Roth, Corrosion behaviour of reactor coolant system materials in nuclear power plants, Materials and Corrosion 53(10) (2002) 727–739.

[102] F.P. Ford, P.W. Emigh, The prediction of the maximum corrosion fatigue crack propagation rate in the low alloy steel-de-oxygenated water system at 288°C, Corrosion Science 25(8–9) (1985) 673–692.

[103] J.Y. Huang, M.C. Young, S.L. Jeng, J.J. Yeh, J.S. Huang, R.C. Kuo, Corrosion fatigue behavior of low alloy steels under simulated BWR coolant conditions, Journal of Nuclear Materials 405(1) (2010) 17–27.

[104] F.P. Ford, Environmentally assisted cracking of low-alloy steels, EPRI NP-7473-L, Palo Alto, CA, USA, 1992.

[105] F.P. Ford, Status of research on environmentally assisted cracking in LWR pressure vessel steels, Journal of Pressure Vessel Technology 110(2) (1988) 113–128.

[106] P.L. Andresen, Modelling the effect of sulphur on the threshold environmental cracking rate of steels in high temperature water, Proc. 3rd Int. Conf. on Fatigue and Fatigue Thresholds, Midlands, UK, 1987.

[107] P.L. Andresen, Mechanism and kinetics of SCC in stainless steels, Proc. of 10th Int. Conf. on Environmental Degradation of Materials in Nuclear Power Systems - Water Reactors, Lake Tahoe, Nevada, USA, 2001.

[108] F.P. Ford, Predicition of corrosion-fatigue initiation in low-alloy steel and carbon-steel/water systems at 288 °C, in: R.E.S. Gold, E.P. (Ed.) 6. International Symposium on Environmental Degradation of Materials in Nuclear Power Systems: Water Reactors, Minerals, Metals and Materials Society, San Diego, California, USA, 1993, pp. 9–17.

[109] P.L. Andresen, Modelling of water and material chemistry effect on crack-tip chemistry and resulting crack growth kinetics, Proc. 3rd Int. Symp. on Environmental Degradation of Materials in Nuclear Power Systems - Water Reactors, 1988.

[110] A.W. Thompson, I.M. Bernstein, The role of metallurgical variables in hydrogen assisted environmental fracture, Advances in Corrosion Science and Technology, Plenum Press, New York, 1980, pp. 53–175.

[111] H.P. Seifert, S. Ritter, J. Hickling, Environmentally assisted cracking of low-alloy RPV and piping steels under LWR conditions, Proc. 11th Environmental Degradation of Materials in Nuclear Power Systems - Water Reactors, Stevenson, WA, USA, 2003.

[112] T. Shoji, Z.P. Lu, Quantification of the effects of crack tip plasticity on environmentally-assisted crack growth rates in LWR environments, in: S.A. Shipilov, R.H. Jones, J.M. Olive, R.B. Rebak (Eds.), Environment-Induced Cracking of Materials, Elsevier 2008, pp. 107–122.

[113] R.P. Gangloff, Fracture mechanics characterization of hydrogen embrittlement in Cr-Mo steel, Present Situation on Steels for Hydrogen Pressure Vessels, Creusot-Loire Industrie, Le Creusot, France, 1998.

[114] P.M. Scott, D.R. Tice, Stress corrosion in low alloy steels, Nuclear Engineering & Design 119(2–3) (1990) 399–413.

[115] H.P. Seifert, S. Ritter, U. Ineichen, U. Tschanz, B. Gerodetti, RIKORR-I Risskorrosion in druckführenden Komponenten des Primärkreislaufes von SWR, Paul Scherrer Institut, PSI Report No 03–10, Villigen, Switzerland, 2003.

[116] J.D. Atkinson, J. Yu, The role of dynamic strain - ageing in the environment assisted cracking observed in pressure vesselsteels, Fatigue Fracture Engineering Materials Structure 20(1) (1997) 1–12.

[117] P.K. Liaw, W.A. Logsdon, J.A. Begley, Fatigue crack-growth behavior of pressure-vessel steels and submerged-arc weldments in a high-temperature pressurized water environment, Metallurgical and Materials Transactions A 20 (1989) 2069–2085.

[118] J.W. Kim, Investigation of dynamic strain aging in SA106 Gr. C piping steel, Nuclear Engineering and Design 172(1–2) (1997) 49–59.

[119] K.C. Kim, J.T. Kim, J.I. Suk, U.H. Sung, H.K. Kwon, Influences of the dynamic strain aging on the J-R fracture characteristics of the ferritic steels for reactor, Nuclear Engineering and Design 228(1–3) (2004) 151–159.

[120] L.P. Kubin, Y. Estrin, Evolution of dislocation densities and the critical conditions for the Portvin-le Chatelier effect, Acta Metallurgica et Materialia 38(5) (1990) 679–708.

[121] G. Gottstein, Physical foundations of materials science, Springer-Verlag Berlin Heidelberg 2004.

[122] Y.H. Jung, K.L. Murty, Effect of Interstitial Impurities on Fracture Characteristics of A533-B Class 1 Pressure Vessel Steel in: F.A. Garner, C.H. Henager, N. Igata (Eds.) Influence of Radiation on Material Properties: 13th International Symposium, ASTM STP 956, American Society for Testing and Materials, Philadelphia, 1987, pp. 395–407.

[123] K.L. Murty, Interstitial-impurity radiation-defect interactions in ferritic steels, Journal of Metals 37(10) (1985) 34–39.

[124] A. Roth, Investigation of dynamic strain ageing effects of low alloy steels and their possible relevance for environmentally-assisted cracking in oxygenated high-temperature water, Proc. 11th Int. Conf. on Environmental Degradation of Materials in Nuclear Power Systems - Water Reactors, Stevenson, WA, USA, 2003.

[125] H.P. Seifert, S. Ritter, Effect of Temperature and Loading Frequency on the SICC and Corrosion Fatigue Crack Growth Behavior of Low-Alloy RPV Steels under BWR/NWC ConditionS, Proc. 11th Int. Conf. on Environmental Degradation of Materials in Nuclear Power Systems - Water Reactors, Stevenson, WA, USA, 2003.

[126] P.J. Ferreira, Hydrogen effects on the interaction between dislocations, Acta Materialia 46(5) (1998) 1749–1757.

[127] X. Wu, Y. Katada, I.S. Kim, S.G. Lee, Hydrogen-involved tensile and cyclic deformation behavior of low-alloy pressure vessel steel, Metallurgical and Materials Transactions A 35(5) (2004) 1477–1486.

[128] H. Erhart, H.J. Grabke, Equilibrium segregation of phosphorus at grain boundaries of Fe-P, Fe-C-P, Fe-Cr-P, and Fe-Cr-C-P alloys, Metal Science 15(9) (1981) 401–408.

[129] M.J. Balart, Low temperature fracture properties of DIN 22NiMoCr37 steel in fine-grained bainite and coarse-grained tempered embrittled martensite microstructures, Engineering Fracture Mechanics 75(8) (2008) 2480–2513.

[130] L. Novak, Temper-embrittlement in 15Cr2NiMoV steel, International Journal of Pressure Vessels and Piping 49(1) (1992) 109–120.

[131] V.V. Zabil'skii, Temper embrittlement of structural alloy steels (Review), Metallovedenie i Termicheskaya Obrabotka Metallov 29(1) (1987) 32–42.

[132] Y. Nishiyama, K. Onizawa, M. Suzuki, Phosphorus segregation and intergranular embrittlement in thermally aged and neutron irradiated reactor pressure vessel steels, Journal of ASTM International 4(8) (2007) 1–12.

[133] C.A. English, S.R. Ortner, G. Gage, W.L. Server, S.T. Rosinski, Review of phosphorus segregation and intergranular embrittlement in reactor pressure vessel steels, in: S. Rosinski, M. Grossbeck, T. Allen, A. Kumar (Eds.) Effects of Radiation on Materials: 20th International Symposium, ASTM International,, West Conshohocken, PA, 2001, pp. 151–173.

[134] W.R. Corwin, R.K. Nanstad, D.J. Alexander, R.E. Stoller, J.A. Wang, G.R. Odette, Thermal embrittlement of reactor vessel steels, 13. International Conference on Structural Mechanics in Reactor Technology, Porto Alegre, Brazil, 1995.

[135] R. Pelli, J. Forsten, Effect of thermal ageing on impact ductility of the nuclear reactor pressure vessel steel SA533B and its weld metal, Theoretical and Applied Fracture Mechanics 8(1) (1987) 25–31.

[136] A. Andrieu, A. Pineau, P. Joly, F. Roch, On modeling of thermal embrittlement in PWR steels using the local approach to fracture, 13th international conference on fracture, Beijing, China, 2013.

[137] H.K. Wang, T. Xu, B. Shou, A method to evaluate the temper embrittlement from step cooling test, ASME 2014 Symposium on Elevated Temperature Application of Materials for Fossil, Nuclear, and Petrochemical Industries, Seattle, Washington, USA, 2014, pp. 116–125.

[138] Z.Q. Zhai, Y. Miyahara, H. Abe, Y. Watanabe, Effects of thermal history and microstructure on segregation of phosphorus and alloying elements in the heat-affected zone of a low alloy steel, Metallurgical and Materials Transactions A 45(13) (2014) 6163–6172.

[139] J.A. Hudson, S.G. Druce, G. Gage, M. Wall, Thermal ageing effects in structural steels, Theoretical and Applied Fracture Mechanics 10(2) (1988) 123–133.

[140] M. Guttmann, P. Dumoulin, M. Wayman, The thermodynamics of interactive Co-segregation of phosphorus and alloying elements in iron and temper-brittle steels, Metallurgical Transactions A 13(10) (1982) 1693–1711.

[141] M. Tsubota, H. Sakamoto, TsuzukiR., Intergranular stress corrosion cracking of low-alloy and carbon steels in high-temperature water, Proc. 6th International Symposium on Environmental Degradation of Materials in Nuclear Power Systems - Water Reactors, TMS, San Diego, California, USA, 1993.

[142] H.K.D.H. Bhadeshia, Bainite in steel: Theory and Practice, Maney Publishing, Wakefield, UK, 2015.

[143] E. Lucon, E.V. Walle, M. Scibetta, Optimum use of broken Charpy specimens from surveillance programs for the application of the master curve approach, International Journal of Fracture 116 (2002) 231–244.

[144] M. Serrano, Direct measurement of reactor pressure vessel steels fracture toughness: Master Curve concept and instrumented Charpy-V test, International Journal of Pressure Vessels and Piping 77(10) (2000) 605–612.

[145] J.S. Lee, I.S. Kim, C.H. Jang, A. Kimura, Irradiation embrittlement of cladding and HAZ of RPV steel, Nuclear Engineering and Technology 38(5) (2005) 405–410.

[146] J.M. Hyde, C.A. English, 9 - Microstructural characterisation techniques for the study of reactor pressure vessel (RPV) embrittlement, in: N. Soneda (Ed.), Irradiation Embrittlement of Reactor Pressure Vessels (RPVs), Woodhead Publishing Series in Energy 2015, pp. 211–294.

[147] J. Koutský, K. Šplíchal, Hydrogen and radiation embrittlement of CrMoV and CrNiMoV ferritic RPV steels, International Journal of Pressure Vessels and Piping 24(1) (1986) 13–26.

[148] M. Tomimatsu, T. Hirota, T. Hardin, P. Todeschini, 4 - Embrittlement of reactor pressure vessels (RPVs) in pressurized water reactors (PWRs), in: N. Soneda (Ed.), Irradiation Embrittlement of Reactor Pressure Vessels (RPVs) in Nuclear Power Plants, Woodhead Publishing Series in Energy 2015, pp. 57–106.

[149] C.S. Seok, K.L. Murty, Effect of dynamic strain aging on mechanical and fracture properties of A516Gr70 steel, International Journal of Pressure Vessels and Piping 76(14–15) (1999) 945–953.

[150] K.L. Murty, Strain aging behavior of irradiated and denitrided mild steel, Materials Science and Engineering 59(2) (1983) 207–215.

[151] E.A. Krasikov, Reactor pressure vessel steel embrittlement under the combined action of neutron field and hydrogen, 19th European conference on fracture: Fracture mechanics for durability, reliability and safety (ECF19), 2012.

[152] A. Ulbricht, J. Böhmert, Small-angle neutron scattering study on the effect of hydrogen in irradiated reactor pressure vessel steels, Journal of Nuclear Materials 336(1) (2005) 90–96.

[153] H. Anzai, J. Kuniya, E. Kikuchi, N. Ohnaka, Evaluation of hydrogen behaviour in low alloy steel under high temperature conditions, Proc. 4th Environmental Degradation of Materials in Nuclear Power systems-Water Reactors, 1989, pp. 104–115.

[154] T. Shoji, H. Nakajima, H. Tsuji, H. Takahashi, T. Kondo, Effect of Microstructure and Strength of Low-Alloy Steels on Cyclic Crack Growth in High-Temperature Water, in: T. Crooker, B. Leis (Eds.) Corrosion Fatigue: Mechanics, Metallurgy, Electrochemistry, and Engineering, ASTM International, West Conshohocken, PA, 1983.

[155] T. Shoji, H. Takahashi, N. Nakajima, T. Kondo, Role of Loading Variables in Environment Enhanced Crack Growth for Water Cooled Nuclear Reactor Pressure Vessel Steels, Proc. of the International Atomic Energy Agency Specialists' Meeting on Subcritical Crack Growth, 1981, pp. 143–171.

[156] W.E. Pennell, Heavy-Section Steel Technology Program, Oak Ridge National Laboratory Oak Ridge, TN, 1995.

[157] J. Föhl, T. Weissenberg, D. Gómez-Briceño, J. Lapeña, M. Ernestová, M. Žamboch, H.P. Seifert, S. Ritter, A. Roth, B. Devrient, U. Ehrnstén, Crack growth behaviour of low alloy steels for pressure boundary components under transient light water reactor operating conditions (CASTOC), Staatliche Materialprüfungsanstalt (MPA), Universität Stuttgart 2004.

[158] Reference manual on the IAEA JRQ correlation monitor steel for irradiation damage studies, International Atomic Energy Agency IAEA-TECDOC-1230 Vienna, Austria 2001.

[159] I.I. Reformatskaya, L.I. Freiman, Precipitation of sulfide inclusions in steel structure and their effect on local corrosion processes, Protection of Metals 37(5) (2001) 459–464.

[160] T.V. Venkatasubramanian, T.J. Baker, Role of MnS inclusions in hydrogen assisted cracking of steel exposed to H2S saturated salt solution, Metal Science 18(5) (1984) 241–248.

[161] J. Landes, Z. Zhou, K. Lee, R. Herrera, Normalization method for developing J-R curves with the LMN function, Journal of Testing and Evaluation 19(4) (1991) 305–311.

[162] H.W. Viehrig, Bruchmechanische Werkstoffcharackterisierung zur überwachung der Neutronenversprödung von Reaktordruckbehältern für den Langzeitbetrieb von Kernkraftwerken, Forschungszentrum Dresden Rossendorf, Dresden, Germany, 2009.

[163] P. Paris, R. Johnson, A method of application of elastic-plastic fracture mechanics to nuclear vessel analysis, in: C. Shih, J. Gudas (Eds.) Elastic-Plastic Fracture: Second Symposium, Volume II Fracture Resistance Curves and Engineering Applications, STP803V2-EB, ASTM International, Conshohocken, PA, 1983, pp. 5–40.

[164] P. Paris, H. Tada, H. Ernst, A. Zahoor, Initial experimental investigation of tearing instability theory, in: J. Landes, J. Begley, G. Clarke (Eds.) Elastic-Plastic Fracture, STP668-EB, ASTM International, West Conshohocken, PA, 1979, pp. 251–265.

[165] H. Ernst, Some salient features of the tearing instability theory, in: C. Shih, J. Gudas (Eds.) Elastic-Plastic Fracture: Second Symposium, Volume II Fracture Resistance Curves and Engineering Applications, ASTM International, West Conshohocken, PA, 1983, pp. 133–155.

[166] S. Zaefferer, Theory and application of electron channelling contrast imaging under controlled diffraction conditions, Acta Materialia 75 (2014) 20–50.

[167] I. Gutierrez-Urrutia, D. Raabe, Study of dislocation substructures in high-Mn steels by electron channeling contrast imaging, Materials Science Forum 783–786 (2014) 750–754.

[168] L. Ryde, Application of EBSD to analysis of microstructures in commercial steels, Materials Science and Technology 22(11) (2006) 1297–1306.

[169] A.J. Wilkinson, G. Meaden, D.J. Dingley, High resolution mapping of strains and rotations using electron backscatter diffraction, Materials Science and Technology 22(11) (2006) 1271–1278.

[170] L.N. Brewer, D.P. Field, C.C. Merriman, Mapping and assessing plastic deformation using EBSD, in: S. A., K. M., A. B., F. D. (Eds.), Electron Backscatter Diffraction in Materials Science, Springer, Boston, MA 2009, pp. 251–262.

[171] R. Petrov, L. Kestens, A. Wasilkowska, Y. Houbaert, Microstructure and texture of a lightly deformed TRIP-assisted steel characterized by means of the EBSD technique, Materials Science and Engineering: A 447(1–2) (2007) 285–297.

[172] V. Gavriljuk, Influence of interstitial carbon, nitrogen and hydrogen on the plasticity and brittleness of steel, Steel in Translation 45(10) (2015) 747–753.

[173] Z. Que, H.P. Seifert, P. Spätig, A. Zhang, S. Ritter, G.S. Rao, Environmental degradation effect of high-temperature water and hydrogen on the fracture behavior of low-alloy reactor pressure vessel steels, Procedia Structural Integrity 13 (2018) 926-931.

[174] Z. Que, H.P. Seifert, P. Spätig, A. Zhang, S. Ritter, G.S. Rao, Environmental reduction effect of high temperature water and hydrogen on fracture resistance of low alloy reactor pressure vessel steels, FONTEVRAUD 9, Avignon, France, 2018.

Appendix

Database of elastic-plastic fracture mechanics tests on the investigated RPV steels

Materials and specimen			**EPFM test conditions**				**Fracture resistance *J* (kN/m)** $J = C_1 \cdot \Delta a^{C_2}$				
Materials	Specimen type	Orientation	Environment	Test temperature [°C]	LLD rate [µm/min]	Crack growth [mm]	J_Q	J_{DCPD}	$J_{0.1}$	C_1	C_2
Biblis C BM	1T C(T)	TL	BWR-HWC	288	250.0	12.5	290	218	649	411	0.51
			BWR-HWC	288	350.0	11.4	336	256	717	447	0.47
			BWR-HWC	150	350.0	8.0	353	270	879	491	0.63
			BWR-HWC	288	350.0	5.6	331	186	782	464	0.56
			BWR-HWC	288	350.0	10.6	251	167	631	389	0.58
			BWR-NWC	288	350.0	8.7	299	184	728	407	0.64
			BWR-HWC	288	350.0	4.1	293	167	620	400	0.44
			BWR-HWC	288	35.0	0.1	220	88	-	398	0.68
			BWR-HWC	288	0.35	6.0	364	231	941	519	0.65
			BWR-HWC	288	35.0	8.2	276	190	684	408	0.54
			BWR-HWC	288	3500.0	5.8	220	158	563	350	0.53
			BWR-HWC	288	3.5	4.2	359	247	861	498	0.59
			BWR-HWC	288	2500.0	4.3	277	196	590	386	0.45
			BWR-HWC	150	2500.0	3.6	400	248	750	501	0.53
			BWR-HWC	288	35.0	0.3	220	88	-	398	0.68
			BWR-HWC	150	2500.0	3.4	387	254	782	488	0.51
			BWR-HWC	288	250.0	12.5	290	218	649	411	0.51
			Air	288	350.0	11.4	336	256	717	447	0.47
			Air	150	350.0	8.0	353	270	879	491	0.63

Materials and specimen			**EPFM test conditions**				**Fracture resistance *J* (kN/m)** **$J = C_1 \cdot \Delta a^{C_2}$**				
Materials	Specimen type	Orientation	Environment	Temperature [°C]	LLD rate [μm/min]	Crack growth [mm]	J_Q	J_{DCPD}	$J_{0.1}$	C_1	C_2
HT1	0.5T C(T)	TL	PWR	288	250.0	5.8	333	284	-	395	0.20
			PWR	150	250.0	5.7	160	120	-	274	0.44
			PWR	288	250.0	5.3	278	251	-	311	0.11
			PWR	288	25.0	4.2	226	154	-	362	0.44
			PWR	288	2.5	2.7	241	162	-	408	0.52
			BWR HWC	288	0.25	2.4	258	216	-	352	0.32
			BWR HWC	288	2500.0	5.0	149	137	-	-	-
			BWR NWC	288	25.0	2.3	278	211	-	405	0
			BWR HWC	288	250.0	3.8	196	171	-	247	0.21
			BWR NWC	288	2.5	1.3	249	211	-	329	0.27
			BWR HWC	288	250.0	4.0	199	168	333	267	0.26
			BWR HWC	288	2.5	2.6	282	250	448	356	0.24
			BWR PWR	288	25.0	2.6	255	184	510	372	0.37
			PWR	288	0.25	2.5	212	170	-	321	0.38
			PWR	288	2.50	3.0	256	205	-	332	0.26
			Air	288	25.0	5.5	497	218	-	588	0.25
			Air	150	250.0	3.9	167	124	-	255	0.36
			Air	288	250.0	6.6	226	194	-	258	0.14
			Air	288	2.5	4.8	341	300	-	453	0.33
			Air	288	25.0	2.3	293	259	-	349	0.18
			Air	288	2500.0	2.7	171	146	-	233	0.26
			Air	288	2.5	2.2	302	257	-	334	0.11
			Air	288	250.0	3.1	238	225	310	256	0.07
			Air	288	0.25	1.9	313	213	-	445	0.39

Materials and specimen			**EPFM test conditions**				**Fracture resistance *J* (kN/m)** $J = C_1 \cdot \Delta a^{C2}$				
Materials	Specimen type	Orientation	Environment	Test temperature [°C]	LLD rate [µm/min]	Crack growth [mm]	J_Q	J_{DCPD}	$J_{0.1}$	C_1	C_2
277	1T C(T)	LT	BWR HWC	250	0.35	4.1	276	191	568	380	0.41
			BWR HWC	250	3500	7.0	266	200	695	408	0.56
			BWR HWC	250	35	7.2	271	210	627	392	0.47
			BWR HWC	288	35	6.9	297	231	665	416	0.47
			BWR HPW	288	35	4.9	338	261	790	468	0.52
			BWR NWC	288	35	4.3	394	284	881	536	0.53
			BWR NWC	288	3.5	3.2	436	290	820	552	0.45
			BWR HPW	288	3.5	3.9	415	304	1049	578	0.64
			BWR HWC	288	3.5	3.1	450	303	1072	619	0.66
			BWR HWC	250	3.5	6.5	363	259	958	550	0.58
			BWR HWC	288	350.0	7.0	360	288	793	498	0.52
			BWR HWC	200	35.0	6.6	393	312	810	613	0.49
			BWR HWC	200 (pre-oxidized at 288)	35.0	6.2	372	326	830	499	0.52
			BWR HWC	250 (pre-oxidized at 288)	35.0	6.2	281	228	645	408	0.48
			BWR HPW	288	350.0	7.0	342	279	682	449	0.43
			BWR HWC	288	350.0	7.1	355	280	718	462	0.42
			BWR HWC	150	35.0	7.5	335	277	726	459	0.48
			Air	288	3.5	3.8	501	309	1156	643	0.61
			Air	250	3500.0	7.4	281	215	764	434	0.59
			Air	250	0.35	3.5	372	236	1045	562	0.66
			Air	250	35.00	6.1	317	251	728	440	0.49
			Air	288	35.00	4.1	370	284	974	509	0.66
			Air	250	3.5	5.7	431	270	1145	641	0.65
			Air	288	350.0	6.7	394	318	923	536	0.58
			Air	200	35.0	6.9	454	326	1004	586	0.59
			Air	320	35.0	4.6	436	270	990	580	0.60
			Air	150	35.0	6.6	392	292	898	518	0.56
			Air	25	35.0	6.4	444	343	1000	589	0.55

Materials and specimen			**EPFM test conditions**				**Fracture resistance *J* (kN/m)** $J = C_1 \cdot \Delta a^{C_2}$				
Materials	Specimen type	Orientation	Environment	Temperature [°C]	LLD rate [µm/min]	Crack growth [mm]	J_Q	J_{DCPD}	$J_{0.1}$	C_1	C_2
508	1T C(T)	LT	BWR HWC	288	3.5	5.4	308	244	760	456	0.53
			BWR HWC		35	4.7	316	254	756	457	0.52
			Air		35	6.6	380	285	847	521	0.52
			Air		3.5	4.1	390	238	970	542	0.60
			BWR NWC		35	4.9	338	265	760	467	0.49
			BWR HWC		0.35	3.6	330	260	819	484	0.54
			Air		0.35	4.5	416	286	970	568	0.56
			BWR HWC		350	5.7	325	263	711	448	0.48
			Air		350	5.6	297	252	711	431	0.52
			BWR NWC		3.5	7.6	270	238	494	342	0.34
			BWR HPW		3.5	12.9	337	298	476	389	0.21
			BWR HPW		35	6.1	336	279	638	434	0.39
			BWR NWC		350	6.3	318	270	595	403	0.40
			BWR HPW		350	6.7	296	245	568	395	0.40
			BWR HPW		0.35	5.4	345	270	680	451	0.40
			BWR HPW		3.5	7.2	360	262	788	496	0.49
			BWR NWC		10	7.4	364	238	877	522	0.57

Materials and specimen			**EPFM test conditions**					**Fracture resistance *J* (kN/m)** $J = C_1 \cdot \Delta a^{C_2}$				
Materials	Specimen type	Orientation	Environment	Test style	Temperature [°C]	LLD rate [µm/min]	Crack growth [mm]	J_Q	J_{DCPD}	$J_{0.1}$	C_1	C_2
HSST	0.5T C(T)	TL	PWR	EPFM	288	250.0	2.7	294	166	557	414	0.47
			PWR	SICC+EPFM		250.0	3.1	273	186	575	385	0.46
			BWR NWC	SICC+EPFM		250.0	3.2	255	185	549	374	0.41
			BWR NWC	EPFM		250.0	3.2	270	195	617	386	0.47
			BWR NWC	SICC (Cl^-)+EPFM		250.0	2.3	239	187	-	336	0.40
			BWR NWC	EPFM		25.0	2.7	281	192	601	400	0.48
			BWR NWC	SICC+SCC+EPFM		25.0	1.5	285	183	-	409	0.48
			BWR NWC	SICC+EPFM		25.0	2.6	289	187	628	416	0.50
			BWR NWC	EPFM		2.5	3.1	265	193	417	335	0.31
			BWR NWC	SICC+SCC+EPFM		250.0	3.0	235	163	527	345	0.46
			BWR NWC	SICC (Cl^-)+EPFM		2.5	4.6	189	176	310	237	0.24
			BWR NWC	SICC+EPFM		2.5	1.8	256	135	-	365	0.43
			BWR NWC	SICC+SCC+EPFM		2.5	4.0	154	133	307	217	0.34
			BWR NWC	SICC+EPFM		250.0	4.2	257	214	502	351	0.38
			PWR	EPFM		25.0	2.8	292	221	592	396	0.43
			PWR	SICC+EPFM		25.0	2.6	298	189	598	420	0.48
			PWR	EPFM		2.5	3.2	297	191	639	406	0.43
			PWR	SICC+EPFM		2.5	3.1	294	189	562	422	0.49
			PWR	EPFM		0.25	2.3	327	198	726	469	0.55
			PWR	SICC+EPFM		0.25	2.2	291	177	-	426	0.52
			Air	EPFM		250.0	3.2	302	234	582	377	0.42
			Air	EPFM		2.5	2.6	325	229	568	413	0.36
			Air	EPFM		25.0	2.9	306	185	663	429	0.49
			Air	EPFM		0.25	2.4	366	197	757	506	0.56

Materials and specimen			**EPFM test conditions**				**Fracture resistance *J* (kN/m) $J = C_1 \cdot \Delta a^{C2}$**				
Materials	Specimen type	Orientation	Environment	Temperature [°C]	LLD rate [μm/min]	Crack growth [mm]	J_Q	J_{DCPD}	$J_{0.1}$	C_1	C_2
JRQ AR	0.5T C(T)	TL	Air	288	25	3.1	340	221	770	487	0.56
JRQ AR					2.5	2.4	418	195	950	580	0.64
JRQ SC					25	3.7	316	176	700	450	0.54
JRQ SC					2.5	2.3	366	200	756	497	0.53
JRQ AR			PWR		25	3.6	278	215	540	370	0.38
JRQ SC					25	4.6	260	185	437	338	0.34
JRQ AR					2.5	2.4	328	216	677	437	0.42
JRQ SC					2.5	3.5	306	189	616	444	0.54
JRQ AR					0.25	3.7	364	219	760	493	0.50
JRQ AR					250	3.7	265	200	462	342	0.33
JRQ AR			BWR NWC		25	3.2	305	218	557	401	0.38
JRQ SC					25	4.2	278	217	449	352	0.33
JRQ AR					2.5	4.4	344	255	413	405	0.29
JRQ SC					2.5	4.3	314	278	441	356	0.20

Materials and specimen				**EPFM test conditions**				**Fracture resistance *J* (kN/m)** $J = C_1 \cdot \Delta a^{C2}$				
Materials	Specimen type	Orientation	Environment	Test style	Temperature [°C]	LLD rate [µm/min]	Crack growth [mm]	J_Q	J_{DCPD}	$J_{0.1}$	C_1	C_2
KS12	0.5T C(T)	SL	Air	EPFM	288	250.0	3.1	118	102	178	144	0.17
			Air	EPFM	288	25.0	2.2	118	94	-	140	0.16
			Air	EPFM	288	2.5	2.6	138	99	221	186	0.26
			Air	EPFM	200	25.0	2.8	116	97	226	167	0.32
			Air	EPFM	250	25.0	2.4	142	127	-	165	0.14
			BWR NWC	EPFM	288	250.0	2.4	151	129	240	200	0.25
			BWR NWC	SICC(Cl^-)+SICC	288	250.0	2.8	99	88	171	132	0.25
			BWR NWC	SICC+EPFM	288	250.0	3.7	111	95	210	157	0.29
			BWR NWC	EPFM	288	25.0	3.0	104	94	180	139	0.24
			BWR NWC	SICC+SCC+EPFM	288	25.0	2.8	93	85	167	123	0.22
			BWR NWC	SICC+EPFM	288	25.0	2.3	108	98	178	142	0.23
			BWR NWC	SICC+SCC+EPFM	288	250.0	1.5	116	73	-	214	0.51
			BWR NWC	SICC+SCC+EPFM	288	2.5	6.2	82	79	125	100	0.19
			BWR NWC	EPFM	288	2.5	9.1	121	83	-	180	0.34
			BWR NWC	SICC+EPFM	288	2.5	6.2	104	81	218	159	0.35
			PWR	SICC+EPFM	288	250.0	3.0	107	91	202	149	0.28
			PWR	EPFM	288	250.0	3.5	123	108	232	167	0.26
			PWR	SICC+EPFM	288	25.0	1.7	129	105	-	162	0.19
			PWR	EPFM	288	25.0	2.2	122	104	200	163	0.25
			PWR	EPFM	288	2.5	2.3	138	123	232	180	0.24
			PWR	SICC+EPFM	288	2.5	2.5	123	97	204	161	0.22
			PWR	EPFM	200	25.0	3.5	105	92	201	139	0.24
			PWR	SICC+EPFM	200	25.0	1.9	110	82	-	166	0.33
			PWR	EPFM	250	25.0	3.4	111	94	159	141	0.18
			PWR	SICC+EPFM	250	25.0	2.8	115	93	201	141	0.18
			BWR NWC	EPFM	200	25.0	3.6	105	90	202	159	0.33
			BWR NWC	EPFM	250	25.0	3.5	115	95	225	162	0.29
			BWR NWC	SICC+EPFM	200	25.0	6.0	110	84	223	165	0.33
			BWR NWC	SICC+EPFM	250	25.0	3.2	97	81	194	143	0.31

Curriculum Vitae

PERSONAL DETAILS

Name:	Zaiqing Que	**Gender:**	Male	**Nationality:**	Chinese
Birthday:	27.12.1989	**Phone:**	+41 76 709 41 71	**Email:**	zaiqing.que@psi.ch

EDUCATION

Mar 2015 - Present	**Ph.D. Candidate in Material Engineering** École Polytechnique Fédérale de Lausanne (EPFL) & Paul Scherrer Institut (PSI)
Oct 2012 - Jan 2015	**M.Sc. in Metallurgical Engineering** (3.96/4.0) Rheinisch-Westfälische Technische Hochschule Aachen (RWTH Aachen), Germany
Sep 2008 - Jun 2012	**B.Sc. in Metallurgical Engineering** (3.71/4.0) University of Science and Technology Beijing (USTB), P.R. China

ORAL PRESENTATIONS AT INT. CONFERENCES

Feb. 2019	Invited Speaker in 51th Annual Group Meeting of Fracture Mechanics in Germany Society for Material Research and Testing (DVM)
Sep 2018	9th Int. Symp. Contribution of Materials Investigations to Light Water NPPs' Safety, Avignon, France
Aug 2018	22nd European Conference on Fracture, Belgrade, Serbia
Apr 2018	Annual Meeting of the Int. Cooperative Group on Environmentally-Assisted Cracking of Water Reactor Materials, Knoxville, USA, Paper No LA01 (2018)
Aug 2017	18th Int. Conf. on Environmental Degradation of Materials in Water Reactors, Portland, USA
May 2017	Annual Meeting of the Int. Cooperative Group on Environmentally-Assisted Cracking of Water Reactor Materials, Chester, UK, Paper No LA01 (2017)
Sep 2016	European Corrosion Conference 2016, Montpellier, France, Paper No 52357 (2016)
May 2016	Annual Meeting of the Int. Cooperative Group on Environmentally-Assisted Cracking of Water Reactor Materials, Qingdao, China, Paper No LA02 (2016)

LANGUAGES AND R&D SKILLS

Languages	English: Professional; German: Moderate (B2.1); Mandarin: Mother Tongue
Characterization	SEM, EDX, EBSD, ECCI, FIB, Nano-Indentation, XRD, TEM, TDS, CLSM, TG, DTA
Mechanical Tests	Fracture Mechanics Test, Tensile Test, Charpy Test
Corrosion Tests	SICC, SCC, EPR, ERT, Salt Spray Test
Simulation	SIMUFACT, MATLAB, THERMO CALC, C Programming

PUBLICATIONS (during Ph.D.)

[1] **Z. Que**, H. P. Seifert, P. Spätig, A. Zhang, J. Holzer, G. S. Rao, S. Ritter, Effect of Dynamic Strain Aging on Environmental Degradation of Fracture Resistance of Low-Alloy RPV Steels in High Temperature Water Environments, *Corrosion Science*, in publication.

[2] **Z. Que**, H. P. Seifert, P. Spätig, J. Holzer, A. Zhang, G. S. Rao, S. Ritter, Environmental Degradation of Fracture Resistance of Low Alloy RPV Steels with High S and P Contents in High Temperature Water Environments, *Corrosion Science*, accepted.

[3] **Z. Que**, H. P. Seifert, P. Spätig, A. Zhang, J. Holzer, G. S. Rao, S. Ritter, Environmental Degradation Effect of High-Temperature Water and Hydrogen on the Fracture Behavior of Low-Alloy Reactor Pressure Vessel Steels, *Procedia Structural Integrity* 13 (2018) 926-931. doi.org/10.1016/j.prostr.2018.12.174.

[4] **Z. Que**, H. P. Seifert, P. Spätig, A. Zhang, J. Holzer, G. S. Rao, S. Ritter, Degradation Effects of Hydrogen and High-Temperature Water Environment on the Fracture Resistance of Low-Alloy RPV Steels, 19th International Conference on Environmental Degradation of Materials in Nuclear Power Systems - Water Reactors, Boston, MA, USA, August 18-22, 2019. In preparation.

[5] **Z. Que**, H.P. Seifert, P. Spätig, S. Ritter, G. S. Rao, Effect of High-Temperature Water Environment on the Fracture Behaviour of Low-Alloy RPV Steels, 18th International Conference on Environmental Degradation of Materials in Nuclear Power Systems - Water Reactors, Portland, Oregon, USA, August 13-17, 2017.
The Minerals, Metals & Materials Series, doi:10.1007/978-3-319-67244-1_68.

[6] **Z. Que**, H. P. Seifert, P. Spätig, A. Zhang, S. Ritter, G. S. Rao, Environmental Reduction Effect of High Temperature Water and Hydrogen on Fracture Resistance of Low Alloy Reactor Pressure Vessel Steels, *FONTEVRAUD 9*, Paper No 00032.

[7] **Z. Que**, H.P. Seifert, P. Spätig, S. Ritter, G. S. Rao, High-Temperature Water Effects on the Fracture Behaviour of Low-Alloy RPV Steels, *EUROCORR 2016*, CD-ROM/USB, Paper No 52357.

[8] S. Roychowdhury, H.P. Seifert, P. Spätig, **Z. Que**, Effect of high-temperature water and hydrogen on the fracture behavior of a low-alloy reactor pressure vessel steel, *Journal of Nuclear Materials* 478 (2016) 343-364. doi:10.1016/j.jnucmat.2016.05.033.

[9] G.S. Rao, H.P. Seifert, S. Ritter, P. Spätig, **Z. Que**, Effect of hydrogen on tensile behavior of low alloy steel in the regime of dynamic strain ageing, *Procedia Structural Integrity* 2 (2016) 3399-3406. doi:10.1016/j.prostr.2016.06.424.

[10] S. Roychowdhury, H.P. Seifert, P. Spätig, **Z. Que**, Effect of high temperature water and hydrogen on the fracture behaviour of a low-alloy reactor pressure vessel steel, in Proceedings of 17th International Conference on Environmental Degradation of Materials in Nuclear Power Systems - Water Reactors, Ottawa, Ontario, Canada, August 9-13, 2015.

[11] H.P. Seifert, S. Ritter, P. Spätig, J. Bai, W. Chen, **Z. Que**, "Safe long-term operation in the context of environmental effects on fracture, fatigue and environmentally-assisted cracking," PSI, Villigen, Final report of the SAFE-II project 2018. PSI Report No. 18-03 ISSN 1019-0643.

Ce document a été imprimé au Centre d’impression EPFL,
imprimerie climatiquement neutre, certifiée myClimate.